THE UNIVERSITY *of* EDINBURGH

THE UNIVERSITY *of* EDINBURGH
School of Engineering

A thesis submitted for the degree of

Doctor of Philosophy

Vortex-Induced Vibrations of Dynamic Power Cables for Floating Offshore Wind Turbines: Influence of Currents, Waves, and Cable Properties

---

Peter James Mcleod Elrick

School of Engineering

University of Edinburgh

DECLARATION OF ORIGINALITY

I declare that this thesis has been composed solely by myself and that it has not been submitted, in whole or in part, in any previous application for a degree. Except where states otherwise by reference or acknowledgment, the work presented is entirely my own.

Parts of this work has been published in Elrick, P, & Venugopal, V. "Vortex-Induced Vibrations of Dynamic Power Cable for Floating Wind Turbines." *Proceedings of the ASME 2023 42nd International Conference on Ocean, Offshore and Arctic Engineering*. Melbourne, Australia. June 11–16, 2023. V007T08A026. ASME. https://doi.org/10.1115/OMAE2023-100890

ABSTRACT

This research investigates the influence of vortex-induced vibrations (VIV) on dynamic power cables for floating offshore wind turbines. This was conducted through the use of two different numerical modelling tools, OrcaFlex and Shear7. Shear7, a frequency domain VIV prediction model was coupled with OrcaFlex, a time-domain three-dimensional finite element analysis software. Two popular numerical methods, Iwans and Blevins Wake Oscillator (IBWO), Milan Wake Oscillator (MWO) are employed for predicting cable's VIV. These models are validated against scaled down experimental results for a dynamic power cable. Shear7 produces the most accurate prediction and is chosen for further analysis of additional parameters. MWO seriously struggles and is deemed unsuitable for use in this context. IBWO predicts Root Mean Square (RMS) crossflow displacements up to four times greater than Shear7.

The environment in which dynamic power cables will be deployed will potentially be in locations with extreme subsea currents and waves. As such it is important to understand the influence these will have on the VIV of these cables. Through this research multiple parameters were investigated to determine the impact these have on the VIV behaviour. The current the cable was exposed to was varied to account for known current behaviour at sites likely to host FOWTs. It was found that the profile, direction relative to the plane of the cable, and speed of the currents all have significant effects on the VIV behaviour. Different current directions result in drastically altering the VIV profile of the dynamic power cable by changing the maximum predicted amplitude and location along the cable length. A change from uniform current of 1m/s to a shear profile based on site data at Hywind, with a surface current speed of 1m/s, resulted in a decrease in RMS displacement of 10% at angle 0, 3% at angle 90, and 21% at angle 180.

The deployed cable configuration was studied to observe how this impacted the VIV behaviour and under what conditions would a certain configuration be preferred. A lazy wave, double wave, steep wave, and tethered lazy wave were analysed. It was found that different configurations lead to substantially different RMS crossflow displacements and locations of largest displacement. Current directions and profiles were also shown to impact each configuration uniquely.

The structural properties of an object undergoing VIV are known to greatly impact the response. With various cable designs still being investigated there is no preferred properties in operation. As such, multiple cables are used to determine the scale of this influence on the VIV response. The bending

stiffness, diameter, and mass ratio are all shown to alter the VIV response of the cable. This is not only due to fundamental VIV influence but also changes on the global scale of the cable in terms of sensitivity to deformation and influences this has on the relative velocity. The cable density influences the extent of cable deformation which in turn changes the relative velocity resulting in more extreme variations in amplitude along the cable length the less dense the cable is. The bending stiffness of the cable has a similar impact, where the greater the stiffness the lower the variation in amplitude over cable length. Regarding diameter, the greater the diameter the lower the predicted frequency and less range in amplitude.

Waves are known to influence the VIV behaviour of structural bodies. In offshore sites with high wind speeds, it is likely that the dynamic power cables will be exposed to waves of significant magnitude. The impact of the wave height, period, and direction are studied to assess the importance of this when considering the VIV response for dynamic cables. The wave height was shown to result in large stresses on the cable as it increases. The direction of the waves are also shown to alter the VIV behaviour, this was elevated when compared against current direction as well. Wave height and direction were found to greatly influence the RMS stress the cable was exposed to. A wave height of 8m at angle 0 resulted in stress over three times larger at certain locations compared to just current. For angle 90 a 50% increase could be seen. For angle 180, the mean stress over the full cable length was found to show minimal change.

The influence of all the parameters discussed shows how crucial further investigation and analysis is to fully understand and predict the VIV influence before wide scale deployment.

ACKNOWLEDGEMENTS

I would like to express my deepest gratitude to my supervisor, Venki Venugopal, for his invaluable guidance, support, and encouragement throughout my PhD journey. His expertise and insights have been instrumental in shaping my research.

I am also grateful to my mum and the lunch time walks we took together. These walks provided a much-needed break from my research and allowed me to clear my head and refocus. These moments of respite had an invaluable contribution on keeping my sanity in check when the numerical models just wouldn't behave.

I would like to acknowledge the ESRPC for providing financial support for my research and giving me the opportunity to pursue a PhD.

Finally, I would like to thank my family and friends for their unwavering love, support, and encouragement throughout my academic pursuits.

LAY SUMMARY

This research aims to investigate the vortex-induced vibrations (VIV) on dynamic power cables for floating wind turbines under varying environmental conditions. The environmental conditions and the influence on VIV are investigated through the use of a numerical VIV prediction model software Shear7. This was coupled with OrcaFlex, a time-domain hydrodynamic model.

VIV are a hydrodynamic phenomenon, as fluid flows past an object vortices can develop. These vortices impart a varying force on the object in both the in-line and crossflow direction. This causes the object to vibrate. The frequency of this vibration is initially dictated by the relative velocity of the fluid flow, however, as this frequency approaches the natural frequency of the object a phenomenon called “lock-in” can occur. This results in much larger vibrations at the natural frequency of the object which can cause significant fatigue. Dynamic power cables are located in sites with potentially substantial current speeds and wave conditions which can excite VIV along the cable.

The current conditions explored are speed, direction, and shear profile. All of these are found to greatly influence the VIV response. As the current speed increases the most significant vibrations are found to be increasingly localised to certain sections along the cable length. For an angle of 0 this is towards the touchdown point of the cable and for angle 180 this is towards the hang-off point. An angle of 90 degrees doesn’t showcase this large dependence. A shear profile is seen to reduce the RMS displacement along the cable length compared to a uniform profile. The magnitude of this decrease is dependent on the shear profile.

The wave conditions investigated are height, period, and direction relative to current. As the wave height increase it results in a greater induced stress on the cable. There is no obvious link observed between the wave period and the induced stress on the cable. The wave direction relative to current direction is shown to have a substantial impact on stress. The greatest induced stress is seen when the wave is co-linear to current direction, with this decreasing as it tends to perpendicular and then increasing after this as it tends to being directly opposite. When directly opposite the stress is less than when the wave direction is co-linear.

Dynamic power cables are required to be flexible in nature due to the harsh conditions they are present in. There is no current optimal design of cables due to immaturity of the area, and as such, the cable properties are not determined. The bending stiffness, diameter, and density of the cable are investigated. It is found that all of these parameters influence the VIV response of a full-scale cable. The lower the bending stiffness and density of the cable the more extreme the localisation of the

largest vibrations, this is due to the cable deformation. When the cable deforms due to the current it results in large variations in the relative velocity along its length. This means certain sections of the cable experience larger velocities so are subjected to greater vibrations, compared to other locations where due to the angle of inclination experience much smaller relative velocities.

TABLE OF CONTENTS

LIST OF FIGURES

LIST OF TABLES

1 INTRODUCTION

There have been global initiatives to limit the global warming of the planet, most notably the Paris Agreement which set out to limit the global temperature increase to less than 2 degrees Celsius relative to pre-industrial levels. Electricity and heat generation accounts for over 40% of CO_2 emissions globally (International Energy Agency, 2021), and thus it is an area where substantial improvements can be made. Renewable electricity generation provides a low carbon electricity supply which is vital to curb the increase in CO2 emissions. The UK benefits from having substantial wind and marine resources, over 40% of the wind resource across the whole of Europe (Greenmatch, 2017). On a global scale the demand on electricity has risen annually since records started (International Energy Agency, 2021). With this trend set to continue the necessity for sustainable electricity generation increases.

As suitable near shore sites for fixed bottom wind turbines are exhausted expansion into deeper waters is required. In addition to the benefit of reduced competition for sites, faster and more consistent wind speeds are available. At deeper waters, the preferred base for wind turbines is floating over fixed as the large depths make it excessively difficult to secure the structure to the seabed. When considering the global scene, countries with limited shallow waters, such as France, Japan, and the West Coast of USA, are highlighted as locations for potential huge scale deployment.

There is global interest in FOWT, and there are currently four floating wind turbine arrays: Hywind Scotland 30MW total (Peterhead), Hywind Tampen 95 MW (Norway), Kincardine 50 MW total (Aberdeen) and Windfloat 25 MW total (Portugal). There are other smaller FOWT projects: Fukushima Forward, Groix and Belle-ile, and the Gaelectric Energy Storage Array[1].

Wind generated a record amount of energy in the UK in 2023, supplying 29.4% of electricity demand[2]. The UK Government recently announced their aim to increase the capacity of offshore wind farms in the UK from 10 GW to 40 GW by 2030 (Durakovic, 2020). This substantial increase in capacity will require the deployment of wind farms in deeper waters, where floating wind turbines would be the energy converter of choice. Not only are offshore wind turbines environmentally beneficial they are also economically viable when compared to more traditional sources of generation such as coal and gas. This is shown by the latest Contract for Difference bid for offshore wind turbines which landed on

[1] https://en.wikipedia.org/wiki/Floating_wind_turbine#cite_note-69
[2] https://www.nationalgrideso.com/news/britains-electricity-explained-2023-review

£37.35/MWh[3], below the wholesale electricity price. Unsubsidised electricity delivered from wind turbines highlights their economic success and the future they have in the UK energy mix.

To help meet this pledge for offshore wind the UK government has set a target to deliver 5GW of floating wind by 2030[4]. The Crown Estate recently delivered a new leasing for offshore wind farms to increase capacity by 7.9GW. Crown Estate Scotland announced the outcome of its most recent leasing in January 2022. The results from this are permission for 17 new projects with a total capacity of 24.8GW, with 14.6GW assigned to floating wind.

As an emerging technology there is still lots of room for innovation within the FOWT sphere. One of these is the choice of floating platform. Currently the most promising options are spar, semi-submersible and tension leg platforms. Kincardine and WindFloat wind turbine arrays use the semi-submersible platform. At the Hywind Tampen and Peterhead sites the spar platform is deployed. The platform initially chosen for investigation in this work was a semi-submersible platform based on the work done by NREL FOWT (Jonkman et al., 2010).

Transmitting the electricity generated by offshore wind turbines back to the mainland, where the large demand centres are, is done by power cables. Traditionally offshore wind turbines have foundations secured to the seafloor. This allows the cable to exit at this point and run along the seabed back to the shore. This is not possible with floating wind turbines as there is no solid structure that extends all the way down to the seabed. Instead, the cable must traverse across the water column from floating platform to seabed. This requires a new cable design to survive the hostile environment where typical offshore cables would fail due to the large bending and tension loads.

1.1 General Background of Dynamic Subsea Power Cables

There have been reviews of academic literature conducted around dynamic power cables but minimal discussion surrounding the fatigue inducing factors and failure modes of cables, and next to nothing on VIV behaviour. CoreWind 2020, produced a review of the dynamic power cable system which addresses the current scene, discussing aspects such as installation, cable cross-section and configuration, and operation and maintenance. Taormina et al. 2018, performed a review of the potential environmental impacts of deployment of subsea power cables. Weerheim, 2018, performed

[3]https://renews.biz/78997/update-owic-hails-record-low-offshore-wind-strike-price/#:~:text=The%20offshore%20projects%20landed%20CfDs,price%20ever%20for%20any%20technology.
[4] https://www.thecrownestate.co.uk/en-gb/what-we-do/on-the-seabed/floating-offshore-wind/#:~:text=The%20Government%20has%20set%20an,achieve%20its%20net%20zero%20ambitions.

a literature study of the development of dynamic power cables for floating wind turbines. It discusses potential cable arrangements, the design elements of the cable, cable damages, loads, and fatigue. DNV GL AS 2016, provides a comprehensive overview of the state of subsea power cables for wind turbines, providing useful background information on the full project design process.

There are two main companies in the cable manufacturing industry, these are JDR Cables and Nexans making up 33.9% and 25.7% of the market share, respectively. The following three biggest competitors are NSW, Prysmian and Draka contributing approximately 12.6%, 9.3% and 8.7%, respectively (El Mountassir & Strang-Moran, 2018).

With mooring and anchoring optimised within the oil and gas industry, with lots of this information readily transferrable, the obvious technology requiring further development is the power cables. This is exemplified by the fact that subsea power cables account for 75-80% of the total insurance cost claims for offshore wind whilst only contributing to 9% of the overall cost of the farm (El Mountassir and Strang-Moran, 2018). This is evidently an area where drastic improvements can be made to help further drive down costs and increase up time and profitability.

There are numerous reasons for failure of power cables, the majority of which are not results of the hostile environment where they are often located. The principle reasons for failure are electrical faults 47%, manufacturing and installation 37%, external and environmental 13%, and cable replacements 3% (El Mountassir & Strang-Moran, 2018).

1.1.1 Why Are Dynamic Subsea Power Cables Required?

The power cables used for floating wind turbines are required to be dynamic to be able to absorb the loads they are exposed to in the harsh ocean conditions they are located. These loads are predominantly due to ocean currents, waves, and platform induced motion. Standard stationary power cables would be unable to survive in these conditions due to their inability to effectively absorb motions. This is because of their higher bending stiffness not allowing adequate displacement from static location. The movement and cable deformation allows for absorption and redistribution of incident forces.

Dynamic power cables require additional armour, greater fatigue resistance, greater axial strength, and greater bending stiffness. This leads to larger weight and outer diameter which induces greater tension on the cable itself, especially at the hang off point. To accommodate these requirements the configuration of the cable is of extreme importance. It is important to understand the fatigue life of these power cables as failure is expensive and potentially dangerous.

1.1.2 Where Are Dynamic Subsea Power Cables Deployed?

Dynamic power cables are used offshore for marine energy converters such as tidal turbines, wave energy converters, and floating offshore wind turbines. Orbital (tidal turbine) and Hywind (FOWT array) are two examples that use such cables and are both located in the North of Scotland. Out of these energy converters the one with the greatest potential for large scale deployment is the FOWT. As such these are the focus of the majority of research conducted.

1.2 AIMS AND OBJECTIVES

VIV of the power cable leads to fatigue loading and, eventually, permanent damage reducing the tensile strength of the cable and increasing the likelihood of failure. The potential damage of the VIV has not been comprehensively considered for dynamic power cables. It is important to understand the VIV impact on the power cables prior to full large-scale deployment. This may lead to a reduction in production costs if a lower safety factor is suitable, reduced maintenance if the cable is always within a safe fatigue life, and increased safety if the likelihood of failure is reduced. Additionally, some FOWT sites may be particularly susceptible to VIV fatigue depending on environmental conditions and suppression methods may be required to ensure an adequate safety factor is accounted for.

The VIV of risers and umbilicals for the oil and gas industry is well documented and investigated research area with which similarities can be drawn. The majority of studies are aimed at targeting scaled down experiments owing to the excessive costs for full scale investigation. One of the most significant experiments performed, in terms of scale, was conducted in the Gulf Stream for a composite pipe of length 152m and outer diameter 0.0363m (Jaiswal & Vandiver, 2007). High mode number vibrations were observed, greater than the 10^{th} mode.

This research mainly aims to identify the susceptibility of dynamic power cables to VIV depending on various parameters such as environmental conditions, cable properties, and cable configurations. This allows for the identification of particular locations susceptible to fatigue along the cable length, dependence on current direction, current profile, and the impact of changing cable orientation and configuration.

1.2.1 Main Objectives

1. To study the dynamic power cable by numerical modelling methods using industry standard software tools and evaluate their suitability:

There are numerous vortex-induced vibrations prediction tools available. The suitability of these models is tied to the data set used to calibrate them. The models chosen for this research are the

Milan Wake Oscillator, Iwans and Blevins Wake Oscillator, and Shear7, a frequency domain model. These tools are calibrated against a scaled down dynamic power cable and then compared against one another for a full-scale model. The sensitivity of the numerical parameters of the Shear7 model are also investigated. This is captured within Chapter 3.2, Chapter 4, and Chapter 5.

2. To investigate VIV of the cable for various current profiles and propagation directions:

With deeper waters scoped out for floating offshore wind turbine (FOWT) deployment the environmental conditions may vary drastically from one site to another. This may render some sites highly susceptible to VIV which could impact the fatigue life of the cable. Understanding how different current profiles, speeds, and directions influence the response is important to categorise whether a site is potentially dangerous due to restricting VIV interactions. This is explored in Chapter 7.

3. To investigate the impact of different power cable configurations, power cable designs, and additional physical parameters such as buoyancy modules and marine growth on the VIV behaviour:

There are multiple different cable configurations available, with these having different benefits and costs associated. Understanding the VIV response of these different shapes is important to appreciate the potential limitations and how this may be exacerbated by certain environmental conditions. This is discussed in Chapter 8. With dynamic power cable design still in its infancy, the properties of the cables are likely to go through sizable changes until an optimal design is decided. The properties of an object are known to have an impact on the VIV behaviour, recognising this in the context of dynamic power cables is valuable as certain variables may result in dangerous VIV responses. This is discussed in Chapter 6. Other factors related to external cable properties are investigated, these are the impact of buoyancy modules, straking, and marine growth. Straking is deployed to disrupt the water flow around the cable which reduces the formation of vortices and assists in minimising the induced vibrations. This helps to extend the lifespan of the cables. All of these factors are found to substantially influence the VIV response. Buoyancy module length, and diameter is found to alter the RMS crossflow displacement. Marine growth is predicted to result in greater displacement and frequency response if present. The mode of vibrations for when straking is present compared to not is shown to not sufficiently alter the VIV behaviour of the section of the cable that remains bare. These results are explored in Chapter 8, 9.5, 9.6, and 9.7.

4. To investigate the influence of waves on the VIV behaviour for varying heights periods and propagation directions using Shear7:

In deeper waters there is the potential for considerably large wave heights and storm conditions. While storm conditions aren't investigated in this work, the influences of wave height, direction and period are. The influences of the wave parameters can greatly influence the platform motion response and the VIV of an object. Neglecting this could lead to underestimation of the potential increase in VIV magnitude compared to only currents. This is discussed in Chapter 10.

1.3 Original Contribution

This research aims to better understand the influence of various environmental and numerical parameters on the vortex-induced vibration of dynamic power cables. There exist gaps in literature around understanding the changes to VIV response that are brought on by deploying a highly flexible object in new configurations and hostile environmental conditions. It is important to appreciate the impact of these factors when designing and deploying offshore cables. Shear7 and OrcaFlex have been used previously to model the VIV along dynamic power cables but not in such depth to fully consider the influence of the many different factors. These previous studies are discussed in detail in Chapter 2.7. This research aims to quantify the impact of current direction, speed, and profile, cable configuration, profile, and buoyancy module arrangements, wave heights, period, and direction, and numerical models, and parameters. Covering a broad range of topics allows for an understanding of the multiple different parameters that influence the response of the cable and appreciate which parameters are likely to result in the greatest influence on the cable.

1.4 Thesis Layout and Organisation

This research is organised into multiple chapters with the general layout of an introduction, literature review, methodology, and combined results and discussion section.

The introduction section aims to introduce the reader to the floating offshore wind landscape while introducing the current dynamic power cable scene and highlighting the importance of understanding the knowledge gaps.

The literature review section explains the most relevant work done to date in the field of vortex-induced vibrations and how they relate to the research conducted. An overview on the current dynamic power cable scene is presented, highlighting the shortcomings still present.

The methodology section lays out the numerical models used and explains the underlying theory behind them. The numerical model set-up is explained, informing on the floating wind platform used and different cable configurations. The different environmental parameters are discussed along with

cable properties. There is a validation section outlining the justification of the numerical parameters chosen in this research and how the models were calibrated.

The results and discussion chapter is split into six sections, with each aiming to explore a different theme. These are the cable configuration, cable properties, current profile, wave parameters, numerical models, and numerical parameters.

2 LITERATURE REVIEW

There have been some investigations into dynamic power cables for offshore energy converters but mainly in the context of measuring tension, platform motion, and over-bending. These studies have predominantly focused on investigating the benefits of a lazy-wave design over catenary and situations where failure may occur. These configurations can be seen in Figure 2.7. Investigations into the behaviour of the internal components of the cable have been conducted. specifically discussing the stick-slip behaviour and the potential impact this has on the cable's properties.

Specifically, regarding the VIV of a dynamic power cable there have been very few studies. Delizisis et al. 2022, and de Wilde et al. 2021, performed experiments on a dynamic power cable constrained in the vertical plane with numerical analysis then carried out using Shear7. With the correct hydrodynamic parameters modelling software are able to accurately predict the maximum displacement amplitude relative to current speed. This is highlighted in Chapter 3.2, where it is shown that when correctly calibrated the numerical predictions closely follow the experimental results (Delizisis, 2022). The gap in literature is predominantly centred around the lazy wave and alternative configurations and the impact that has on the VIV of dynamic power cables. There have been few studies focusing on the VIV of flexible risers in the catenary and lazy wave configuration, but this data isn't categorically transferrable due to differences in the material properties.

2.1 POWER CABLE BACKGROUND

The electrical cables used for FOWT are of the umbilical typology, meaning there are multiple internal components in addition to electrical conductors such as data cables. This is because they provide service support from the main station to the individual turbines to ensure things such as correct orientation and operation of the FOWT farm (Sobhaniasl et al., 2020). Umbilicals are most commonly seen in the offshore oil and gas industry where they are of the steel variety and the curvature of these cables governs the fatigue problem (Dai et al., 2020). These large curvatures typically occur at large wave heights and near wave periods of resonance resulting in large amplitude of oscillations (Yang et al., 2018) .

Table 2-1: Dynamic vs Static Power Cable Configuration (JDR via CoreWind, 2020)

Dynamic Power Cable	Static Power Cable
Image source: JDR Cable Systems 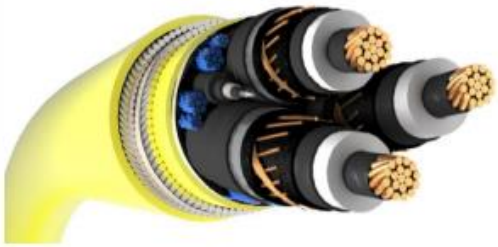	Image source: JDR Cable Systems 
Outer Protective Sheath	Light Protective Rovings
Even number of Contra-helical Armour Wire Strength Member Layers	Single Armour Wire Strength Member Layer
Inner Bedding Layer Sheath	Inner Bedding Layer Rovings
Twisted Triad Bundle of Fibre Optic Cable and Electrical Cores with Wire based Screen	Twisted Triad Bundle of Fibre Optic Cable and Electrical Cores with Screen
Good Torsional Balance Greater Axial Strength (Max Tension) Greater Fatigue Resistance Greater Bend Stiffness Greater Weight and Outer Diameter Greater Abrasion Protection and Impact Resistance	Coil-able for low cost basket vessels Sufficient Axial Strength for shallow installation Light Weight Greater Flexibility (Smaller Minimum Bend Radius)

2.1.1 Cross-Sectional Components

When considering dynamic power cables two standards are used to provide criteria and guidance for design and analysis. These standards are DNVGL-ST-0359 and DNV-OS-J10, the DNVGL-ST-0359 standard is shown in Figure 1 (DNVGL, 2016). The cable consists of numerous components with the most influential being the choice of conductor and armour sheathing.

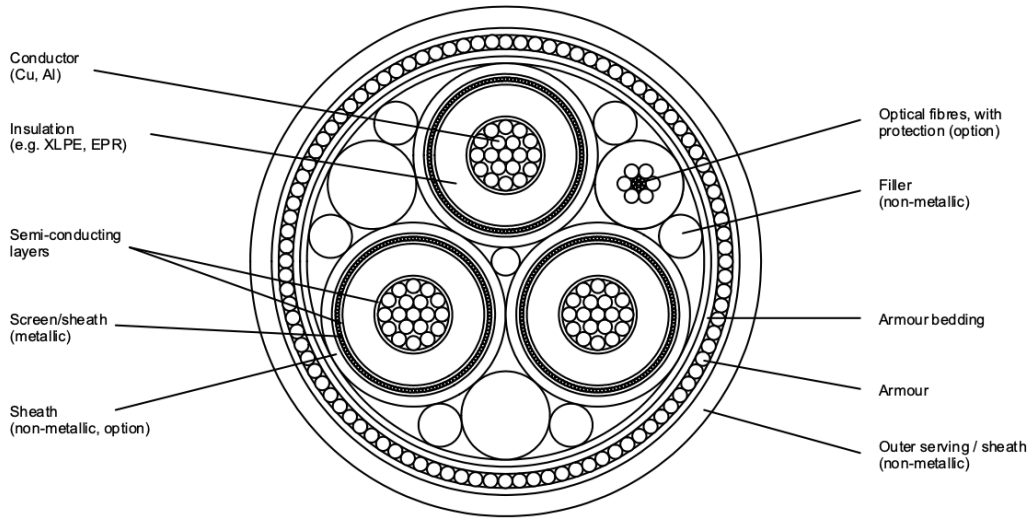

Figure 2-1: Cross-section of a dynamic power cable (DNVGL, 2016)

The internal structure is very similar to that of an umbilical, internal friction between components is possible as is slipping of one structure over another. This impacts the bending stiffness and as such this is dependent on factors such as helical winding and bending curvature.

Karlsen et al. 2009, looked into the lay angles of copper phases and armouring layers, as well as controlling the friction forces between conductors and load carrying elements. This is important to ensure the desired stress distribution and prevent mechanical overloading of the conductors. This investigation was conducted using UFLEX2D, a non-linear FEA stress analysis software, and experimental testing. It was found that a dynamic deep-water power cable requires stress relief to prevent creep on the copper. Creep is progressive deformation of a material under constant stress. Altering the lay-up angles of both copper conductors and armouring layers can help relieve creep. The frictional forces between copper wires and armouring layers are more than sufficient to prevent copper slipping occurring.

2.1.1.1 Optical Fibre

Fibre optic cables are included within the subsea power cables to form a communication network allowing for the relaying of data readings from each turbine and thus intervention if required. The exact composition of the fibre optic cable is heavily dependent on the communication requirements, for windfarm applications a single cable can obtain up to 96 fibres (CoreWind, 2020). The fibre bundles are contained within a steel tube with an additional layer of armour and sheathing required to ensure adequate protection. The size of the fibre optic cable is dependent on the requirements desired and the outer diameter of the power cable.

2.1.1.2 Conductor

There are two preferred choices for conductors within a subsea power cable: aluminium and copper. The core size of the cable has the greatest impact on the total cable outer diameter and is largely determined by the conductor choice. Copper has a higher conductivity than aluminium meaning that for an aluminium cable to meet the same current carrying requirements for the output power a larger core size is required. Aluminium is, however, substantially less dense than copper. A cable with a larger diameter is more susceptible to exciting VIV. Comparatively speaking, when comparing the two conductor choices over the scale of the entire cable length the difference in costs is minimal and site dependent on which is preferable. The most important property, and why copper is the preferred conductor of choice, is that copper has a greater stress fatigue resistance to amplitude vibrations which results in an increased life (Boone & Christiaan, 2015) . Copper is also less prone to failure due to corrosion; aluminium is highly reactive and susceptible to seawater corrosion and thus requires additional protection.

Thies et al., 2019, investigated the suitability of aluminium conductor compared to copper via a global load analysis, taking into account the forces and motions acting on the cable due to the ocean environment and the aero-hydrodynamic response of the floating structure. The aerodynamic model was produced using FAST and the hydrodynamic model was produced using OrcaFlex. The results show that aluminium is capable of performing as a conductor for subsea power cables and leads to lower peak tension at attachment points and lower effective tension across the cable when compared to copper. This is however a trade off against the requirement for increased cable diameter. To adequately assess the capability a local analysis would also have been required, which would have analysed the aluminium within the cross section of the cable including internal interactions such as stick-slip and friction.

Regarding failure due to the conductors within dynamic power cables Karlsen 2010 and Nasution et al. 2012, investigated the fatigue of copper wires. Karlsen used an experimental method to assess the impact of friction, creep properties, and high tension on wire interaction. This was done through rotational bending at 112 rotations per minute with an applied tension of 8kN and 2kN both examined. Failure was defined as the first rapid elongation of the wire not due to tension increase. The results show that a higher tension decreases the number of cycles to failure and that fretting plays a less dominating role than high tension. Nasution et al. 2012, investigated the fatigue performance of a single wire 95 mm^2 copper conductor and the impact of geometrical irregularities in the wires due to the manufacturing process. Fatigue testing was conducted by applying axial tension to the wire and

the corresponding strain was analysed using UFlex3d, a finite element software. The results show that surface irregularities can result in differences in fatigue performances between layers.

2.1.1.3 Insulation

Cross-linked polyethylene (XLPE) is the most prominent material utilised for insulation in submarine power cables and has been in use since 1973. XLPE consists of cross-linked long molecular chains of LDPE forming a three-dimensional network. Low density polyethylene is the alternative, but XLPE is preferred due to its superior dielectric loss characteristic property, resulting in the minimisation of insulation thickness (Nexans, 2013).

2.1.1.4 Armour

The armour of the dynamic power cable is subject to high mechanical loading from the floating platforms response to waves, wind, swell, and subsea currents, as well as the risk of wear due to contact. Since retirement and replacement of a cable is not envisioned, the robustness and fatigue resistance are vital to ensure the viability of floating offshore wind turbines. Dynamic cables often have double armouring to increase torsional stiffness whereas static cables only require a single layer of armour.

Dynamic high voltage subsea power cables require sheathing to protect the insulation from water ingress and provide a means to handle potential short circuit currents (IEC 60840, 2004). The choice of sheathing is limited for this application due to the dynamic conditions. Lead is often chosen for static power cables due to its chemical stability and ductility. Lead alloys, however, are strongly influenced by time-dependant phenomena such as creep and recrystallization. Viespoli et al. 2020, conducted experimental fatigue tests at two different strain rates with analysis of the cables post-mortem done via scanning electron microscopy. The results indicate that lead alloys are influenced by creep deformation resulting in shorter fatigue life when deformation occurs. The deformations investigated were at a much smaller scale than those present in a dynamic power cable highlighting the unsuitability of lead for this application. Instead, longitudinally welded copper sheaths or non-metallic water barriers are preferred (Sonerud et al., 2012).

2.1.1.5 Bend Stiffeners

Bend stiffeners are deployed at both the hang-off and touchdown point of the cable to help extend the life of umbilicals and power cables. This is achieved by increasing the local stiffness of the cable to limit bending stresses and curvature. They are often made from an elastomeric material to function in the constant loading environment they are found due to wave and current-induced motions. They

prevent structural damage to the cable due to overbending and have a conical shape to provide gradual increases in stiffness of the cable to prevent over bending at its termination point.

Figure 2-2: Bend stiffener example (Marinet, 2015)

CRP Subsea, Hellenic Cables, and University of Exeter conducted two tests on a dynamic power cable and bend stiffener combination (Marinet, 2015). The first test involved bending the cable at a 3.7° angle held in places by a constant force (40, 60, 80kN) of varying degree at a 10s period. The second test involved increasing the headstock angle to 4° and decreasing the cycle period from 10s to 1s. The results were compared for using a bend stiffener and not using a bend stiffener. The results showed that when utilising a bend stiffener, the power cables survived 3.7 times as many cycles as without and also was on average 72.5% stiffer than the power cable alone. These results highlight the importance of deploying bend stiffeners when considering power cables for floating wind turbines.

2.1.2 Stick-Slip Phenomenon

Due to the nature of the power cable, and its numerous internal components, modelling fatigue life is difficult due to the complex internal interactions. A stick-slip phenomenon is observed where the bending stiffness of the cable changes after a certain curvature due to the cable not being restricted by friction internally but instead the components are able to slide over one another reducing the bending stiffness. This can extend the fatigue life of the cable through damping or reduce the fatigue life if the initial high bending stiffness is not taken into account.

Coser et al. 2016, conducted cantilever beam tests and three-point bending tests on a power cable to determine how the bending stiffness varied under axial tensions from 0 - 212kN. The axial tension had

a substantial influence on the bending stiffness, increasing it from 0 to 2kN resulted in the stick bending stiffness increase by 146%. Further to this, viscoelastic behaviour was observed due to the multi-layer structure. The results were calibrated against a numerical model which showed good agreement for high tensions but less so for lower tensions.

2.2 Cable Configuration

There are many different potential cable arrangements, as shown in Figure 2-7, with the most common being the catenary and the lazy wave shape. The catenary design is often the preferred choice for mooring lines and other subsea structures, such as risers and umbilicals in the oil and gas industry, but in the context of dynamic subsea power cables the lazy wave appears to be the optimal design. Often when discussing a lazy wave cable configuration, the sag and hog bend are referred to. These can be seen in Figure 2-3, the sag bend is the dip seen in the cable a third along the length and the hog bend is the peak seen two thirds along the length.

The different configurations investigated in this study are a lazy wave, a steep tethered wave, a double wave, and a steep wave. The predominant differences between the configurations are the location of the buoyancy modules and thus, the resulting cable shape. Figure 2-3, Figure 2-4, Figure 2-5, and Figure 2-6 show the model configurations within OrcaFlex that are investigated in this study. In this study, the cable's hang-off point is at x = 0.

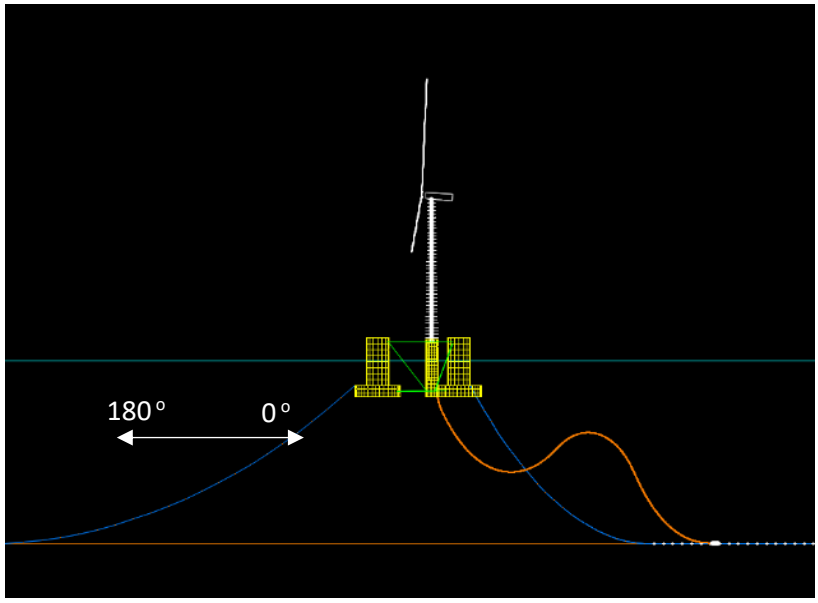

Figure 2-3: OrcaFlex model of the NREL FOWT and lazy wave dynamic power cable with current direction labelled

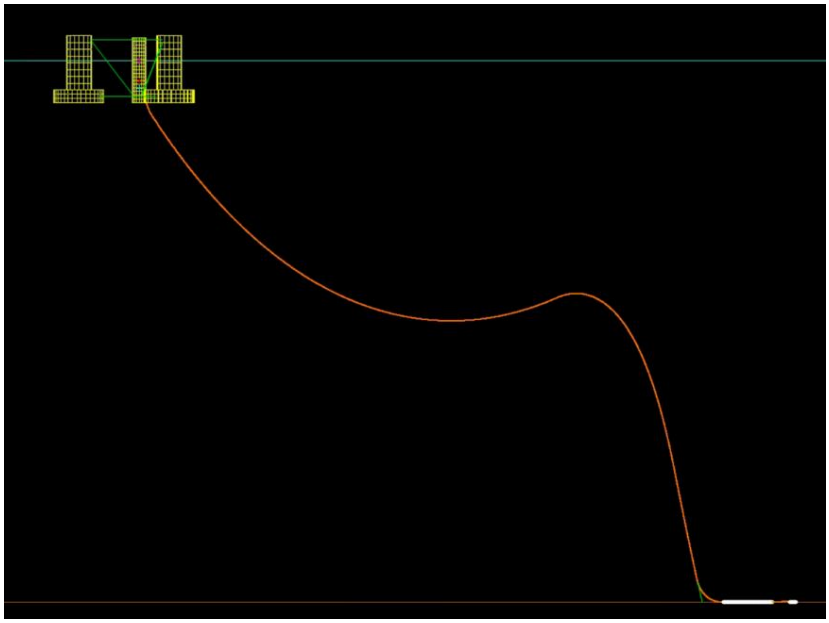

Figure 2-4: OrcaFlex model of the steep tethered wave dynamic power cable configuration

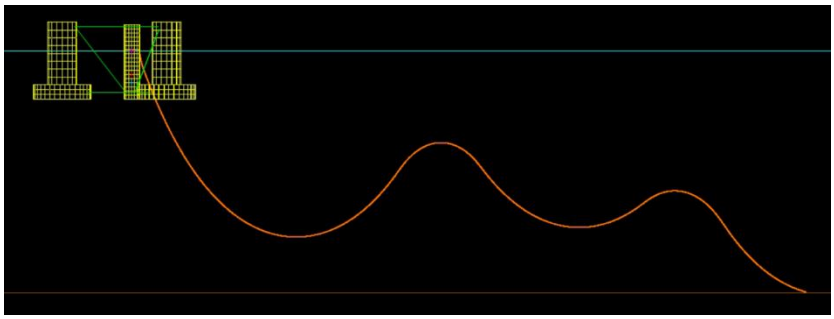

Figure 2-5: OrcaFlex model of the double wave dynamic power cable configuration

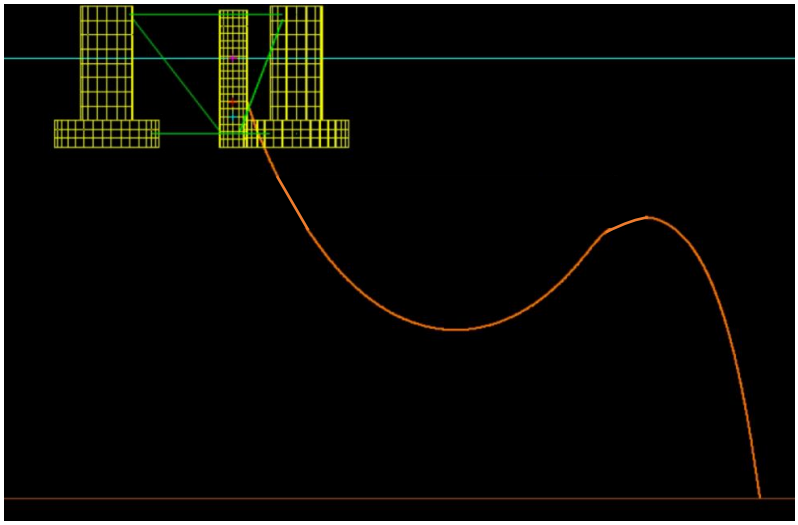

Figure 2-6: OrcaFlex model of the steep wave dynamic power cable configuration

The cable shape can have a substantial influence on the response to the environment. The catenary configuration is known to have a high risk of compression and as such is not generally considered for dynamic power cables. The lazy wave configuration is the currently preferred design due to requiring minimal subsea infrastructure, compared to a steep wave which often requires a subsea base and

subsea bend stiffeners. The steep wave does better maintain the configuration when exposed to environmental loads, so in scenarios where this compliance is important then they may be the configuration of choice. The double wave configuration is a more complex structure due to having multiple buoyancy sections. The predominant benefits of this configuration are in shallow water conditions where there is a reduction in curvature at the hang-off and touchdown points compared to the other cable configurations due to the more gradual decrease in water depth over the cable's length.

Rentschler et al. 2019, investigated catenary and lazy wave cable configurations for subsea dynamic umbilicals for FOWTs using OrcaFlex and analysing the tension and curvature at different water depths under gravitational loading. The lazy wave shape was preferable in all scenarios with the catenary configurations unfeasible in water depths over 100m due to critical tension at the hang-off point. The use of a bend stiffener was recommended to prevent over-bending for all scenarios. Dynamic loading due to the ocean environment has a substantial impact on the cable, without consideration of this a cable arrangement is not validated.

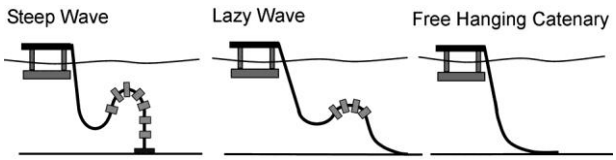

Figure 2-7: Typical flexible cable configurations (Clausen & D'Souza, 2001)

Silva et al. 2018, investigated the length of the buoyancy section of flexible risers in a lazy wave configuration using DEEPLINES, a FEA software, with global loading due to wind, wave and current conditions assessed. The buoyancy section length was varied over four different cases, ranging from the original lazy wave design to the no buoyancy section free hanging catenary. It was found that reducing the buoyancy section by 50% still resulted in a configuration classified as high safety (chance of failure in last operation year less than 10^{-5}), highlighting potential cost savings through reduction in material required.

Boo and Yang 2019, assessed the performance of two lazy-wave shape configurations of lengths 180m and 520m via a fully coupled dynamic analysis of a hybrid platform varying the power production loading and sea conditions using OrcaFlex. The cable was assessed by considering the tension load, hang-off load, touch down angles, and minimum bend radius. Both arrangements satisfied design requirements, the 180m cable was preferred due to lower variations in hang-off load angles. Fatigue analysis was conducted, and it was observed that the most significant damage occurred at the touch down point for both arrangements.

Zhao et al. 2021, compared the use of a double wave and a typical lazy wave configuration for a FOWT under wind, wave, and current loading using a fully coupled model within SIMO/REFLEX, a time-domain global analysis software. The S-N curve, with a rain flow counting method, was used to estimate the fatigue damage of the copper conductor. Both configurations were capable of withstanding a harsh environment, the double-wave showed superior performance in compression mitigation, anti-bending, and fatigue life. This is due to the extra wave arc providing improved compliance with the wave motion transfer and energy dissipation. For both configurations, the point of most significant fatigue was the hang-off point. The responses for both mooring lines and dynamic cables were dominated by the floating platform motion and sea current. Other protective ancillary equipment, such as bend stiffeners, were not modelled which would have supported the hang-off point.

When considering the VIV response, platform choice is unlikely to have the most substantial impact, compared to the current being the dominating environmental influence. Platform motion induced responses, due to waves and wind, could also play a significant part in overall behaviour and should be investigated further.

2.2.1 Buoyancy Modules

Buoyancy modules are deployed along the midsection of the cable so that it complies with the lazy wave shape. Figure 2-8 shows an example of buoyancy modules attached to a cable. As can be seen, the modules have significantly larger diameters than the cable and enclosed air inside to provide a buoyancy force to the cable midsection.

Figure 2-8: Buoyancy module example[5]

Over time these modules can lose their buoyancy as water seeps in, resulting in adjusting the cable shape. This needs to be accounted for when accurately modelling over an entire cable's life span. The length of buoyancy modules, diameter, and distance between modules are all factors that influence cable shape and response to incident loads. These parameters are investigated within this research. There is no preferred buoyancy module to cable spacing ratio with each individual deployment employing a unique configuration.

2.3 FAILURE

Power cables must be able to survive in the hostile conditions they are located. This involves being able to withstand substantial cyclic loads from waves, currents, and wind. loads lead to dynamic motion along the cable length which induces stress; accumulation of these stresses can eventually lead to fatigue. To reduce the impact of this, the fatigue strength of the cable is considered with double armouring and bend stiffeners deployed to prolong its life. The cost of cable failure is

[5]https://www.crpsubsea.com/crp-subsea-awarded-a-major-contract-to-provide-distributed-buoyancy-modules-dbms/

considerable, especially when taking into account not only repair costs but also generation revenue loss. From 2014-2017 cable failures in UK projects resulted in a total generation loss of 1.97TWh, around £227M (El Mountassir & Strang-Moran, 2018). It is estimated that 95% of all offshore wind farms experience cable related insurance pay-outs (CODAN, 2017). This further highlights the necessity to understand the cable behaviour to prevent failure in any situation it can be avoided. Dynamic power cables have additional costs associated with them as well, such as repairing and replacement being more difficult than for static power cables.

The most critical points of failure for the power cables occur at the touchdown and hang-off points. The hang-off point is the area of highest effective tension, (Thies et al., 2019), due to supporting the weight of the cable, whereas the touchdown point is at risk of compression leading to bird caging reducing the tensile strength of the cable permanently (Rentschler et al., 2019). Bird-caging is a type of stranded wire distortion where the strands of the wire unravel and expand outward compromising the integrity of the wire.

Curvature of the cable has a substantial influence on the induced fatigue of the cable. It has been observed previously, in the context of steel umbilicals, that curvature governs the fatigue problem (Dai et al., 2020). The larger the curvature, generally, the greater the fatigue induced. These larger curvatures typically occur at large wave height and near wave periods of resonance (Yang et al., 2018). With the lazy wave shape resulting in large curvature at points along the cable it is important to factor this in when determining the fatigue impact along the entire cable length.

2.3.1 Compression

Compression of the cable leads to serious damage, permanently reducing its tensile strength and potentially leading to failure. This circumstance must be avoided and is commonly done through the use of touchdown protectors at the point of contact between cable and seabed.

The risk of compression is dependent on multiple factors with the most prominent being the cable configuration. A catenary cable shape is more susceptible to compression than a lazy wave shape (Thies et al., 2012a). A lazy-wave design suppresses the dynamic motion response of the floating platform better than a catenary. Further to this, the lazy-wave configuration results in fewer fatigue cycles compared to the catenary and a reduced maximum tension. Different cable properties may be required depending on site conditions. Oud et al. 2021, investigated cable deployment at two different sites and found that in high current environments a lightweight cable was susceptible to compression and over-bending. It is important to investigate this risk before full-scale deployment.

2.3.2 Minimum Bending

Dynamic power cables have a minimum bending radius, this is the smallest radius that the cable must be bent to otherwise there is a risk of cracking leading to permanent cable damage. Thies et al. 2017, investigated the sensitivity of a dynamic subsea power cable to differing environmental conditions by varying the tidal range, current speed, and current direction using OrcaFlex. The minimum bending radius and effective tension along the power cable were analysed, as was the cable's weight to determine the influence this had on the mechanical loads. The marine energy converter was modelled as a floating-point absorber and based on a generic 3.25t buoy deployed at the Southwest Mooring Test Facility (SWMTF). The buoy located here had been installed with different three-leg catenary hybrid (rope-chain) mooring configurations between 2010 and 2016 (Harnois et al., 2013). As the water depth increased the effective tension across the cable increased and the lazy wave shape loses compliance. Low tides can lead to risk of compression at the touchdown point, which is one of the highest risks of cable failure. The direction of the tidal currents have significant impacts on the bending radius of the cable. The most impacted location identified, in terms of bend radius, is at the touchdown point where the bend radius can vary from 2m to 10m, depending on the current direction, with an angle of 0 relative to cable plane being the worst. The cable weight dictates the static tension of the system. A larger cable weight increases tension across the entire cable length with this most noticeable at the hang-off point.

2.3.3 Over Tension

Over-tension can lead to permanent damage of the cable, and in extreme cases, even snapping. Snapping is dangerous and requires replacement of the entire cable. This can be reduced through spreading the tension across the length of the cable and strengthening the cable at certain positions, preventing a concentration at a particular point. Bend stiffeners are also deployed to assist with this. The use of buoyancy modules also has an influence on the tension profile over the cable length and can be used to assist in alleviating locations with excessively high tension.

2.3.4 Marine Growth

Power cables provide appropriate conditions for the developments of reefs along their lengths. Living organisms make their home here and coral is often developed. The introduction of this impacts the behaviour of the cable: the diameter is changed locally, roughness is increased ,and the mass per unit length increases as well. In addition, these marine species adhering to the power cable results in an increase in axial tension and bending stiffness. There are means to reduce this through methods such as anti-bio fouling, but even the impact of these is limited. If strakes are deployed, to reduce the magnitude of VIV, these have their effectiveness reduced due to presence of marine life. The impact

of marine growth needs to be accounted for when modelling offshore structures due to the large influence they can have on the cable properties and thus VIV behaviour.

Griffiths 2022, investigated the marine growth behaviour for bottom spanning power cables. It was observed that marine growth is highly asymmetric. This has a substantial impact on the cable and leads to variations in flexibility, density, and size around the circumference of the cable. This influences the lift force on the cable. The influence of the marine growth is also shown to be dependent on the Reynolds number.

2.3.5 Installation

Installation of dynamic power cables is a difficult task and requires specialist ship vessels to do so, and also appropriate calm and safe weather conditions. The cables are substantial in length and diameter, and as such require large vessels to transport them many kilometres offshore. The installation stage is a time where damage is likely to occur due to unpredictable sea conditions or human error. Any faults introduced here can substantially influence the fatigue life. These can be due to kinks in the cable, anchoring damages from the laying vessel or inadequate coordination of the vessel as the cable is placed. The positioning and arrangement of the cable is important, and hence why different configurations are considered in this study. This positioning, however, can be lost during storms or installation and has the potential to result in cable failure.

Yuan et al. 2021, provided an overview of the different vessels for submarine cable laying. The demand for more advanced vessels is continually increasing with the ability to bury cables, scan the sea floor, and greater load capacity as wind turbines move further away from shore.

2.3.6 Future of FOWTs

Considering the future of FOWTs, where wide scale deployment is seen, there are numerous potential innovations that may become common place. A few examples of these are: further automation where the floating wind turbines are capable of installing themselves; further deployment of subsea vehicles that automatically repair cables and faults without requiring a human operator; and increased use of network sensors to constantly monitor cable conditions and detect any fluctuations that may be due to a fault or surge.

2.4 General VIV Discussion

Vortex induced vibrations are a well-known problem in fluid mechanics with a large number of studies being conducted in the area. Comprehensive review papers are available (Ali et al., 2021; Gabbai & Benaroya, 2005; T. Sarpkaya, 2004; Williamson & Govardhan, 2004). There have been numerous

experimental and numerical investigations conducted to help further understand this phenomenon. The majority of research within this area focuses on subsea marine risers and umbilicals for the oil and gas industry, tension cables for bridges, and subsea power cables on the sea floor, with a notable number of academic studies on rigid, elastically mounted rigid and flexible cylinders also present. As of now, there has been very limited investigation into the VIV of dynamic subsea power cables required for floating renewable energy converters such as FOWTs and wave energy converters.

2.5 GOVERNING PARAMETERS

When considering the frequency response of an object subject to VIV, this is tied to the following frequency parameters:

- f_{vac}: natural frequency in a vacuum
- f_{com}: lock-in frequency
- f_{ex}: frequency of oscillation
- f_{st}: vortex shedding frequency of a body at rest
- f_{vs}: vortex shedding frequency of a body in motion

For a cylinder, vortex shedding is related to the non-dimensional Strouhal number. The Strouhal number, St, describes an oscillating flow and is defined as (Strouhal, 1878):

$$St = f_{st}\frac{D}{U} \qquad \text{Eq. 2.1}$$

where U is the velocity of the ambient flow and D is the object diameter.

The Strouhal number emerges as the most robust parameter. The Strouhal number represents the ratio of inertial forces, due to the local acceleration of the flow, to the inertial forces, due to the convective acceleration. In flows characterized by a periodic motion, the Strouhal number is associated with the oscillations of the flow because of the inertial forces relative to the changes in velocity due to the convective acceleration of the flow field.

The frequency parameters, in turn with the flow, dictate the reduced velocity the object is exposed to:

$$V_r = \frac{U}{f_{ex}\mathrm{D}} \qquad \text{Eq. 2.2}$$

Where V_r is the reduced velocity.

The Strouhal number varies according to the Reynolds number and roughness of the cylinder. Different flow regimes are observed around a circular cylinder depending on the Reynolds number of the flow. Figure 2-9 shows the different behaviour that can be expected for different flow regimes (Blevins, 1977).

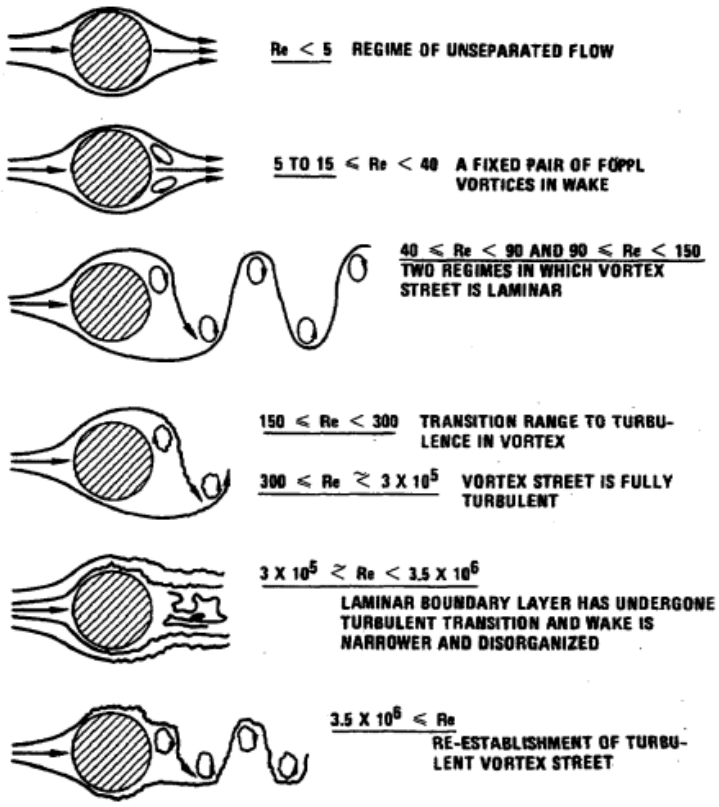

Figure 2-9: Flow regimes for fluid flow around a circular cylinder (Blevins, 1977)

There is significant documentation at low Reynolds Number, Re, but more research is necessary to understand the impact at higher subcritical Re and through the critical range as many practical applications occur within these regimes. Modelling at high Re is more difficult due to increased computing power required to model the small-scale hydrodynamic interactions and large-scale experimental set-ups required.

Unsteady hydrodynamic loads arising from the transverse pressure gradient acting on a body can excite a dynamic response. The natural frequencies of the structure can lead to large oscillations and excitation. When the vortex shedding frequency approaches one of the natural frequencies of the object it diverges from the Strouhal vibration frequency and begins to follow the excited natural frequency, this is known as lock-in. In the lock-in region, the oscillation of the cylinder can have a large amplitude which results in significant fatigue damage. At subcritical Re, the energy containing frequencies are confined to a narrow band and the Strouhal number is about 0.2 for smooth cylinders. In general, it is nearly constant around a value of 0.2 for the subcritical Reynold number range which

spans from 300 – 2x10^5 (S. S. Chen, 1977), but at higher and lower Reynolds numbers the Strouhal Number can substantially diverge from this.

Table 2-2: Flow Classification for Rigid Smooth Cylinders (T. "Sarp" Sarpkaya, 2010)

Regime	Reynolds Number Range	Characteristics	Strouhal Number
Subcritical	$< 2 \times 10^5$	Laminar flow into development of Karman vortex street	$0.212 - \frac{2.7}{Re}$
Critical	$2 \times 10^5 - 5 \times 10^5$	Unstable boundary layer, increase in Strouhal number, decrease in wake width	$0.2 - 0.35$
Supercritical	$5 \times 10^5 - 3 \times 10^6$	Unstable regime and loss of wake periodicity	$0.35 - 0.45$
Post-Supercritical	$> 3 \times 10^6$	Reappearance of wake periodicity	~ 0.28

This research is generally conducted within the upper subcritical to the lower supercritical flow regimes, the flow regimes are outlined in Table 2-2. The dependence of Strouhal Number on Reynolds number is shown further in Figure 2-10. These flow regimes aren't solved within Shear7, but it is important to understand the large variation in Strouhal Number that is seen experimentally and appreciate the issues when setting the Strouhal Number.

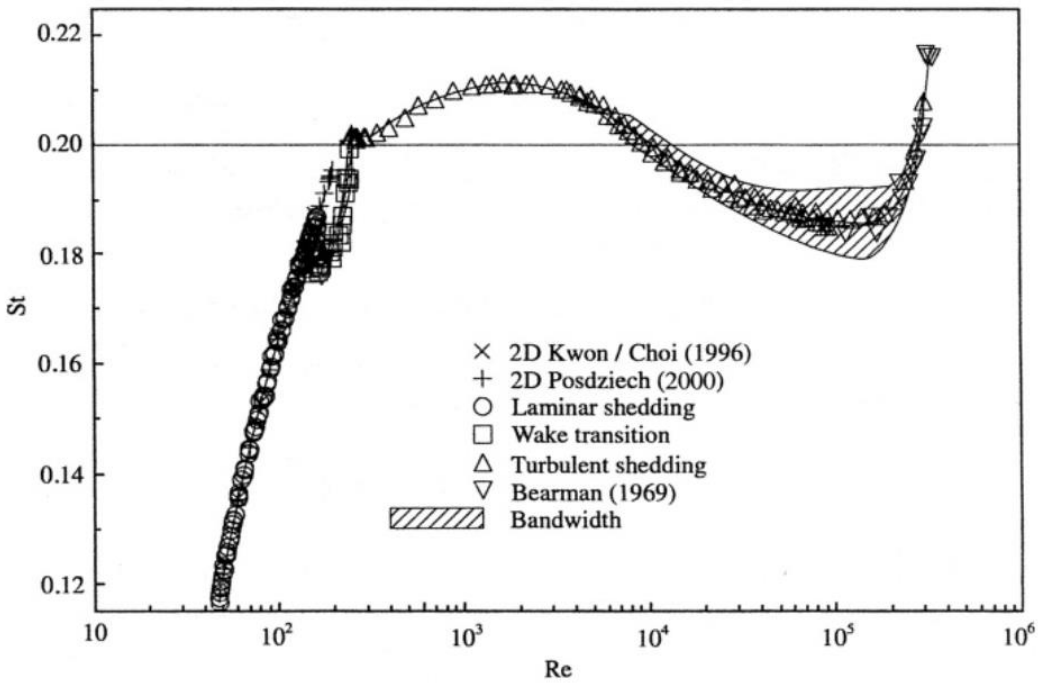

Figure 2-10: Comparison of experimental results relating Strouhal Number and Reynolds Number (Sarpkaya, 2010)

Experiments conducted at the UK National Physical Laboratory, 1969, have shown that, when the cylinder is free to oscillate, the sharp rise in the Strouhal number does not occur and remains at a

value nearly equal to that found at subcritical Reynolds numbers. This is shown in Figure 2-11 where the large jump wasn't observed.

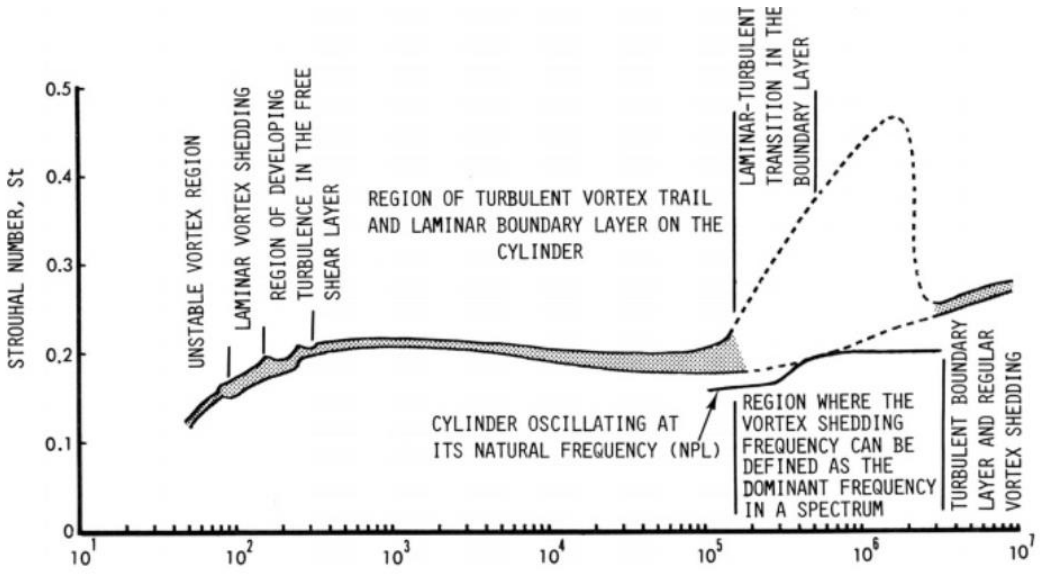

Figure 2-11: Strouhal number - Reynolds Number Relationship (Lienhardt, 1966)

Bearman, 1969, conducted VIV experiments in a wind tunnel with a 17.8 cm diameter smooth rigid cylinder to investigate the dependence of Strouhal number on Reynolds number. Large variations in Strouhal number were observed with the maximum value of 0.46 reported at Re of 5.5×10^5.

Resvanis et al. 2012, investigated the impact of Reynolds number on lift coefficient based on experimental data. This was done through the use of a towing tank and three different flexible cylinders. The velocity was varied from 0.25 - 3.45 m/s, Re range 5,000 – 220,000 with both shear and uniform currents investigated. It was found that increasing the Reynolds number results in an increase in amplitude of vibration, change in Strouhal number and lift coefficient. The best fit line for Strouhal number against Reynolds number based off of smooth pipe results was:

$$St = -0.0065 \ln(Re) + 0.21 \qquad \text{Eq. 2.3}$$

This trend was followed up to 1.4×10^5 and approached a limiting value of around 0.13. This differs from stationary cylinders where it is predicted that Re remains constant at 0.2 until around Re = 2×10^5.

The Strouhal number is a user-defined parameter within OrcaFlex and Shear7. It is important to calibrate this value as it dictates the VIV response. This is done in this research by calibrating the numerical model against experimental results.

2.5.1 Added Mass

Du Buat 1822 and Bessel 1828, conducted experiments with spheres and pendulums oscillating in water, and air and concluded that it is necessary to attribute an added mass Δm to the spheres, making it behave as if it had a mass of $m + \Delta m$. In reality, there is no mass change of the body, and the physical shape remains the same but the increase of kinetic energy of the fluid required to produce accelerations manifest themselves as added mass.

The added mass coefficient is a user-defined parameter within OrcaFlex. It can influence the VIV behaviour and requires calibration. Calibration is achieved through validating simulation results against experimental data.

2.5.2 Lift Force

Figure 2-12 shows how the lift coefficient varies with Reynolds number for numerous different experiments. These results show how sensitive the lift coefficient is to Reynolds Number, and a variety of other parameters.

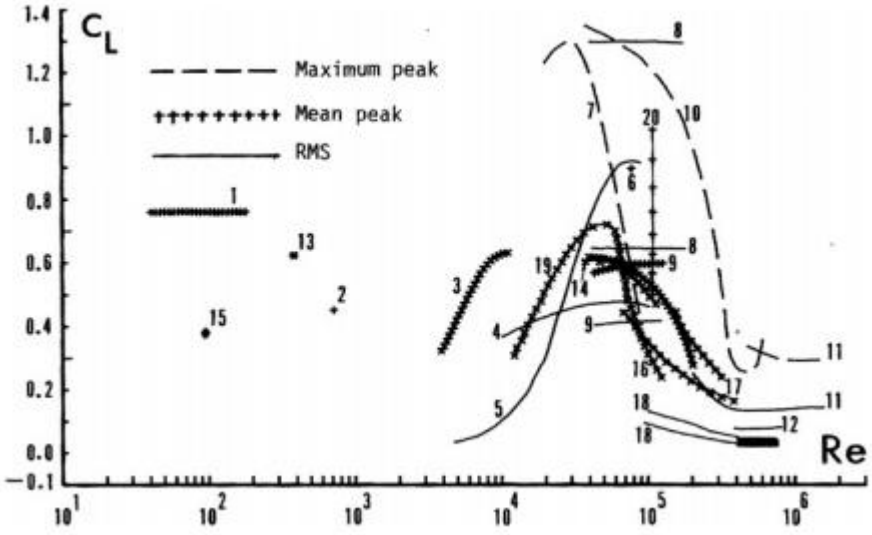

Figure 2-12: Lift coefficient against Re for circular cylinders 1) (Phillips, 1956) 2) (Schwabe, 1935) 3) (Bishop & Hassan, 1963) 4) (Keefe, 1962) 5) (Gerrard, 1961) 6) (Bingham, H. H., Weimer, D. K., and Griffith, 1952) 7) (Macovsky, 1958) 8) (Vickery, B. J. and Watkins, 1962) 9) (McGregor, 1957) 10) (Humphreys, 1960) 11) (Fung, 1960) 12) (Schmidt, 1965) 13) (Jordan & Fromm, 1972) 14) (Macovsky, 1958) 15) (Dawson & Marcus, 1970) 16) (Weaver, 1961) 17) (Goldman, 1958) 18) (Bublitz, 1971) 19) (Warren, 1962) 20) (Schmidt, 1965)

The lift coefficient in our research is defined with Shear7 via a user supplied lift table. The table chosen can influence the predicted VIV response notably. This is shown in Chapter 5.2. The table chosen in our research has been calibrated against experimental results.

Lock-in can occur at a wide range of flow velocities. There are two distinct roles played by the vortices: excitation and driving.

- Excitation means the vortices can, and do, excite the body, even when the out-of-phase component of their lift force is relatively small, provided that f_{vs} is close to the prevailing frequency of the body. Even weak vortices can excite a body to large amplitudes when the body and vortices arrive at a common frequency, in the region of about f_{ex}/f_{st} = 0.5 - 0.9.
- Driving ability of the vortices ensues from the particular modal dynamics and leads to a sufficiently large out of phase lift component in regions f_{ex}/f_{st} = 0.9 - 1.0. The effectiveness of the driving function depends on a number of parameters (range of f_{ex}/f_{st}, Re, damping, virtual mass, and others).

For long structures, the phenomenon is further complicated by the fact the structure tends to respond at a variety of frequencies over its length. This is known as multi-mode interaction. This gives rise to additional and omnidirectional fluid forces whose prediction is at best an approximation.

2.5.3 Experimental and Numerical Review

2.5.3.1 Relevant Fundamental Experimental Work

The existence of vortices leads to the generation of oscillatory lift and drag forces with shedding frequencies of Ω_f and $2\Omega_f$ respectively (Blevins, 1974). For a stationary cylinder, the drag and lift forces act in the inline and crossflow directions. This, however, is not always the case for an oscillating cylinder where the directions of apparent drag and lift forces can be arbitrary. The lift frequency being half that of the drag frequency is what leads to the development of the figure of eight shape for the cable displacement in the drag/lift plane (Xu et al., 2018). In this research, the focus is solely on the crossflow vibrations due to the lift force due to limitations of the software because Shear7 only allows the modelling of crossflow vibrations. This means the figure of eight displacement profile isn't modelled and the influence this may have on displacement and frequency is not accounted for.

Govardhan and Williamson 2006 and Klamo et al. 2005, have both shown that the peak amplitude response of a rigid cylinder is influenced by Re. T. Sarpkaya 1995, discussed the significance of two-directional free oscillations with the results of this discussion shown in Figure 2-13. From this, one can see that the variation of the normalised amplitude, A/D, with V_r, for the case of the same natural frequency in the inline and crossflow directions, resulted in around 20% larger amplitudes over a 20% larger range of $V_r St = f_{st}/f_{ex}$, at a Re of about 3.5 × 10^4. However, the variations of A/D for other natural frequency ratios were more difficult, indicating that dramatic changes in the wake impact the amplitude of vibrations.

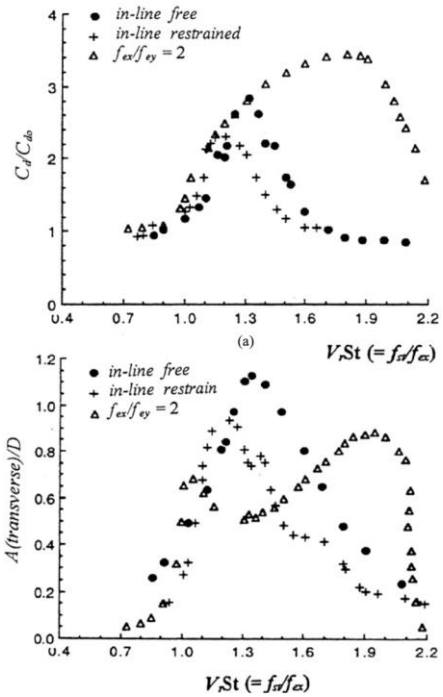

Figure 2-13: Normalised drag coefficient and A/D at Re = 35,000 for inline free, inline restricted and forced vibrations at $f_{ex}/f_{ey}=2$

W. L. Chen et al. 2015, investigated the vortex induced vibrations of a flexible cable at an inclined angle under a shear flow within a wind tunnel. It was observed that at lower velocities only single mode vibrations occurred with crossflow displacement larger than the inline. At larger velocities multi-mode vibrations were observed. Multimode vibrations occur when different modes of vibrations are excited along a structural body's length. This is due to different incident relative velocities caused by either shear current profiles, turbulence, or a non-linear angle of inclination of the body relative to the flow. For a lazy wave power cable, all of these factors are present and influence the VIV behaviour. For the larger flow velocities, multi-mode vibrations were observed, with the crossflow and inline displacement smaller than that of the single mode vibrations. Both multi and single-mode vibrations resulted in similar maximum accelerations.

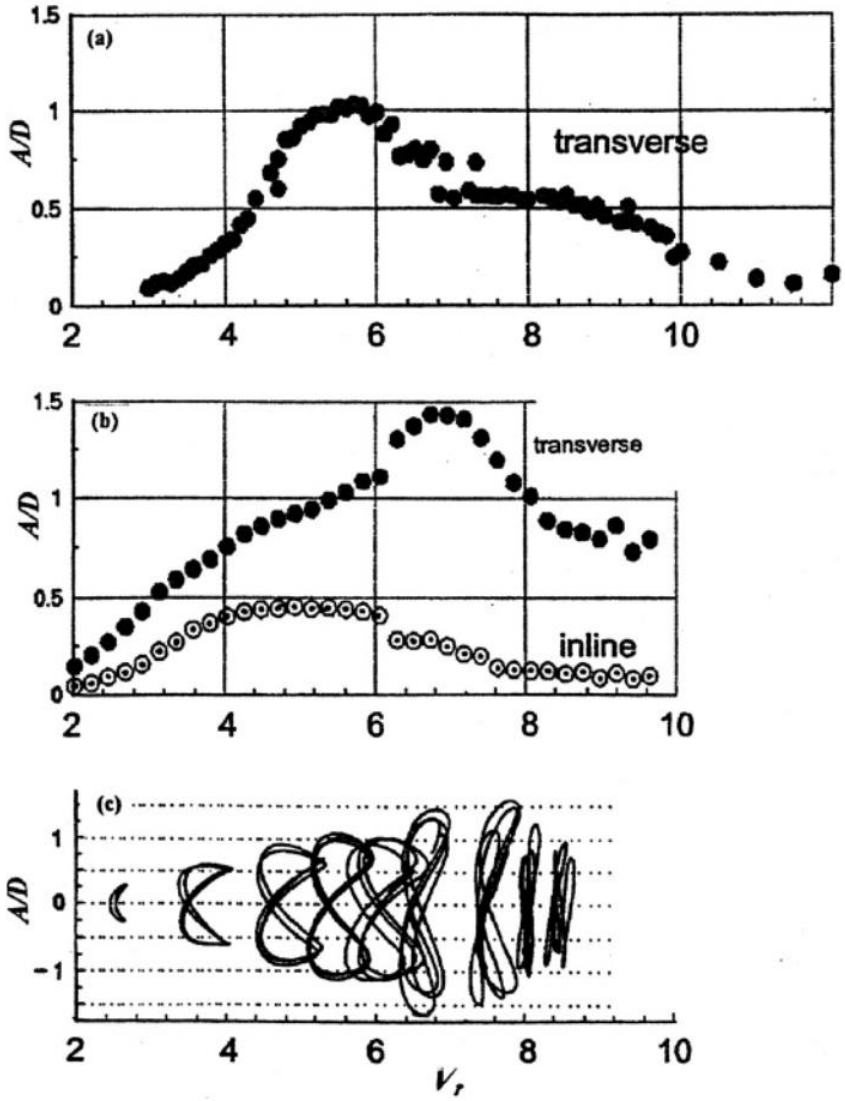

Figure 2-14: a) 1DOF rigid cylinder b) flexible cylinder c) inline and transverse trajectories (Re = 30,000, L/d = 26, m = 3.0, damping = 0.035)*

Triantafyllou et al. 2003, carried out experiments with a rigid cylinder (1DOF) and a flexible cylinder (2DOF) at MIT. These were done at Re = 3×10^4, aspect ratio = 26, m^* = 3, and ζ =0.035. The results from this are shown in Figure 2-14. The amplitude of A/D reached a maximum 1.0 at V_r ≈ 5.6 for a rigid cylinder and reduced to very small values after V_r ≈ 11 is reached. In Figure 2-14b**,** the flexible cylinder shows overall the same behaviour as the rigid cylinder, however, the V_r for the maximum A/D was at about 7, the value for A/D was around 1.5, and after the V_r continued to increase the amplitude plateaued at around 0.75 A/D. Figure 2-14c shows the motion trajectories of the flexible cylinder, it can be seen that the largest excursions in the in-line direction occurred when V_r ≈ 5.5 and not 7 which was when the maximum amplitude in transverse direction happened. This shows that inline and transverse oscillations don't reach their maxima at the same time, the former precedes the latter. Unfortunately, inline vibrations are not modelled in this research due to software limitations, but it is important to understand the relationship regardless.

Allen & Henning 1997, conducted towing tank tests for two different 2m long smooth flexible cylinders at Reynolds numbers ranging from $2 \times 10^5 - 6 \times 10^5$ for an 89 mm outer diameter ABS pipe, and $6 \times 10^5 - 1.5 \times 10^6$ for a 141 mm outer diameter PVC pipe. The results showed that the amplitude of VIV is strongly linked to the Re, as is the drag coefficient.

Fu et al. 2013, investigated VIV of a flexible cylinder within an ocean basin. The cylinder was positioned horizontally and clamped at one end with a force transducer connected to the other. The frequency and amplitude of vibrations were varied over three scenarios: smaller than, equal to, and larger than the natural frequency. In all three cases, three regions could be observed during the development of VIV: build-up, lock-in and dying-out. As the vortex shedding frequency increased the lock-in region widened. A pure lock-in region was responsible for cases with a large amplitude of vibration.

2.5.3.2 Cable Relevant Experiments

Delizisis et al. 2022, performed scaled down VIV experiments for a dynamic subsea power cable. This was done in a towing tank with the cable arranged vertically extending over 7m. The results from this experiment were compared against numerical results produced from simulations ran via coupling OrcaFlex and Shear7. A sensitivity analysis was conducted investigating the impact of the lift coefficient, Strouhal number, reduced velocity bandwidth, added mass coefficient, and damping coefficient. It was shown that these user-specified parameters do influence the behaviour, and a set of values were proposed for investigating at similar Reynolds number for full scale deployment $(11 \times 10^3 - 44 \times 10^3)$. These parameters were predominantly aimed at low mode excitation which over the span of a full-scale cable is likely to only be sufficient at very low velocities.

Le Cunff et al. 2004, numerically investigated the influence of current angle on the VIV of an inclined steel catenary riser. The amplitude of the vibrations was larger when the current angle was perpendicular to the plane of the inclination of the cable than parallel. The amplitude of vibrations at touchdown point was especially dependent on the direction of current.

Chaplin and King 2018, performed laboratory experiments on a flexible catenary riser model with low bending stiffness, high curvature, tensioned by its weight and drag up to a *Re* of 70,000. Different current angles saw significant differences in the cylinder displacement. The acceleration and displacement spectra were broad banded with multiple peaks. The amplitude of motion was generally within one diameter, but peak frequency was often well below the expected range of 0.16 to 0.2. The crossflow response at a current angle of 0 degrees was uniform along riser length. The drag coefficient deduced from the angle relative to horizontal was estimated at between 2.0 and 2.8.

Srinil et al. 2018, performed 2D experiments on a rigid curved circular cylinder with a low mass ratio to investigate the impact of flow direction and cylinder curvature on VIV behaviour. Current angles 0, 90, and 180 degrees were considered up to *Re* of 50,000. The results showed that current angle 90 degrees resulted in the largest maximum displacement amplitude, followed by 180, and then angle 0.

Zhu et al. 2023, experimentally investigated the VIV of a flexible free spanning submarine power cable exposed to uniform currents, with the impact of bending stiffness and sag considered. It was shown that the VIV behaviour was strongly dependent on modal properties: single mode was observed when the frequencies of vibrations were widely separated and the transition to multi-mode occurred when they were close enough. The VIV behaviour was significantly affected by the sag of the cable. The maximum vibration displacement for lower sags was greater than the higher sags overall. As velocity increased so did the amplitude of maximum vibration.

Han et al. 2017, experimentally investigated the dynamic response of a towed flexible cylinder with an angle of declination of 45 degrees with *Re* = 800 – 16,000. The maximum response amplitude reached a value of 3.0D in the crossflow direction. The dominant frequencies increased linearly with the reduced velocity. Multimode VIV was observed at higher velocities. The drag coefficients calculated were in the range of 0.9 - 2.6.

Vieira et al. 2021, experimentally investigated the angle of inclination of a flexible cylinder relative to different directions of current flow. The differences in dynamic behaviours were attributed to differences in mean tension along the cylinder's length due to drag forces from towing direction.

Hu et al. 2022, experimentally and numerically investigated the bending behaviour of a multilayer copper conductor for a dynamic power cable. Non-linear bending performance was observed. This was predominately in the transition stick-slip zone and the full slip zone. The friction coefficient between the sheath layer and the copper wire had an obvious influence on the slip transition zone, the friction coefficient between copper wires mainly impacted the full slip zone. The radial extrusion pressure of the outer sheath layer had an obvious influence on the nonlinearity of the bending of the copper conductor. When analysing fatigue life, attention should be given to the nonlinear characteristics of the bending performance.

Vandiver et al. 2006, performed towing experiments within a lake on a 33mm diameter 122m long pipe to investigate fatigue damage caused from high mode VIV. The contribution to RMS stress from higher harmonics was more than 50% in the areas with the highest RMS stresses observed. This highlights the danger of high mode VIV and the large damage that this can result in.

2.6 Stress Load Cycles and Fatigue Life Estimation

Marinet 2015, investigated the bending stiffness characterisation and fatigue life of dynamic power cables for FOWT via experimental testing by applying complex loading regimes to simulate dynamic loads exposed to during offshore deployment. Test specimens were 5.5m long sections of a three-core x 50mm^2 conductors submarine MV power cable with rated voltage 12/20/24 kV designed according to IEC60502-2 standard (IEC, 2014). The fatigue loading regimes applied to the cable were based on numerical results obtained from OrcaFlex under storm conditions with a lazy-wave shape. The section of the cable that was exposed to the most severe loading regime within OrcaFlex was identified and the loading time series and curvature were used for the experimental fatigue test. At higher curvature values the bend stiffness increases more significantly as it deviates from the cable mechanical model. A hysteresis curve was also observed for all test cases confirming that structural damping for power cables is significant. Substantial damage was not observed for any component except the copper conductor.

Marta et al. 2015, investigated the mechanical loading on a power cable via FEA and physical experimentation for a variety of floating marine energy converters based on the hydrodynamic loading results from an OrcaFlex simulation. The most significant issue identified was due to cyclic bending loading which resulted in both extreme bending and fatigue damage for all scenarios investigated. Fretting of the copper conductor was observed due to internal friction as deformation occurred and compression was identified as a potential issue with anti-buckling protection recommended to prevent this.

Tjahjanto and Ab, 2019, performed 3D FEA and analytical analysis on the mechanical properties of large HVAC subsea power cables exposed to tensile loads, focusing on tension-twist coupling and stress response of internal components. The numerical model was compared to experimental results, where one end of the cable was fixed and exposed to a tensile load while the other was free to rotate with the elongation, rotation, and induced twist all measured. Good agreement between FEA and experimental results was observed, regarding both elongation response and tension-twist behaviour but it did not account for the radial deflection of helical components. This highlights the difficulty of accurately modelling structures with complex internal structures and that these different components all influence the full structure behaviour.

Sobhaniasl et al. 2020, modelled a FOWT in FAST one-way coupled this with ANSYS AQWA to model the power cable and then validated this against the published results of Phase IV of the NREL 5 MW FOWT [88]. A total of 20 different sea states from the South China Sea were investigated (Qiao et al.,

2014). The fatigue damage was highly dependent on the location with different points along the cable experiencing large deviations from one another. The suggested safety factor of 10 was used for this project (DNV GL, 2012). It was found that coupling of the loading due to the rotating wind turbine blade is fundamental to achieve reliable estimations as dismissing it leads to large differences in damage evaluation.

Pan et al. 2019, investigated the behaviour of a submarine platform connecting a wellhead platform to a floating production, storage, and offloading platform using OrcaFlex. Local stress analysis of the cable was conducted using FEM software. It was determined that the minimum fatigue life occurs at the hang-off point due to the large bending and tension cycles caused by the dynamic motions of the floating platform. An experimental test was conducted on a cable, failure modes consisting of cracks and individual wire fretting were observed but these didn't result in direct loss of service under electrical tests.

Yang et al. 2018, produced a numerical model of a wave energy converter system and performed global analysis on the corresponding power cable. DNV DeepC and RIFLEX were used in a coupled simulation model to simulate the motion and structural response with stress-based fatigue analyses carried out separately to predict the fatigue damage. Three cable design parameters were investigated, mass, bending stiffness, and length with the scope to optimise least risk of contact and longest fatigue life. Large curvature response typically occurred at high wave heights and near wave period of resonance, an exception to this was a current at angle 90 degrees which resulted in wave period having limited influence and height dictating the response.

Beier et al. 2023, investigated the fatigue life of a suspended inter-array cable connecting two FOWTs. The calculations were done through a simplified method based on stress factors. It was noted that the suspended cable had a long fatigue life resulting from low cyclic loadings. The critical areas for damage were at the hang-off points and next to the buoys, this was noted to be due to bending. The buoy and cable properties had a notable influence on the fatigue life. The effects of marine growth were investigated, and it was found to not have too great an impact, mainly due to the cable's depth not being appropriate for marine growth over large lengths.

Poon et al. 2023, experimentally investigated the fretting of a copper conductor material via piezoelectric wear tests. Piezoelectric Effect is the ability of certain materials to generate an electric charge in response to applied mechanical stress. This was done to measure the cyclic evolution of the coefficient of friction and wear coefficient, as these are noted as key inputs to local fretting wear modelling. A 2D fretting fatigue simulation was developed using Abaqus, a FEA software, for the

copper material. General agreement was found when comparing to measured data. Neglecting the impact of fretting wear in fatigue life prediction for copper conductor material led to significantly over conservative life predictions for slip conditions and significant under-prediction for partial slip conditions.

2.7 VIV MODELLING SOFTWARE (SHEAR7, MWO, IBWO, ORCAFLEX)

Chaplin et al. 2005, performed experimental VIV analysis of a riser in a stepped current and compared the observations with 11 different numerical model's blind predictions, the results are shown in Figure 2-15. The empirical models were found to perform better than the CFD models used. Both Shear7 and the MWO model were tested. The MWO model performed very well, predicting the maximum crossflow displacement as 95% of the experimental data. Shear7 also performed well, estimating the crossflow displacement at around 105% of the experimental data. Both models are capable of accurately predicting crossflow displacement for a riser in a stepped current.

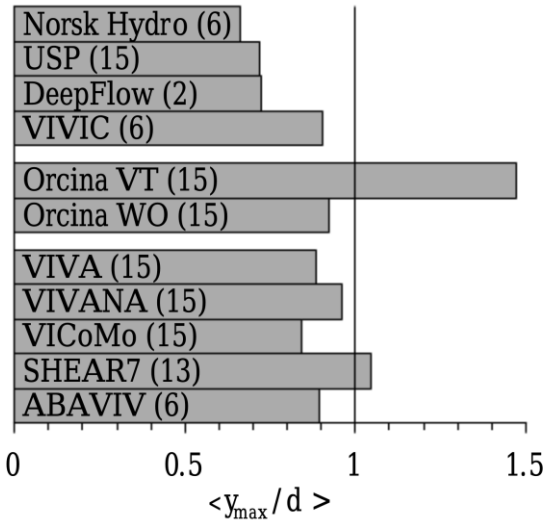

Figure 2-15: Normalisation of predicted and experimentally measured crossflow displacement (J. R. Chaplin et al., 2005)

Dos Santos et al. 2014, investigated the VIV of a free span pipe experimentally and compared the result against numerical simulations from software Shear7, VIVANA, and a wake oscillator vortex-tracking model from OrcaFlex. The pipe was 6m long and 0.02m in outer diameter. All of the models were noted to struggle to capture the lock-in range at the current speeds modelled.

2.7.1.1 Where Has Each Model Been Used Before?

2.7.1.1.1 Shear7

Dillon-Gibbons et al. 2017, used Shear7 coupled with OrcaFlex and a wake oscillator model to investigate impact of waves on heave-induced vibrations. A steel lazy wave riser was used in this study.

The wake oscillator model produced much more conservative results, an order of magnitude one larger compared to Shear7 regarding fatigue damage.

Y. Zhang and Tan 2011, investigated the VIV of a flexible riser using Shear7, IBWO, and Vortex Tracking within OrcaFlex and assessed the fatigue damage. All models predicted similar displacement and frequency of vibration. This was a preliminary study with no validation against experimental results.

Lee et al. 2017, investigated the fatigue life of a steel catenary riser using Shear7 coupled with OrcaFlex. The parameters within Shear7 were varied to determine the influence. A larger lift coefficient resulted in larger input power and greater fatigue loads.

Nallayarasu 2020, performed experimental tests on a 1.56 m long 15mm outer diameter flexible cable and compared the results against Shear7. Shear7 matched experimental results well, it was also observed that the Strouhal number depended on Reynolds number.

Fuglsang et al. 2023, investigated the HVIV response of a lazy wave and a W shaped cable under varying wave conditions. Peak locations of fatigue damage were observed towards the hang-off point, where the largest relative velocities were observed. The incident wave direction had a notable impact on VIV response, a wave angle of 0 degrees, relative to the cable plane, resulted in greater relative velocities and increased fatigue damage. The methodology for this study followed the procedure of splitting each wave period into ten separate time instances and these being used to model fatigue life in the frequency domain separately with this then averaged out.

2.7.1.1.2 Wake Oscillator Models

A significant number of wake oscillator models base their equation of wake on the van der Pol equation. The van der Pol oscillator is a non-conservative oscillating system with non-linear damping accounted for. The wake oscillators used in our research are explained in more detail in the Methodology Section.

2.7.1.1.2.1 Iwans and Blevins Wake Oscillator

Trarieux 2004, compared experimental data for an umbilical lazy wave cable against an existing semi-empirical model. This semi-empirical model was based on Iwans and Blevins wake oscillator (IBWO) model (Iwan & Blevins, 1974). The experimental measurements were taken by measuring the strain at three separate locations within the hang-off point bend stiffener. Only measuring at this location allowed for validation of curvature response at this point but failed to capture the vibrations along the rest of the cable, specifically at the sag and hog bends. The numerical model was shown to provide

good predictions when the flow was mainly out-of-plane of the structure but suffered inaccuracies once the flow becomes highly sheared.

2.7.1.1.2.2 Milan Wake Oscillator

Zhou et al. 2017, investigated the use of the Milan wake oscillator (MWO) within OrcaFlex to model VIV of a free span pipe under different arrangements with soil-bed interaction. The numerical simulation outputs were compared to experimental results. MWO produced conservative results, with it noted that changing the transverse force factor of the MWO produces predictions closer to experimental results. The modelled amplitude displacement was slightly over-estimated compared to the experimental data.

Carneiro et al. 2008, presented simulation results for the wake oscillator and vortex tracking models within OrcaFlex. The MWO responded well to a uniform current but struggled for a sheared current profile, IBWO over-estimated for the uniform current but shear current predictions were extremely close to experimental results. Vortex tracking over-estimated the displacement in all situations.

2.7.1.2 Alternative Wake Oscillator Models

The literature below is for alternative wake oscillator models that have been used to analyse the response of catenary or curved flexible cylinders. The outputs from these studies are directly relevant in providing context around the influence of deformation on the VIV response of an object.

Ma and Srinil 2023, performed numerical simulations using a distributed wake oscillator model based on the van der Pol equation. Predictions of multidimensional VIV of a long flexible curved catenary riser under different flow configurations was achieved. Numerical predictions were noted to result in discrepancies due to a low mode order approximation and the corresponding phenomenological and empirical assumptions of the fluid structure interaction model. These are based on a time-independent inclined curved configuration in dormant fluid. For a current angle of 90 degrees standing waves were observed at low velocity and travelling waves at higher velocity. A current angle of 0 degrees resulted in travelling waves due to spanwise vortex excitation frequencies. An angle of 180 degrees resulted in hybrid travelling standing waves with a change in wave propagation direction towards the centre riser section. Such features are due to nonlinearity of the sheared flow and become more complex at higher velocities due to greater amplitude and frequency variations in both space and time. Deformation of the riser due to drag forces played a substantial role since this dynamic feature is nonlinearly coupled with VIV. A current angle of 90 degrees results in a curved symmetrical profile, whereas for 0 and 180 degrees asymmetric displacement was observed. This impacted the

natural frequencies, modal shapes, and associated vortex shedding frequencies which leads to complex multi-modal responses. This response is also seen in this research for a flexible power cable in the lazy wave configuration. Different current angles influence the response and exhibit asymmetric deformation. As the current velocity increased the riser was dominated by higher-order modes, with multimodal contributions also increasing, depending on flow-cylinder orientation. As the riser is displaced due to drag forces the relative velocity fluctuates which dynamically impacts the response features and hydrodynamic force excitations. The crossflow vibrations are predicted to dominate in all scenarios. Both crossflow and inline amplitudes for angles 0 and 180 degrees are less than that of 90, due to the impact of nonlinearly sheared flows. This assists in providing confidence that only focusing on the crossflow displacement in this research is adequate.

Cheng et al. 2021, investigated the VIV of a steep wave riser that was subjected to oblique uniform currents. A 3D non-linear time domain FEM was used and coupled with a wake oscillator model based on the van der Pol equation. The results from this paper predict much smaller vibration displacement at current angle of 90 degrees, due to the large out of plane deformation of the riser. This is significantly different from the results of other studies and the research conducted in this thesis. Different modelling techniques, riser properties, and riser configurations are all impacting factors. A standing wave dominated the hang-off section of the cable, whereas a travelling wave appeared in the buoyancy and touchdown sections. Different VIV behaviour at different current angles was observed due to the large out of plane deformations. The parameters of the buoyancy modules had a significant influence on the cable deformation and the lift forces. It was noted that increasing the length of the buoyancy segment could potentially mitigate VIV power at the touchdown section.

Ma and Srinil 2021, used a 3D van der Pol wake oscillator time-domain model to predict the VIV response of a flexible catenary riser subjected to planar and non-planar flows. The flow orientation was shown to significantly affect the VIV of the riser. An angle of 90 degrees resulted in the largest amplitudes with the lowest vibrations predicted for a current angle of 180 degrees.

Li et al. 2021, used the intrinsic finite element model VFIFE to model a catenary riser. This was compared against experiments and the result showed good agreement. Current angle relative to the catenary plane had an influence on mode transition, frequency, energy transfer, and the internal forces. The mode number increased as velocity increased for all current angles. The critical velocity for mode transition was different for each current angle. The displacement amplitude at a current angle of 90 degrees was larger than that at 180 degrees.

2.7.1.2.1 Computational Fluid Dynamics

There have been various investigations into CFD for offshore risers, umbilicals, and power cables (J. Chaplin et al., 2005; Z. S. Chen & Kim, 2010; Constantinides et al., 2016; S. Lee et al., 2020; Stabile et al., 2018). Due to the large computational demands many CFD studies are conducted at low Reynolds numbers and as such aren't relevant to our research. This project does not use CFD due to time constraints required to sufficiently learn the required software and computational power demand.

2.7.1.3 Turbulence Impact

Turbulence is often not considered in studies due to the added complexity in both numerical and experimental modelling. Kang et al. 2019, investigated the influence of different mass ratios and frequency ratios over a Re range from 1450 – 91800 via OpenFoam, a CFD software. By utilising a modified SST turbulence model the coupled Unsteady Reynolds-Averaged Navier–Stokes equations and double-degree-of-freedom vibration equations were solved. For a cylinder with mass ratio of 2.6 an increase in Re led to an increase in crossflow and inline vibration amplitudes but for a mass ratio of 13 the inline amplitude decreased with an Re increase. In our research the impact of turbulence is not considered due to software limitations.

2.7.1.4 Cable Properties

There are a large range of potential cable properties due to the lack of maturity in this area meaning a preferred cable, and corresponding properties, doesn't exist. To account for this, numerous different cables of varying weight, diameter, voltage and bending stiffness were investigated in this research.

These cables are from a 220kV floating substation (Guignier et al., 2020a), 11kV umbilical (Martinelli et al., 2010), 33kV aluminium core power cable (de Wilde et al., 2021), and polymer braid cable and steel wire armour aluminium core cable (Oud et al., 2021) . The configuration of the cable shape can also be varied greatly. Numerous different configuration were investigated such as a lazy wave (Thies et al., 2012b), double wave (Guignier et al., 2020a), tethered wave Gran Can, and Steep Wave West Barra (Oud et al., 2021). The properties of these cables are shown in the methodology section in Table 3-3.

2.7.2 Buoyancy Module

Wu et al. 2017, conducted experimental forced motion tests for a rigid cylinder with staggered buoyancy elements. It was observed that the VIV behaviour was influenced by both buoyancy element dimensions and arrangement over the cylinder length.

Jia et al. 2022, performed experimental tests on a flexible riser with different configurations of both buoyancy modules and helical strakes. Helical strakes are deployed to suppress VIV by disrupting the induction of a regular vortex stream. A multi-frequency response was observed due to different diameters of buoyancy modules and riser. It was observed that when the bare riser was fully covered with strakes the only frequency excited was due to the buoyancy module. The helical strakes had little effect on the added mass coefficient of either the buoyancy modules or bare riser section. The helical strakes had a damping effect on both the bare riser and the buoyancy modules.

Lekkala et al. 2020, investigated different buoyancy module distribution using Shear7 and calibrated numerical parameters against experimental results. The ratio of buoyancy module to riser was shown to substantially impact the VIV response and fatigue damage rate by altering the response frequency and RMS crossflow displacement.

Vandiver and Peoples 2003, investigated the impact of staggered buoyancy modules on the VIV of a riser. Results showed that, depending on the buoyancy module arrangement, the fatigue damage rate can be decreased, this is provided that the ratio of mass to tension hasn't increased too substantially.

Wu et al. 2020, used VIVANA, a semi-empirical finite element analysis software, to model risers with buoyancy elements. The hydrodynamic coefficients chosen were derived from experiments. Five different arrangements were investigated with results being noticeably dependent on this. The optimal final dataset produced results notable different from the bare riser default dataset with the RMS curvature, mode, frequency, and amplitude all impacted. The large deviations observed when applying to different configurations was due to complex interactions between bare riser and buoyancy elements.

All of the literature cited above conducted or related their research to experimental tests that had buoyancy modules distributed over the full length of a riser. This differs from a lazy wave configuration, where the buoyancy modules are relatively localised and only cover a small portion of the cable. Further investigation into the influence of buoyancy modules constrained to a certain section is required to better understand the overall impact on the VIV behaviour for the full-scale cable with buoyancy modules deployed at the mid-section.

2.7.3 Waves

Waves are known to impact power cables due to platform induced motion and incident forces along the upper end of the cable. This can cause failure due to compression, over-tension, and excessive

bending. To account for this, a dynamic power cable is deployed to absorb the motion, and the platform is moored to withstand the heave induced forces and motions.

Thies et al. 2012a, assessed the mechanical loading and failure modes of dynamic power cables, focussing on the point of maximum loading over the cable and the influence of external parameters: wave height, wave period, regular or irregular sea state, and cable configuration. This was done through OrcaFlex and experimental testing at a 1/20 scale. In a regular sea state, an increase in wave height leads to an increase in tension and bending moment of the cable, whereas a greater wave period leads to a reduction in these. An irregular sea state results in higher loads induced and an increased number of fatigue cycles.

Numerical simulations were performed by W. Chen et al. 2014, to predict the impact of top end heave on the VIV along a riser's length. The VIV displacement amplitude increased when top end heave motion was present compared to when it wasn't. It was also noted that the VIV response amplitude increased as the tension ratio increased, almost linear with tension ratio.

Zhang et al. 2021, used a van der Pol wake oscillator model to predict the behaviour of a top tensioned riser in varying wave and current conditions. This was compared against experimental data. At lower current velocities, the heave motion of the platform resulted in a significantly larger VIV response. As the amplitude of the heave motion was increased the vibration and bending stresses also increased. The dominant vibration frequency was noted to be insignificantly impacted by the heave motion in higher currents. The VIV frequency response was dominated by the relative flow of the current. However, when the platform heave amplitude and heave frequency were large enough the heave frequency appeared in the VIV frequency spectrum.

Yin 2022, used VIVANA-TD, an empirical time-domain VIV solver, to predict the crossflow VIV responses induced due to heave motion and compared the predictions to experimental data for a lazy wave riser. It was noted that the vessel motion induced normal relative velocity along the riser, with this being largest towards the hang-off point. The lazy wave riser response was dominated by the bare riser frequency over the buoyancy modules or heave frequency. A significant portion of the lazy wave riser was dominated by travelling wave responses with standing waves observed locally towards the touchdown point.

3 METHODOLOGY

3.1 NUMERICAL MODELLING

3.1.1 OrcaFlex

All analysis presented in this work was performed with OrcaFlex 11.2a (Orcina Ltd., 2022), a three-dimensional finite element program for time domain dynamic analyses. Within OrcaFlex each line is discretised into segments, which are modelled by massless segments connected to a node at each end. This is shown in Figure 3-1. The nodes model the mass, weight, buoyancy, and drag properties of the line segments. The node properties are defined by each half-segment attached. Forces and moments are then applied at these nodes. Segments are used to model the axial and torsional properties of the line.

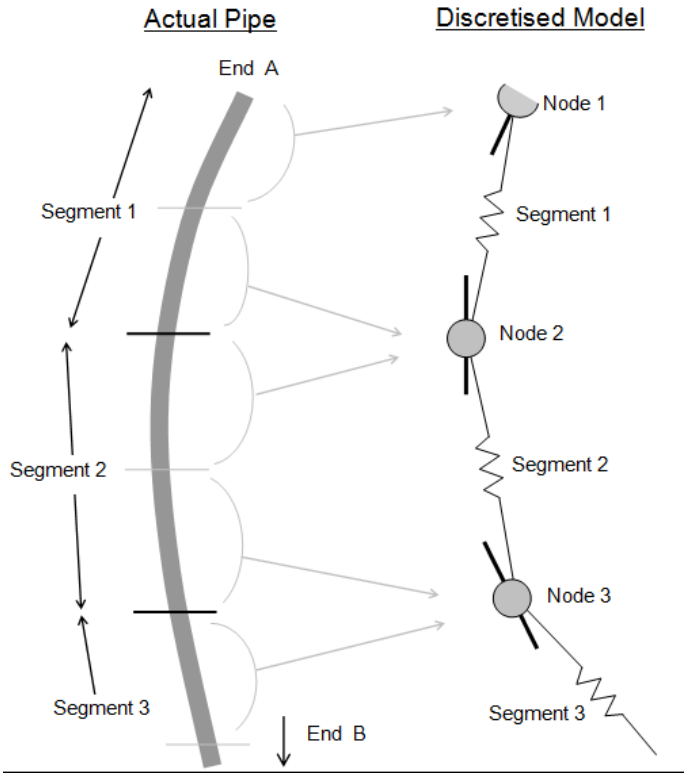

Figure 3-1: Diagrams showing how a pipe is discretised within OrcaFlex

There are three different types of spring dampers used to model within OrcaFlex, shown in Figure 3-2:

- Axial stiffness is modelled at the centre of each segment and applies an equal and opposite effective tension force to the nodes at each end of the segment.
- Bending properties are captured using rotational spring dampers either side of each node.
- Torsion is modelled using a torsional spring damper at the centre of each segment applying equal and opposite torque moments to the nodes at the end of the segment.

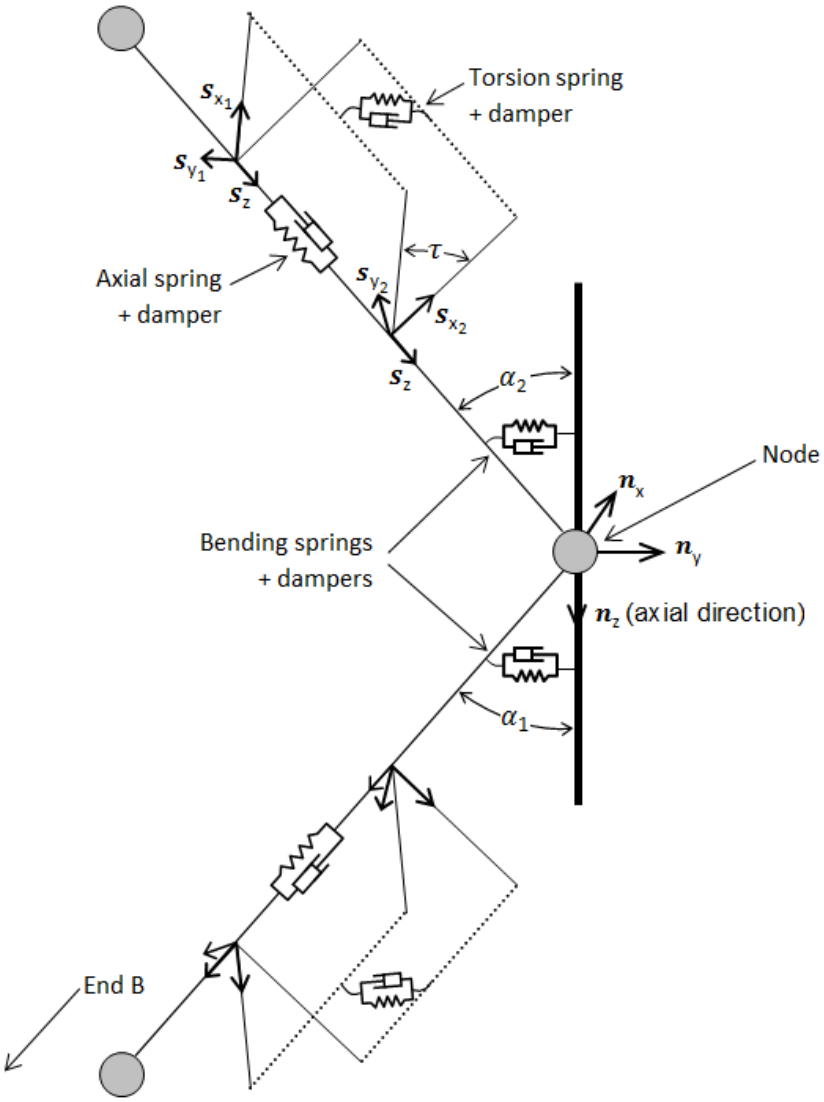

Figure 3-2: Diagram showing spring damper and directions within OrcaFlex

3.1.2 Static and Dynamic analysis

OrcaFlex calculates the forces and moments on the line in five stages: tension forces, bending moments, shear forces, torsion moments, and total load. Analysis is then conducted in two parts, an initial static analysis followed by a dynamic analysis.

3.1.2.1 Static Analysis

The static analysis determines the positions and orientations for each element in the model, such that all forces and moments are in equilibrium. This is done through an iterative method:

1. Initially the DOFs of all objects, other than lines, are fixed.
2. The line statics are then determined.
3. Then all DOFs are released and a whole system statics is performed using Newton-Raphson's method with an initial guess coming from the first two stages.
4. The static solution is then used for the start of the dynamic analysis.

3.1.3 Dynamic Analysis

The time domain analysis is nonlinear, with mass-damping stiffness and loading evaluated at every time step. Numerical time-stepping algorithms are utilised to solve the equation of motion:

$$M(p,a) + C(p,y) + K(p) = F(p,y,t) \quad \text{Eq. 3.1}$$

where $M(p,a)$ is the inertia load, $C(p,y)$ the damping load, $K(p)$ stiffness load, $F(p,y,t)$ external load, p, v and a are position, velocity, and acceleration vectors respectively, and t is the simulation time. An explicit integration time stepping scheme, the semi-implicit Euler, is used with a chosen constant time step.

The equation of motion (Newton's Law) is then formed for each free body and line node:

$$M(p,a) = F(p,y,t) - C(p,y) - K(p) \quad \text{Eq. 3.2}$$

This equation of motion is applied locally for each free body and line node. The local equation of motion is solved for each acceleration vector at the start of each time step and then integrated using semi-implicit Euler integration.

3.1.3.1 Line Forces

3.1.3.1.1 Tension

Tensions in the segments are calculated through distance and the rate of change between nodes at the ends of the segment. The tension in the axial spring-damper is given by the effective tension, T_e:

$$T_e = T_w + (a_0 p_0 - a_i p_i) \quad \text{Eq. 3.3}$$

where T_w is wall tension, defined in Eq. 3.4, p_i is the internal pressure, p_0 is the external surrounding fluid pressure, $a_i = \frac{\pi}{4} ID^2{}_{stress}$ is the internal cross sectional area of the stress annulus with ID_{stress} the internal stress diameter of the line type, and $a_0 = \frac{\pi}{4} OD^2{}_{stress}$ is the internal cross sectional area of the stress annulus with OD_{stress} the external stress diameter of the line type.

For linear axial stiffness, the wall tension is:

$$T_w = EA\epsilon - 2\nu(a_0 p_0 - a_i p_i) + k_{tt}\frac{\tau}{l_0} + EAc\frac{dl}{dt}\frac{1}{l_0} \quad \text{Eq. 3.4}$$

where EA is the axial stiffness (E is Young's Modulus and A is the cross sectional area), ϵ is the total mean axial strain ($(1 - \lambda l_0)/(\lambda l_0)$, l is the instantaneous length of segment, λ is the expansion factor

of segment, l_0 is the unstretched length of segment, ν is the poisson ratio, k_{tt} is the tension/torque coupling, τ is the segment twist angle, and c is the damping coefficient in seconds (defined in Eq. 3.5).

The damping coefficient represents the numerical damping in the line and is calculated from the formula:

$$c = \frac{\lambda_a}{100} c_{crit} \quad \text{Eq. 3.5}$$

where λ_a is the expansion factor of the segment, $c_{crit} = \sqrt{\frac{2ml_0}{EA}}$ is the unstretched length of the segment, and m is the segment mass.

3.1.3.1.2 Bending Moment

The bending moments are calculated via the bending spring dampers either side of each node. Each of these dampers applies a bend moment on the node depending on the spanning angle, α, between the node's axial direction and corresponding segment's axial direction. For linear isotropic bending stiffness, which is considered in this research, the bend moment generated by the bending spring damper is:

Magnitude:

$$|m_2| = EI|c| + d\frac{d|c|}{dt} \quad \text{Eq. 3.6}$$

Direction:

$$b = unit\ vector\ in\ direction\ (s_z \times n_z) \quad \text{Eq. 3.7}$$

where EI is the bending stiffness, $d = \frac{\lambda_b}{100} d_{crit}$: λ_b is the target bending damping, and $d_{crit} = \sqrt{mEIl_0}$ is the bending critical damping value for a segment.

3.1.3.1.3 Shear Force

Each line segment is modelled as a straight stiff rod in which bending moment varies linearly from one end, m_1, to the other, m_2. The shear force is thus a constant vector representing the rate of change of bending moment along the length:

$$f_s = s_z \frac{1}{l}(m_2 - m_1) \quad \text{Eq. 3.8}$$

where s_z is the shear force is a vector applied to both ends of each segment.

3.1.3.1.4 Pipe Stress Calculation

The stress results from OrcaFlex only apply to simple pipes because it assumes the loads on the line are for a simple cylinder whose inside and outside diameters are given by the stress diameter specified on the line-types form. It assumes a cylinder of uniform material, as such it is not suitable for umbilicals or dynamic power cables with complex internals.

3.1.3.1.5 Hydrodynamic Loads

OrcaFlex calculates the hydrodynamic loads on lines using an extended form of Morison's equation (Morison et al., 1953):

$$f = C_m \Delta a_f + \frac{1}{2}\rho C_d A V_f |V_f| \quad \text{Eq. 3.9}$$

where f is the fluid force per unit length on the body, C_m is the inertia coefficient for the body, Δ is the mass of fluid displaced by the body, a_f is the fluid acceleration relative to earth, ρ is the density of the fluid, C_d is the drag coefficient of the body, and V_f is the fluid velocity relative to earth.

These same principles can be applied to a moving body, here the inertia term is reduced by $C_a \Delta a_b$ and the fluid flow relative to the body V_r:

$$f = (C_m \Delta a_f - C_a \Delta a_b) + \frac{1}{2}\rho C_d A V_r |V_r| \quad \text{Eq. 3.10}$$

where C_a is the added mass coefficient for the body, a_b is the fluid acceleration relative to the body, and V_r is the fluid velocity relative to the body.

The value C_m is taken to be $1 + C_a$, extending Morison's equation to be:

$$f = (\Delta a_f + C_a \Delta a_r) + \frac{1}{2}\rho C_d A V_r |V_r| \qquad \text{Eq. 3.11}$$

where $a_r = a_f - a_b$ is the fluid acceleration relative to the body.

The term in the parentheses represents the inertia force and the second term represents the drag force on the body. The drag force is a result of the velocity of the flow that passes the object, while the inertia force is a result of the acceleration of the flow and consists of two parts: one proportional to fluid acceleration relative to earth (Froud-Krylov component) and one proportional to fluid acceleration relative to the body (added mass component).

3.1.3.1.6 Inertia Force

Froude Krylov

The Froude-Krylov component is the integral over the surface of the body of the pressure due to the incident wave, undisturbed by the presence of the body. In other words, the force introduced by the unsteady pressure field generated by undisturbed waves. It can be imagined by removing the body and replacing it with equivalent volume of water. This water would have mass Δ and undergo acceleration a_f and thus experience a force Δa_f. If the body now replaces the water the same force must act on the body.

Added Mass

The added mass load on each line segment follows the inertia term of Morison's equation.

3.1.3.1.7 Drag Force

Within OrcaFlex, the drag forces are determined using the crossflow principle. The fluid velocity relative to the line is split into its components normal and parallel to the line axis. The drag force normal to the line axis is calculated by V_n and $V_{x,y}$, the drag force parallel uses V_Z. In OrcaFlex the drag force is defined as:

$$f_D = \frac{1}{2}\rho C_d A V_r |V_r| \qquad \text{Eq. 3.12}$$

where A is the drag area.

3.1.3.1.8 Lift Force

If a symmetric cross-section is used this results in no lift force calculated as there is no pressure difference across the line.

3.1.4 Wake Oscillators

Wake oscillator models offer the opportunity to model the response of the object to a flow without adjusting the flow physically. This limits the model's accuracy, but previous studies have shown that wake oscillator models are capable of reliably predicting the response of a cylinder in uniform flow and are much less computationally expensive than models that simulate the flow response. There are two wake oscillator models available within OrcaFlex, the Milan wake oscillator and the Iwan and Blevins wake oscillator model. The suitability of these models to predict the VIV for a dynamic power cable in a lazy wave configuration is investigated in this research and discussed in Chapter 3.2 and Chapter 4.

3.1.4.1 Milan Wake Oscillator Model

The Milan Wake Oscillator model is a time-domain and heuristic model operating in a single degree of freedom to represent the cylinder wake, proposed by Falco et al. 1999. The oscillation of the wake is a function of time obeying a differential equation, the wake equation of motion. The wake oscillation generates a lift force, and the model determines the lift force magnitude and applies this to the cylinder determining its motion. In turn, further development of the wake is dependent on the cylinder motion. The MWO model calculates the drag force on the cylinder and then adds the standard Morrison drag force. The motion of the cable is heavily influenced by the drag coefficient specified for the transverse direction. Within the OrcaFlex environment the transverse drag coefficient is initially set to 1.2. The data set used for this scenario was the original OrcaFlex data set as this was calibrated to work with a thin flexible cable exposed to sea currents. The Strouhal Number is assumed to be constant at 0.2, as this is what the Milan model is calibrated at, but at higher *Re* it can vary between 0.14-0.4. This is a potential source of inaccuracy.

3.1.4.2 Iwan and Blevins Wake Oscillator Model

In the Iwan Blevins model (Iwan & Blevins, 1974), the wake degree of freedom obeys a van der Pol equation. The rate of change of the wake degree of freedom is a measure of the fluid momentum in the transverse direction. The model was calibrated against experimental results for both fixed and forced cylinders and the model's prediction was then compared against experimental results for spring mounted cylinders. The Morrison drag force is included in the transverse direction, however, when using the model OrcaFlex suppresses the transverse component of the drag force (the drag

coefficient for the transverse direction is not considered). The fundamental fluid oscillator expression is shown below (N. Minorsky, 1962):

$$\ddot{z} + K' \frac{u_t}{D} \omega_s z = (a_1' - a_4') \frac{U}{D} \dot{z} - a_2' \frac{\dot{z}^3}{UD} + a_3' \ddot{y} + a_4' \frac{U}{D} \dot{y} \qquad \text{Eq. 3.13}$$

Where ω_s is the shedding frequency, K' is a proportionality constant, a_i' are dimensionless constants, D is the diameter of the cylinder, U is the fluid velocity, and u_t is translational velocity of the vortex street.

3.1.5 Shear7 (Frequency Domain)

Shear7 operates within the frequency domain to predict the VIV behaviour along an object through mode superposition. It has been used previously, as discussed in the literature review section, to predict the vibrations for steel and power cables in the lazy wave configuration. Shear7 is the predominantly used tool in this research because it has been calibrated against experimental results for a scaled down dynamic power cable and has industry wide use. The derivation that follows is based off of the work of Vandiver and Li, 2005.

Shear7 initially characterises the structural behaviour of the body being investigated. The equation of motion for a tension beam, with no damping, is:

$$m_t \ddot{y} + EIy'''' - Ty'' = 0 \qquad \text{Eq. 3.14}$$

where m_t is the linear density of the beam (including the added mass effect), EI is bending stiffness, and T is tension.

Let the displacement be:

$$y = Ae^{j(kx+\omega t)} \qquad \text{Eq. 3.15}$$

with A amplitude, k the wave number, ω the frequency, and x and t spatial and temporal variables.

Substituting this into the beam equation results in:

$$-m_t \omega^2 + EIk^4 + Tk^2 = 0 \qquad \text{Eq. 3.16}$$

A parameter which characterises the beam behaviour is defined as:

$$P = \frac{T}{EIk^2} \qquad \text{Eq. 3.17}$$

If P > 30 the structure is essentially a taught string and bending stiffness should be discounted.

Solving Eq. 3.17 for the wave number yields the dispersion relation:

$$k^2 = \frac{-T \pm \sqrt{T^2 + 4EI\omega^2 m_t}}{2EI} \qquad \text{Eq. 3.18}$$

P can more conveniently be expressed as:

$$P = \frac{2}{-1 + \sqrt{1 + \frac{4EIm_t}{T^2}\omega^2}} \qquad \text{Eq. 3.19}$$

Numerical studies have shown that when P is less than 30 the bending stiffness is important and therefore the beam model should be used. In this research the value is always less than 30. This means the bending stiffness is considered when computing the modal response of the structure. The natural frequencies and mode shapes are defined within OrcaFlex separately from Shear7, regardless. The parameter P is used throughout this study to justify the continued assumption of bending stiffness dominated response.

The parameter $n\varsigma_n$ characterises finite or infinite structural behaviour, where ς_n is the *n*th modal damping ratio and is given by:

$$\varsigma_n = \frac{R_n}{2\omega_n M_n} \qquad \text{Eq. 3.20}$$

with R_n being the nth modal damping constant, ω_n the nth natural frequency and M_n the nth modal mass. When $n\varsigma_n$ is greater than 2 infinitely long structural behaviour dominates. When it is less than 0.2 spatial attenuation is small. Our models tend to fall within this range ~1, meaning spatial attenuation is relevant and is not treated as an infinitely long model.

Shear7 requires both the natural frequency and the mode-shapes to be calculated and from this it evaluates the modes most likely to be excited based on the minimum and maximum excitation frequencies:

$$\omega_{min} = \frac{2\pi S_t V_{min}}{D}, \qquad \text{Eq. 3.21}$$

$$\omega_{max} = \frac{2\pi S_t V_{max}}{D} \quad \text{Eq. 3.22}$$

where V_{min}, and V_{max} are the minimum and maximum flow velocities, respectively.

J. Kim Vandiver and Marcollo, 2003, introduced the reduced velocity bandwidth. This is a measure of "the ability of the wake to synchronise with the motion of a vibrating cylinder in a shear flow". It is based on the idea that at a certain vibration frequency and amplitude there is a flow velocity, V_c, which is ideal for lock-in. This ideal flow speed is at the centre of a range of velocities which make up the region possible of inducing lock-in. This ideal reduced velocity is defined as:

$$V_{RC} = \frac{V_c}{f_v D} \quad \text{Eq. 3.23}$$

f_v is the vibration frequency, not a fixed natural frequency.

Lock-in is able to occur over a range of values, ΔV. This variation, when divided by the centre velocity provides the lock-in bandwidth dV_R:

$$dV_R = \frac{\Delta V}{V_c} = \frac{V_{R,U} - V_{R,L}}{V_{Rc}} \quad \text{Eq. 3.24}$$

where $V_{R,U}$ is the upper reduced velocity capable of wake synchronisation and $V_{R,L}$ is the lowest.

This parameter is used to predict the extent of a potential lock-in region. 0.4 is the default value and interpreted as meaning lock-in can occur for $\pm$20% around the centre velocity. The reason for low mass ratio cylinders to have such a large lock-in range in uniform flow is because the natural frequency increases with flow speed.

Shear7 is given the natural frequency, mode shape, and curvature of the modes from OrcaFlex. Shear7 then identifies the potentially excited modes by comparing the minimum and maximum excitation frequencies with the natural frequencies supplied from OrcaFlex. When considering added mass in Shear7, this is deemed to primarily affect the predicted natural frequencies and has minimal influence on the Shear7 calculations.

The added mass coefficient was initially set to equal 0.5, based off of the work by Delizisis et al. 2022. At large Reynolds number and current speeds the predicted VIV are much less sensitive to the value of the added mass coefficient. At large modes the difference between modes is much less significant,

i.e. vibrating at a mode of 30 or 31 will result in similar fatigue stresses on the cable. The added mass coefficient is investigated in Chapter 5.4.

Figure 3-3 shows how nodes at the boundary are handled:

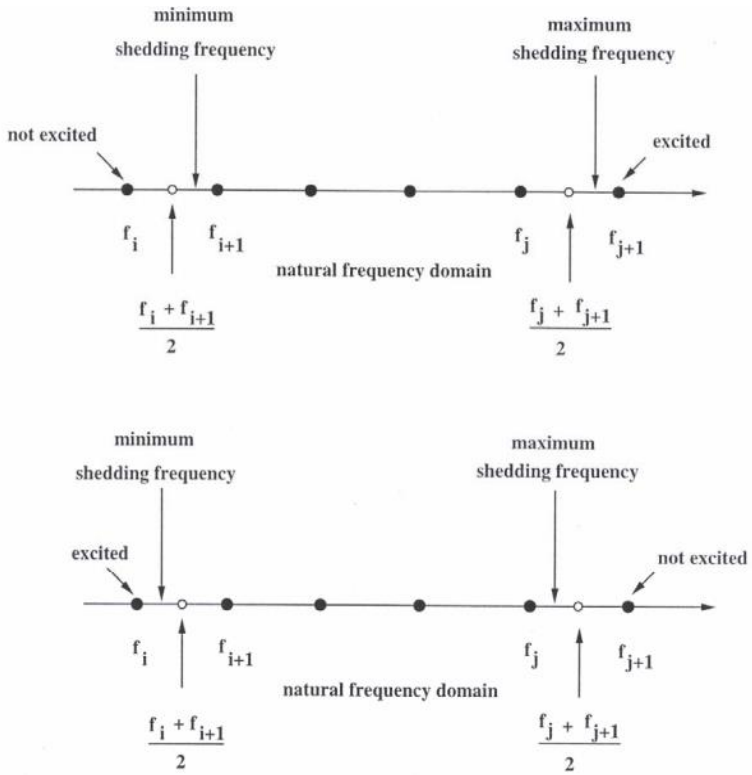

Figure 3-3: Identification of the boundary of the potentially excited modes

The range of modes used to compute the VIV response is from the first mode to the mode whose natural frequency is 1.5 times higher than the highest vortex shedding frequency. The reason for this large range is because to be able to correctly model spatial attenuation non-resonant modes are required to be included in the response calculation. Spatial attenuation is the loss of energy due to dispersion as it travels through a medium.

A rough estimation of the power of each mode is then calculated:

$$\Pi^2 = \frac{|Q_r|^2}{2R_r} \qquad \text{Eq. 3.25}$$

Where Q_r is the modal force and R_r is the modal damping:

$$Q_r = \int_0^{L^r} \rho_f C_L(x, V_{R(x)}) D(x) V^2(x) Y_r(x) dx \qquad \text{Eq. 3.26}$$

$$R_r = \int_0^{L-L^r} R_h(x) {Y_r}^2(x) \omega_r dx + \int_0^{L} R_s(x) {Y_r}^2(x) \omega_r dx \quad \text{Eq. 3.27}$$

where R_h and R_s are the modal hydrodynamic and structural damping and Y_r is the *r*th mode shape of the system. L^r is the excitation region for mode r and is determined by lower and upper limits result from user-selected, multi-mode, reduced velocity bandwidth.

A comparison is then made as to the significance of the input power of each mode, based on a user selected value where lower power modes are discounted. The user selected value is known as the power-in ratio. The value is calibrated from experimental results. Delizisis et al. 2022, set a value of 0.05, this was to ensure that lower power modes were included in determining the VIV displacement response. For a highly flexible cable at lower relative velocity, the lower modes may, wrongfully, be ignored if typical calibrated parameters are used.

If the number of modes above cut-off is one, then a single mode response is predicted, otherwise multi-mode is predicted. The method for identification of modes is shown in Figure 3-4.

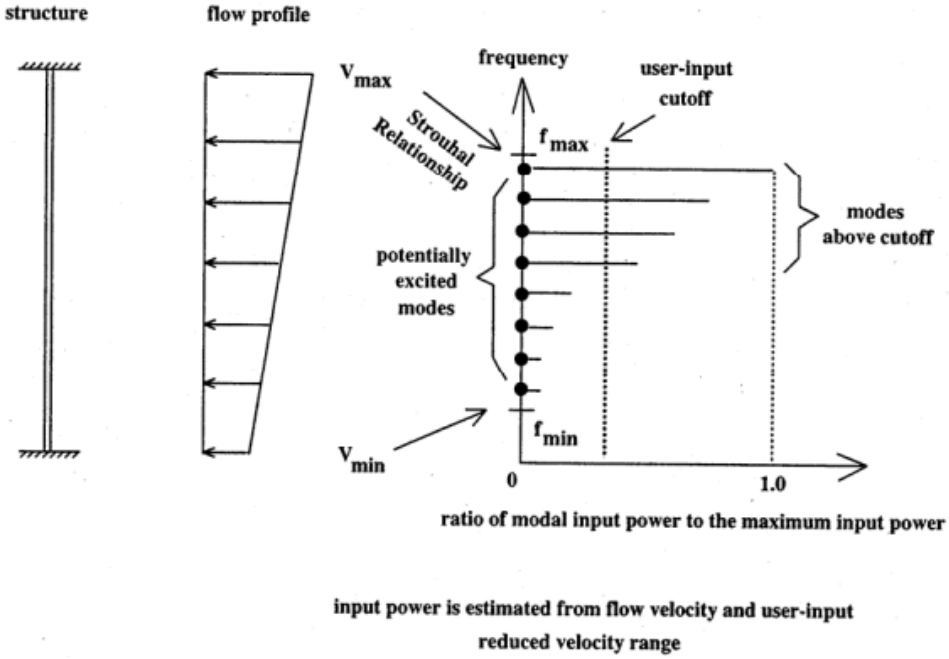

Figure 3-4: How OrcaFlex identifies the most important modes

The length of the power-in region for each excited mode is calculated:

$$V_r = \frac{V(x)}{f_r D} \quad \text{Eq. 3.28}$$

where $V(x)$ is the local flow velocity at x, D(x) is the local diameter of the cylinder, $V_r(x)$ is the reduced velocity at x for mode r, and f_r is the rth natural frequency of the structure.

As previously discussed, the Strouhal number is heavily influenced by the Reynolds number. Based on a conservative maximum current speed of 2m/s the maximum predicted Re is 4.2×10^5 for the power cable and 1.4×10^6 for the buoyancy section. This is for the largest power cable investigated which is designed for a substation at 220kV. Referring to Blevins 1977, this Re results in a predicted Strouhal number range from approximately 0.18 - 0.4, depending on the roughness of the cylinder. Shear7 requires a user defined number to be used for the Strouhal Number. The impact of this value on VIV is investigated in Chapter 5.1.

Since $V(x)$ varies with location a reduced velocity power-in region is defined. This is done to define the portion of the structure which contributes to the resonant response of one mode. It is assumed that whenever V_r at x for mode r is within the reduced velocity bandwidth for mode r the fluid will excite the structure and contribute to the structural response.

This process divides the entire structure into different power-in regions which have the same range of reduced velocity, but vary in location because each region is defined by a different natural frequency. The number of these regions is the number of modes above cut-off. For every excited mode there are power-in and power-out (damping) regions. The power-in region for mode r is L^r and the length of the power-out region for mode r is $L - L^r$. Figure 3-5 shows how this is done.

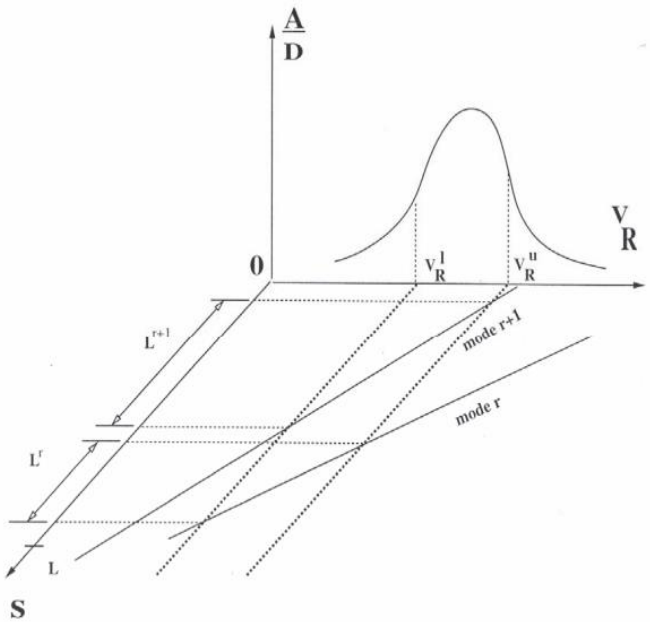

Figure 3-5: The division of the Power-In region

If there is overlap between adjacent power-in regions, then the program will perform a mode overlap elimination. The criterion for elimination is that the power-in region length for each mode involved in the overlap shrinks equally until the overlap disappears. For each mode r in the power-in region the lift force is assumed to occur at the natural frequency of that mode.

The governing equation for the behaviour of the structure in Shear7 is:

$$m_t\ddot{y} + R\dot{y} + Ty'' = P(x,t) \qquad \text{Eq. 3.29}$$

where m_t is the mass per unit length (including the added mass), $\ddot{y}$ is the acceleration of the structure, R is the damping per unit length (including both structural and hydrodynamic), $\dot{y}$ is the velocity of the structure, T is the tension, y'' is the second derivative of the displacement of the structure with respect to the spatial variable, and $P(x,t)$ is the excitation force per unit length (lift force distribution).

The system displacement response can be written as the superposition of modal responses:

$$y(x,t) = \sum_r Y_r(x)q_r(t) \qquad \text{Eq. 3.30}$$

where $Y_r(x)$ is the rth mode shape of the system. Substituting this relation into the governing equation and performing the standard modal analysis leads to:

$$M_r\ddot{q}_r(t) + R_r\dot{q}_r(t) + K_r q_r(t) = P_r(t) \qquad \text{Eq. 3.31}$$

Where:

Modal Mass: $M_r = \int_0^L {Y_r}^2(x)m_t dx$

Modal Damping: $R_r = \int_0^L {Y_r}^2(x)R(x)dx$

Modal Stiffness: $K_r = -\int_0^L T{Y_r}''(x)Y_r(x)dx$

Modal Force: $P_r(t) = \int_0^L Y_r(x)P(x,t)dx$

In the power-in region for mode r, it is assumed that the local force and rth modal velocity are always in phase. Hence, the formula for the calculation of the rth modal force in the rth mode power in region is:

$$P_r(t) = \int_0^L |Y_r(x)|P(x,t)dx \quad \text{Eq. 3.32}$$

The lift force per unit length, with frequency ω_r can be written as:

$$P(x,t) = \frac{1}{2}\rho_f D V^2(x) C_L(x,\omega_r) sin(\omega_r t) \quad \text{Eq. 3.33}$$

where ρ_f is the fluid volume density, D is the diameter of the cylinder, $V(x)$ is the flow velocity, and $C_L(x,\omega_r)$ is the lift coefficient amplitude for mode r.

Let the modal velocity for mode r be:

$$\dot{q}_r(t) = A_r \omega_r sin\,(\omega_r t) \quad \text{Eq. 3.34}$$

where A_r is the modal displacement amplitude of the structure for mode r.

The rth modal input power is the rth modal excitation force times the rth modal velocity:

$$\Pi_r^{in} = \int_0^{L^r} \frac{1}{2}\rho_f D V^2(x) C_L(x,\omega_r) sin^2(\omega_r t)|Y_r(x)|dx \quad \text{Eq. 3.35}$$

where L^r represents the length of the power-in region for the *r*th mode.

The time-average of the modal input power over one period P is:

$$\langle \Pi_r^{in} \rangle = \frac{1}{P}\int_0^P \Pi_r^{in} dt = \frac{1}{4}\int_0^{L^r} \rho_f D V^2(x) C_L(x,\omega_r) sin^2(\omega_r t)|Y_r(x)|dx \quad \text{Eq. 3.36}$$

The time-average of the modal output power over one period P is:

$$\langle \Pi_r^{out} \rangle = \frac{1}{P}\int_0^P \Pi_r^{out} dt = \frac{1}{2}\int_0^L R(x) {Y_r}^2(x) {A_r}^2 {\omega_r}^2 dx \quad \text{Eq. 3.37}$$

It is assumed that, for mode r, input and output power are in balance. Equating these leads to the following expression:

$$\frac{A_r}{D} = \frac{\frac{1}{2}\int_0^{L^r} \rho_f V^2(x) C_L(x,\omega_r)|Y_r(x)|dx}{\int_0^{L-L^r} R_h(x){Y_r}^2(x)\omega_r dx + \int_0^{L} R_s(x){Y_r}^2(x)\omega_r dx} \quad \text{Eq. 3.38}$$

where the damping has been separated into the hydrodynamic part (R_h) and the structural part (R_s) because they have different integration intervals, and $L - L^r$ denotes the length of the power-out region.

An initial user determined value is assigned within OrcaFlex to the lift and damping coefficients. An iteration calculation is then performed, with the lift force and damping updating, until convergence is reached:

$$\left(\frac{A_r}{D}\right)_{i+1} = \left(\frac{A_r}{D}\right)_i + \alpha\left[\left(\frac{A_r}{D}\right)_{i+0.5} - \left(\frac{A_r}{D}\right)_i\right] \quad \text{Eq. 3.39}$$

This iterative process is completed for each mode above the cut-off. After convergence, the modal responses are used to calculate the total RMS response of the cylinder.

Damping results in the dissipation of energy from the system. Bahmani and Akbari 2010, investigated the impact of damping ratios on VIV for a circular cylinder. It was observed the damping ratio influences both the lock-in range as well as the amplitude of vibrations. A larger damping resulted in a reduced lock-in range as well as a reduced maximum amplitude value. It is well known that smaller structural damping ratio leads to larger amplitudes of vibration (Williamson & Govardhan, 2004, and J K Vandiver, 1993). The predicted value of damping is dependent on the exact cable specifications. A very conservative estimate would set the damping to be equal to 0.3%, which is common for subsea risers. The dynamic power cable configuration is similar to that of an umbilical so a damping configuration similar to this would be more appropriate.

Shear7 determines the lift coefficient value compared to a supplied table of values. The lift coefficient values are dependent on the response amplitude and reduced velocity. The lift coefficient is updated according to a function of the non-dimensional response amplitude (A/D). Figure 3-6 shows an example lift coefficient curve:

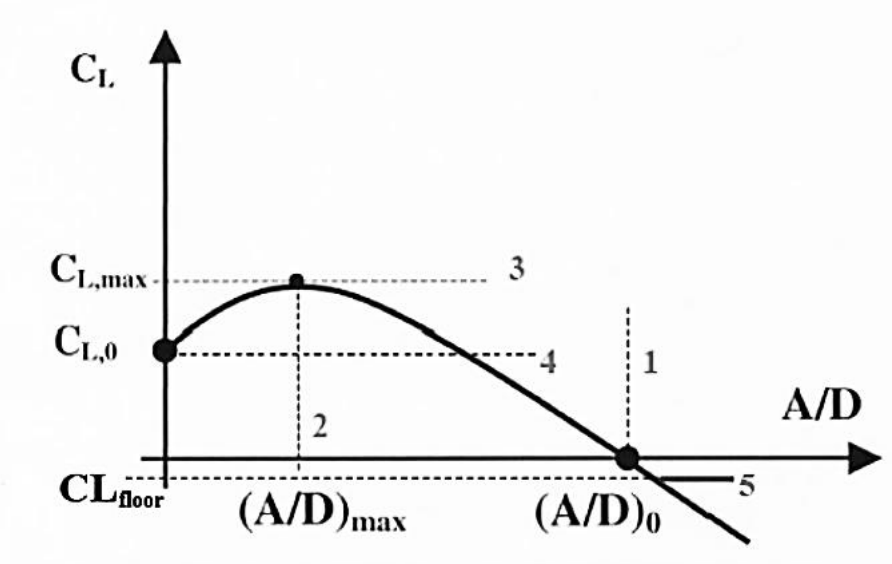

Figure 3-6: Example of a smoothed lift coefficient curve in Shear7 (Vandiver & Li, 2005)

The lift coefficient curve is generated by fitting two parabolas through four user-defined values, shown in Figure 3-6. These values are:

- $(A/D)_0$: value of A/D when C_L is equal to 0
- $(A/D)_{max}$: value of A/D when C_L is at its maximum,
- $C_{L,max}$: is the maximum value of C_L,
- $C_{L,0}$: the value of C_L when (A/D) is equal to 0.

A parameter $C_{L,floor}$ is used to limit the maximum negative value of the lift coefficient. This is specified by the user. Shear7 contains C_L tables which are calibrated against experimental results. The tables used in this research are:

- Table 1:
    - Conservative table with a single curve independent of frequency ratio.
- Table 2:
    - Non-conservative table based on experimental data fit, a three-dimensional lift coefficient curve that varies based on A/D and frequency ratio.
- Table 4:
    - A lift table developed for high Reynolds Number experiments.
- Table 5:

- Conservative model of strakes

- Table 6:
  - Ideal, no marine growth, undamaged strakes based on 25% high, 17.5 pitch ratio.

Table 1 is based off of a linear function of lift coefficient vs A/D and is independent of the frequency ratio. Table 2 is based on a functioned based smooth lift coefficient vs A/D curve fitted to non-conservative experimental data. Table 2 is predominantly used due to its calibration to experimental data, and it has been shown to accurately model at high modes, and at low modes for a power cable previously. The other lift coefficient tables are investigated as well. This value can be the hardest to calibrate as it can vary for different cable sections, such as the buoyancy modules. Without appropriate experimental data to adequately determine the impact of buoyancy modules on the lift coefficient tables it is decided to utilise the same lift tables for the whole cable length in this research.

The full Shear7 procedure is shown in Figure 3-7:

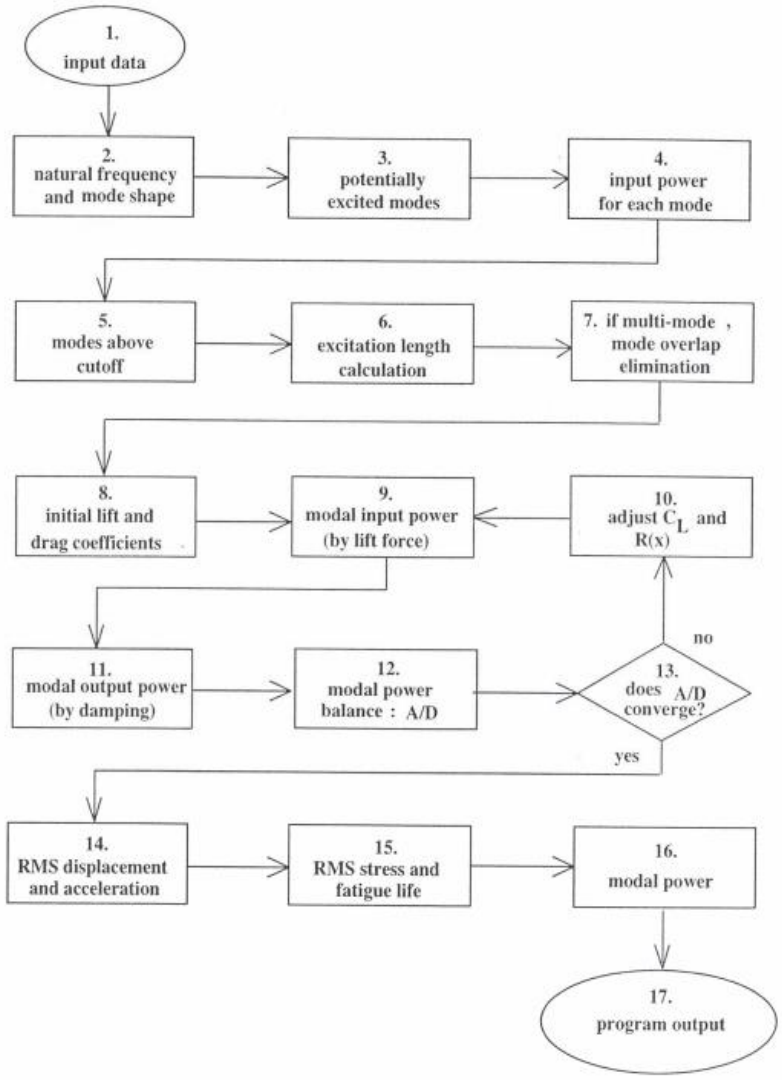

Figure 3-7: Flow-chart of the shear7 mode superposition solution (Vandiver & Li, 2005)

There are two methods for utilising Shear7 used in this project. Both of these methods are described below with the fully coupled method being preferred due to communicating between both Shear7 and OrcaFlex to reach convergence.

Fully coupled:

1. Line's drag coefficients are specified within OrcaFlex.
2. The static position of the line is determined according to the specified drag coefficients.
3. Shear7 is ran to analyse VIV at that position, the line drag coefficients are then updated.
4. The static position of the line is recalculated based on the new drag coefficients.
5. Steps 3 and 4 are repeated until convergence is achieved.

Independently defined modes of vibration:

1. The modes of vibration are determined within OrcaFlex, typically from still water.
2. The normal relative velocity to the object is extracted from OrcaFlex for the chosen conditions.
3. The normal relative velocity is used by Shear7 to predict the mode excitation and predict the VIV behaviour.

The drag coefficient was set to equal 1.2 as this is standard for a smooth cylinder. In reality marine growth would attach itself to the cable and change the value of this. Marty et al. 2021, investigated the impact of mussels on the forces experienced by a cylinder under varying current conditions. They found that depending on the mussel configuration the drag coefficient, lift coefficient, and Strouhal number all vary over a range of Re = 0.5 – 3.5 × 10^5. Shear7 determines the drag coefficient through coupling until convergence is reached, as such varying the initial drag coefficient value has no impact on results.

The hydrodynamic parameters within Shear7 are defined and calibrated for a cable perpendicular to the direction of the fluid flow. As the angle of inclination of the cable changes, due to factors such as the cable configuration and current direction, the originally specified and calibrated coefficients may no longer be suitable, especially at extreme angles. This is because the parameters are calculated for specific reduced velocities, and when the cable is deformed to such an extent the reduced velocity is substantially altered, and the coefficients may incorrectly predict the VIV behaviour. This incorrect response is nullified in most situations. This is due to the vibrations over the rest of the cable, where such extreme angles of inclination are not present, dominate the response.

3.1.6 Frequency Prediction Process for Shear7

Shear7 operates using mode superposition. The likelihood of the excitation of each mode is determined along the cable's length. Figure 3-8, Figure 3-9, and Figure 3-10 show the probability of excitation of each mode's corresponding frequency for a current angle of 0, 90, and 180 degrees respectively.

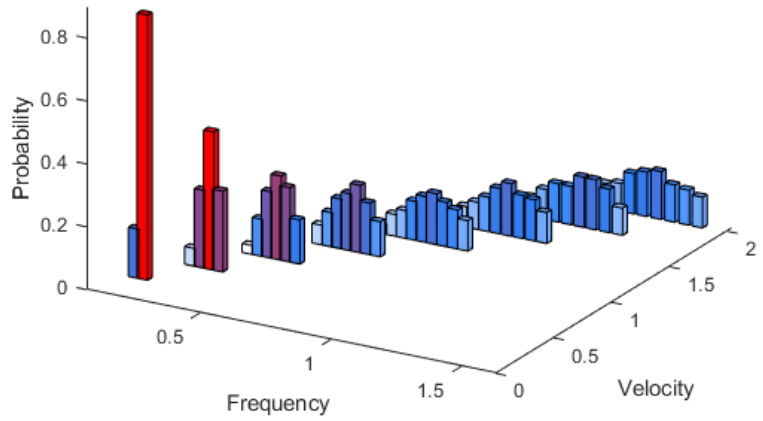

Figure 3-8: Probability of excitation frequencies for a uniform current at a speed of 1m/s and angle of 0 degrees

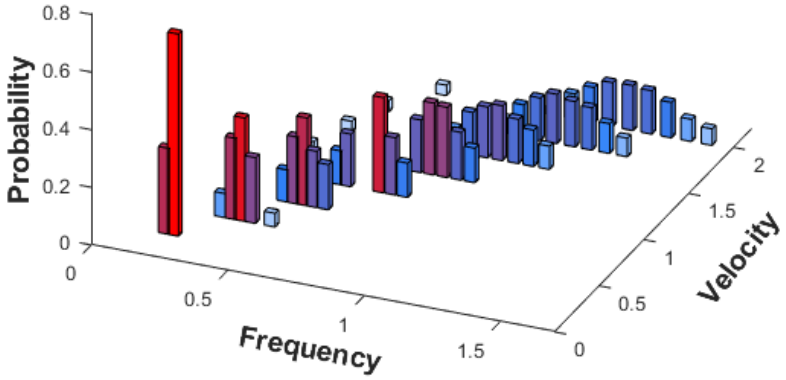

Figure 3-9: Probability of excitation frequencies for a uniform current at a speed of 1m/s and angle of 90 degrees

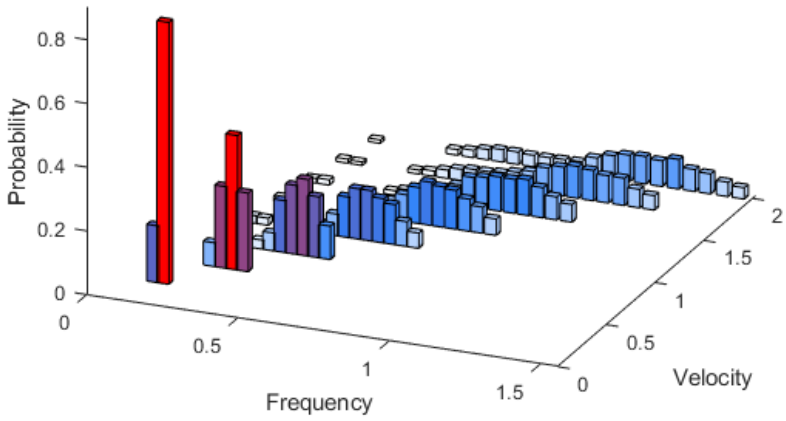

Figure 3-10: Probability of excitation frequencies for a uniform current at a speed of 1m/s and angle of 180 degrees

The mode with the largest probability of excitation is used for analysis and comparison from the Shear7 output results. As can be seen, there are, especially evident at higher velocities, multiple modes that are similar in probability. This is acknowledged as limiting the accuracy but accepted because the maximum probability value is still very similar in frequency value to the other modes with large probabilities. This can explain discrepancies seen in frequency predictions. Spectral analysis is conducted to determine the frequency of vibrations using the IBWO model.

3.1.6.1 Wave Modelling Using Shear7

The methodology for discerning the impact of waves on the VIV profile was influenced by that of Dillon-Gibbons et al. 2017. OrcaFlex is initially run in the time domain for the chosen environmental load case. Time instances are extracted over the wave period at twelve equally spaced time intervals. The normal relative velocity for each node along the cable is extracted for each of these instances. These twelve individual normal relative velocity vectors are then run within Shear7 with the mode file supplied separately. The output Shear7 results are then analysed for each separate time instance. A time domain VIV prediction model would be preferred in this situation to better capture the time-varying behaviour as well as additional interactions, such as wave and heave induced frequencies of vibration. Without access to an appropriate time domain model this is not attempted in this research.

3.1.7 Limitations

Naturally, all numerical models are limited by their relevance to the problem proposed and the dataset used to calibrate them. A dynamic power cable in the lazy wave configuration lacks full scale experimental data to calibrate any numerical model. The parameters chosen for Shear7 in this project were determined from scaled down power cable experiments. de Wilde et al. 2021 and Delizisis et al. 2022, conducted an experiment on a scaled down power cable in the vertical plane and then replicated this behaviour using Shear7. It is noted that the parameters from Delizisis were calibrated for lower modes of vibration and for a scaled down power cable. The parameters from Delizisis' study are compared to additional sets of parameters. These parameters were calibrated for higher modes and for a high aspect ratio riser, therefore are appropriate in terms of higher mode VIV but fail to accurately account for the flexible power cable behaviour and the lazy wave shape. This is discussed in Chapter 5.2.

3.2 VALIDATION

The three different models that are used in this study, IBWO, MWO, and Shear7, were validated and calibrated against experimental results from Flotant, FLOTANT is a Cooperation Research Project funded by the European Union´s Horizon 2020 research and innovation programme. Flotant released two public deliverables which provided experimental results for VIV along a power cable (de Wilde et al., 2021 and Oud et al., 2021).

3.2.1 Flotant Tow Tank Tests

Flotant ran experimental tests on a scaled down dynamic power cable to observe and analyse the VIV behaviour. The cable used was a 48mm outer diameter, simplified, scale 1:3 representation of a 144 mm outer diameter, full scale, 66 kV submarine electrical cable. The cable was tested via forced oscillations in air, water, and also through VIV tow tank tests.

The cable used in the experiments consisted of a simplified single conductor core consisting of stranded aluminium 29mm in diameter. The outer layer was XLPE, commonly used in cabling. The properties of the full cable are shown in Table 3-1.

Table 3-1: Flotant Cable Properties

Parameter	**Value**
Outer Diameter	48mm
Length	6.4m
Mass in air	2.8 kg/m
Bending Stiffness	3.0 kNm^2
Natural Frequency	1.77 Hz

Only the tow tests from Flotant were used for comparison when investigating the VIV prediction models. These two tests were performed by attaching the top end of the vertically hanging cable to a moving carriage and attaching the lower end of the cable to a 200 kg block. The carriage ramped up to the required speed and, after a sufficiently long distance, the VIV was measured. Within OrcaFlex the block was modelled as an additional line module and the current was modelled as uniform. The model set-up within OrcaFlex is shown in Figure 3-11.

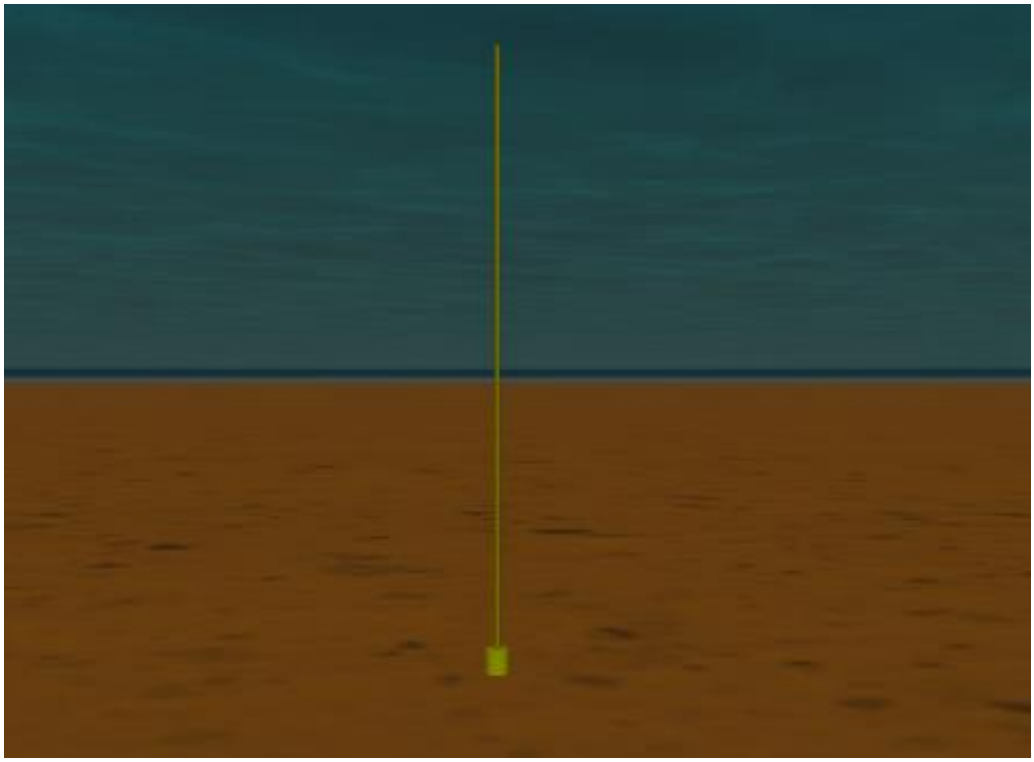

Figure 3-11: Cable model within OrcaFlex according to Flotant

From the experimental tests it was observed that the crossflow displacement was roughly 3 to 4 times larger than the inline displacement, with VIV of notable amplitude seen.

Comparisons of the predictions produced from the different models against the experimental data has been undertaken. A drag coefficient of 1.2 was used for the MWO and IBWO models, otherwise the default parameters for these models were used. The numerical parameters chosen for Shear7 were taken from a study conducted by Delizisis et al. 2022 and discussed previously.

3.2.2 VIV Model Comparison

The results from the different models are compared at different intervals along the cable length, these being *0.5L, 0.75L*, and *L*.

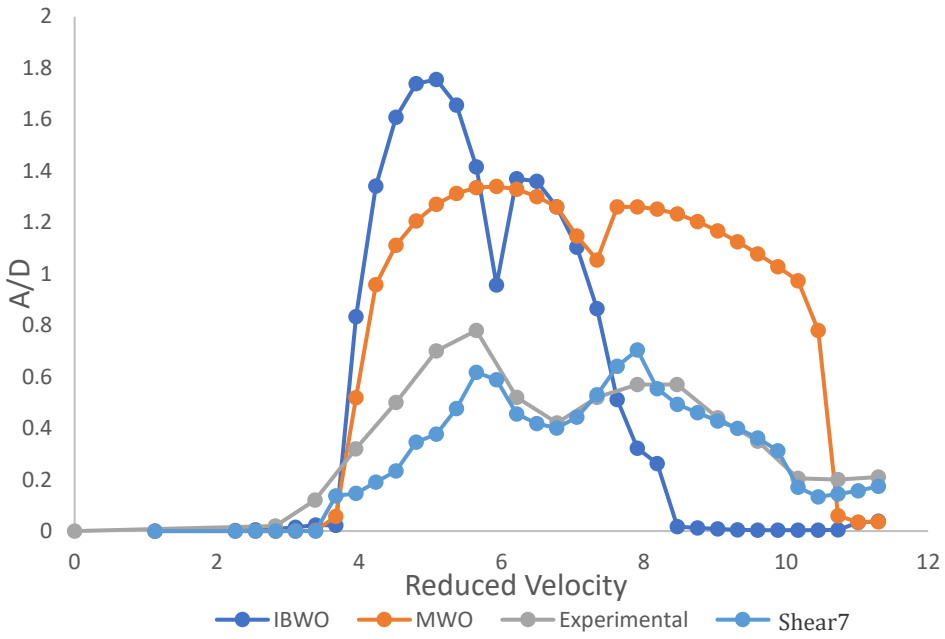

Figure 3-12: Numerical and experimental model comparison of the RMS displacement at 0.5L

As can be seen in Figure 3-12 there were notable discrepancies between the predictions of the different VIV models. Generally, all the models accurately predicted the reduced velocity at which the first mode of vibration developed, around 3.9. However, there were large differences in the magnitude of the RMS displacement predicted. Comparing the model results to experimental results, IBWO predicted a peak in displacement at a reduced velocity of 4.9 and a second lower peak at 6.3. These peaks were at lower reduced velocities than for the experimental results, and also at magnitudes greater than double the displacement. The MWO predicted a first peak at a reduced velocity of 5.8 which is very similar to the experimental data, albeit at a magnitude 70% greater. The second peak was predicted at 7.5, again similar to the experimental results, before a gradual decline in amplitude as the reduced velocity continued to increase, then followed by a rapid drop to close to 0 A/D at 11. Shear7 predicted the closest VIV response out of the numerical models in terms of both magnitude and relationship to reduced velocity. Shear7 predicted the first and second peak at similar reduced velocities to the experimental results, albeit underestimating the first peak amplitude by 25% and overpredicting the second peak amplitude by 15%. When comparing the different model's accuracies, Shear7 is the obvious preferred choice despite the discrepancies in the magnitude of the amplitude.

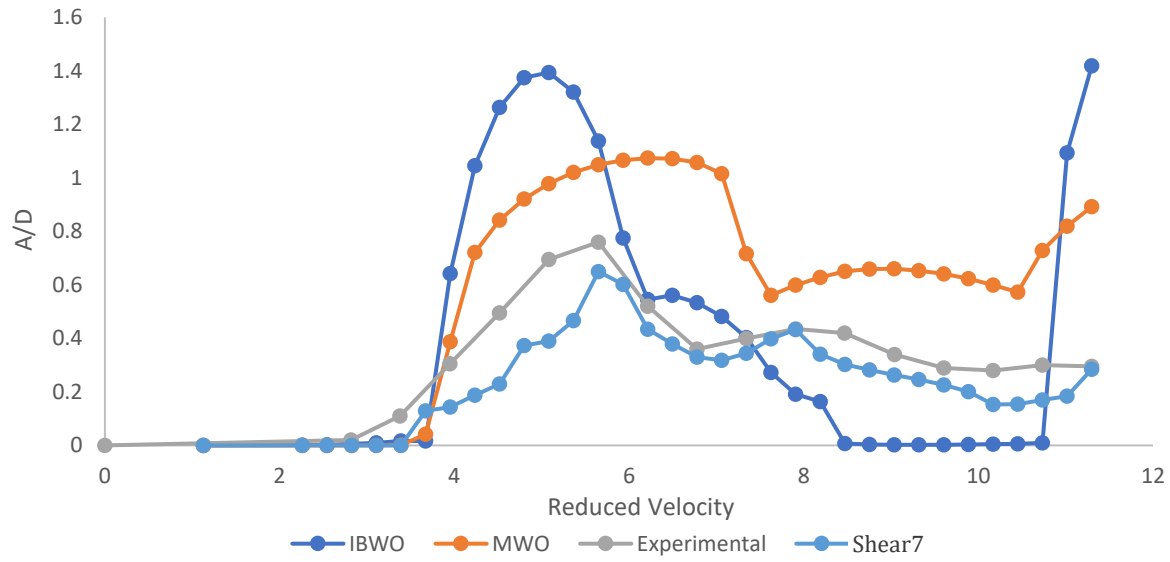

Figure 3-13: Numerical and experimental model comparison of the RMS displacement at 0.75L

Figure 3-13 showcases similar trends in the VIV model outputs as observed in Figure 3-12. The IBWO model predicted the first peak at a reduced velocity of 5, compared to the experimental peak which was at 6. The amplitude of vibration was also substantially larger than the experimental results, nearly double in magnitude. MWO predicted the first peak in displacement over a range of reduced velocity from 4 – 7, also at a greater magnitude than the experimental data. Shear7 predicted that peak at the same reduced velocity as the experimental data but at a smaller magnitude. After the peak, Shear7's predictions closely matched the experimental data, in terms of the influence of reduced velocity on amplitude of vibrations, while slightly underestimating the magnitude of the displacement.

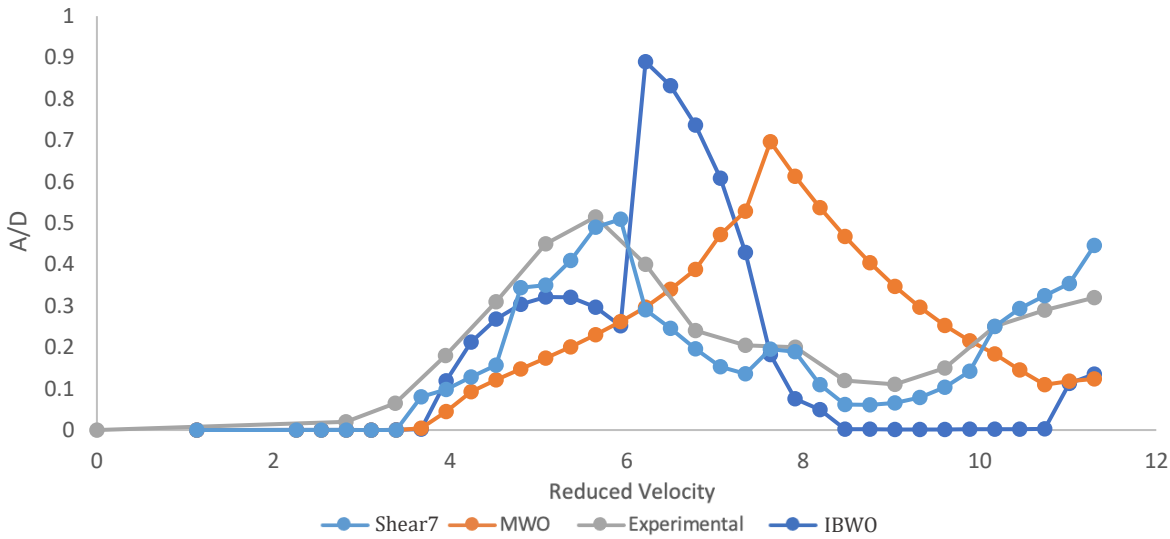

Figure 3-14: Numerical and experimental model comparison of the RMS displacement at L

Both the wake oscillator model's predictions substantially diverged from the experimental data for the length *L/L*, shown in Figure 3-14. IBWO predicted a sharp peak at a reduced velocity of 6 followed by a sudden decrease back to no prediction VIV displacement at a reduced velocity of 8.3. MWO predicted a gradual increase in displacement from a reduced velocity of 3.7 up to 7.7, which was then followed by a gradual decrease as the reduced velocity continues to increase. Both the wake oscillator models predicted much larger magnitudes of displacement compared to the experimental values and substantially different relationships between displacement and reduced velocity. Shear7 predicted the first peak in RMS displacement at a very similar reduced velocity to the experimental data, 5.8, as well as at a similar displacement, 0.52 A/D. It then followed a similar trend regarding the relationship of displacement amplitude to reduced velocity, as the reduced velocity continues to increase both the experimental and Shear7 amplitudes gradually decreased until a reduced velocity of around 9, after which a gradual increase is seen.

When comparing the results from the three different VIV prediction models against the experimental data Shear7 produced the most accurate predictions regarding both the magnitude of displacement and the relationship between reduced velocity and amplitude of vibrations. IBWO predicted both a sharp increase and decrease around the same reduced velocity as seen in the experimental peak, except at magnitudes of displacement nearly double. MWO predicted a similarly rapid increase in displacement but predicts a wider range of lock-in reduced velocities with an elongated peak. Both the wake oscillator models vastly over-predicted the RMS displacement, often in the magnitude of over double that of the experimental data. Based on these observations, Shear7 is chosen as the preferred model for predicting the vibrations for a dynamic lazy wave power cable.

3.2.3 CableDyn Experiments

Experiments were undertaken within the FloWave facility at the University of Edinburgh as part of the CableDyn Project (EPSRC CableDyn Project, 2022). A lazy wave power cable was deployed within the 2m deep tank. This was scaled down from a water depth of 100m and based on the full-scale configuration used as the lazy wave power cable configuration in this thesis. Currents were generated within the facility ranging from 0.1-0.8 m/s at intervals of 0.1 m/s. The direction of the current was varied at angles 0, 90, and 180 degrees relative to the plane of the cable. The cable's internal components can be seen in Figure 3-15.

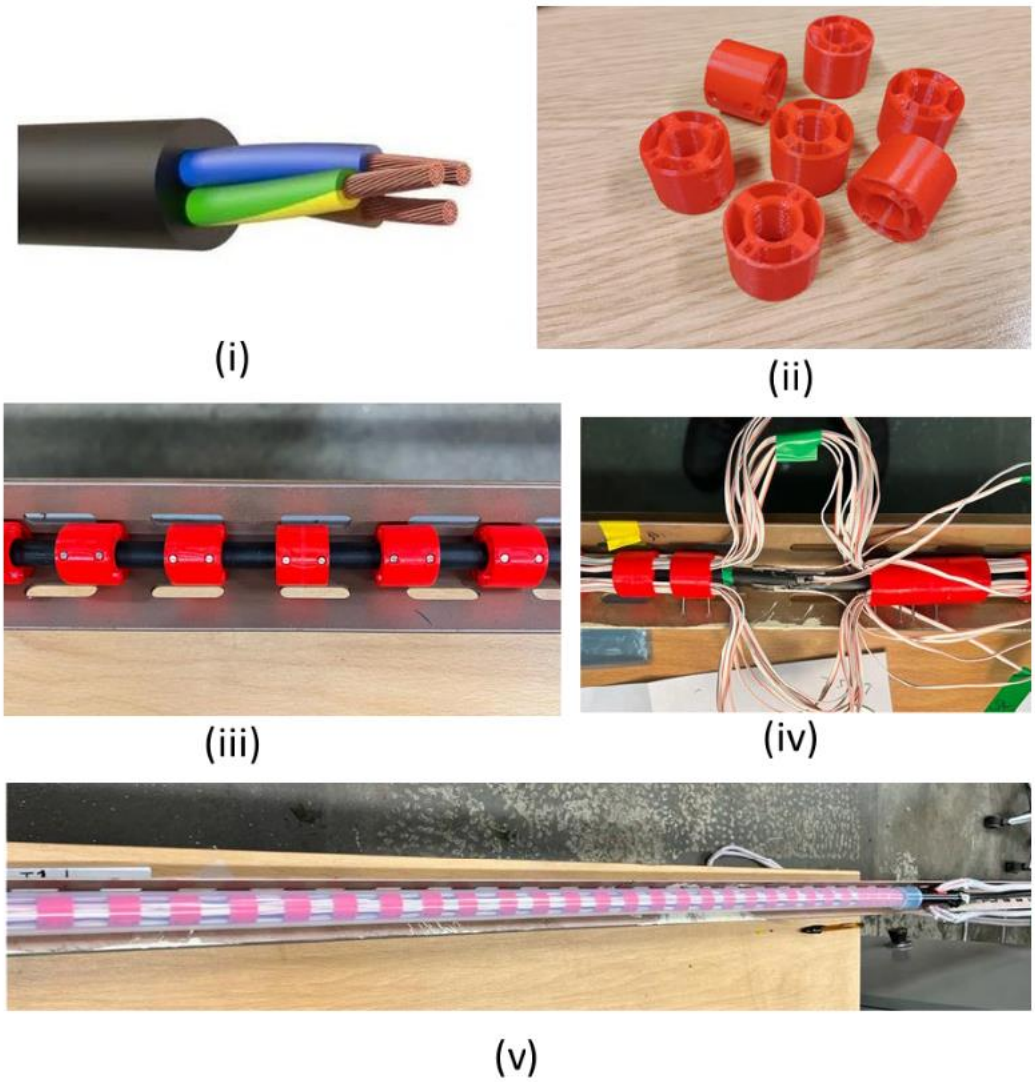

Figure 3-15: Cable internal components (i) inner core cable (ii) 3d printed spacers (iii) spacers fixed on the inner cable (iv) strain gauge fixing at individual locations (v) cable setup inside the silicon tube (EPSRC CableDyn Project, 2022)

The properties of the scaled-down cable were determined from a plain cable sample using the TecQuipment SM1004 Beam Apparatus at the University of Exeter. Both a simply supported beam and a cantilever beam arrangement were used to determine the cable properties. The linear bending stiffness of the instrumented cable was 0.265 Nm^2 with a quoted error of 24%.

The damping of the cable was determined via free decay tests in both air and water. In air, the damping was 6% and water 3.8%. The water damping of 3.8% is similar to the 2.8% damping observed in the Flotant experiments discussed previously. The full cable properties are shown in Table 3-2.

Table 3-2: Properties of the Scaled Cable Model (EPSRC CableDyn Project, 2022)

Properties	
Inner cable	
Length (m)	5 m
Total weight	4.113 kg
Outside diameter (m)	0.031
Inner core cable	H07RN-F 3 core rubber cable
Inner core cable diameter (m)	9.8 mm
Inner core cable weight (g/m)	134 g/m
Mass ratio	1.09
Submerged length of cable in water	4.5 m
Touchdown zone	1.08 m
Buoyancy section	1.12 m
Top section	2.279 m
Spacers	
Numbers	118
Weight (g/piece)	4.4
Total weight	519.2 g
Silicon tube weight	250 g/m
Weight of strain gauges wires	461 g
Weight of water filled	1108.2 g
Buoyancy modulus (BM)	
Outside diameter	70 mm
Inside diameter	31 mm
Length	40 mm
Density	100 kg/m3
No. of BM	5
Distance between BM	0.184m
Cable structural properties	
Natural frequency in air	0.61 Hz
Damping in air	0.59 %
Bending stiffness	0.27 Nm2

The exact cable configuration is shown in Figure 3-16. There were strain gauges located along the cable's length. The strain isn't an output from our research and as such the strain measurements weren't used. The RMS displacement results compared in this section were output from CableDyn. There were notably large error margins reported due to the use of Qualisys to determine the displacement. Qualisys uses underwater cameras to measure the displacement and struggled to pick up section along the cable length at certain markers. There were also difficulties experienced with extracting the RMS displacement from the Qualisys output data due to the large deformations the cable saw.

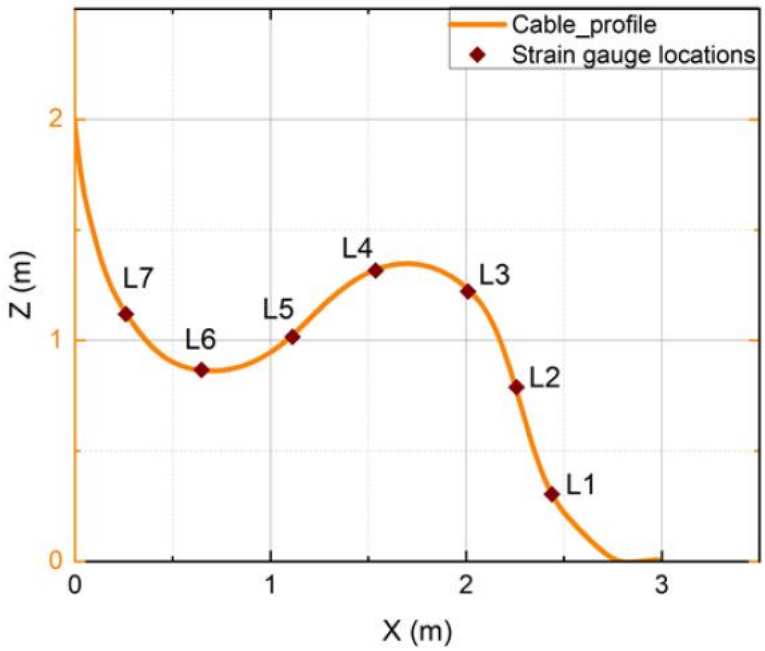

Figure 3-16: Cable configuration with locations of strain gauges

Qualisys was also used to determine the displacement of the cable around the strain gauge locations. The resulting displacement was compared against an OrcaFlex and Shear7 coupled model replicating the experimental setup. The current speed for each comparison was uniform and 0.1 m/s. Shear7 uses numerical parameters calibrated from the experiments performed by Flotant discussed previously.

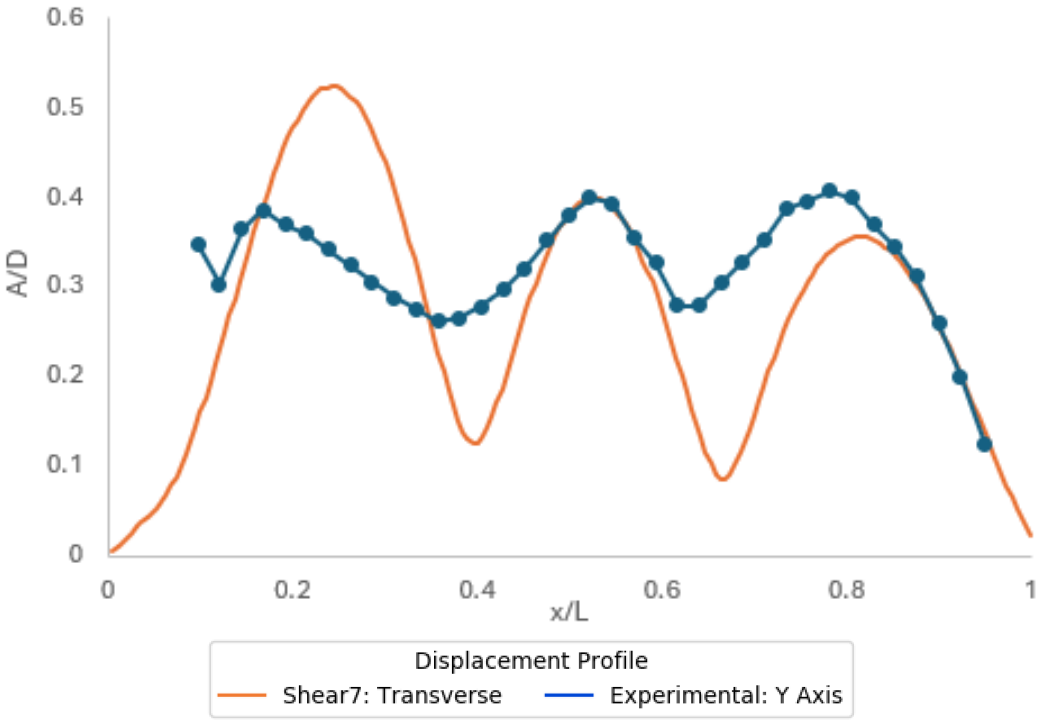

Figure 3-17: Experimental and numerical comparison of the RMS displacement for a current angle of 0 degrees

As can be seen from Figure 3-17, Shear7 predicted a similar mode of vibration and peaks at locations along the cable length. There were some notable differences in magnitude with the experimental data predicting three peak displacements and all at approximately 0.4A/D. Shear7, however, predicted a larger displacement towards the hang-off point at the first peak, around 0.5 A/D, which decreased to 0.4 A/D for the second peak and 0.35 A/D for the third peak. Shear7 also predicted much more drastic dips between the peak whereas the experimental data predicted a much smaller trough between the peaks. The large dips seen for the Shear7 results were likely due to the prediction of a standing wave. This trend was seen for all current angles. The limitations of the accuracy of the RMS displacement results have been previously discussed and also will have influenced the output. Shear7 is capable of modelling travelling waves via modal superposition. Vibrations develop within the 'power-in regions' and then travel along the cable. This is determined via an internal Shear7 excitation force model.

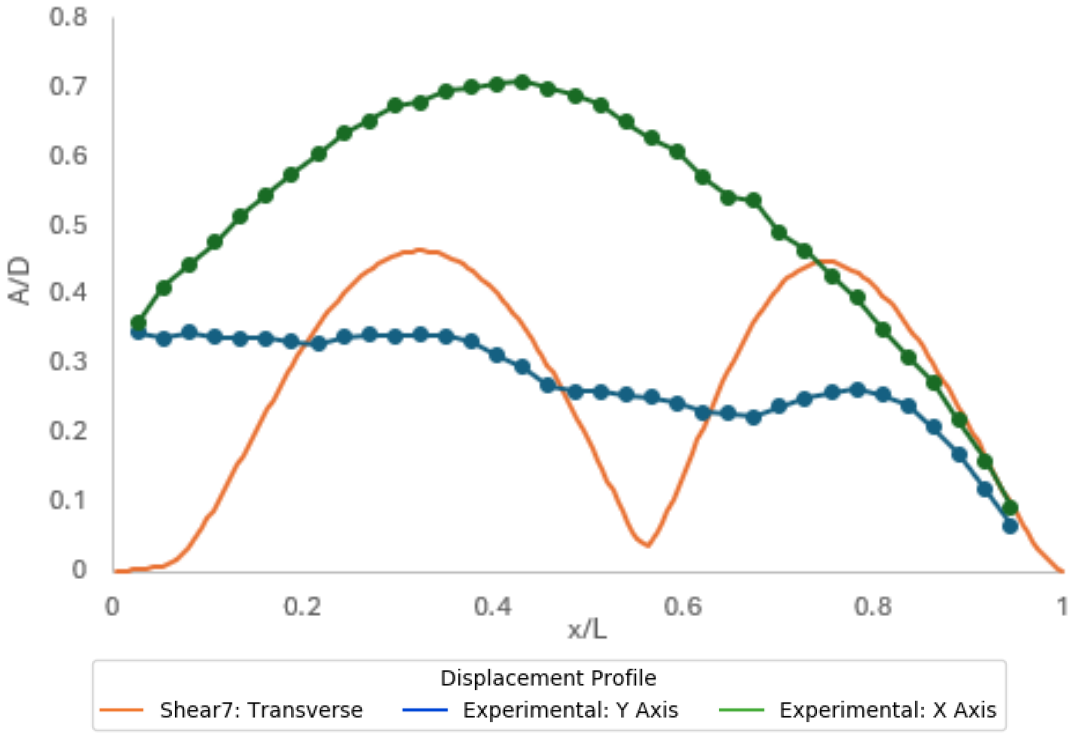

Figure 3-18: Experimental and numerical comparison of the RMS displacement for a current angle of 90 degrees

Figure 3-18 shows how the RMS displacement in the X and Y directions compared to the transverse RMS displacement. Shear7 outputs displacement in terms of the local cable orientation, and as such, due to the nature of the deformation for a current angle of 90 this wasn't contained within one plane. To allow for comparison against the experimental data the displacement along both axes has been included. It is difficult to draw conclusions about the VIV profile. One main conclusion that can be drawn is that the magnitude of RMS displacement predicted by Shear7 was within a similar magnitude for both the X and Y RMS displacement. Shear7 handles the different current angles by using the

reduced velocity determined in OrcaFlex and modelling the crossflow vibrations at each section along the cable as perpendicular to the incident current direction at each section. Qualisys is not able to define the normal direction of the flow along the full cable length for a current angle of 90 degrees.

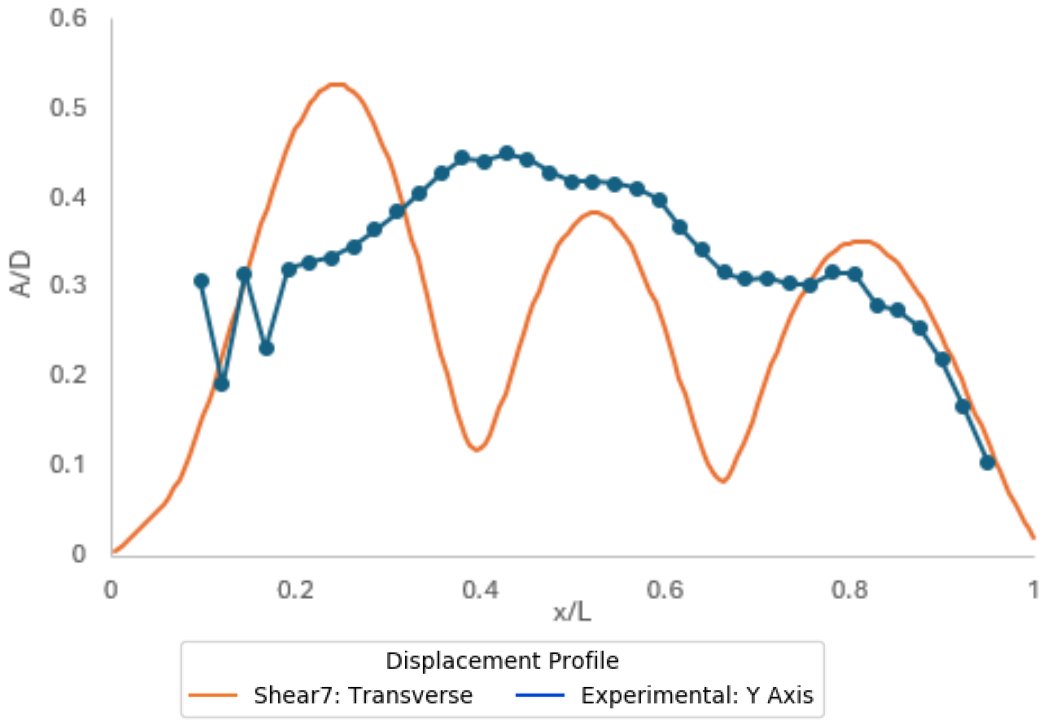

Figure 3-19: Experimental and numerical comparison of the RMS displacement for a current angle of 180 degrees

The experimental RMS displacement profile seen in Figure 3-19 was not as well defined as for current angle 0. The peaks were less obvious but what is discernible is that there were still some maximums in displacement evident at the midsection and towards the touchdown location. Overall, the magnitude of the vibrations was similar for the Shear7 predictions compared to experimental data, however, similar to the other current angles, the experimental data didn't see as drastic a decrease in displacement between the peaks and maintains, overall, a larger mean RMS displacement.

3.3 Numerical Model Set – Up

In order to investigate the cable dynamics a suitable floating platform is required. This is necessary to allow for realistic wave and current induced motions. The displacement of the platform has an impact on the cable configuration and also deflection, these parameters will impact the VIV the cable experiences. The full model setup is shown in Figure 2-3, Figure 2-4, Figure 2-5, and Figure 2-6 below with the different cable configurations investigated.

3.3.1 Floating Offshore Wind Turbine Platform

The semi-submersible turbine platform used in this study was based off of the NREL OC4 (NREL, 1996). The environment modelled is that of the Buchan Deep Hywind Site (Mathiesen et al., 2014). There are floating wind turbines currently located at this site. The water depth was set initially to 107m which is within the range of depths at this location.

3.3.2 Description of Power Cable

A dynamic power cable is made up of many internal components, as shown in Figure 2-1. Armouring is required to protect the cable, resulting in a larger diameter than for a similarly rated static power cable. Four different power cables were chosen for investigation. These were all taken from published literature and are as follows: a) 11kV umbilical for a wave-energy converter (Martinelli et al., 2010), b) 33kV lightweight power cable designed by Fulgor S.A (Oud et al., 2021), c) a 220kV dynamic export cable for a floating substation (Guignier et al., 2020), and d) a heavier cable for a shallow water steep wave (Oud et al., 2021).

The properties of these cables are shown in the Table 3-3 (Gran Canaria and Flotant are the same cable):

Table 3-3: Power Cable Properties

	Martinelli	**Flotant 33kV**	**Substation 220kV**	**Gran Canaria**	**West Barra**
Cable					
Diameter (m)	0.2	0.147	0.29	0.147	0.165
Bending Stiffness ($kN.m^2$)	10	6.24	41	6.24	7.46
Axial Stiffness (MN)	700	42.1	1419	42.1	578.7
Mass per unit Length (kg/m)	80	22.9	139	22.9	42.02
Minimum Bending Radius (m)	2	2.3	5.3	2.3	2.5
Buoyancy Module					
Diameter (m)	0.68	0.5	1	0.5	0.56
Bending Stiffness ($kN.m^2$)	1340	835	5800	835	835
Axial Stiffness (MN)	700	42.1	1419	42.1	1200
Mass per unit Length (kg/m)	208	176	500	75.1	107.47

For floating offshore wind turbines an armoured and dynamic power cable is required to adequately allow for adjustment to environmental conditions, such as subsea currents, waves, and platform motion, to ensure it can withstand the load cycles to which it is exposed. The cable properties for Martinelli are for an umbilical which has been used previously to investigate the power cables for

floating marine energy converters by Rentschler et al. 2020, Sobhaniasl et al. 2020, and Thies et al. 2012. The power cable configuration was initially modelled as a lazy wave to allow for better absorption of the induced motion, compared to that of a catenary arrangement which is at increased risk of compression towards the touchdown point.

Bend stiffeners were deployed at the hang-off and touchdown point of the cable. These were modelled as a hollow pipe covering the power cable with a large bending stiffness to reduce deflection at these points to prevent compression, and over-bending and are 5m in length. The distribution of the buoyancy section along the power cable length was influenced by Harnois et al. 2013, replicating the relative proportions from this study. The cable length was 193.13 m in total with the hang-off/top-end cable section extending up to 89.7m. The buoyancy section extended from 89.7 – 142.7m with the configuration of 1 m of armoured cable followed by 0.8m of buoyancy section repeated. The buoyancy section was modelled as individual buoyancy elements with the same properties as the cable, except for a larger diameter and different mass per unit length. The touchdown/bottom-end section of the cable extended from 142.7 to 193.13m.

Buoyancy modules are an added challenge for VIV modelling due to differences in their properties, most notably diameter. The difference in diameter of the buoyancy attachments and cable means two distinct frequencies are excitable (Constantinides et al., 2016). The buoyancy configuration influences the VIV behaviour and as such is a parameter that should be considered (Constantinides & Zhang, 2014). The buoyancy modules were included in the VIV analysis within Shear7. This was done by assigning them as sections of the cable with larger diameters, bending stiffness and a different mass ratio. This ensured they were factored in by Shear7 and their influence accounted for.

3.3.3 Mooring Lines

The mooring lines were modelled from the NREL OC-3 OrcaFlex example model (Ross & Mckinnon, 2018). There were three mooring lines in total, all equally spaced 120 degrees apart. There was no investigation on the influence of the mooring lines and all differences in water depths resulted in the mooring line being scaled accordingly. The mooring lines did play a significant part in the platform induced motion and displacement of the FOWT and, accordingly, the cable shape but this was not investigated in this research.

3.3.4 Wind Turbine

The wind turbine was modelled based on the NREL offshore 5-MW wind turbine (NREL, 1996). The platform chosen was semi-submersible. It is noted that the optimum wind turbine platform is yet to be decided and as there is no industry standard out there the semi-submersible platform is chosen.

3.3.5 Environmental Parameters

3.3.5.1 Waves

The waves modelled were regular 5th-order Stokes waves. The wave height, period, and direction are all parameters that were investigated in this research and contained within Chapter 10.

3.3.5.2 Current

In total, five different current profiles were investigated. These were a uniform profile, a power law profile to 1/7, Hywind site shear current profile (Mathiesen et al., 2014), West of Barra current profile (Oud et al., 2021) and Gran Canaria current profile (Oud et al., 2021). The data for Hywind, West Barra, and Gran Canaria are shown in Table 3-4. Sheared current profiles can lead to multi-frequency responses and reduce the amplitude of VIV (Constantinides et al., 2016).

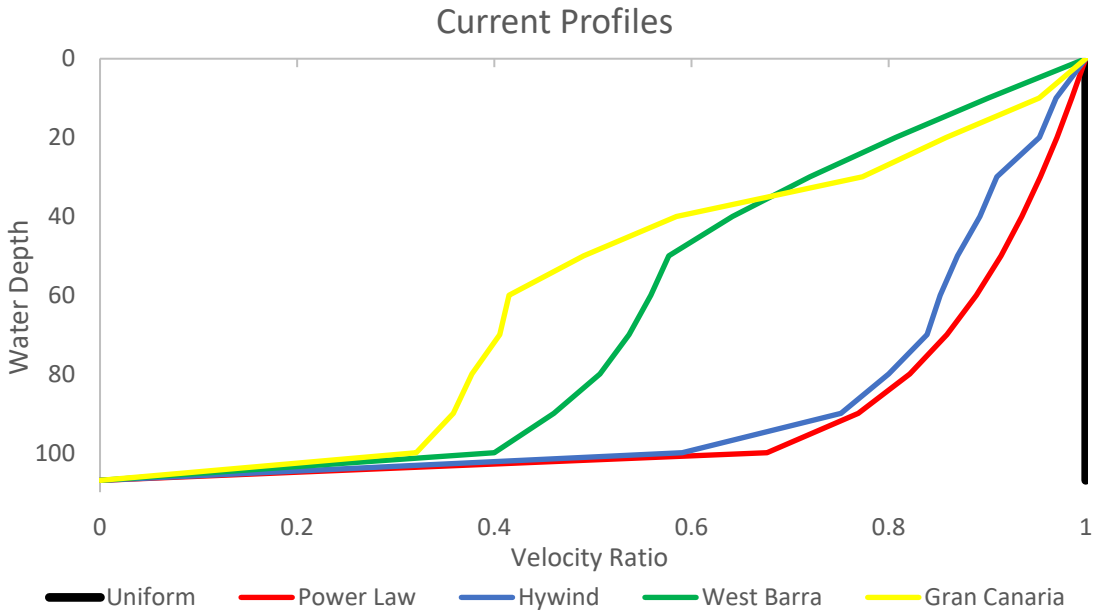

Figure 3-20: Comparison of all the current profiles investigated

Table 3-4: Current Profile Data From Sites

	West Barra	**Gran Canaria**	**Hywind**
Depth (m)	**Current Speed (m/s)**		
0	1.82	1.06	/
10	1.64	1.01	/
20	1.47	0.96	/
25	/	/	1.42
30	1.31	0.91	/
40	1.17	0.87	132.7
50	1.05	0.82	/
60	1.02	0.77	127.3
70	0.98	0.72	124.6
80	0.92	0.67	/
90	0.84	0.62	112.6
100		0.57	
110		0.52	
120		0.47	
130		0.44	
140		0.44	
150		0.43	
160		0.42	
170		0.41	
180		0.4	
190		0.39	
200		0.38	
210		0.36	
220		0.34	
230		0.31	
240		0	

The different current profiles investigated are shown in Figure 3-20**.** These current profiles were taken from different sites where either floating wind turbines are located or are noted as potential deployment sites in the future.

Shear7 operates by assuming the structure is constrained within the vertical plane. To allow the lazy wave shape to be accounted for, Shear7 is supplied with the normal relative velocity from OrcaFlex for the cable in a lazy wave shape. The local normal relative velocity profile is shown in Figure 3-21 for the different current profiles discussed. This shows how significant an impact the current profile has.

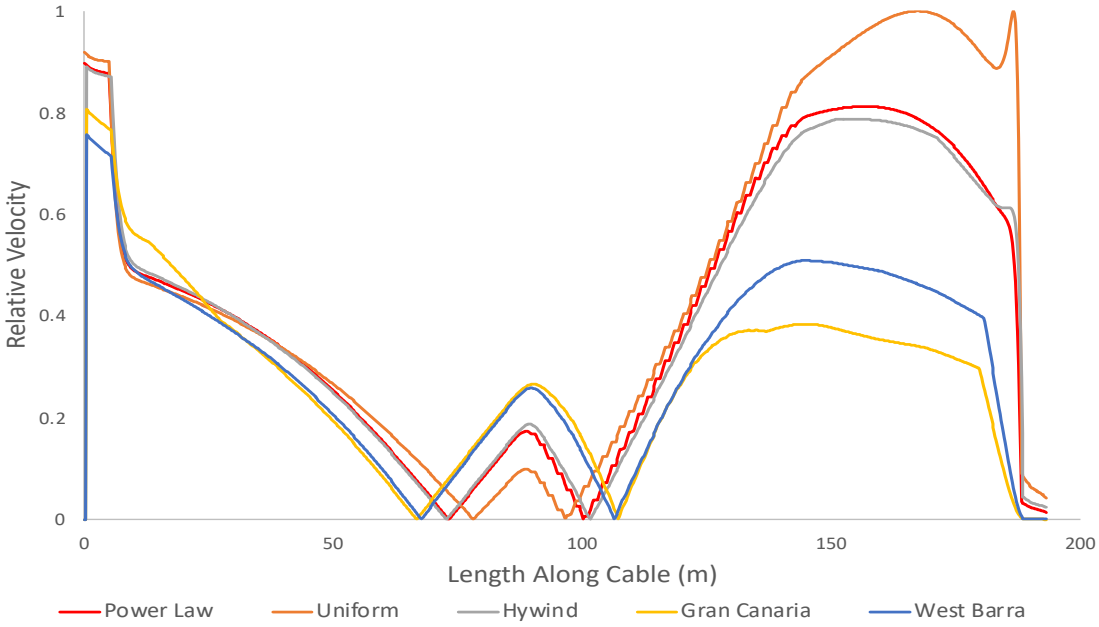

Figure 3-21: Comparison of the relative current velocity along the cable and the influence of current profile

Varying the current direction also had an even larger influence on the normal relative velocity. This is shown in Figure 3-22 which was for a uniform current profile of 1m/s. The hang-off point is at x = 0.

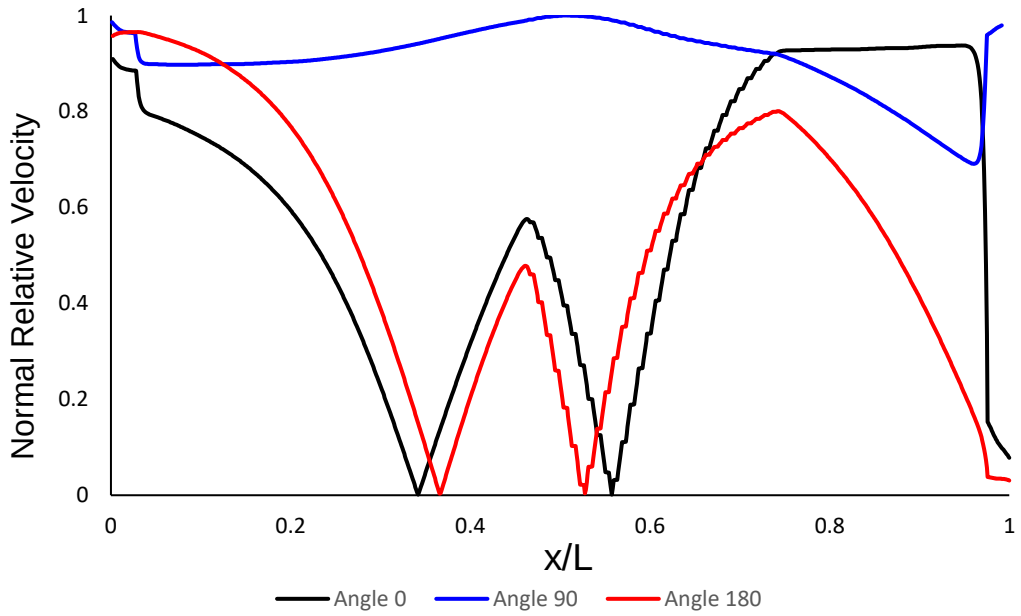

Figure 3-22: Comparison of the normal relative velocity for different current angles under a uniform current profile

Figure 3-22 shows how the normal relative velocity varied across the cable's length for different current angles. The impact of the buoyancy section can most obviously be seen for current angles 0 and 180 degrees with large decreases at the cable mid-section. This behaviour was due to the sag and hog bends, resulting in changing the angle of inclination relative to the current direction. This did not

have a substantial impact on 90 degrees as at this current direction, for the static orientation the cable is perpendicular to the current direction. There was still a notable decrease in the relative velocity towards the touchdown point due to cable deformation seen.

3.3.5.3 Wind

No wind was modelled. It was decided to focus on other parameters and the influence these have on the VIV.

4 Results and Discussion – Numerical Models

Three different VIV models were investigated to predict the cable's response. The models chosen were the Milan Wake Oscillator, Iwan and Blevins Wake Oscillator, and the Shear7 frequency domain model, which have been compared previously (Elrick and Venugopal, 2023). In the following sections, the x-axis is *x/L*, where *x* represents the distance along the cable and *L* the full cable length. The y-axis is *A/D*, where *A* represents the RMS crossflow amplitude and *D* the diameter of the cable. The hang-off point is at x = 0.

4.1 Uniform Current

The VIV transverse displacement along the length of the cable is shown in Figure 4-1 for three angles of current propagation, 0°, 90° and 180°, three different types of cables, and three different VIV models. The x-axis is *x/L*, where *x* represents the distance along the cable and *L* the full cable length. The y axis is *A/D*, where *A* represents the RMS crossflow amplitude and *D* the diameter of the cable. The current speed was 1m/s with a uniform profile.

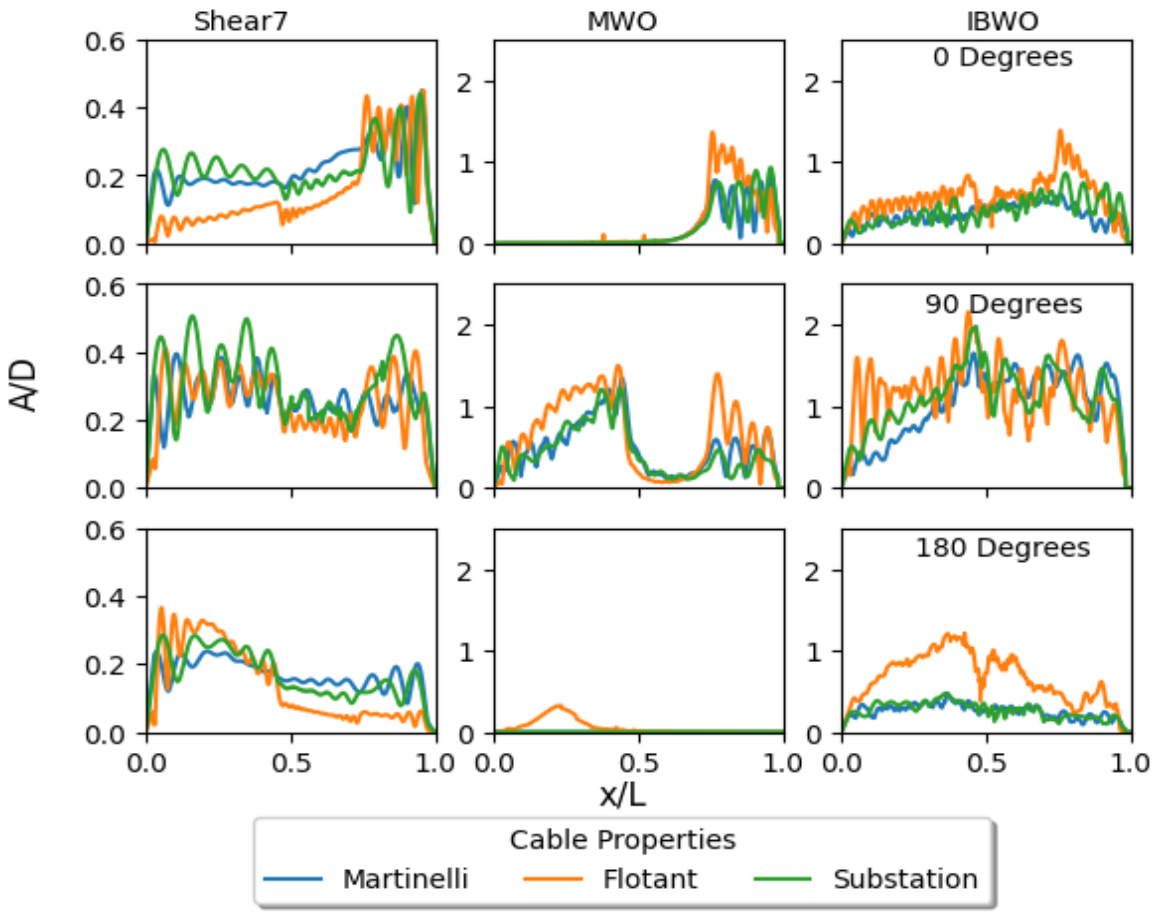

Figure 4-1: RMS transverse displacement along the length of the cable for different propagation directions, models, and cables (top – 0°, middle – 90°, and bottom –180°) for uniform current 1m/s

Figure 4-1 shows that the different models predicted substantially different magnitudes of VIV. The wake oscillator models predicted maximum amplitude of vibrations of up to 2 A/D, which was up to five times larger compared to Shear7. Previous studies have shown similarly large discrepancies between wake oscillator models and Shear7 (Dillon-Gibbons et al., 2017), it was commented that improved benchmarking can assist for tuning wake oscillator models. Currently, the wake oscillator models are calibrated for a bare cylinder.

The MWO model predicted no vibrations near the hang-off point for a current angle of 0 degrees and close to no VIV along the entire cable length for a current angle of 180 degrees. This prediction was substantially different from the other models. The MWO is more sensitive to the orientation of the cable relative to the flow than the other models and as such struggles to effectively predict the VIV of the cable in the lazy wave configuration. It was previously documented to struggle in shear flows, and this is shown in the results. IBWO and Shear7 predicted a similar VIV profile, albeit at significantly different magnitudes.

Figure 4-1 also shows that the VIV profile was strongly dependent on the incident current direction for all models. All models predicted that for a current angle of 0 degrees the most substantial RMS displacement occurred towards the touchdown section. Prior to this, the angle of inclination of the cable, relative to the current direction, varied between 0 - 45 degrees and thus smaller vibrations were predicted. After the mid-section, the cable's angle of inclination, relative to the current flow, tended to perpendicular which resulted in a greater relative velocity and led to substantial VIV excitation, resulting in the large displacement observed.

The largest vibrations were observed for all three cables, models, and different current propagation angles at a current angle of 90 degrees. This was due to the initial plane of the cable being normal to the flow direction. There was a noticeable decrease in amplitude for the section where the buoyancy attachments are located, for all the models.

A similar sensitivity of the RMS displacement to current direction was seen for a current angle of 180 degrees as well. MWO was incapable of modelling the VIV, but IBWO and Shear7 both predicted similar behaviour, where the largest displacement was observed towards the hang-off point before decreasing along the rest of the cable length. Unlike for the other current angles, IBWO and Shear7 had a similar displacement profile, except for the Flotant cable. The Flotant cable is substantially more flexible than the other cables allowing for greater deformation.

When considering the RMS displacement, in terms of A/D, the magnitude was similar for all cables, as was the VIV profile over the cable length. However, when considering the displacement in absolute

units (metres) there were large differences in the amplitude of vibrations. The substation cable has the largest diameter and mass per unit length and the models predicted the largest RMS displacement (in metres) for this cable. The second greatest magnitude of vibrations were seen for Martinelli, with middle values of these parameters. The difference between the predicted vibration amplitude for Martinelli and Flotant was less than that for Substation. These results indicate that the cable properties have a substantial impact on the VIV behaviour with the substation cable on average predicting transverse VIV displacement up to three times the value of Flotant cable for the same environmental conditions, when considering the displacement in metres.

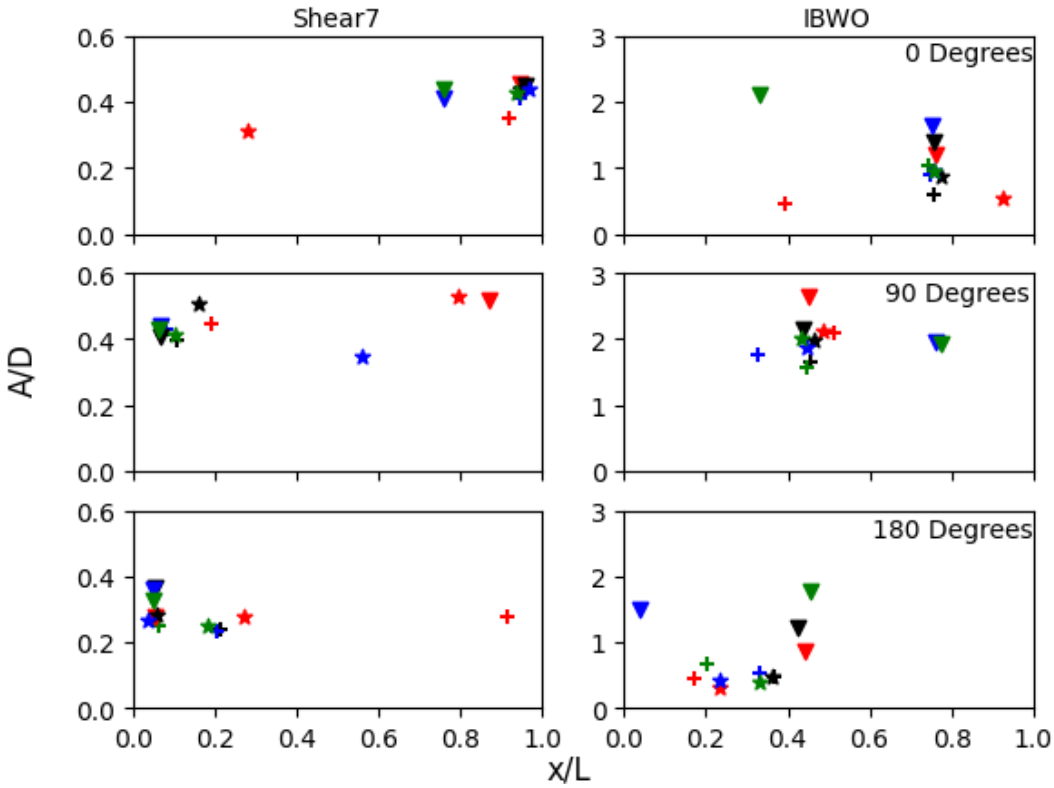

Figure 4-2: Effect of current speed on Location and Magnitude of Maximum VIV Displacement; Substation☆, Martinelli ╪ and Flotant ▽(Red 0.5 m/s, Black 1 m/s, Blue 1.5 m/s and Green 2 m/s)

The effect of varying current speeds was investigated, and the results are shown in Figure 4-2. Current speed was varied from 0.5 - 2 m/s, in steps of 0.5 m/s. Generally, the current speed had a minimal influence on the location along the cable where the maximum amplitude was situated for all current speeds greater than 0.5 m/s. At a current speed of 0.5 m/s, the models all predicted low-mode excitation which resulted in large amplitudes over the full cable length. The location of maximum vibrations along the cable was dependent on the model, with all current speeds closely grouped for each angle. The locations of maximum displacement for a current angle of 0 degrees were near the touchdown for both models, for angle 90, and 180, the maximum displacement location was towards the hang-off point for Shear7 and just before the beginning of the buoyancy section for IBWO.

The impact of vibration frequency against current speeds is shown in Figure 4-3 for Shear7 and IBWO simulations. Both models predicted a similar trend in frequency, with a linear increase in frequency with current speed. The current angle of propagation was also shown to have a minor influence on frequency with no obvious trend for either model's predictions. The cable properties were shown to have a substantial impact on the frequency of vibrations, with different bending stiffness and mass per unit length resulting in different predicted values for the frequency of excitation. It is obvious that the three cables produce three sets of frequency grouping, and Flotant, which has the smallest diameter, resulted in larger frequency of vibrations.

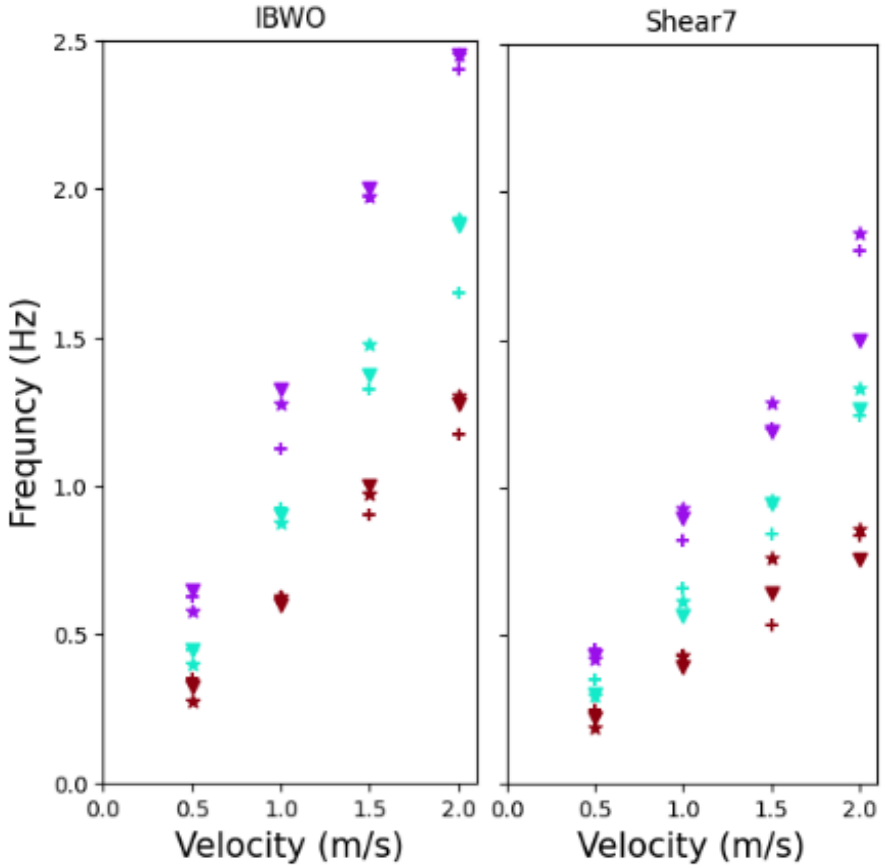

Figure 4-3: Effect of current speed and direction on vibration frequency☆ 0,✢ 90 and ▽180 Degrees (Purple Flotant, Cyan Martinelli, Crimson Substation)

When comparing models, all results were within ±40% of each other. The primary reason for the discrepancy is due to the different Strouhal number used for each model, when the same value was used the predicted frequencies are within ±18%. When comparing the frequencies of different cables Flotant's cable was on average 40% larger than Martinelli's cable for both Shear7 and IBWO. The substation cable was on average 32% or 30% smaller than Martinelli for Shear7 and IBWO, respectively.

4.2 SHEAR CURRENT

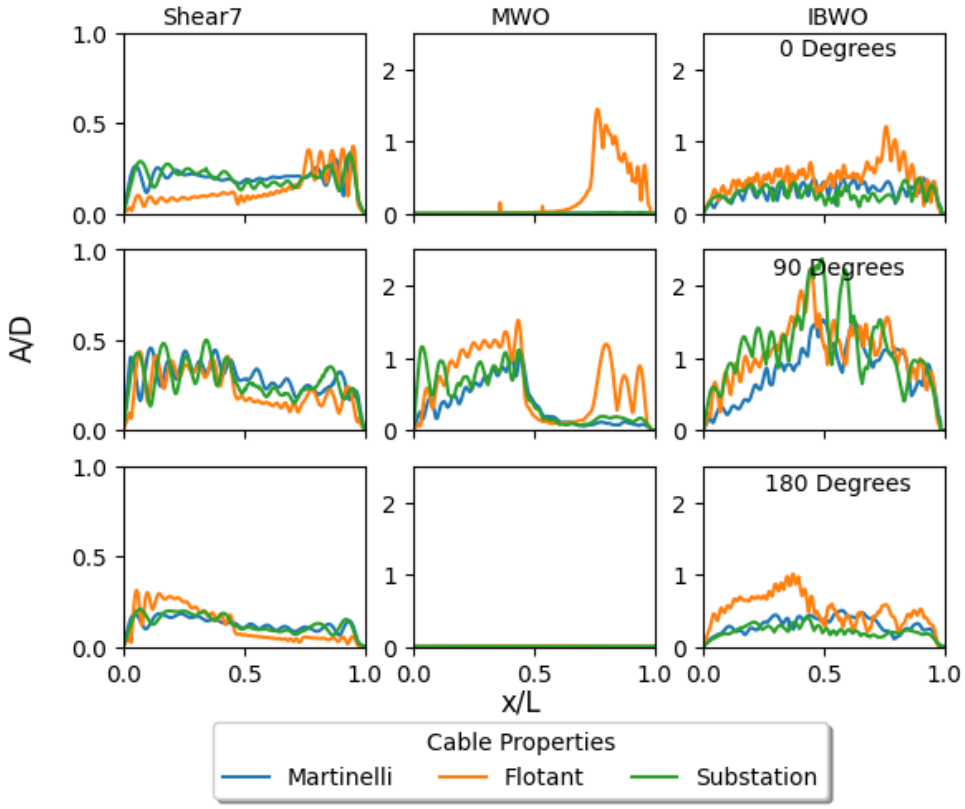

Figure 4-4: RMS transverse displacement along the length of the cable for different propagation directions, models and cables (top – 0°, middle – 90°, and bottom – 180°) for shear current profile 1m/s at the sea surface

The influence of a shear current profile on the RMS displacement was investigated for the chosen VIV models. The RMS crossflow displacements are shown in Figure 4-4. Similar to the uniform results, the shear current also resulted in large discrepancies between different models, cables, and current angles of propagation. A constant trend observed is that, when compared to the uniform current the amplitude of vibrations towards the touchdown point is reduced across all cables, angles, and for all models. This is due to the lower current velocity at this point. When comparing the VIV profile towards the hang-off point it is similar for both current profiles.

For Shear7, average reductions in RMS displacement over the full cable length, for all cables, were 10% at angle 0, 3% at angle 90, and 21% at angle 180. For IBWO the average reductions were 19% at angle 0, 8% at angle 90, and 9% at angle 180. The largest vibrations were predicted for a current angle of 90 degrees. It was also noted that the RMS displacement was not as sensitive to current speeds, with large amplitude even at lower current speeds. The decrease in amplitude for an angle of 90 degrees is expected to be less compared to the other angles when changing to a shear current profile. Current angles 0 and 180 degrees showed a larger dependence on the cable deformation, which is

heavily influenced by the shear current when compared to a uniform profile. This resulted in a larger decrease in average amplitude when compared to a uniform profile.

4.3 CONCLUSION

When comparing the predicted VIV behaviour all three models predicted substantially different outcomes.

The Milan Wake Oscillator model struggled and didn't predict any vibrations at certain locations along the cable for some current angles, which was drastically different from the other models. Due to these obvious limitations, it was not used further in this research, and it is noted that further calibration and work is needed on the model for it to be suitable in this context.

Iwans and Blevins Wake Oscillator predicted an RMS crossflow displacement up to four times larger than Shear7 at certain locations along the cable length. However, it did predict displacement along the full cable length while also predicting similar locations of maximum displacement as Shear7. Similar sensitivities to current angles are seen for IBWO and Shear7, albeit at significantly different amplitudes. Regarding the frequency of vibrations, there were differences of up to 40% between Shear7 and IBWO. IBWO predicted the greater frequency of vibrations.

When comparing the influence of a shear and uniform current profile, both IBWO and Shear7 predicted notable decreases in displacement. This is to be expected due to the lower relative velocity along the cable length. Observations from this were that a current angle of 90 degrees was least susceptible to the current profile, compared to other angles, and showed the smallest mean decrease in RMS displacement over the cable length for both models. Shear7 predicted a current angle of 180 degrees to be more sensitive to current profile whereas IBWO predicted an angle of 0 degrees.

Going forward, it is decided to focus on Shear7 as the model of choice due to having calibrated parameters for a relevant cable experiment.

5 Results and Discussion – Numerical Parameters

5.1 Strouhal Number

The Strouhal Number is a user-defined input for Shear7, it is typically determined experimentally from relevant experiments. When calibrating the models, it is important to note the impact of the Strouhal number. Strouhal number has an obvious impact on the VIV behaviour for all VIV models because it is used to determine the frequency of vibrations, and in turn the amplitude. The most relevant experiment to the VIV of dynamic power cables comes from Delizisis et al. 2022, who used a scaled down dynamic power cable based on Flotant in a tow tank to determine the hydrodynamic coefficients for Shear7. The Strouhal number most applicable from this was 0.14, this was however, at lower Reynolds number and as the regime transitions from the sub-critical regime to the critical regime the Strouhal Number may change further. The impact of the Strouhal number on a lazy wave Flotant cable for a uniform current profile of 1m/s is investigated in Figure 5-1.

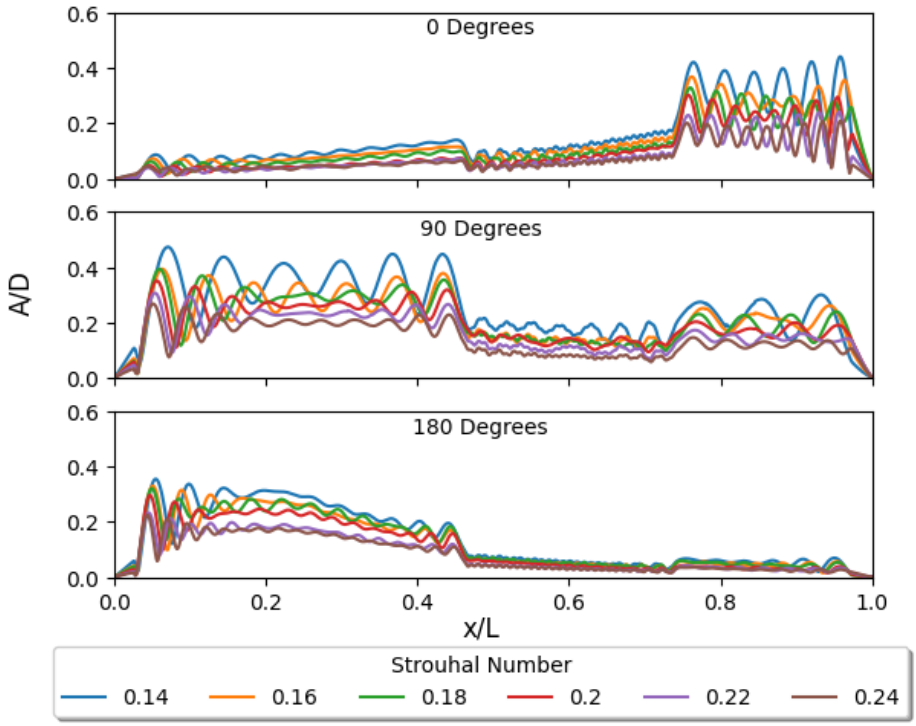

Figure 5-1: Comparison of the influence of the Strouhal number on rms crossflow displacement

There was an obvious increase in RMS displacement for all current angles, and, along the cable length as the Strouhal number decreases. Strouhal number was used to determine minimum and maximum potentially excited modes. As the Strouhal number increases so does the maximum potentially excited mode and thus frequency of vibration.

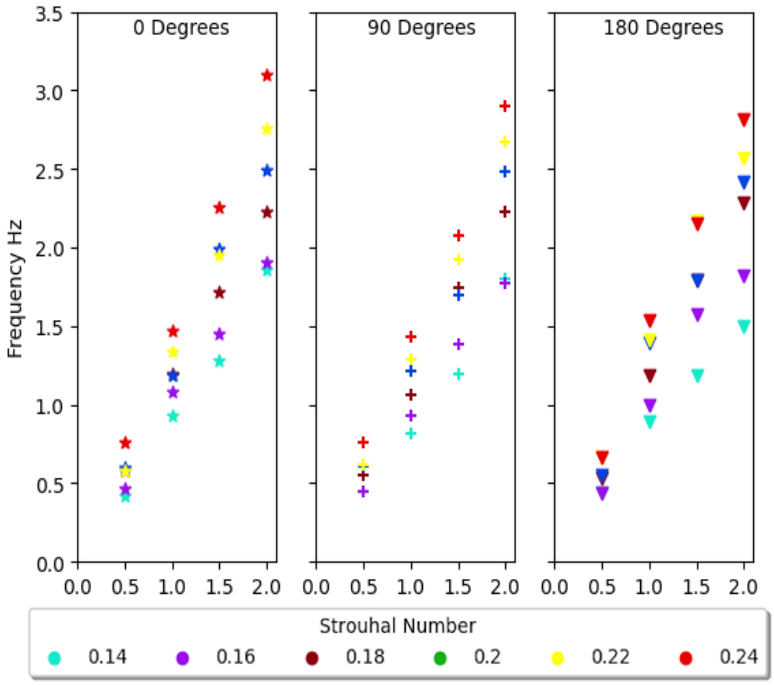

Figure 5-2: Comparison of the influence of the Strouhal number on VIV frequency

As can be seen in Figure 5-2, generally, the larger the Strouhal number the greater the frequency of vibrations that are observed. There were some discrepancies from this trend. This is to be expected due to the determination of the maximum potential excited modes within Shear7.

5.2 Dataset Comparison

The cable properties chosen for comparing the impact of different datasets were Flotant. Table 5-1 shows the parameters that were changed between the datasets. Shear7 supplies additional lift tables that may also be used to investigate the VIV behaviour. 'Lift Table 4' was also used, which was calibrated against high mode VIV experiments for a Strouhal number of 0.18. Cables are exposed to high Reynolds numbers and as such this lift table is included to investigate the impact it has on VIV behaviour compared to other datasets. The Default dataset is a dataset from Shear7 that was calibrated for a riser. All the other hydrodynamic parameters for this dataset are the same as the default dataset except for using a different lift table.

Table 5-1: Dataset Comparison

Dataset	**Delizisis**	**Default**	**Lift Table 4**
Strouhal Number	0.14	0.18	0.18
Bandwidth	0.8	0.4	0.4
Power Ratio	0.1	0.05	0.05
Lift Table	2	2	4
Added Mass	0.5	1	1
Damping Coefficient	2.8%	2.8%	2.8%

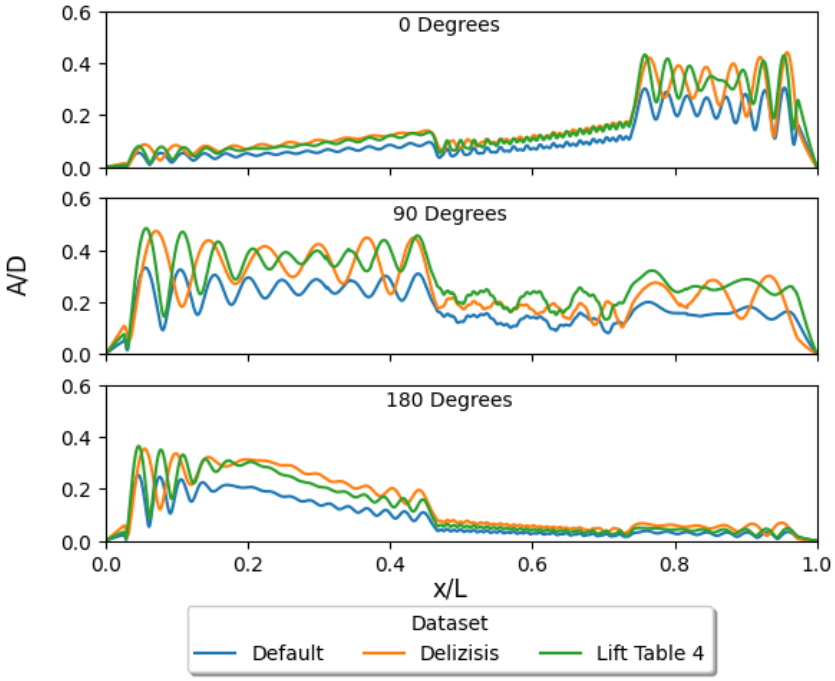

Figure 5-3: Influence of the dataset used on RMS displacement

When comparing the RMS displacement profiles over the cable length, shown in Figure 5-3, Delizisis and Lift Table 4 predicted very similar profiles at similar A/D magnitudes, albeit at different modes. The default parameters replicated similar behaviour regarding the location of largest displacement along the cable's length but consistently predicted this to be at a lower amplitude. These trends are observed at all current angles.

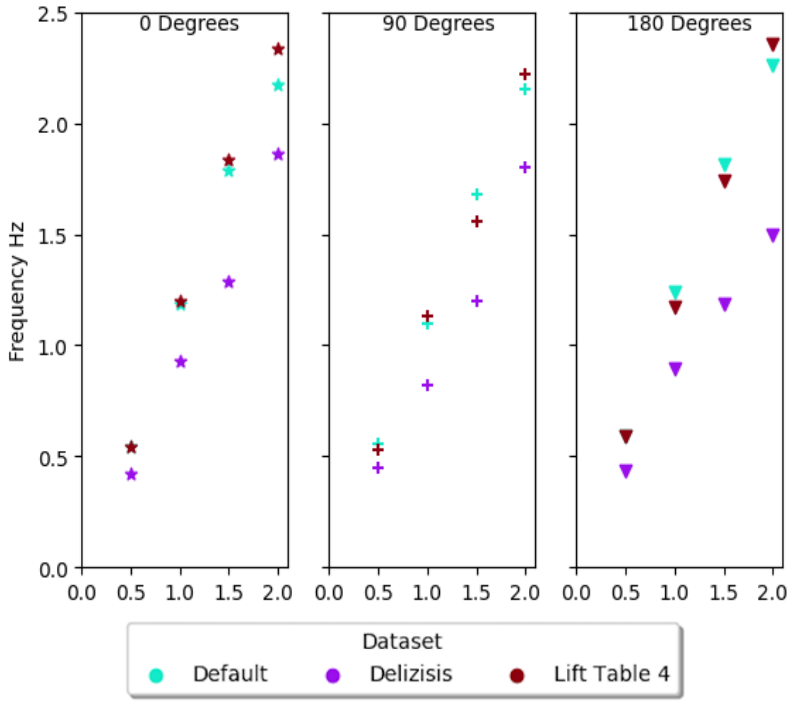

Figure 5-4: The influence of the chosen dataset on VIV frequency

When comparing the frequency of vibrations, there was a strong dependence on the dataset chosen, highlighted in Figure 5-4. This is largely due to different Strouhal numbers for each dataset. Delizisis operated at a Strouhal Number of 0.14, and the others at 0.18. As discussed before this has a notable impact on frequency. Further to this, using a different lift coefficient table resulted in predicting different amplitudes of vibrations, drag coefficients, and mode shapes. These all influence the frequency as well, which is why Default and Lift Table 4 have different excitation frequencies.

5.3 Normalised Dataset RMS Displacement Comparison

The impact of changing the chosen lift table was investigated by normalising the RMS displacement from alternative datasets against the RMS displacement from using Delizisis parameters. The current profile was uniform and varied in increments of 0.5 m/s and the cable used was Flotant. A_{CL2} represents the RMS displacement when the Lift Table 2 is used.

5.3.1 Current Velocity 0.5m/s

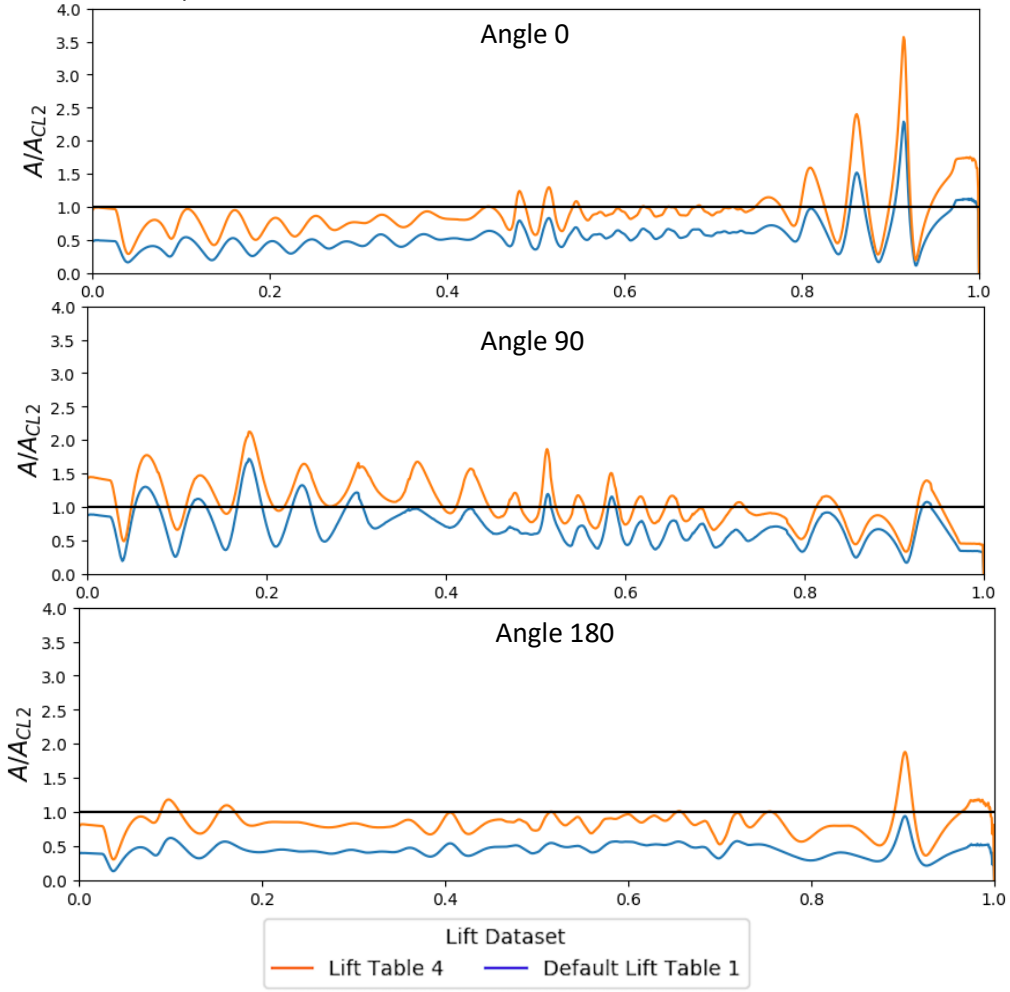

Figure 5-5: A normalised comparison of the datasets for a current velocity of 0.5 m/s

As is shown in Figure 5-5, at a current speed of 0.5 m/s and for a current angle of 0 degrees the overall displacement profile is similar for all datasets until the touchdown section. The discrepancies seen

here are likely due to prediction of different modes, resulting in out of sync vibrations at certain lengths and the large peaks and troughs observed. The default dataset predicted the lowest RMS displacement followed by the Lift Table 4. This is a reoccurring trend.

For a current angle of 90 degrees, the displacement profile predicted that for both the Default and Lift Table 4 larger vibrations were observed towards the hang-off point than for the Delizisis data set. This then reduces along the rest of the cable length.

A current angle of 180 degrees resulted in a similar displacement profile for all datasets, albeit at different magnitudes. Again, the Default dataset predicted the lowest magnitude of vibrations, 50% over the full cable length. Lift Table 4 predicts an almost uniform decrease of 10% over the full cable length.

5.3.2 Current Velocity 1m/s

It can be seen in Figure 5-6 that for a current angle of 0 degrees the overall displacement profile was very similar for all datasets, except at different magnitudes. There were also some extreme variations at both the hang-off and touchdown points. The discrepancies seen here are likely due to prediction of different large displacement modes at these locations. The mean difference between Delizisis dataset and Lift Table 4 is considered negligible. The Default Lift Table resulted in a decrease of 30% over the full cable length.

For a current angle of 90 degrees the displacement profile was similar for the different datasets but varied in magnitude. Lift Table 4 resulted in the largest RMS displacement over the full cable length, with a mean increase over the full length of around 25%, and Default resulted in the smallest displacement with a mean decrease of around 25%. There was a substantial deviation from the Delizisis dataset observed towards the touchdown section, likely due to the large curvature and influence this had on VIV depending on the dataset used.

A current angle of 180 degrees predicted similar displacement profiles for all datasets, albeit at different magnitudes, with again the Default dataset predicting the lowest vibrations and the Delizisis set the largest. One notable difference is that other datasets predicted a larger displacement decrease from the hang-off point towards the touchdown section than for Delizisis dataset.

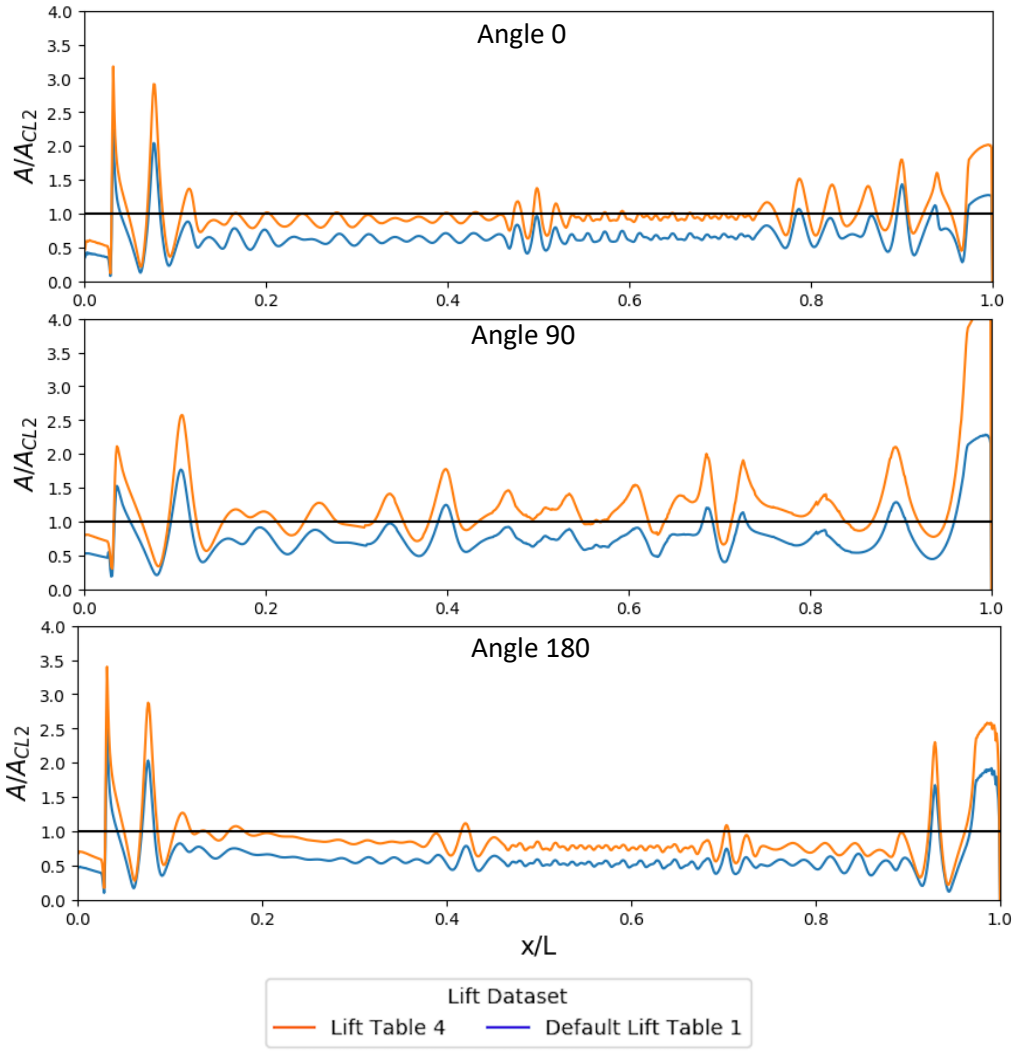

Figure 5-6: A normalised comparison of the datasets for a current velocity of 1 m/s

5.3.3 Current Velocity 1.5m/s

Figure 5-7 shows that after the current speed increased to 1.5 m/s substantial differences in the RMS displacement for a current angle of 0 degrees were observed. This is especially evident at the hang-off point, which was greater than a magnitude of four larger. This large difference was due to the different handling of the cable deformation and the impact this had on the VIV profile. The Delizisis dataset predicted a much greater VIV dependency on the cable deformation than the other data sets, with little displacement predicted at the hang-off point. Whereas the other datasets still predicted there to be substantial displacement along this section which is why such disparity in amplitude of vibrations is observed.

For a current angle of 90 degrees a similar trend is observed for the other current speeds where the displacement profile was similar for the different datasets but varied in magnitude. The Default dataset still resulted in the lowest magnitude of displacement followed by Lift Table 4. Another notable observation was the substantial displacement predicted at the hang-off point for both Lift

Table 4 and the Default Lift Table. This was likely due to different handling of the bend stiffener and curvature of the cable at this point.

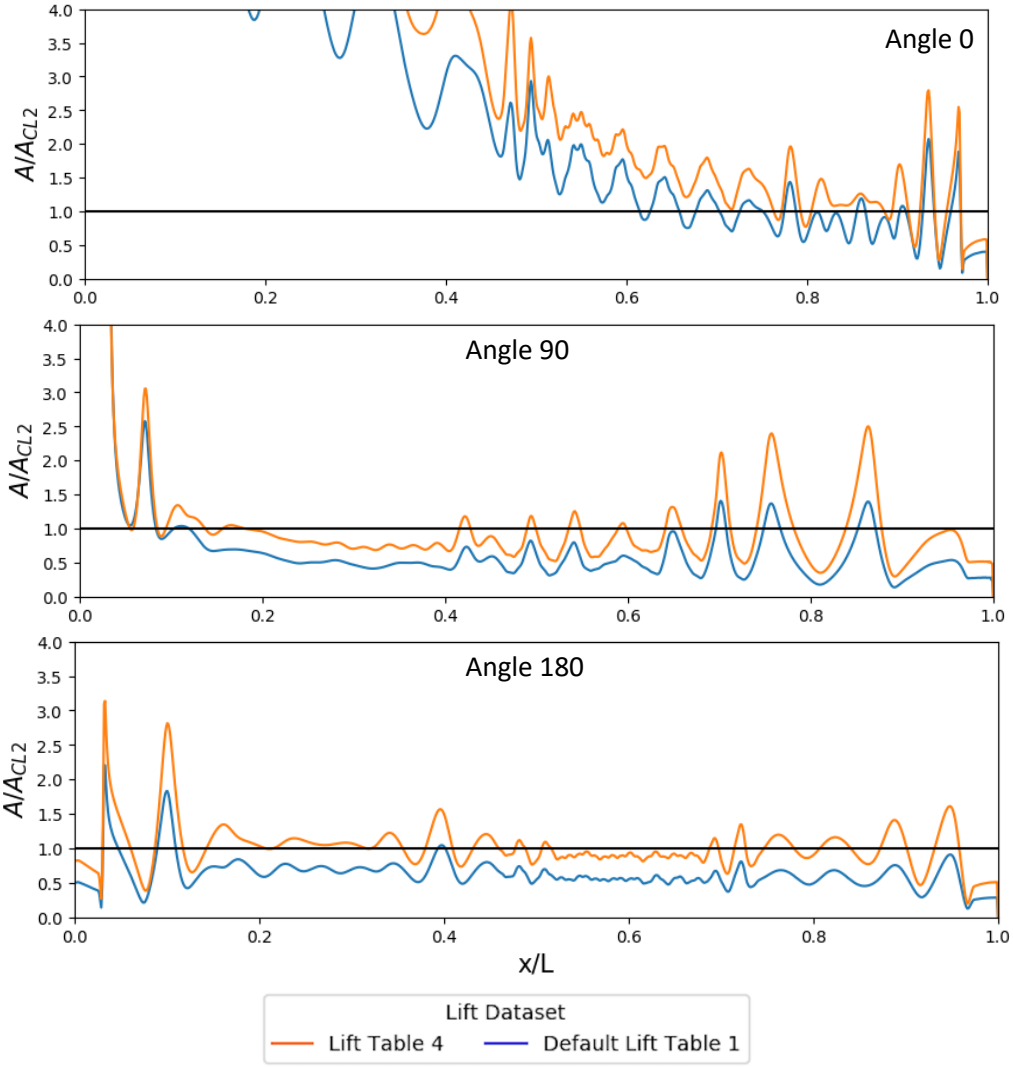

Figure 5-7: A normalised comparison of the datasets for a current velocity of 1.5 m/s

For a current angle of 180 degrees there were more substantial discrepancies compared to the lower current speeds. The Default Lift Table and Lift Table 4 predicted larger amplitudes of vibrations towards the hang-off point, this was due to the deformation observed as well as the handling of the bend stiffener. After the hang-off section both these datasets predicted a general decrease in the mean RMS displacement as the cable tends to the touchdown point. For Lift Table 1, this was at a much lower magnitude than the Delizisis dataset.

5.3.4 Current Velocity 2m/s

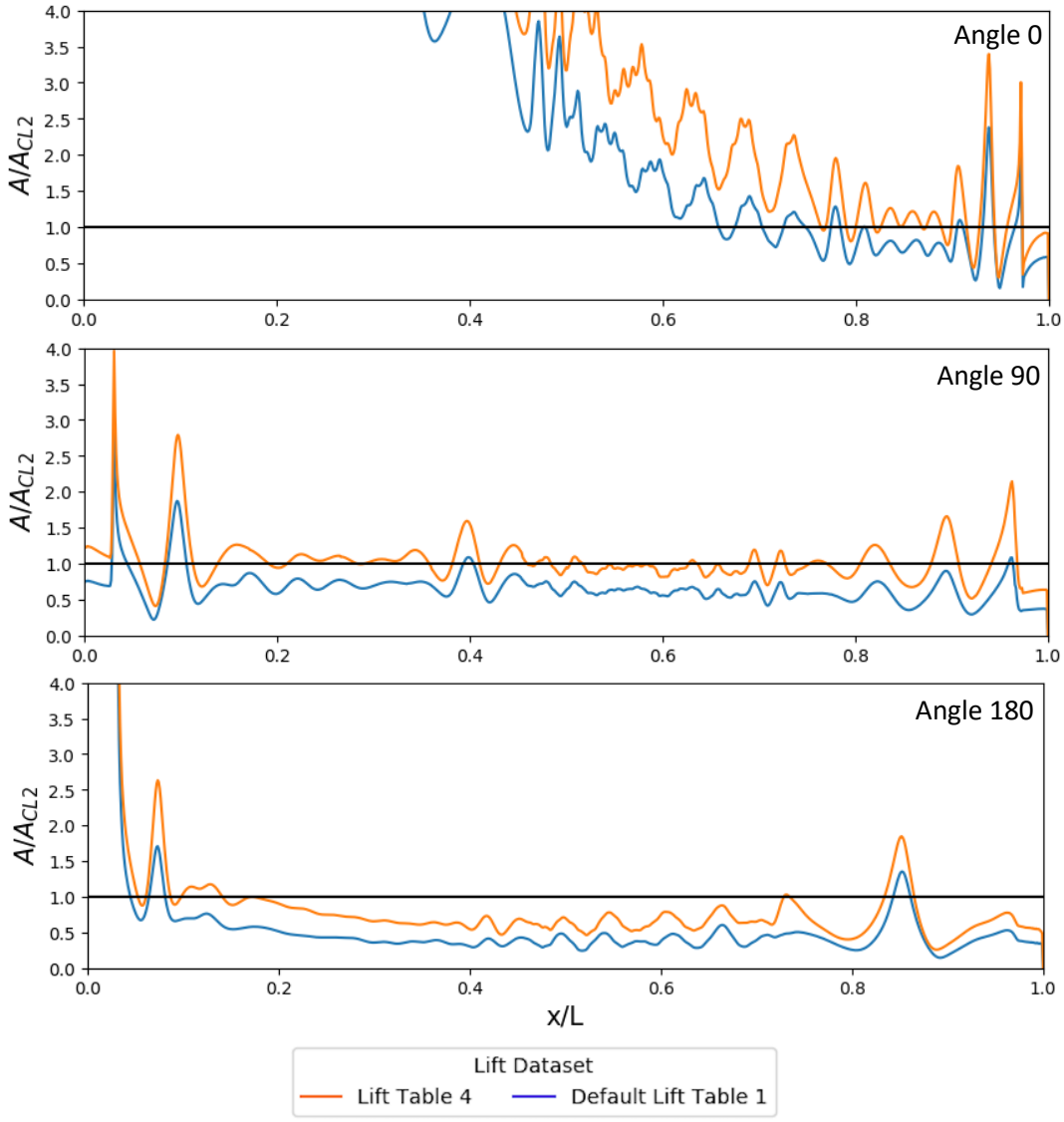

Figure 5-8: A normalised comparison of the datasets for a current velocity of 2 m/s

The displacement profile for a current angle of 0 degrees was vastly different, as can be observed in Figure 5-8. This is because Delizisis predicted little to no amplitude of displacement at the hang-off section whereas the other datasets still predicted vibrations of substantial amplitude. These datasets don't expect the cable deformation and changes in the angle of inclination to result in as large an influence on the RMS displacement.

A current angle of 90 degrees follows the previously discussed trend where Lift Table 4 and Delizisis produced very similar profiles and amplitudes of VIV. The Default dataset produced a similar profile but at a lower magnitude. The large discrepancies at the hang-off point are noted.

For a current angle of 180 degrees the displacement profile was similar to that of 1.5 m/s, including the large deviation at the hang-off point. The difference between the magnitude of RMS displacement

for the datasets was more substantial than for the other current speeds with both the Default and Delizisis dataset predicting smaller magnitude than for 1.5 m/s.

5.4 Added Mass Coefficient

The added mass coefficient predominantly influences the response of OrcaFlex, which has a knock-on impact to Shear7. The added mass coefficient was used within OrcaFlex to determine the fluid acceleration on the body. This changed the deformation of the cable. The added mass coefficient also impacted the natural frequency, mode shape, and curvature.

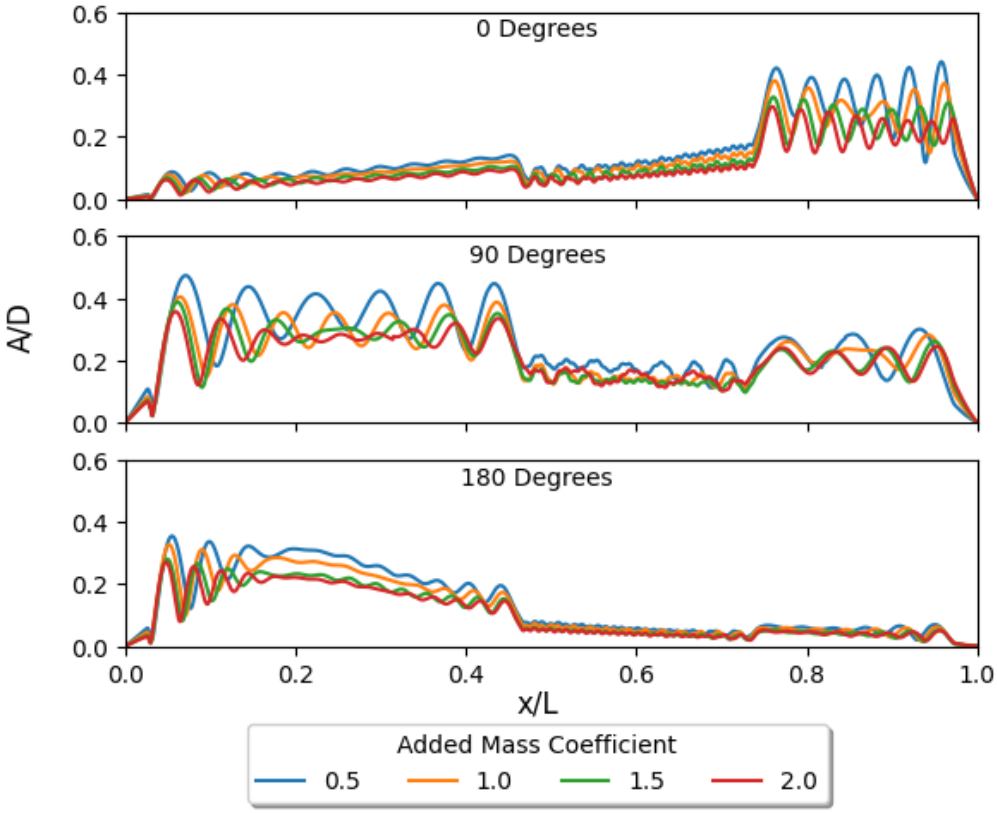

Figure 5-9: A comparison of the impact of the added mass coefficient on the RMS crossflow displacement

Observing Figure 5-9, it can be seen that the added mass coefficient had a substantial impact on the displacement. This was due to the change of deformation and the impact on the modal analysis. As the added mass coefficient increased the RMS displacement decreased. This increase was almost uniform across the entire cable length. Similar trends were still observed along the cable length for the different angles, these being that the locations of maximum displacement are consistent and extreme variations in amplitude over the cable length were present.

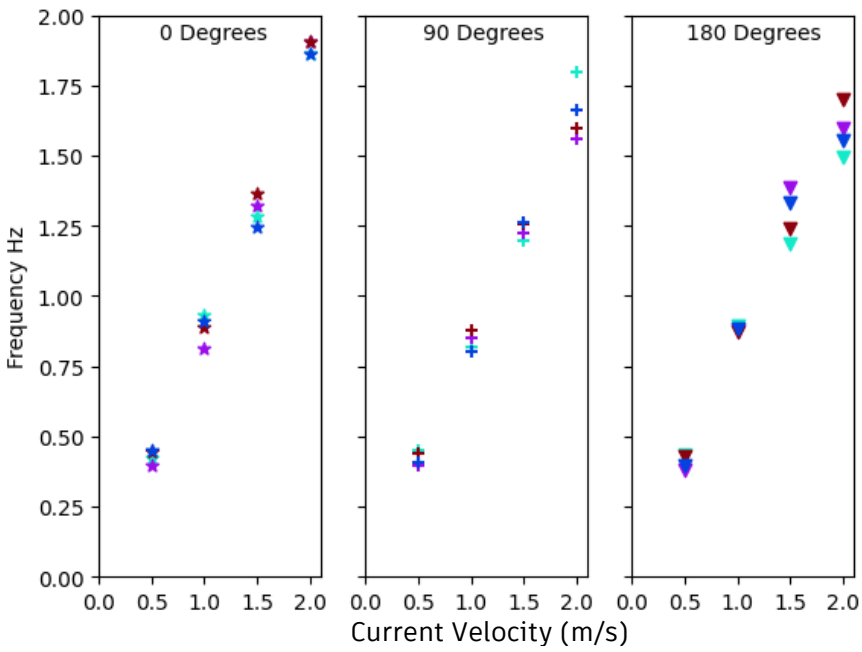

Figure 5-10: A comparison of the impact of the added mass coefficient on the frequency of vibrations (Cyan: 0.5, Purple: 1.0, Crimson: 1.5, Navy: 2.0)

There was no obvious dependency on the frequency of vibrations when compared to the added mass coefficient, shown in Figure 5-10. One notable observation is that a current angle of 0 degrees resulted in the greatest predicted frequency compared to the other angles.

5.5 Reduce Velocity Bandwidth

The reduced velocity bandwidth determines the range of modes that are considered within Shear7 to model the VIV behaviour. The greater the bandwidth the greater the number of modes that are considered within Shear7. More modes can lead to greater modal damping and intermodal interactions.

The reduced velocity bandwidth is shown in Figure 5-11 to have a notable influence on the RMS displacement. As it decreases so does the amplitude of vibrations, albeit not substantially. This is due to fewer modes influencing the VIV behaviour compared to lower values. There was little obvious change in the VIV profile over the length of the cable. Locations of maximum displacement were consistent across all bandwidths.

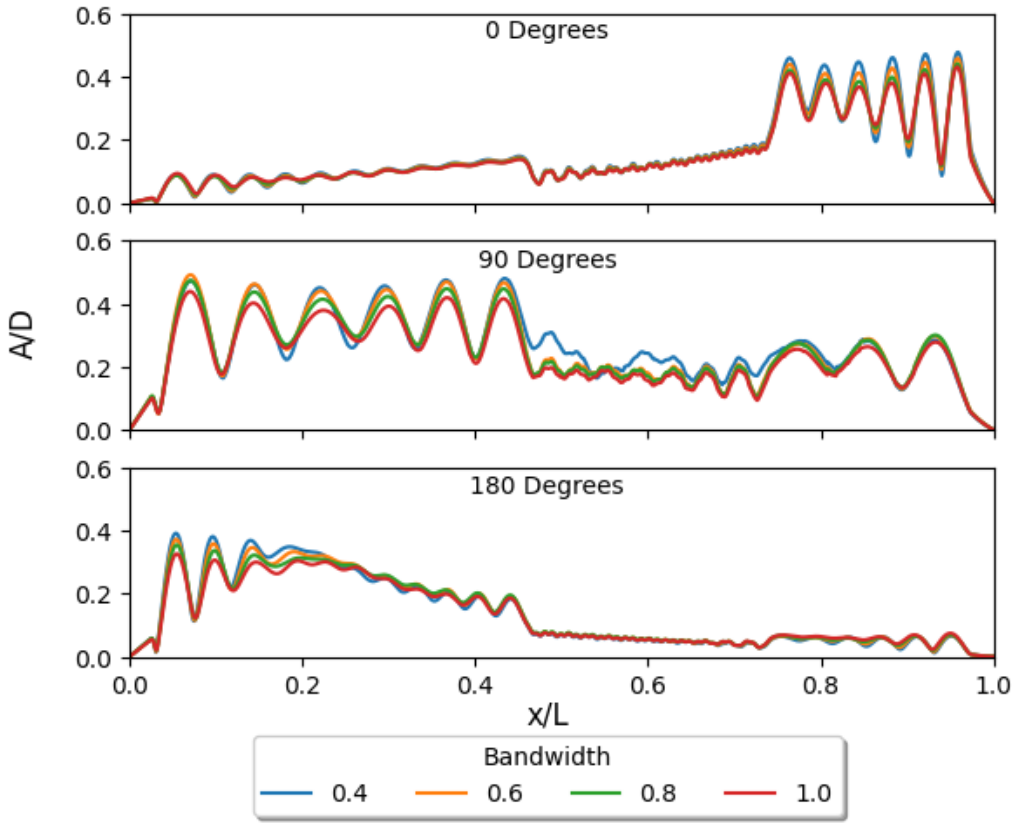

Figure 5-11: A comparison of the impact of the reduced velocity bandwidth on the RMS crossflow displacement

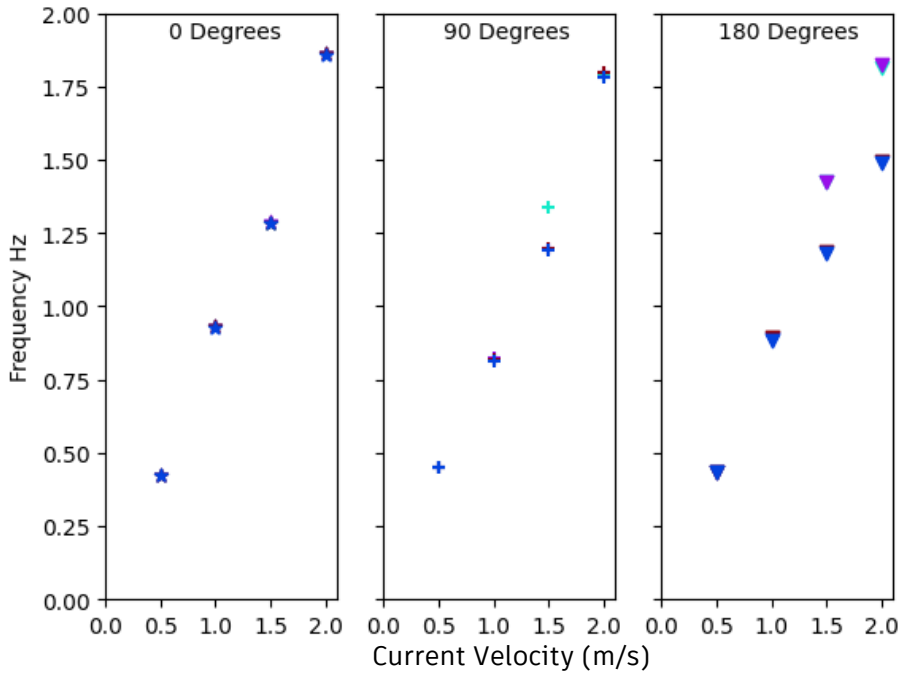

Figure 5-12: Impact of Reduced Velocity Bandwidth on Frequency (Cyan: 0.4, Purple: 0.6, Crimson: 0.8, Navy: 1.0)

The influence of the reduced velocity bandwidth on VIV frequency can be seen in Figure 5-12. There was little noticeable impact on the frequency, except for a few anomalies. The bandwidth didn't

substantially alter the most dominant mode of vibration. The bandwidth is shown to have a relatively small influence on both the RMS displacement prediction and the frequency of vibration.

5.6 Numerical Parameters Conclusion

It has been shown that the VIV predictions are sensitive, to varying degrees, to the numerical parameters defined with the semi-empirical Shear7 frequency domain model. The Strouhal Number is noted as the most consequential numerical parameter, with large discrepancies between the predicted RMS displacement and frequency observed. When this is combined with a different lift table dataset, large differences in the predicted VIV behaviour are seen. This is to be expected but further amplifies the importance of using the correct dataset to predict vibrations. The added mass coefficient and bandwidth are shown to influence the VIV behaviour; however, the outputted results are not as sensitive as for other parameters. Without an appropriate dataset available for a full-scale experiment a scaled down model has been calibrated against and extrapolated.

6 Results and Discussion – Cable Properties

The structural properties of an object are known to influence the VIV response. Further to this, they also dictate the global response of the cable to incidental environmental forces, which has an additional influence on VIV behaviour. In this section the impact of various parameters are investigated: damping, density, flexural rigidity, and diameter.

6.1 Damping

Damping is well known to have an impact on the VIV behaviour of any structure. Dynamic power cables are subject to potentially large damping. This is in part due to the internal cable structure, which allows for stick-slip behaviour, other complex interactions of the different internal components (Beier et al. 2023), and the properties of the cable components. Damping results in absorbing the energy of motion and thus reducing the intensity of VIV. The numerical parameters used to derive the results in this section are taken from Delizisis' work.

The results of varying the damping are shown in Figure 6-1. The x-axis is *x/L*, where *x* represents the distance along the cable and *L* the full cable length. The y axis is *A/D*, where *A* represents the RMS crossflow amplitude and *D* the diameter of the cable. The cable used for this was Martinelli's and was exposed to a uniform current of 1m/s.

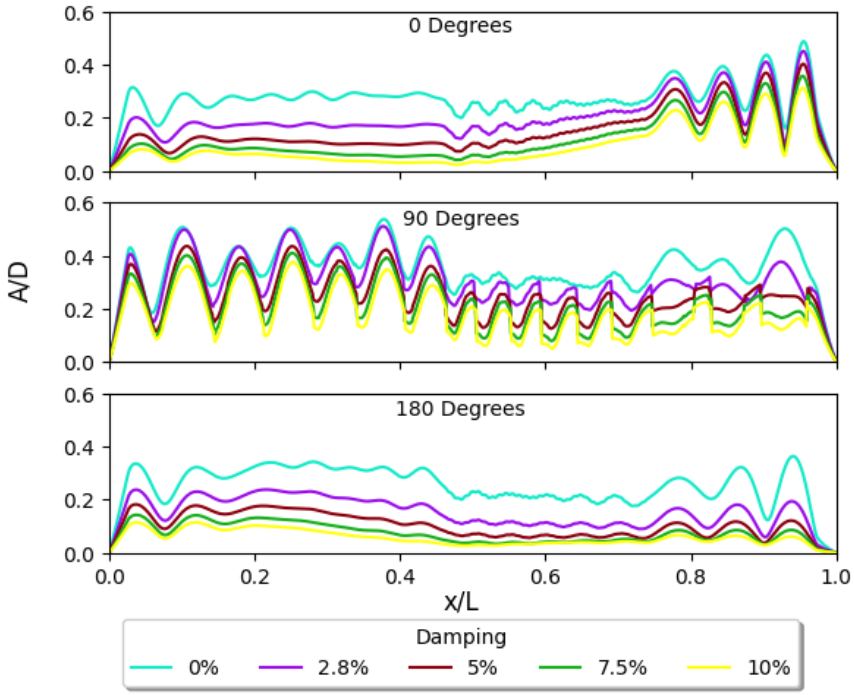

Figure 6-1: A comparison of the impact of the damping ratio on the RMS crossflow displacement

As can be seen in Figure 6-1, for all current angles damping has a substantial influence on the amplitude of vibrations. The larger the damping, the smaller the RMS displacement. When comparing the RMS displacement profile, altering the damping coefficient is predicted to have a minimal influence. The predominant impact was over the mode or frequency of vibration. The location of maximum displacement along the cable length was the same for different damping coefficients. This highlights the lack of impact that the damping has on the frequency of vibrations, and also amplifies that there are other more influential parameters, such as incident current angle, which alters the VIV displacement profile. It is important to fully understand the damping coefficient for the cable deployed as under or over-estimating can drastically impact the predicted fatigue damage. This could lead to manufacturing for a much shorter fatigue life than what is required on site.

To allow for further comparison the plots in Figure 6-1 were normalised against a damping coefficient of 2.8%, from Delizisis' study, which is shown as $A_{2.8}$.

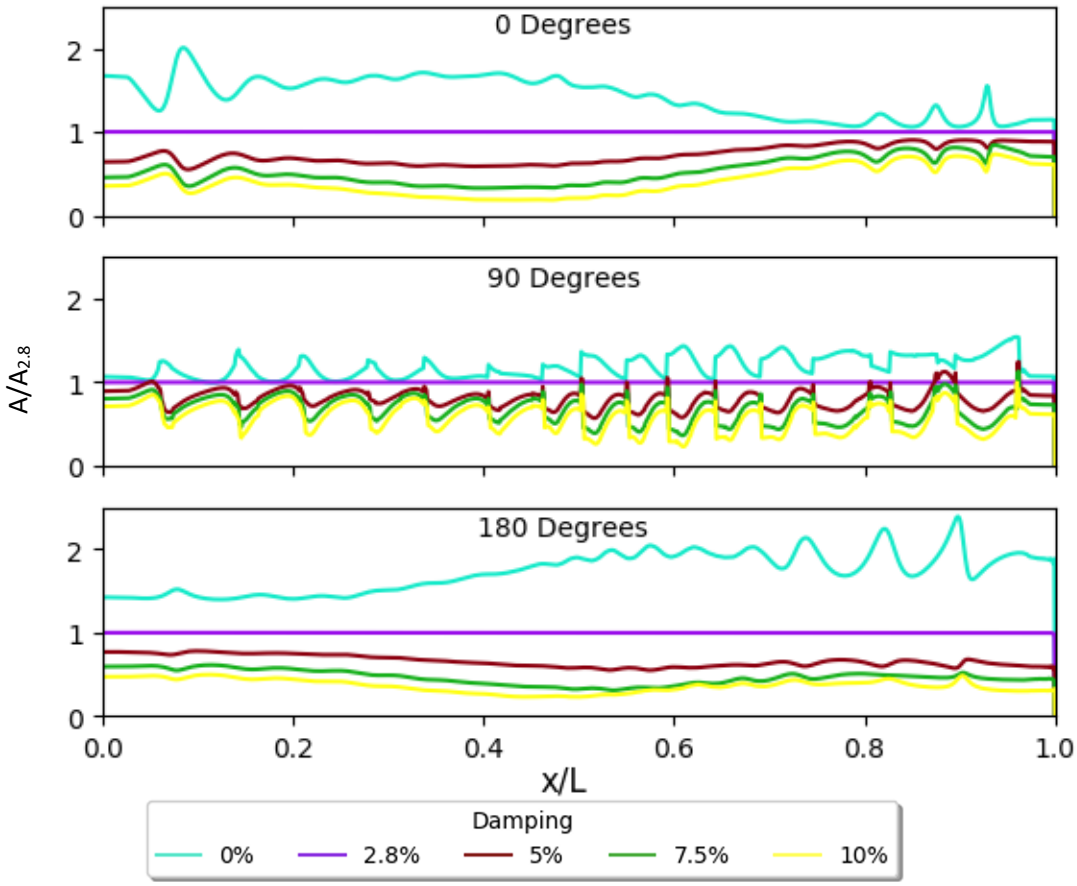

Figure 6-2: A normalised comparison of the impact of damping ratio on the RMS crossflow displacement

Figure 6-2 further highlights how impactful the damping coefficient is, assuming no damping can lead to vibrations double the magnitude in amplitude or, on the other hand, overestimating can lead to predicting vibrations halve the magnitude. The overall trend is that the larger the damping, the smaller

the RMS displacement amplitude. When comparing the mode of vibration and RMS displacement profile the changing of the damping coefficient is predicted to have a minimal influence. It is important to fully understand the damping coefficient for the cable being deployed to accurately predict the VIV behaviour.

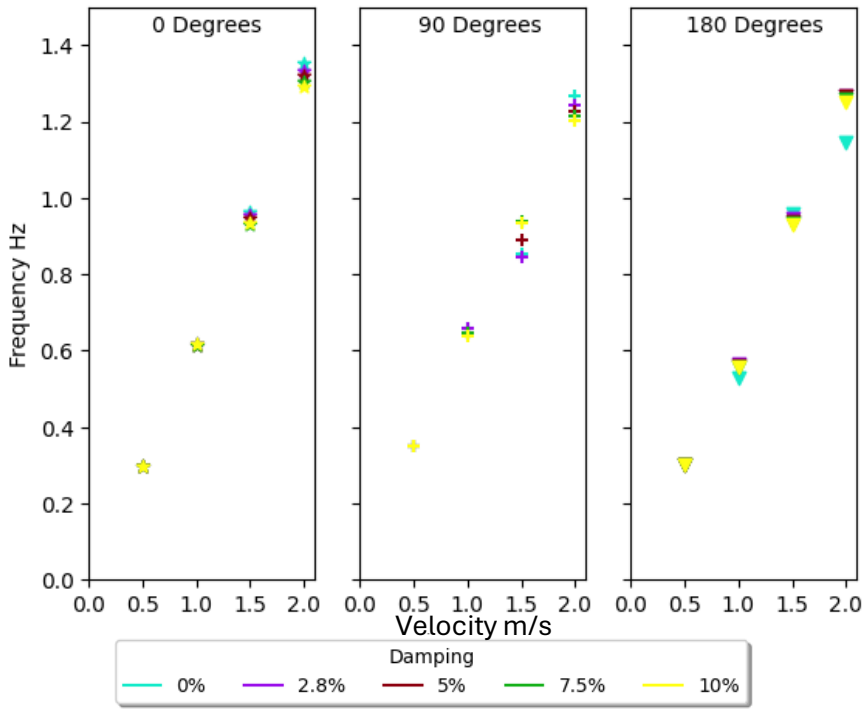

Figure 6-3: A comparison of the impact of damping on frequency of crossflow vibrations

When comparing the frequency of vibration and its dependency on the damping coefficient, seen in Figure 6-3, it can be observed that there is no real trend in vibration frequency between different damping that is consistent over all current angles. At higher current speeds, the vibrations did start to differentiate further from each other, but still within 10%. For a current angle of 0 degrees the frequency was similar for all damping at current speeds 0.5 and 1 m/s. Greater than this current speed, a trend emerges where the lower the damping the greater the frequency of vibration. For current angles 90 and 180 degrees a similar trend could be seen, with a few noted anomalies digressing from this. Outside of the results for a current speed of 1.5 m/s, at a current angle of 90 degrees a similar trend was seen where the lower the damping the greater the VIV frequency. A current angle of 180 degrees had a very tightly grouped frequency spread with damping. 0% damping was shown to be the most variable and diverged from the otherwise consistent trend of the greater the damping the lower the frequency seen for all current speeds. Another observation is that a current angle of 0 degrees resulted in the greatest frequency of vibration compared to the other angles.

6.2 Impact of Density

Cable deformation is noted be one of the most impactful factors on the VIV behaviour. It is also shown to be sensitive to all of the different cable properties. The deformation of the cable is dependent on mass ratio, current angle, current profile, current speed, bending stiffness, and diameter of the cable. To exemplify how greatly the deflection can vary over just one of these parameters Figure 6-4, Figure 6-5, and Figure 6-6 compare the deflection of the cable for different current angles and mass ratios.

Table 6-1: Mass Ratio for Different Cables

Cable	Flotant	Martinelli	Substation
Mass Ratio	1.316	2.484	2.053

The mass ratio of the cable was varied according to Table 6-1 and taken from the cables discussed earlier. All other parameters, such as bending stiffness and diameter, were taken from Martinelli's cable.

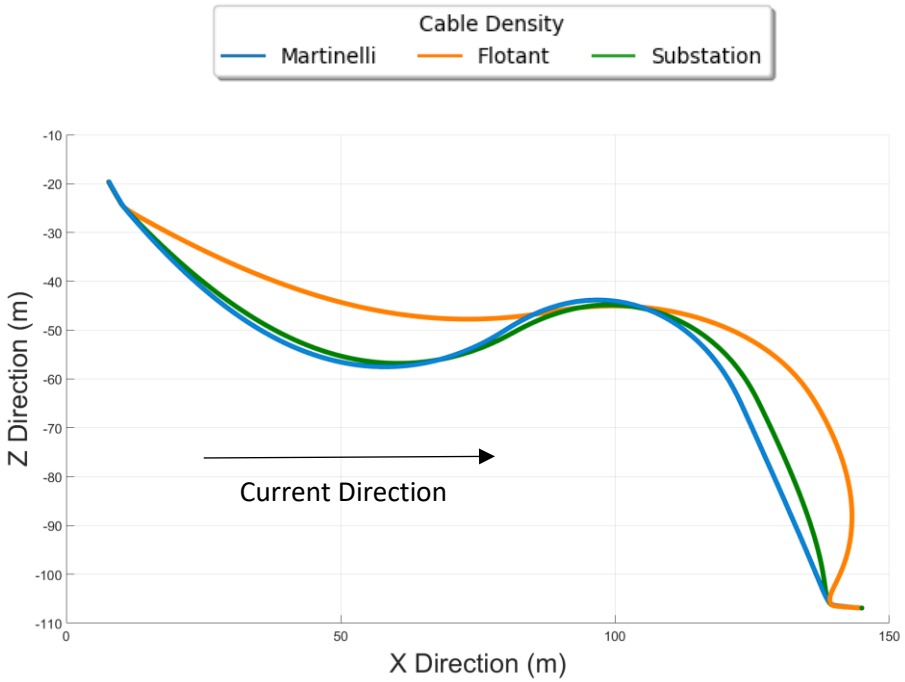

Figure 6-4: A comparison of the impact of the mass ratio on cable deflection for a current angle of 0 degrees

For a current angle of 0 degrees, the lowest mass ratio cable was deflected to such an extent that it was perpendicular to current direction towards the touchdown point and tending to parallel towards the hang-off point. This in turn resulted in a larger relative velocity at the touchdown point and a lower relative velocity at the hang-off point compared to the larger mass ratio cables. All the cables still exhibited a high RMS amplitude variability with location along the cable length, but this was amplified by the further a cable deflected.

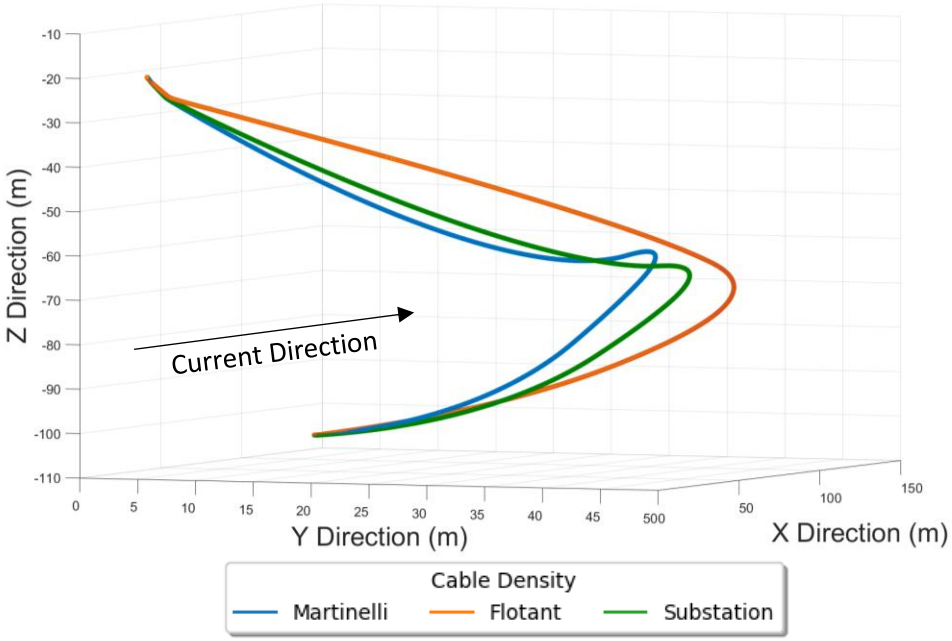

Figure 6-5: A comparison of the impact of the mass ratio on cable deflection for a current angle of 90 degrees

A current angle 90 didn't exhibit as a large dependence on the RMS displacement on the mass ratio compared to the other angles. This was because the static plane of the cable at this current angle was naturally perpendicular to current direction over the full cable length, there were no changes in angle of inclination. It can be seen in Figure 6-5 that the lower the mass ratio the greater the deflection, but the influence of this was less impactful on the RMS displacement than for the other current angles.

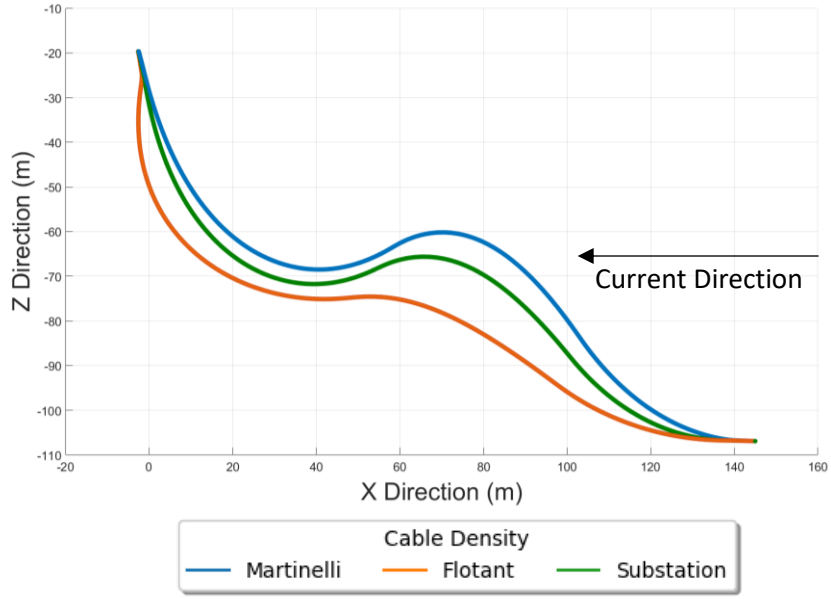

Figure 6-6: A comparison of the impact of the mass ratio on cable deflection for a current angle of 180 degrees

A current angle of 180 degrees showcased similar behaviour to that of 0 degrees, where greater deflection was observed for the lower mass ratio which resulted in a greater RMS displacement dependency on the location along cable length. The cable followed the opposite deflection behaviour to angle 0 degrees, where it tended to perpendicular at the hang-off point and the angle of inclination reduced towards the touchdown point. This resulted in opposing displacement profiles where the greatest magnitude of VIV was towards the hang-off point rather than the touchdown point for a current angle of 0 degrees.

As can be observed, the lower the mass ratio the greater the cable deflection for all current angles. This is to be expected. This had the knock-on impact of altering the normal relative velocity that the cable was exposed to by changing the angle of inclination relative to flow direction. This resulted in the extreme discrepancies in the RMS displacement amplitude over the cable length.

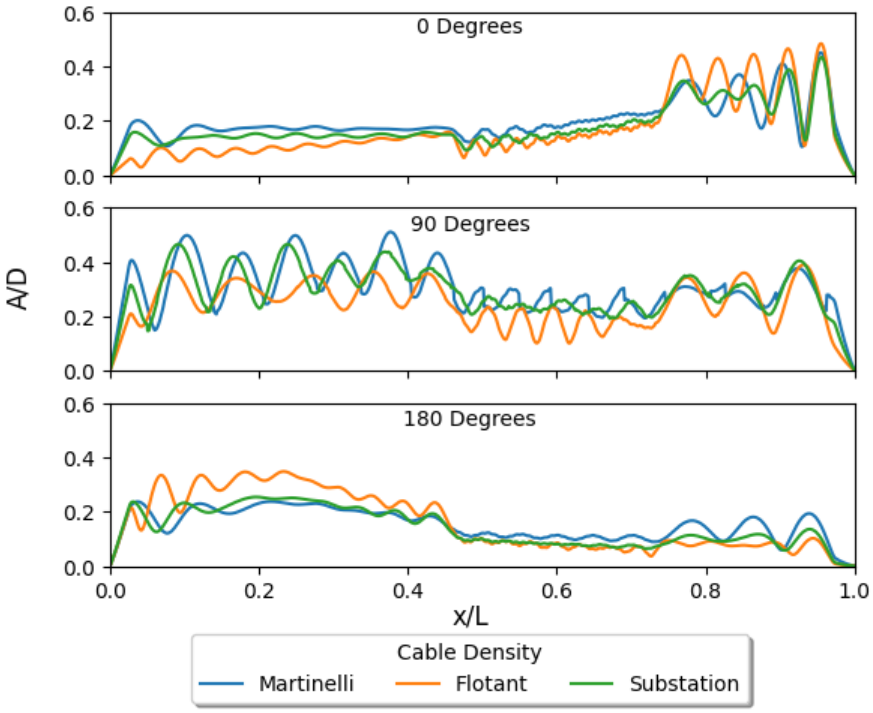

Figure 6-7: Influence of Mass Ratio on RMS Displacement

The results shown in Figure 6-7 indicate that altering the mass ratio impacts the RMS displacement profile. For a current angle of 0 degrees, the smallest mass ratio cable resulted in a larger RMS displacement amplitude observed towards the touchdown point and a reduced displacement towards the hang-off point. The cable with smaller mass ratio resulted in greater deflection as it was more susceptible to induced drag forces from the sea currents. This resulted in greater cable deflection which in turn changed the relative velocity the cable was exposed to. For a current angle of 90 degrees the cable exhibited the same behaviour of increased deflection with a reduced mass ratio. However,

there were fewer extreme variations in RMS displacement along the length due to the angle of inclination and relative velocity not varying as greatly along the cable length because the initial spatial plane of the cable was perpendicular to the current flow. The RMS displacement profile for a current angle 180 degrees can be explained by the same logic as for a current angle of 0 degrees, except with the deflection resulting in the extreme amplitudes at opposite ends of the cable.

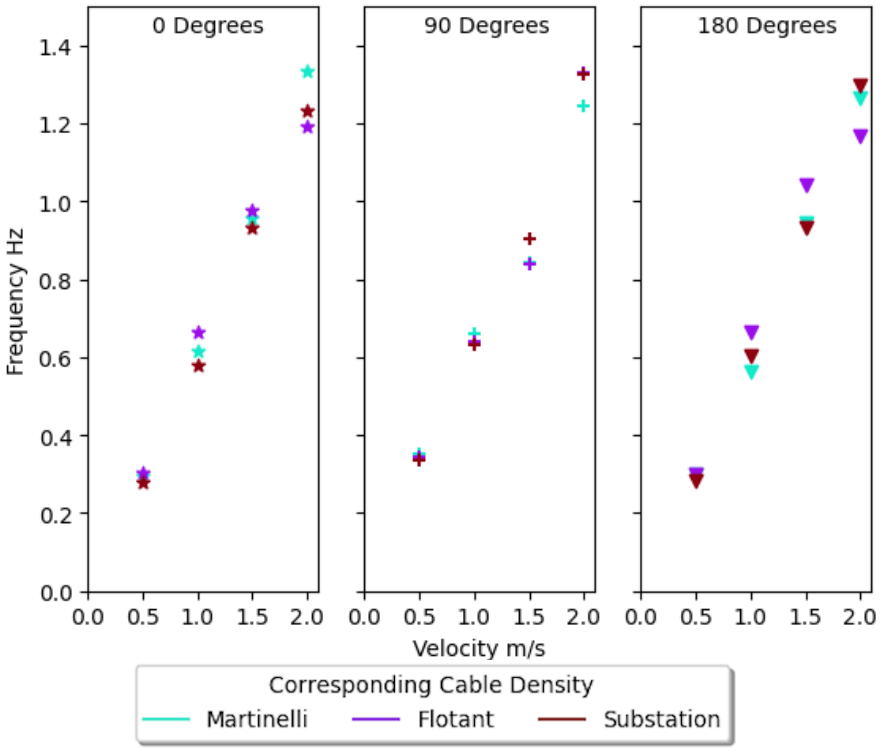

Figure 6-8: A comparison of the impact of cable density on frequency of vibrations

When observing Figure 6-8, for current angles 0 and 180 degrees there is a trend where the lowest mass ratio cable resulted in the largest frequency of vibrations up to 1.5m/s. However, for a current speed of 2m/s, it resulted in a predicted lower frequency compared to the other cable densities. This is because at 2m/s the cable deformation was so great the cable extended beyond perpendicular and the cable was exposed to a lower relative velocity than for the less deformed cables of lower density. For an angle of 90 degrees there is no obvious relationship between mass ratio and frequency of vibration. All of the current angles resulted in similar frequency of vibrations.

6.3 Impact of Cable Choice

Four different power cables are used in this study to examine the influence they have on the VIV response in a lazy wave configuration. These cable properties are shown in Table 3-3.

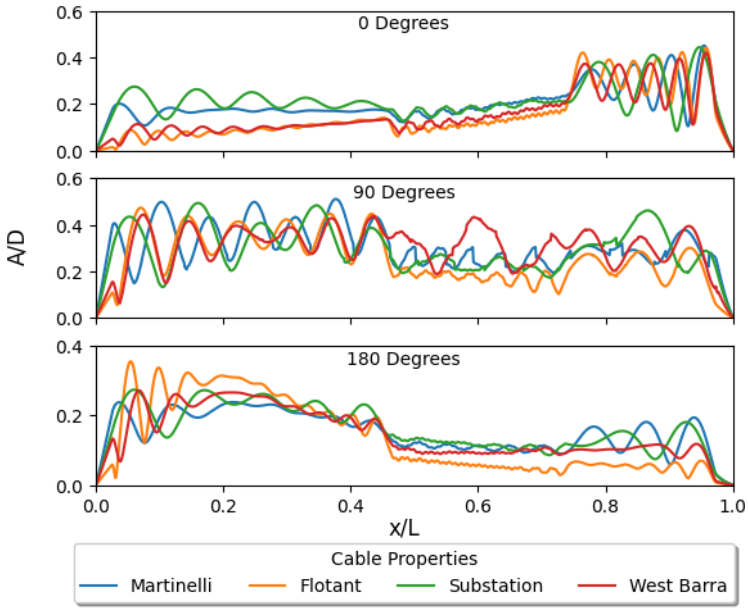

Figure 6-9: A comparison of the impact of the cable properties on the RMS crossflow displacement for a uniform current of 1m/s

There are notable differences in the VIV behaviour profile over the full cable length depending on the cable chosen, seen in Figure 6-9. Substation and Martinelli cables are greater in diameter and bending stiffness than the other cables, and thus were less perceptible to deformation due to subsea currents. This deformation resulted in large variations in the normal relative velocity along the cable length, which in turn resulted in the extreme differences in VIV magnitude depending on location along the cable length. This was exemplified by a current angle of 0 degrees where Flotant and West Barra showed minimal displacement towards the hang-off and greater than a magnitude of four larger at the touchdown, this behaviour wasn't as exaggerated for the other cables. A current angle of 90 degrees, in terms of magnitude of RMS displacement, resulted in very similar results for all cables. A current angle of 180 degrees exhibited similar behaviour to an angle 0 degrees. The cables that were more flexible and lower diameter resulted in more extreme variations in amplitude over the full cable length.

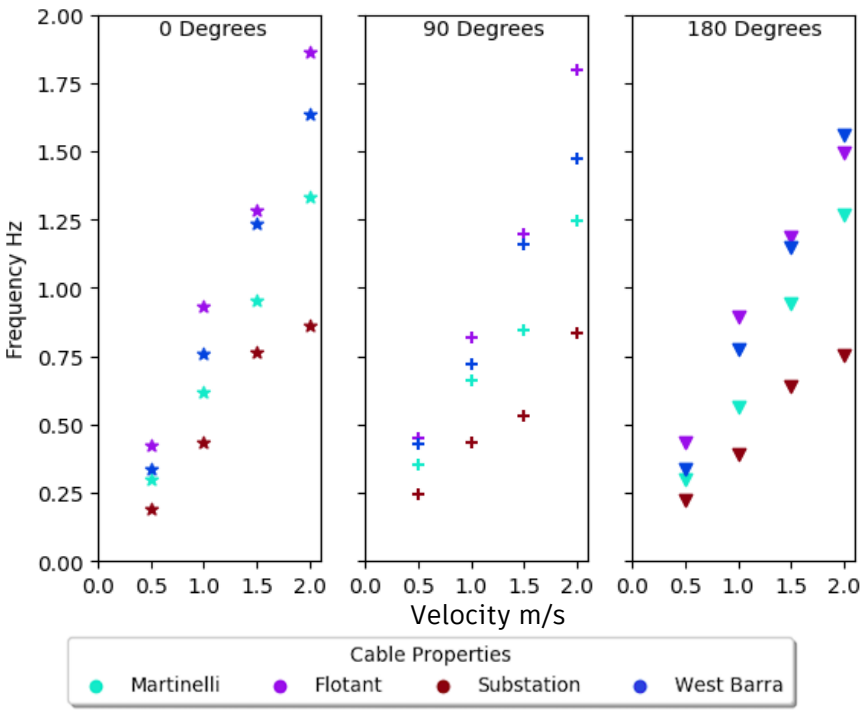

Figure 6-10: A comparison of the influence of cable's properties on the VIV frequency for Martinelli's cable

There are obvious differences in the frequencies of vibration for the different power cables. This is owing to their different properties resulting in producing distinctive sets of natural frequencies. This is presented in Figure 6-10. When comparing the frequencies, the ranking in terms of magnitude is that Flotant produced the largest, followed by West Barra, then Martinelli, and finally Substation. This is expected as the frequency of vibrations decreased as both diameter and mass per unit length increased. When comparing average frequency Flotant was largest, 10% greater than West Barra, which was 23% greater than Martinelli, which was 49% greater than Substation.

6.4 Impact of Diameter

The impact of cable diameter on VIV behaviour was investigated for Martinelli, Flotant, and Substation cables (refer to Table 3-3 for cable properties). The elastic modulus and mass ratio for each different diameter was kept constant, this involved scaling the bending stiffness and mass per unit length accordingly. The parameter D_0 is equivalent to the original diameter of each respective cable. When determining the A/D for the RMS displacement, it is important to stress that the D is determined for each different cable diameter and is not set to simply be D_0.

6.4.1 Martinelli

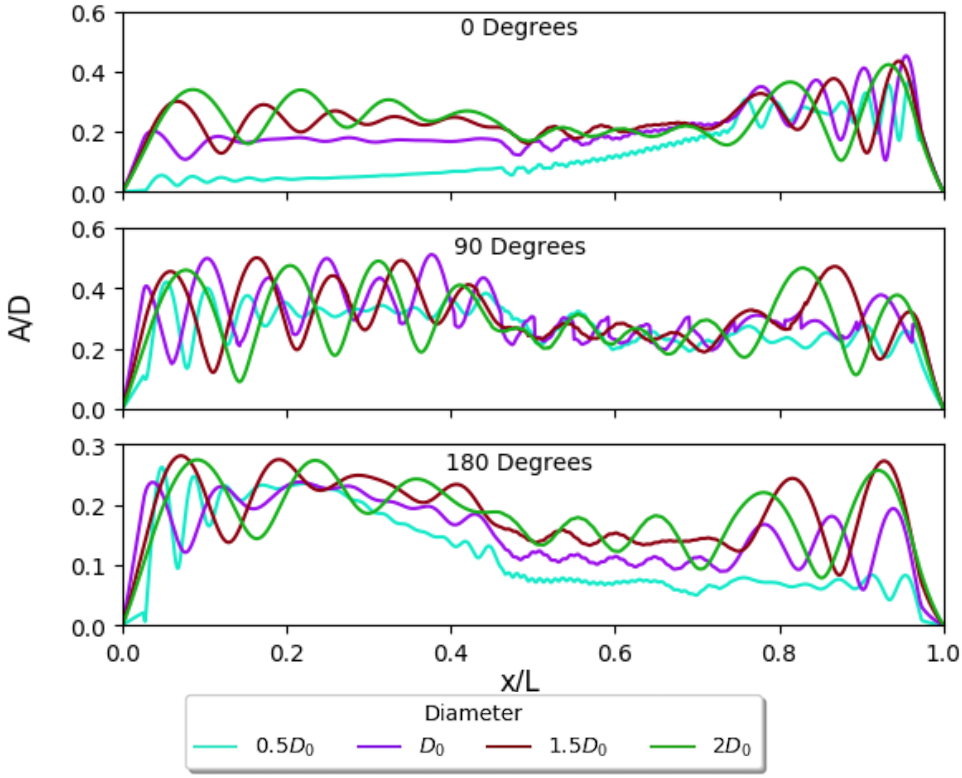

Figure 6-11: A comparison of the impact of the cable's diameter on the RMS crossflow displacement for Martinelli's cable at a uniform current speed of 1 m/s

Figure 6-11 shows that there was an obvious impact of cable diameter on the RMS displacement. As the diameter increased, generally, the mean displacement over the entire length of the cable also increased. This was due to the excitation of lower modes of vibration. The increase in amplitude was not linearly relative to the increase in diameter. As the diameter increased, it can be observed that the variation in RMS displacement along the cable length also decreased. This was likely due to both a lower mode of vibration, resulting in a larger RMS displacement, and also a reduction in the cable deformation, meaning that the greater the diameter the less the reduced velocity varied along the cable length. This reduction in cable deformation in turn reduced localised large differences in displacement along the cable length. The current angles most susceptible to extreme variations in RMS displacement over the cable length were 0 and 180 degrees.

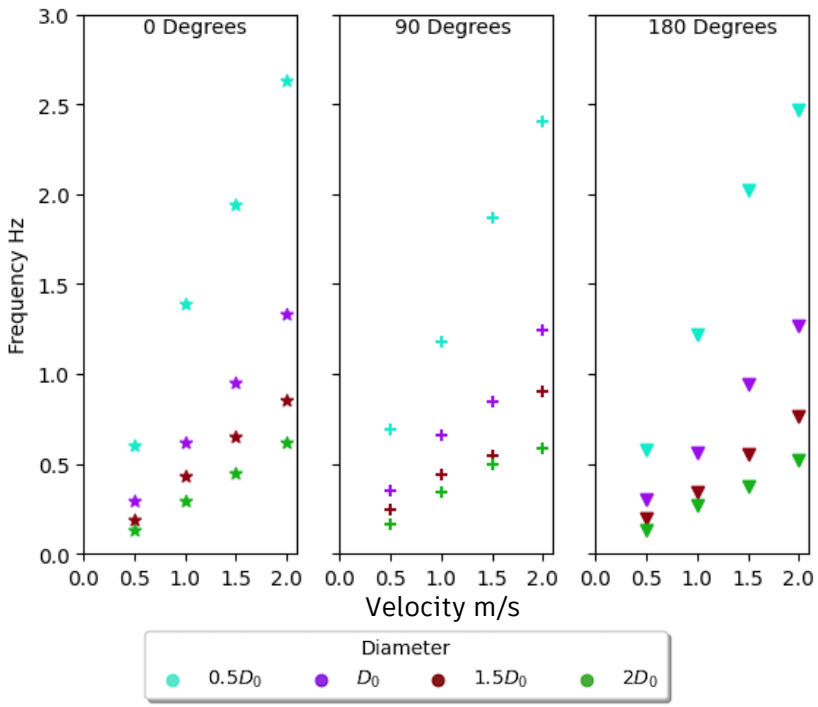

Figure 6-12: A comparison of the impact of the cable's diameter on vibration frequency for Flotant's cable

As discussed, and shown in Figure 6-12, the mode of vibration of the cable was significantly influenced by the cable diameter. The smaller the diameter the greater the frequency of vibration. The difference in magnitude in frequency was relative to the diameter, i.e., a diameter of $0.5D_0$ was approximately twice that of D_0. The frequency of vibration was determined within Shear7 and was directly dependent on the cable diameter. A smaller diameter cable is more susceptible to the excitation of high modes. The impact of this on fatigue is dependent on the internal parameters of the cable, such as the S-N curve. Over all current speeds, a current angle of 0 degrees resulted in the greatest frequency of vibrations compared to the other angles.

6.4.2 Flotant

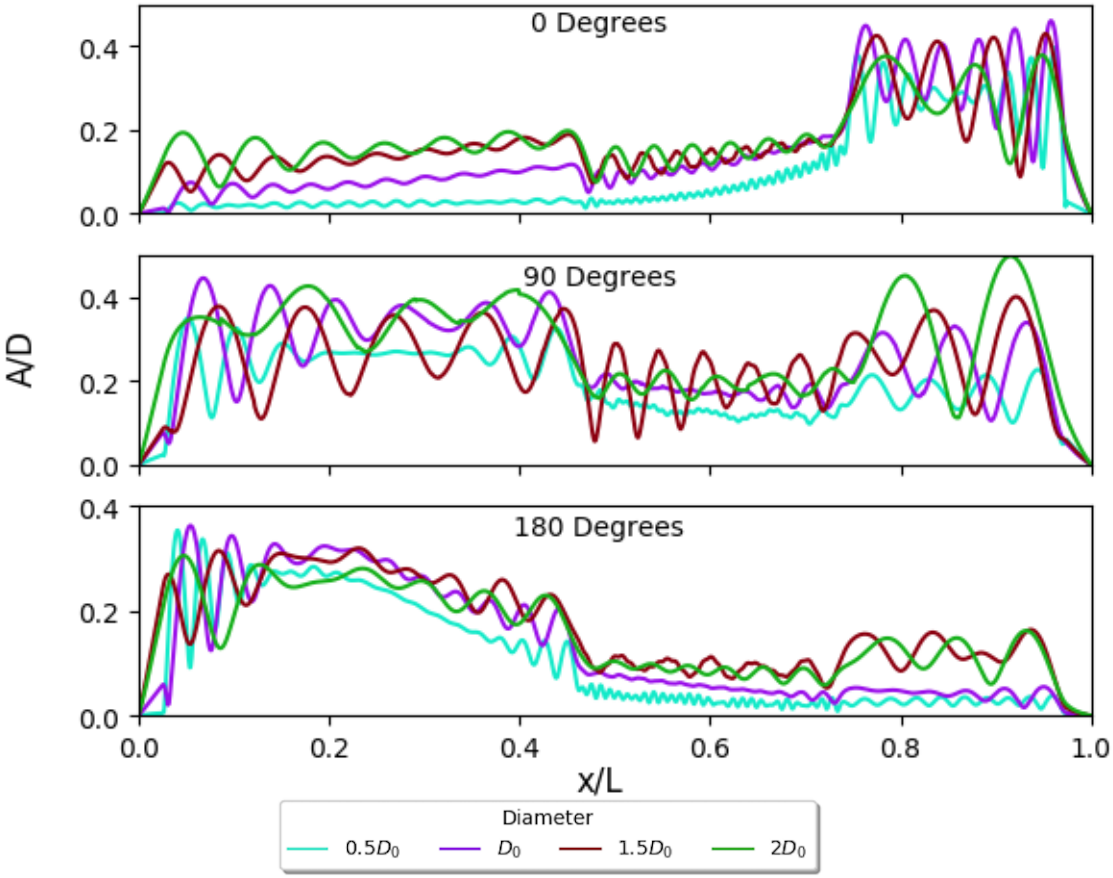

Figure 6-13: A comparison of the impact of the cable's diameter on the RMS crossflow displacement for Flotant's cable at a uniform current speed of 1 m/s

Flotant's cable followed the same trend as Martinelli's, where the smaller the diameter the smaller the amplitude of vibration that was observed, highlighted in Figure 6-13. One noticeable difference, when compared to Martinelli's cable, was that the RMS displacement profile wasn't as considerably impacted by changes in diameter. There is still an evident trend where, as the diameter increased there were fewer extreme differences in amplitude along the length but compared to Martinelli this was much less substantial. This was likely due to D_0 for Flotant being smaller than Martinelli and also having a smaller elastic modulus, meaning that even at large diameters the cable was still subjected to substantial deflection meaning large variations in reduced velocity along the cable length occur.

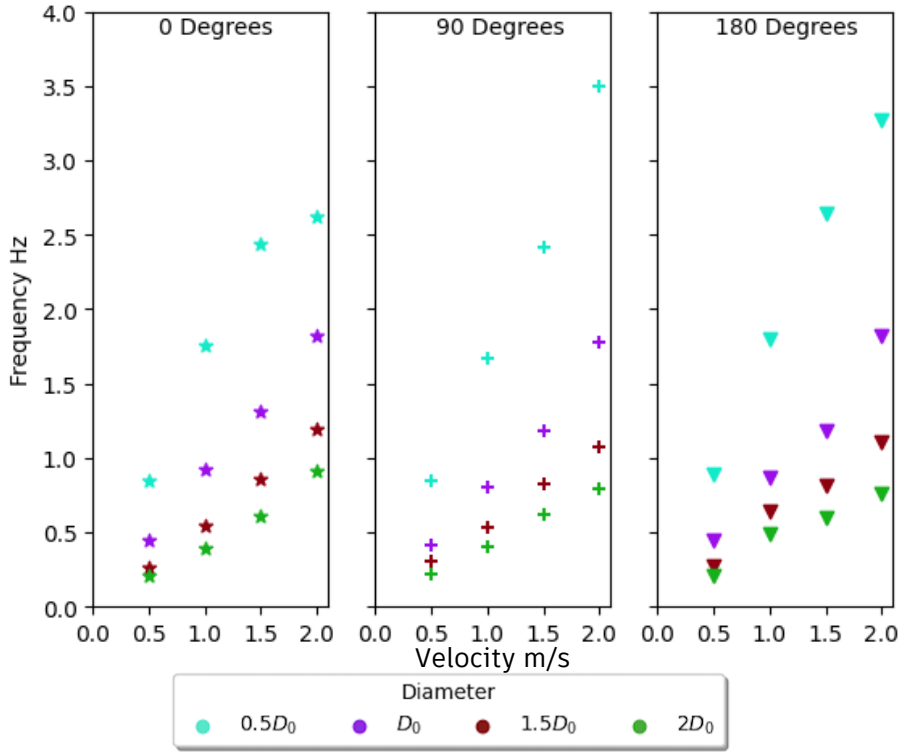

Figure 6-14: A comparison of the influence of the cable's properties on the VIV frequency for Flotant's cable

The vibration frequency versus current speed plots in Figure 6-14 show that as diameter decreased the frequency of vibrations increased, this followed the same trend as for Martinelli with one notable anomaly observed for diameter of 0.5 D_0 at a current speed 2m/s. This discrepancy was likely due to the cable deflection at this current speed being so substantial that the cable deformed past perpendicular to the seabed. This influenced the normal relative velocity and the VIV response at this section.

6.4.3 Substation

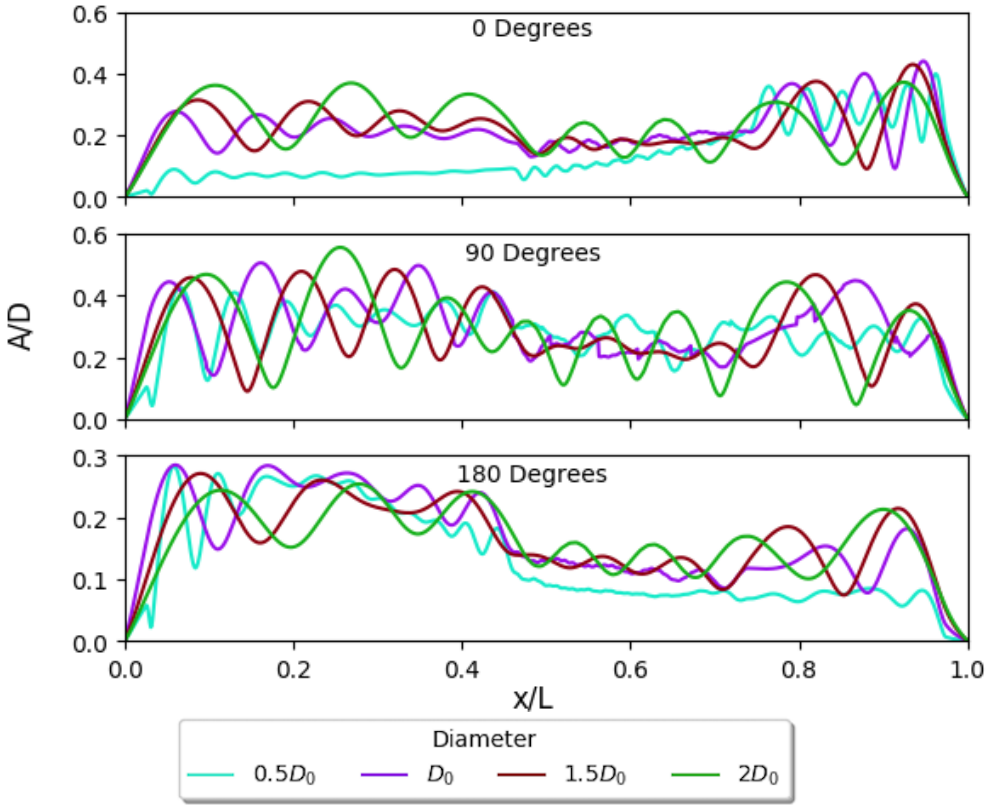

Figure 6-15: A comparison of the impact of the cable diameter on the RMS crossflow displacement for Guignier's substation cable at a uniform current speed of 1 m/s

Similar to the other cables, it can be seen in Figure 6-15 there is an evident impact of cable diameter. However, the discrepancies in RMS displacement profile over the cable's length were much smaller. Substation is already a large diameter cable with a large elastic modulus meaning it was not subjected to as large deflection with current speed compared to the other cables. Increasing the diameter and making the cable stiffer and less susceptible to deflection didn't impact the normal relative velocity as much as for the other cables because the cable deflection was already so limited. The most obvious difference seen was when the diameter was reduced to $0.5D_0$. The reduction in diameter allowed for more meaningful deflection to take place and resulted in the large variations in displacement over the cable's length observed, which was seen for the other cables. For cable diameters of D_0 and greater there was much smaller variations in amplitude over the cable length due to the stiffness of the cable.

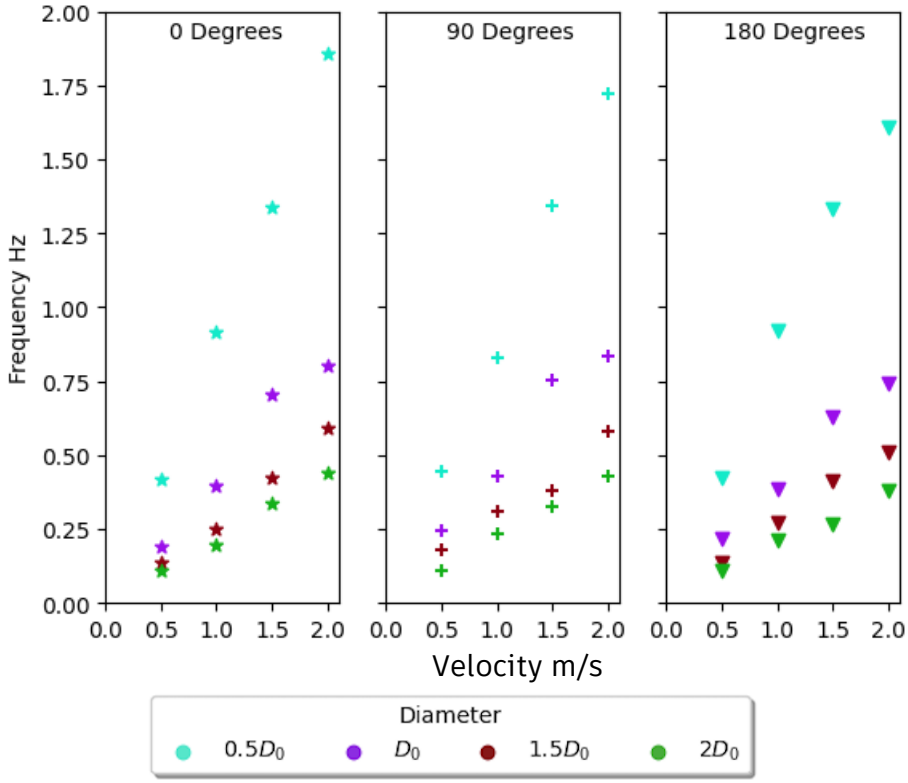

Figure 6-16: A comparison of the influence of the cable's properties on the VIV frequency for Guignier's cable

The impact of diameter on the frequency of vibrations followed the same trend as the other cables, where the frequency increased as the diameter decreased, shown in Figure 6-16. This trend was still seen, despite the displacement profile not being as substantially influenced by changes in diameter. A current angle of 0 degrees resulted in the greatest frequency of vibrations.

6.5 Impact of Bending Stiffness

The bending stiffness of the cable dictates how susceptible it is to deformation for a given load. A lower flexural rigidity means, assuming all other parameters are consistent, that greater deformation would occur for a given current speed up to a limiting value.

Table 6-2: Flexural Rigidity for Different Cables

Cable	Flotant	Martinelli	Substation
Flexural Rigidity Nm^2	1.01×10^8	3.82×10^9	2.87×10^9

The bending stiffness of Martinelli's cable was adjusted to determine the influence this had on VIV behaviour. The bending stiffness was altered by adjusting the flexural rigidity according to the values in Table 6-2 for Flotant and Substation cables. A uniform current profile of 1m/s was used.

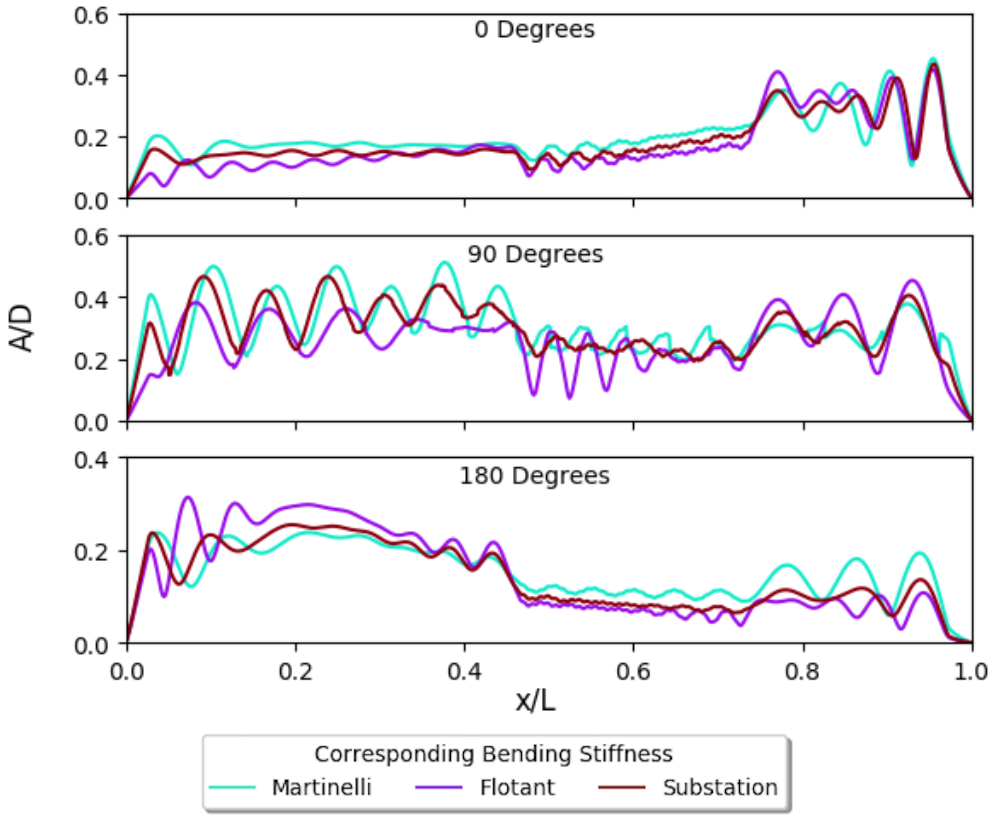

Figure 6-17: A comparison of the impact of bending stiffness on the RMS crossflow displacement

The bending stiffness is shown in Figure 6-17 to have an impact on the RMS displacement for all of the current angles. When comparing whether the VIV behaviour was dominated by tension or bending stiffness the parameter *P* from Eq. 3.19 is used. For a current angle of 0 degrees *P* is equal to 0.516, 0.279, and 0.0785 for Martinelli, Flotant, and Substation respectively. For a current angle of 90 degrees, *P* is equal to 0.47, 1.58, and 2.99 for Martinelli, Flotant, and Substation respectively. For a current angle of 180 degrees *P* is equal to 2.30, 0.474, and 1.51 for Martinelli, Flotant, and Substation respectively. These values indicate that for all current angles and bending stiffness values, the VIV behaviour was bending stiffness dominated.

For a current angle of 0 degrees, it can be observed that as the bending stiffness increased the RMS displacement towards the hang-off point increased. This was because the cable was less susceptible to deflection. This means the variation in reduced velocity over the full cable length is reduced compared to the more flexible cables. The more flexible cables resulted in a greater magnitude of vibrations towards the touchdown point compared to the less flexible cables. The behaviour for current angle 180 degrees can be explained by this as well. The stiffer cables deflected less at the hang-off point; thus, the normal relative velocity didn't vary as greatly along the cable length, still, notable differences in amplitude along the cable length were seen for all bending stiffnesses. The RMS displacement profile for a current angle of 90 degrees was not as greatly influenced by the bending

stiffness because the current direction was perpendicular relative to the initial spatial plane where the cable was present. The cable was still susceptible to deflection, as the bending stiffness decreased greater displacement was seen towards the touchdown point and smaller at the hang-off point.

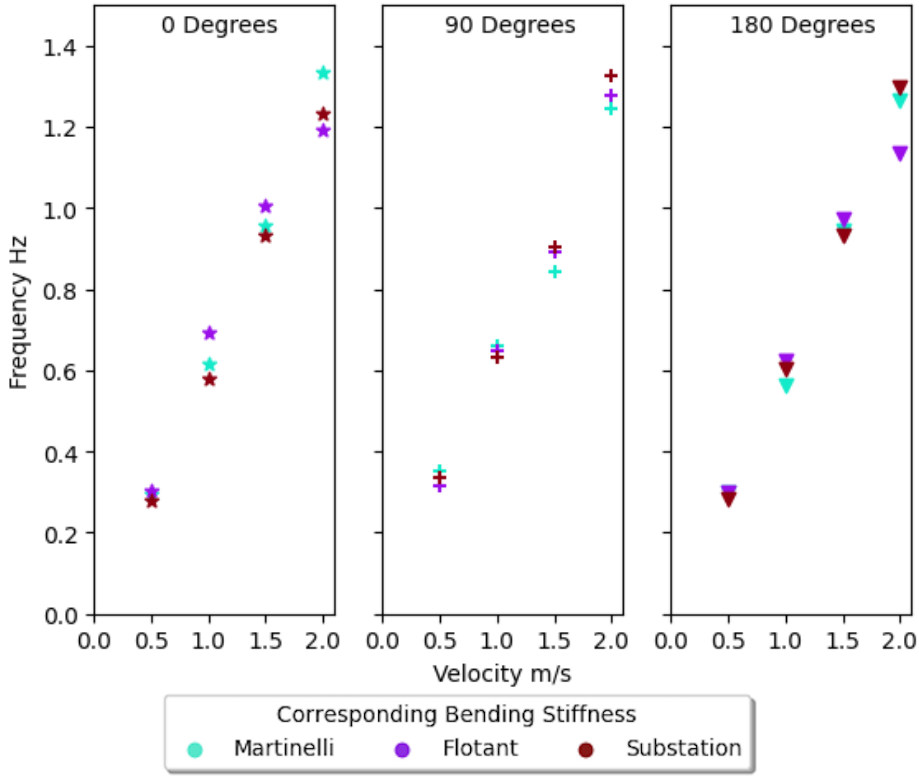

Figure 6-18: A comparison of the impact of the bending stiffness impact on VIV frequency

When comparing the frequency of vibrations in Figure 6-18, there was no obvious influence of bending stiffness on the frequency of vibrations. For current angles 0 and 180 degrees, up to 1.5m/s, the smallest bending stiffness resulted in the greatest frequency of vibration. This was likely due to substantial cable deflection occurring meaning greater relative velocity at certain sections increasing the frequency at this point and skewing the most likely mode of vibration. However, at 2m/s, the cable deflection for all bending stiffnesses was substantial enough so that it was no longer the limiting factor. The smallest bending stiffness resulted in the cable deflecting to such a large extent that it bent past the normal, relative to current direction, and a reduction in reduced velocity occurred. For a current angle of 90 degrees different behaviour was observed. There was no obvious dependency of frequency on the flexural rigidity of the cable.

6.6 Conclusion

The structural properties of the cable were observed to have an influence on the VIV response. The bending stiffness, diameter, and mass ratio were all analysed. A significant proportion of the impacts of these parameters on the VIV behaviour can be attributed to the influence they had on the cable

deformation. Changing the cable deformation notably altered the relative velocity along the cable, which in turn, changed the VIV response. This was particularly noticeable for the bending stiffness and density of the cable. The lower the bending stiffness or density of the cable the greater the localisation of extreme displacements along the cable length because the cable is more susceptible to deformation from the incident forces from the current. When considering the frequency, however, there were no discernible trends on the impact of mass ratio or flexural rigidity.

Regarding the diameter, generally, similar behaviour was seen as the other properties, where the lower the diameter the greater the range in RMS displacement over the cable length. Furthermore, when altering the diameter there were large changes in frequency seen. These changes were a linear increase in frequency with diameter.

7 RESULTS AND DISCUSSION – CURRENT PROFILE

The influence of current on the VIV response of a dynamic power cable was explored. This involved altering the current speed, direction, and shear profile. The current speed was changed in various increments up to a speed of 2m/s. The direction of the current was varied, generally, in increments of 90 degrees. Five different shear current profiles were used to determine their influence on the VIV response.

7.1 UNIFORM CURRENT

7.1.1 Martinelli

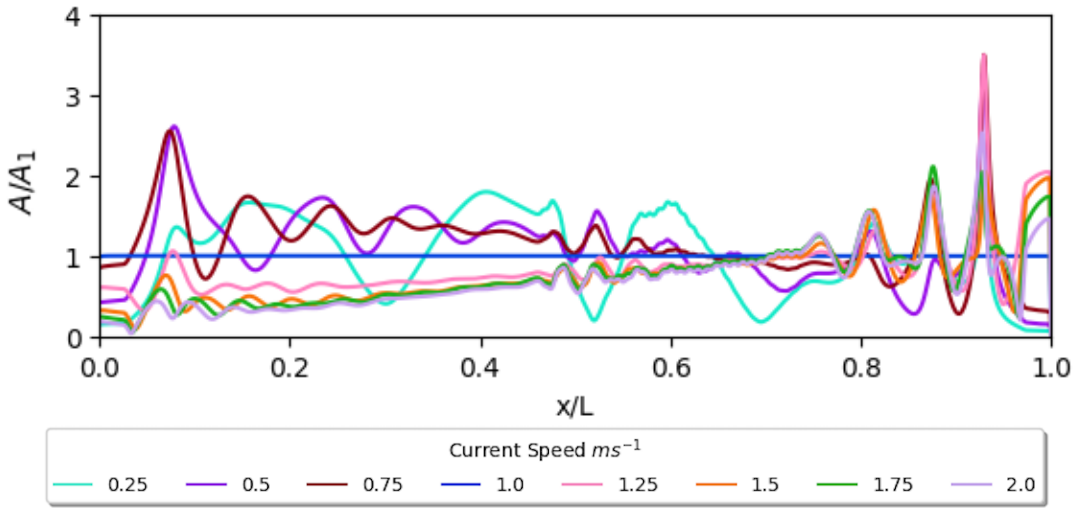

Figure 7-1: A normalised comparison of the influence of current speed on the RMS crossflow displacement for a current angle of 0 degrees for Martinelli's cable

It is shown in Figure 7-1 that as velocity increased the RMS displacement towards the hang-off point decreased for a current angle of 0 degrees. A_1 represents the RMS displacement for a current speed of 1 m/s, and as such a current speed of 1 m/s is represented by a flat line at a value of $A/A_1 = 1$. This was due to the cable deformation; it displaced from its static location at higher velocities due to increased drag force which resulted in the angle of inclination decreasing so that the cable increasingly tended to parallel relevant to current direction. The RMS displacement towards the touchdown increased for higher current velocities. This was due to higher velocities displacing the cable and resulting in it tending towards perpendicular to the current direction along the bottom section. This highlights the impact that cable deformation can have on the VIV behaviour.

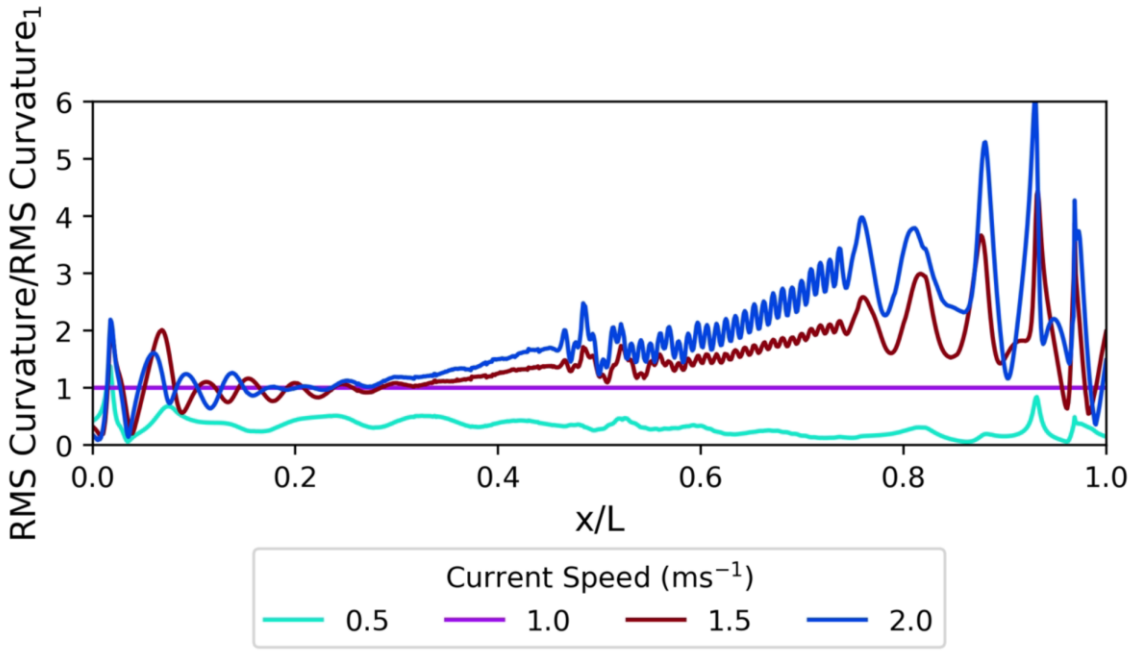

Figure 7-2: A normalised comparison of the influence of current speed on the RMS curvature for a current angle of 0 degrees for Martinelli's cable

Figure 7-2 shows how the curvature along the cable's length varied with current speed. A current speed of 0.5 m/s showed substantially smaller curvature over the full cable length. It can be seen that up to approximately 0.3 *x/L* there was little difference between all current speeds greater than 1 m/s. After this point, however, the curvature for different speeds substantially diverged, with the greater the current speed the greater the curvature observed. This was most evident towards the touchdown section; this was the location where the cable was exposed to the greatest relative velocity. There were notable small variations in curvature along the buoyancy module section. When comparing this to the RMS crossflow displacement, the trend was similar with an increase in both parameters along the cable length. However, the displacement began at a smaller value and didn't increase as substantially as the curvature, relative to the normalised 1 m/s profile.

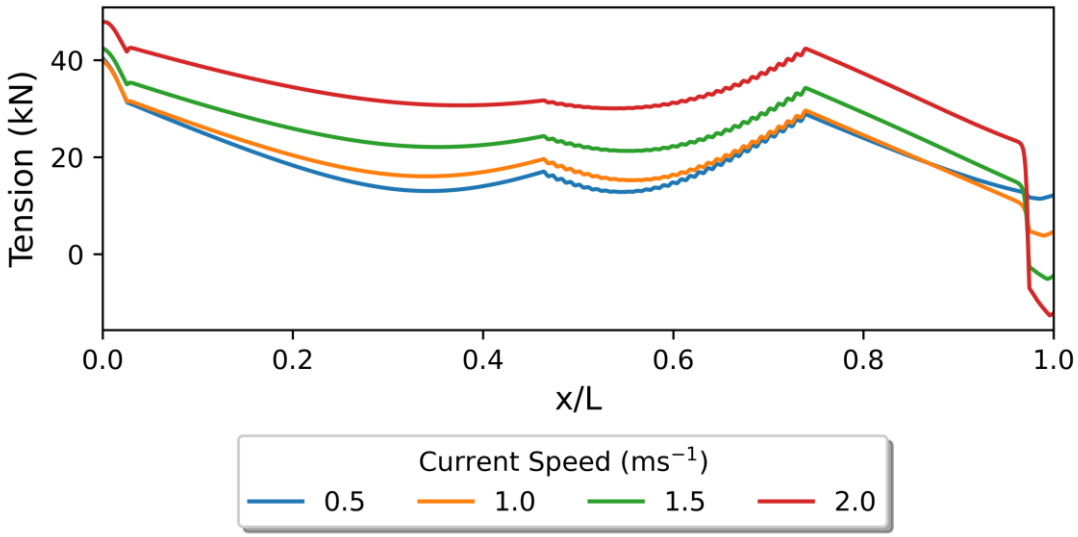

Figure 7-3: A comparison of the influence of current speed on the tension for a current angle of 0 degrees for Martinelli's cable

It can be seen in Figure 7-3 that as the current speeds increased so did the tension over the full cable length, except at the touchdown point where the larger the current speed the lower the tension. This was due to overbending at this point, and it is noted that there was a high risk of compression. It was expected that the tension would increase due to greater induced force from the current flow. When determining the influence of the tension, parameter *P* from equations Eq. 3.17 and Eq. 3.19 is referred to. *P* equalled 5.06, 0.51, 0.29, and 0.68 for current speeds 0.5, 1.0, 1.5, 2.0 m/s respectively. Thus, the beam model was used, as the bending stiffness was important.

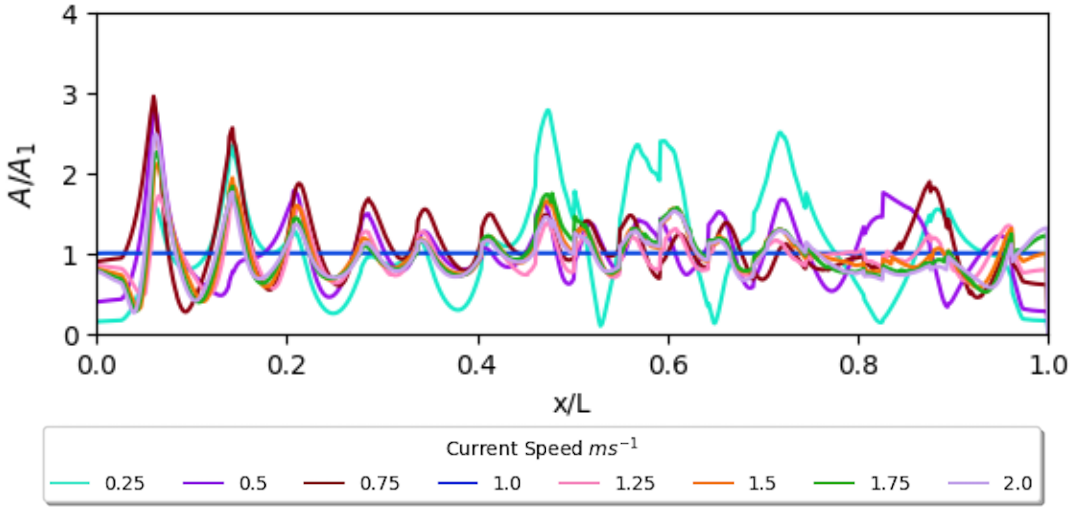

Figure 7-4: A normalised comparison of the influence of current speed on the RMS crossflow displacement for a current angle of 90 degrees for Martinelli's cable

The impact at angle 90 degrees is harder to quantify compared to the other current angles investigated, as seen in Figure 7-4. Generally, there were some large discrepancies, particularly towards the hang-off point, between different current speeds but no obvious trend is discerned as

the current speed increased. The deviation in the VIV profile was likely due to different modes being excited. The deformation of the cable with increased current speed had less influence on the RMS displacement compared to the other current angles.

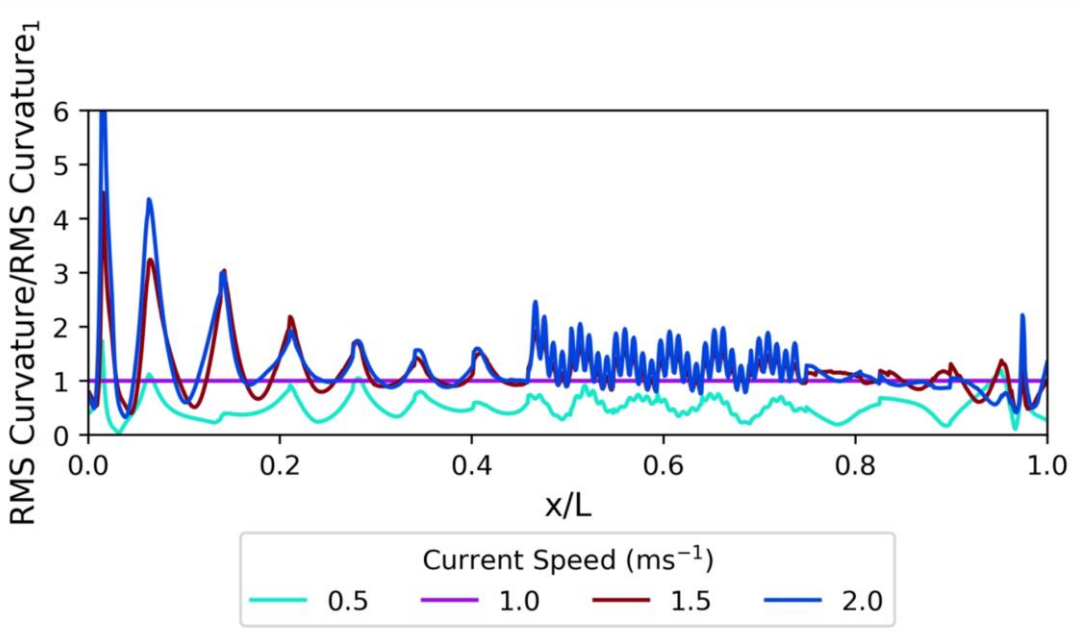

Figure 7-5: A normalised comparison of the influence of current speed on the RMS curvature for a current angle of 90 degrees for Martinelli's cable

Figure 7-5 shows how the RMS curvature varied with current speed. It can be observed that as the speed increased so did the RMS curvature, however above a current speed 1.5 m/s this difference was reduced. The most obvious difference in behaviour along the cable's length were observed at the hang-off point. This was due to the large curvature as the cable exited the bend stiffener. After 0.3 *x/L* the differences in RMS curvature were more uniform over the cable's length. When comparing this to the RMS crossflow displacement the overall profiles are very similar.

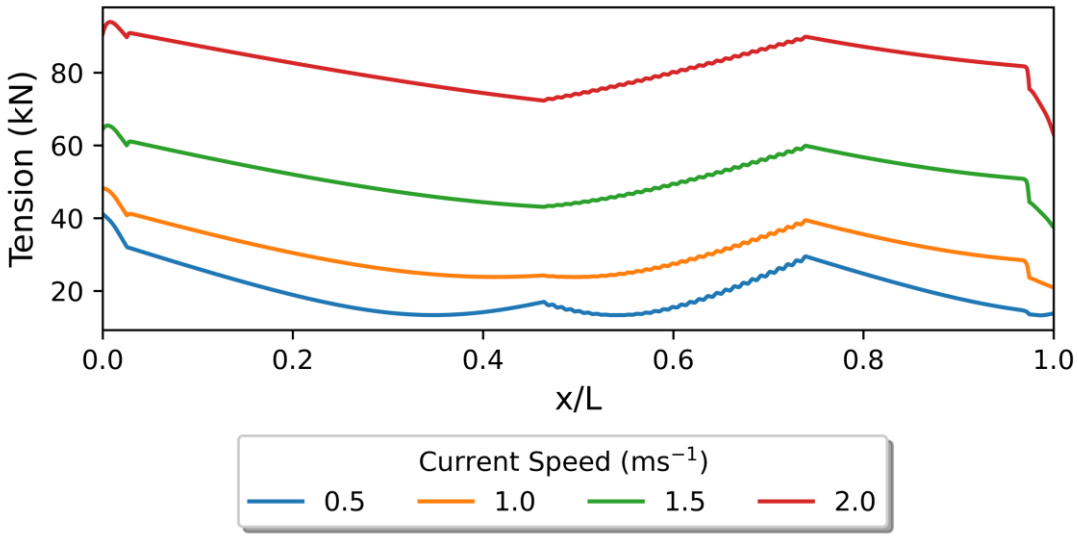

Figure 7-6: A comparison of the influence of current speed on the tension for a current angle of 90 degrees for Martinelli's cable

It can be seen in Figure 7-6, the tension increased with current speed. The first peak seen for a speed of 0.5 m/s was lost for the larger current speeds as the cable deformed. When determining the influence of the tension on the structural dynamic behaviour, parameter *P* from equations Eq. 3.17 and Eq. 3.19 is referred to. *P* equalled 6.11, 4.04, 5.47, and 8.28 for current speeds 0.5, 1.0, 1.5, 2.0 m/s respectively. Thus, the beam model was used as the bending stiffness is important.

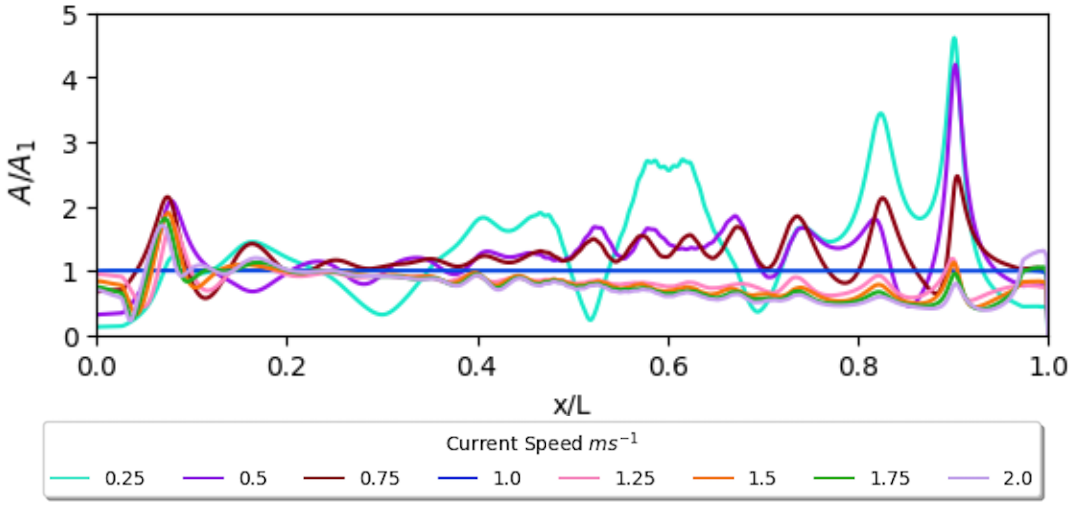

Figure 7-7: A normalised comparison of the influence of current speed on the RMS crossflow displacement for a current angle of 180 degrees for Martinelli's cable

For a current angle of 180 degrees, as the current velocity increased the RMS displacement towards the touchdown point decreased, shown in Figure 7-7. This is due to the cable deformation resulting in an increased relative velocity at the hang-off point relative to the rest of the cable. As the current velocity increased, so does the cable deformation. After a current speed of around 1.5 m/s was reached the rate of decrease in displacement with current speed is less.

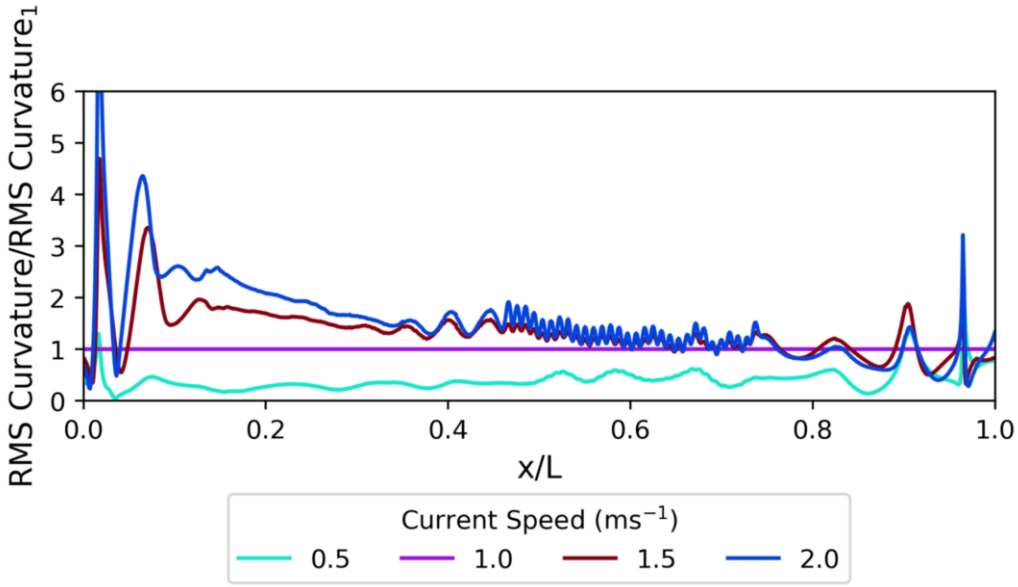

Figure 7-8: A normalised comparison of the influence of current speed on the RMS curvature for a current angle of 180 degrees for Martinelli's cable

It can be observed in Figure 7-8 that the curvature along the cable's length increased as the current speed increased. The most obvious differences were seen towards the hang-off point. This is similar to the behaviour seen for the RMS displacement but to a more exaggerated extent. Towards the touchdown point, the current speeds greater than 1m/s resulted in reduced curvature. This was due to the cable deformation. The large curvature seen at the hang-off point was also due to the deformation of the cable with greater relative velocity seen at this section. When comparing this to the RMS crossflow displacement, both predicted that the maximum curvature was towards the hang-off point and then decreased with cable length. However, the RMS crossflow displacement predicted a smaller difference between the maximum and minimum values.

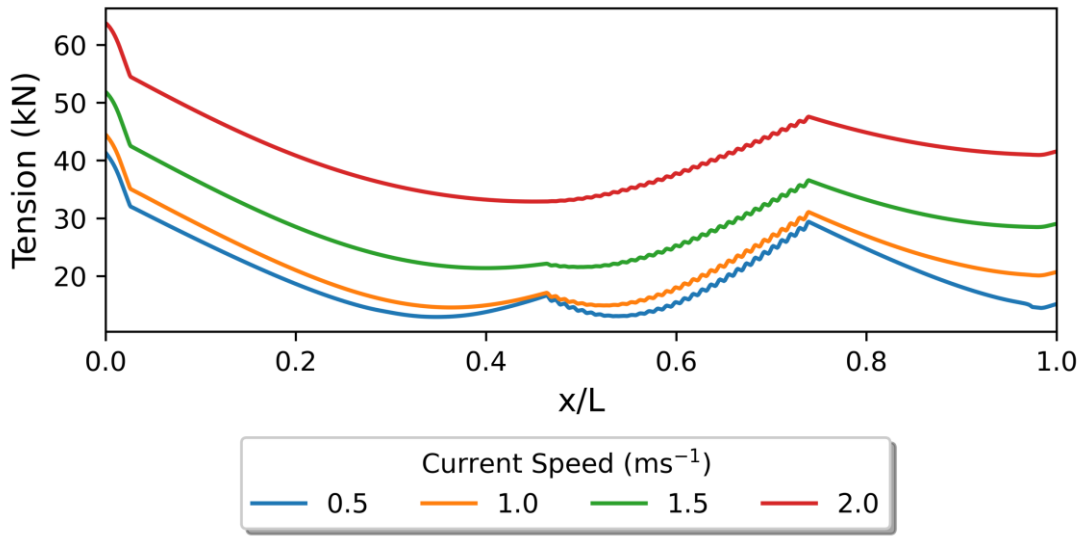

Figure 7-9: A comparison of the influence of current speed on the tension for a current angle of 180 degrees for Martinelli's cable

Figure 7-9 shows how the tension varied with current speed. There was an obvious trend where the greater the current speed the greater the tension over the full cable length. The tension profile also changed, as the current speed increased above 1 m/s the first peak was heavily suppressed for 1.5 m/s and non-existent for 2 m/s. This was due to the cable deformation. *P* equalled 6.56, 2.47, 2.30, and 2.89 for current speeds 0.5, 1.0, 1.5, 2.0 m/s respectively. Thus, the beam model was used as the bending stiffness was important.

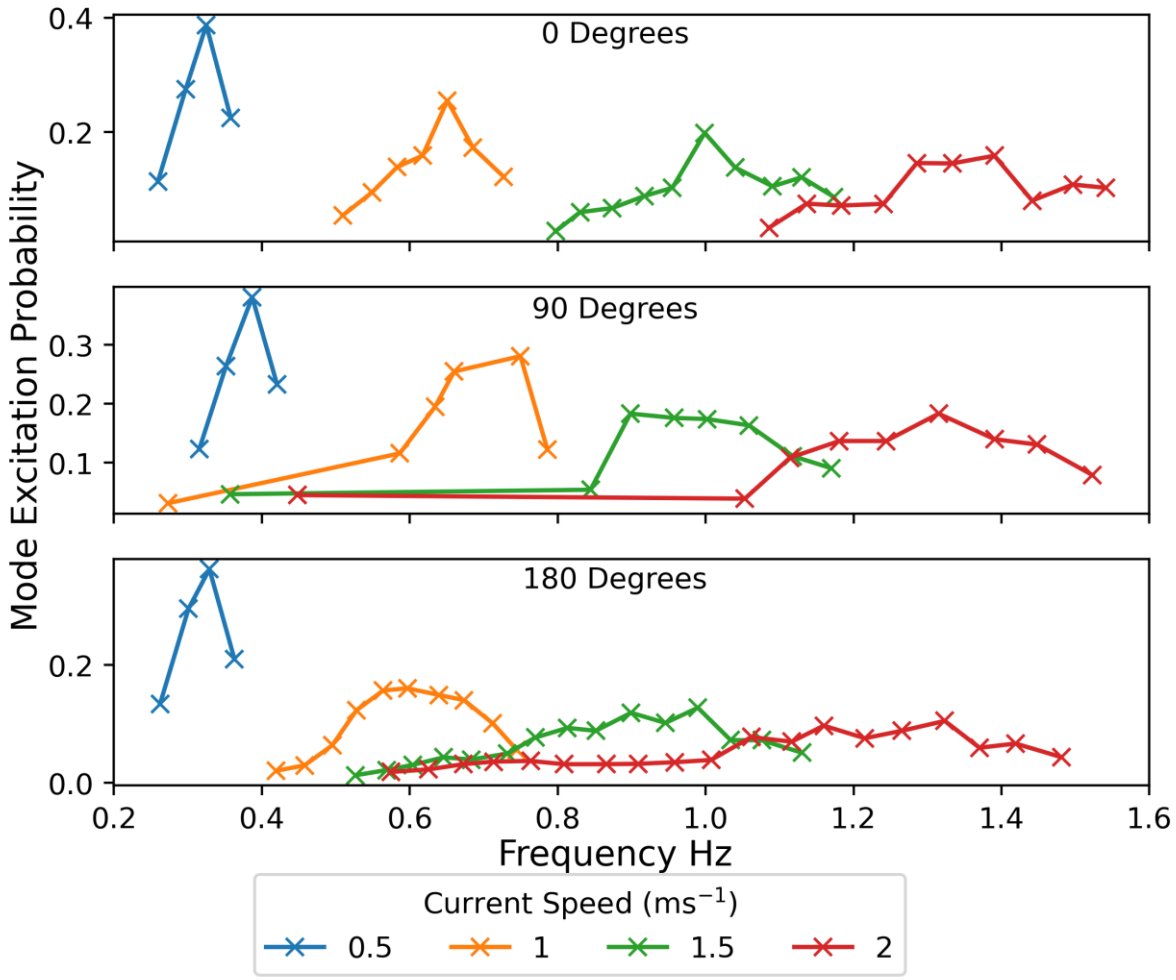

Figure 7-10: Comparison of the modal probabilities and corresponding frequency for different current speeds for Martinelli's cable

Figure 7-10 shows how the modal probability changed with current speed and direction. It can be seen that for all angles when the current speed was lower, there were less potentially excited modes. As the current speed increased there was a greater number of potentially excited modes. This is to be expected, as there was a larger variation in the relative velocity over the cable's length and greater sections of the cable were exposed to velocities large enough to induce VIV. For lower speeds this was limited. A current angle of 180 degrees showed the greatest variation in excited modes. This was because of the deformation of the cable allowing for multiple excitation zones across the cable's length, whereas for 0 degrees this was much more limited towards the touchdown section. Generally, the distribution of the potentially excited modes was around a maximum. In future comparison of frequencies, the maximum was the sole frequency used to allow for ease of comparison over multiple varying parameters.

7.1.2 Flotant

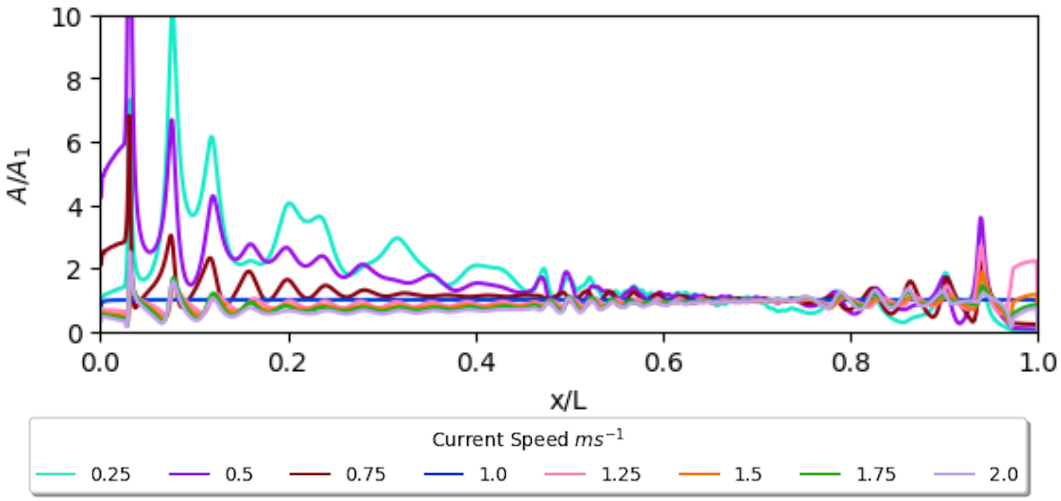

Figure 7-11: A normalised comparison of the influence of current speed on the RMS crossflow displacement for a current angle of 0 degrees for Flotant's cable

For a current angle of 0 degrees, a similar trend can be seen in Figure 7-11 where the greater the current velocity was the smaller the displacement was towards the hang-off point. There was a slight increase in displacement as well at the touchdown section. The reason for this behaviour was due to the cable deformation. As Flotant was a more flexible cable than Martinelli, at lower current speeds substantial deflection occurred. This meant that increasing the current speed didn't result in such large variations in displacement along the cable length and the increase in displacement at this section with current speeds stopped at a much earlier current speed, around 1.25 m/s.

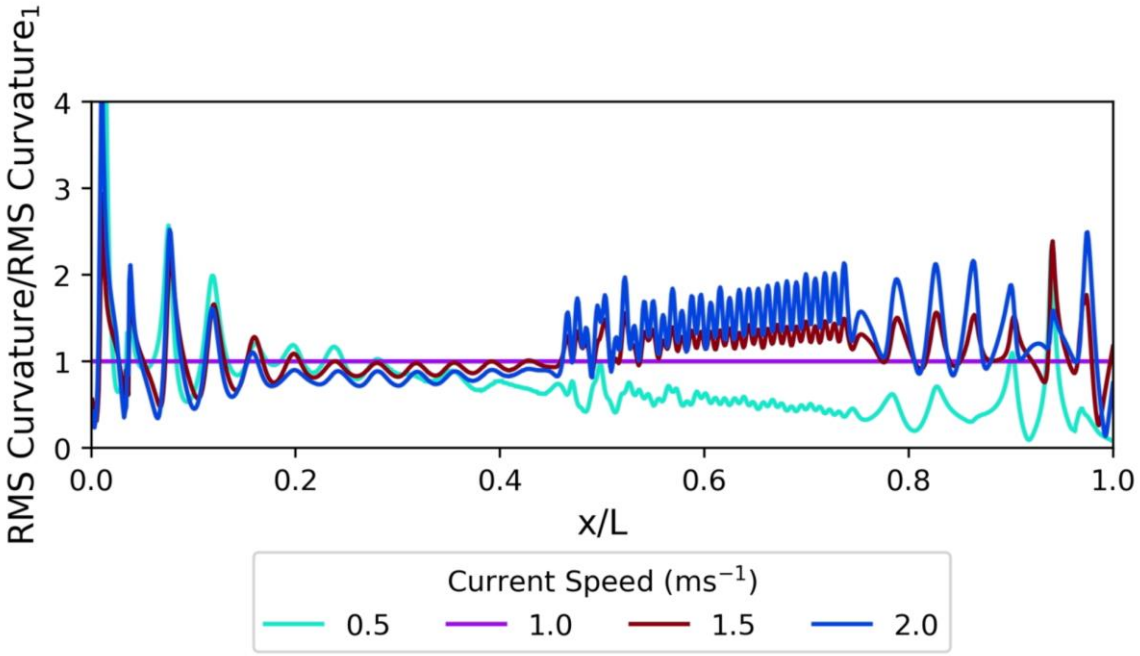

Figure 7-12: A normalised comparison of the influence of current speed on the RMS curvature for a current angle of 0 degrees for Flotant's cable

Figure 7-12 shows how the curvature along the cable's length varies with current speed. U to approximately 0.3 *x/L* the RMS curvature was similar for all other current speeds from 1m/s. After this point, however, the RMS curvature for a current speed of 0.5 m/s decreased as the length increased. As the location along the cable increased past 0.45 x/L the curvature for current speeds greater than 1 m/s began to diverge, the greater the current speed the greater the curvature observed. When comparing this to the crossflow displacement different behaviour was seen. There were deviations for both parameters towards the hang-off point. The profile for 0.5 m/s was not dissimilar.

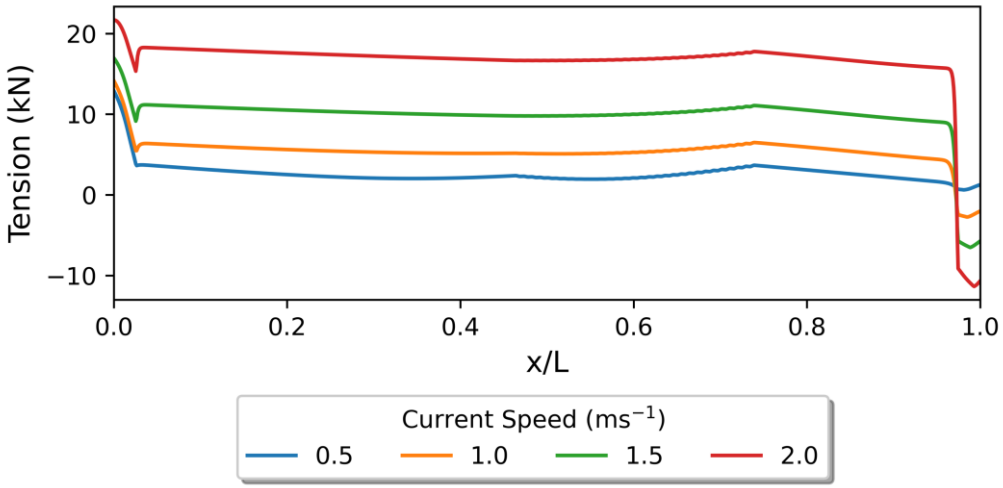

Figure 7-13: A comparison of the influence of current speed on the tension for a current angle of 0 degrees for Flotant's cable

It can be observed in Figure 7-13 how the tension along the cable's length varied with the current speed. This followed a similar trend as for Martinelli's cable whereas current speed increased so did the tension, up to the touchdown point where there was a high risk of compression with larger current speeds. There was greater compression observed here compared to Martinelli because Flotant's cable is more flexible. *P* equalled 1.63, 2.70, 6.94, and 12.8 for current speeds 0.5, 1.0, 1.5, and 2.0 m/s respectively. Thus, the beam model was used as the bending stiffness was important.

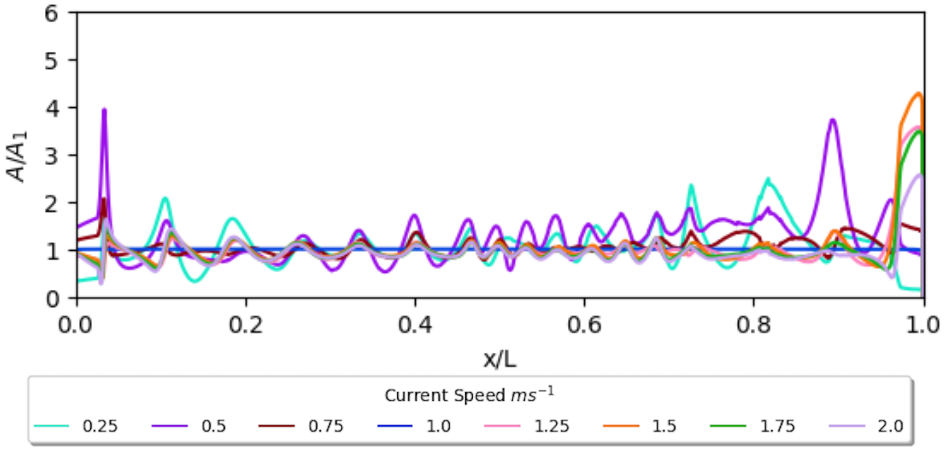

Figure 7-14: A normalised comparison of the influence of current speed on the RMS crossflow displacement for a current angle of 90 degrees for Flotant's cable

For a current angle of 90 degrees, it can be observed in Figure 7-14 that as the current speed increased the vibration profile was impacted. There was a change in mode of vibration, but averaging out over the full cable length, from 1-2m/s there was little difference in the magnitude of vibrations. There were notable discrepancies at both the touchdown and the hang-off points, which were due to the bend stiffeners and extreme bending at these sites. There was no overall trend as current speed increased.

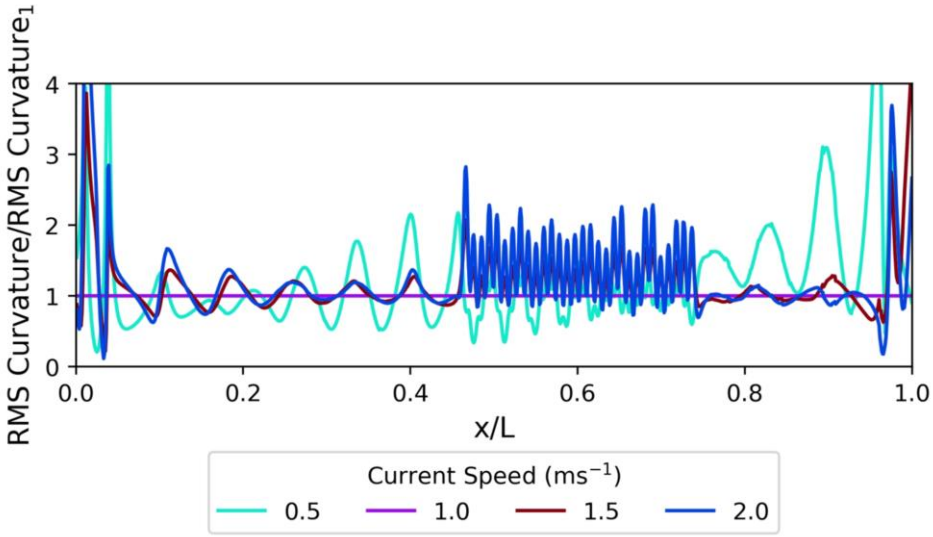

Figure 7-15: A normalised comparison of the influence of current speed on the RMS curvature for a current angle of 90 degrees for Flotant's cable

Figure 7-15 shows how the RMS curvature for current speeds greater than 1 m/s followed a similar profile with larger values compared to 1 m/s with the discrepancy between 2 m/s and 1.5 m/s less than the difference between 1.5 and 1 m/s. The curvature for 0.5m/s substantially diverged from previously seen trends. This was likely due to the tension dominated behaviour seen for the larger current speeds. When comparing this to the crossflow displacement, very similar profiles and trends are seen. Overall, the general magnitudes were similar to the normalised 1m/s values.

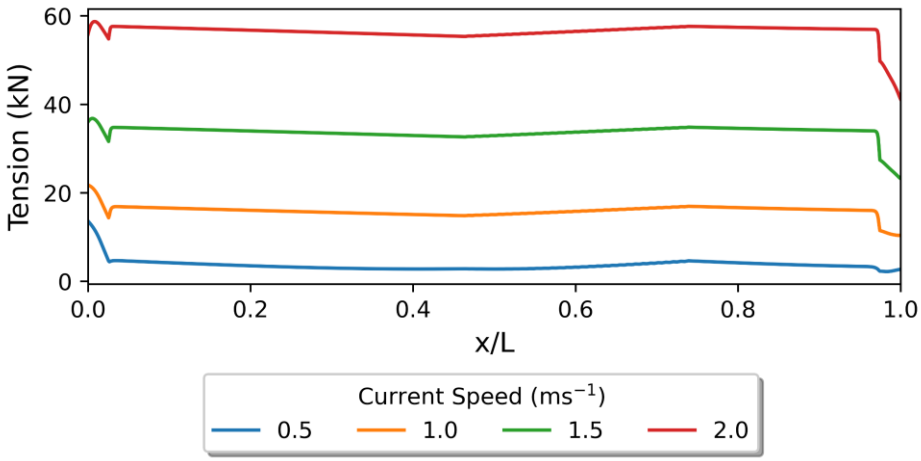

Figure 7-16: A comparison of the influence of current speed on the tension for a current angle of 90 degrees for Flotant's cable

When observing the tension profiles shown in Figure 7-16 an obvious trend was seen where the greater the current speed the greater the tension, with the tension profile over the cable's length very similar. *P* equalled 10.0, 45.8, 100, 178 for current speeds 0.5, 1.0, 1.5, 2.0 m/s respectively. With such large values the behaviour was now tension dominated for speeds greater than 1.0 m/s. This was likely the reason for the substantial differentiation in results between 0.5m/s and the larger current speeds.

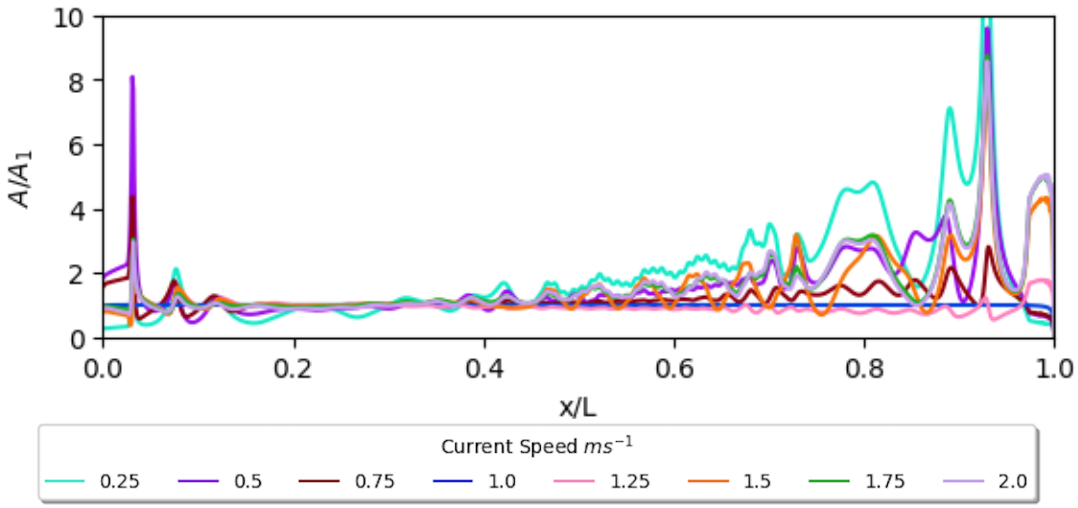

Figure 7-17: A normalised comparison of the influence of current speed on the RMS crossflow displacement for a current angle of 180 degrees for Flotant's cable

As shown in Figure 7-17 for a current angle of 180 degrees the RMS displacement towards the hang-off point was generally similar for all speeds except for a large peak at 0.025 x/L which was where the bend stiffener ended, and large curvature was present. There was no linear relation seen between current speed and RMS displacement at the touchdown point. Generally, as the current speed increased from 0.25-1.25 m/s the magnitude of vibrations towards the touchdown point decreased. However, from 1.25-2 m/s as the current speed increased so did the RMS displacement. The decrease from 0.25-1.25 m/s was likely due to the deformation of the cable. From 1.25-2 m/s the increase in RMS displacement was likely due to the cable deformation having reached its near maximum value. Further increases in deformation were not substantial enough to influence the normal relative velocity over the increases in current speed.

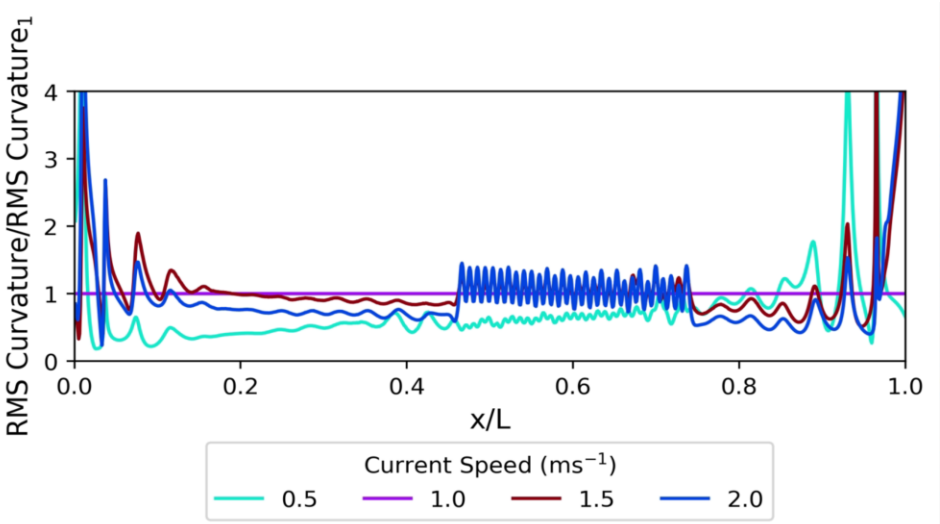

Figure 7-18: A normalised comparison of the influence of current speed on the RMS curvature for a current angle of 180 degrees for Flotant's cable

The behaviour seen in Figure 7-18 substantially deviated from the trends seen for other cables. Generally, a current speed of 1 m/s resulted in the greatest curvatures, except for discrepancies at the hang-off, buoyancy section, and touchdown points. A current speed of 0.5 m/s did not follow the same trend and showed larger curvature at the touchdown point and less toward the hang-off point. This was due to the cable deformation being less for this current speed meaning the relative velocity towards the touchdown point was not as different compared to the hang-off point as it was for the other current speeds. The behaviour for 2m/s can be explained by the VIV behaviour being tension dominated. When comparing this to the RMS crossflow displacement, both predict large discrepancies at the anchor points, but the crossflow displacement followed a different profile with increased displacement along the touchdown section.

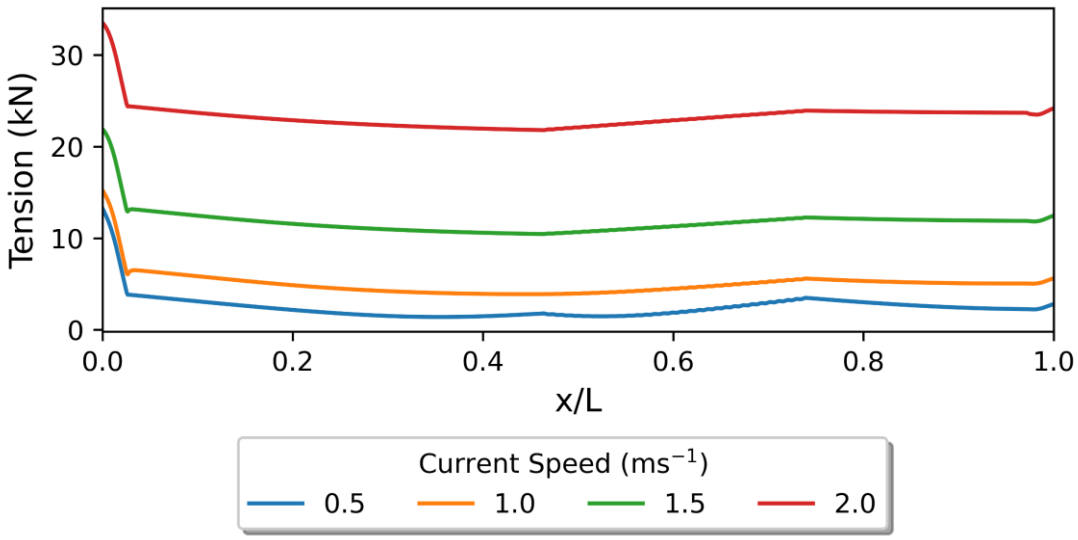

Figure 7-19: A comparison of the influence of current speed on the tension for a current angle of 180 degrees for Flotant's cable

When comparing the tensions shown in Figure 7-19 there was a similar profile seen over the cable length with an almost uniform tension value outside of the hang-off point. As expected, with increased current speed there was an increase in tension. *P* equalled 4.58, 7.19, 21.7, 50.1 for current speeds 0.5, 1.0, 1.5, 2.0 m/s respectively. All the current speeds were treated with the beam model except for 2m/s where it was tension dominated.

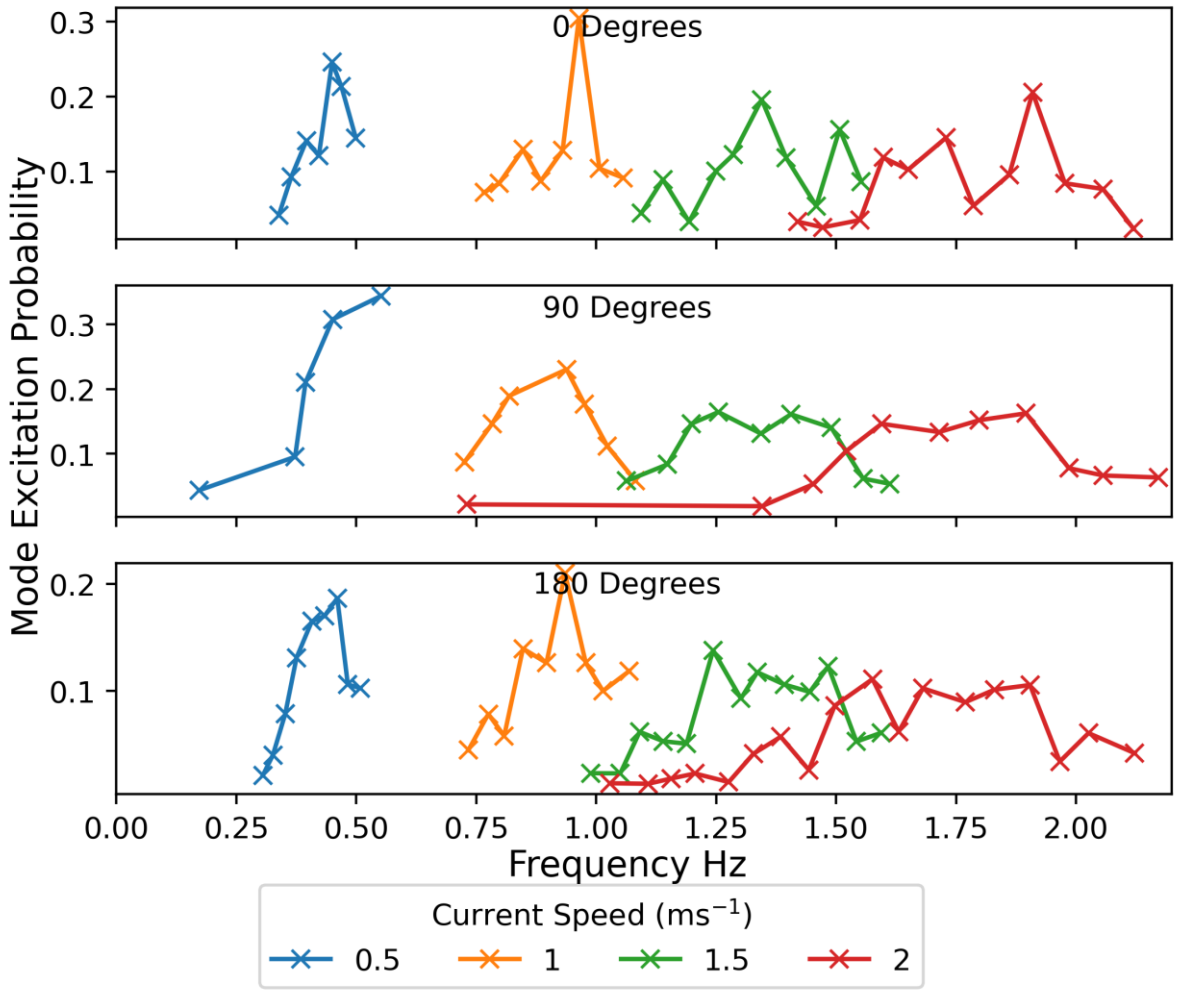

Figure 7-20: Comparison of the modal probabilities and corresponding frequency for different current speeds for Flotant's cable

Figure 7-20 shows how the probability of mode excitation varied with current angle and speed. Similar to Martinelli's cable, for a current speed of 0.5m/s there were limited predicted potential modes of excitation. This was due to lower relative current velocity limiting the potential excitation modes. The number of potentially excited modes increased with current speed. The probability of the excitation of each mode generally shows an expected maximum. However, for some angles the maximum probability was similar to other potential frequencies. This was noted as a limitation in the methodology, but it allowed for easier comparison when many parameters were varied in future frequency comparisons.

7.1.3 Substation

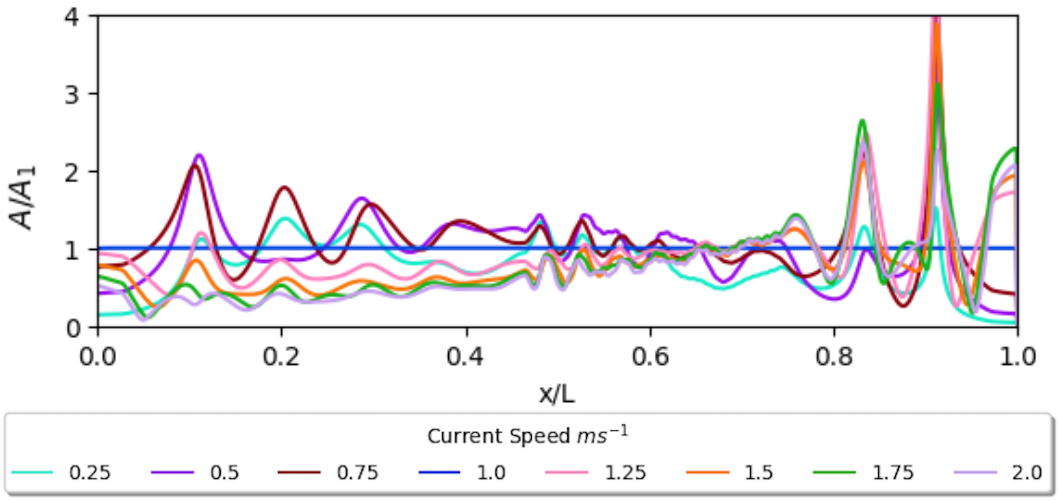

Figure 7-21: A normalised comparison of the influence of current speed on the RMS crossflow displacement for a current angle of 0 degrees for Guignier's cable

The general trend is that for a current angle of 0 degrees as the current speed increased RMS displacement towards the hang-off point decreased, shown in Figure 7-21. This can be attributed to the orientation of the cable relative to current, as the speed increased the orientation of the cable ended up becoming increasingly parallel to the direction of the flow. This resulted in a reduced normal relative velocity along this section. The RMS displacement towards the touchdown point was shown to increase with speed up to a speed of 1.25 m/s. After this speed the displacement was similar for all further increases.

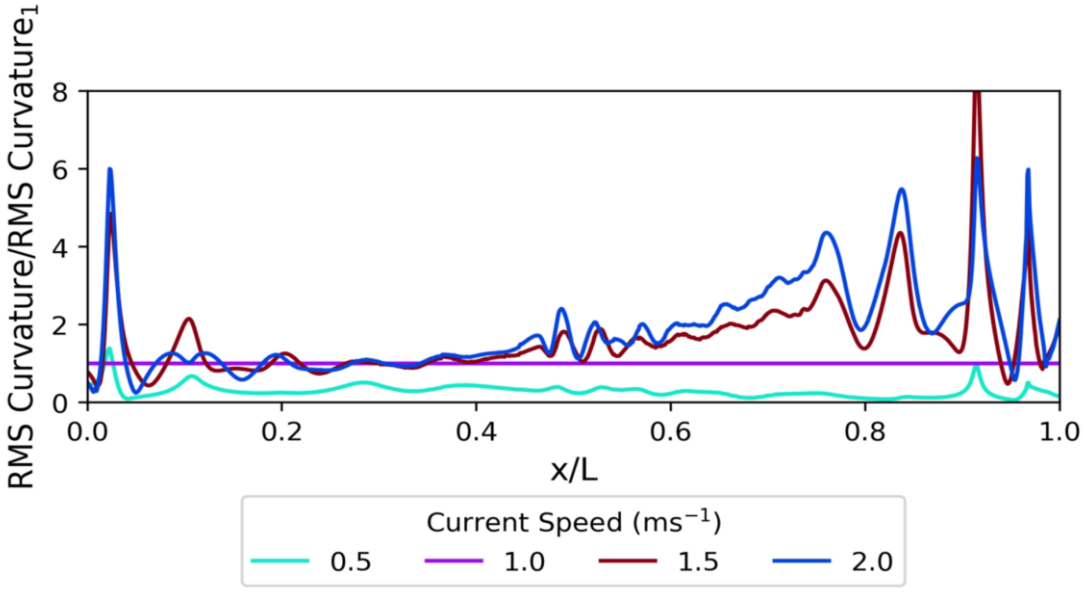

Figure 7-22: A normalised comparison of the influence of current speed on the RMS curvature for a current angle of 0 degrees for Substation cable

Figure 7-22 shows how the RMS curvature of the cable increased with current speed. This was especially prevalent at the touchdown section due to amplification of the relative velocity with greater

cable deformation as the current speed increased. When comparing this to the RMS crossflow displacement, the trend was similar with the maximum differences towards the touchdown, albeit at substantially different magnitudes.

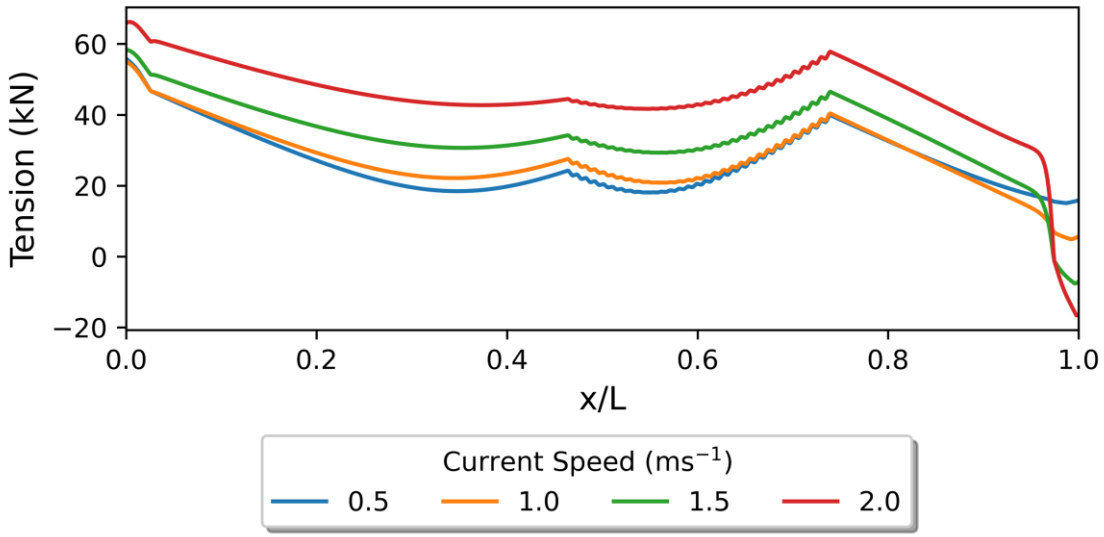

Figure 7-23: A comparison of the influence of current speed on the tension for a current angle of 0 degrees for Substation cable

The trend observed in Figure 7-23 was similar to both Flotant and Martinelli, where tension increased with current speed except at the touchdown section where compression could occur for the larger current speeds. *P* equalled 2.03, 0.253, 0.194, 0.360 for current speeds 0.5, 1.0, 1.5, 2.0 m/s respectively. The VIV behaviour for all current models accounted for the bending stiffness.

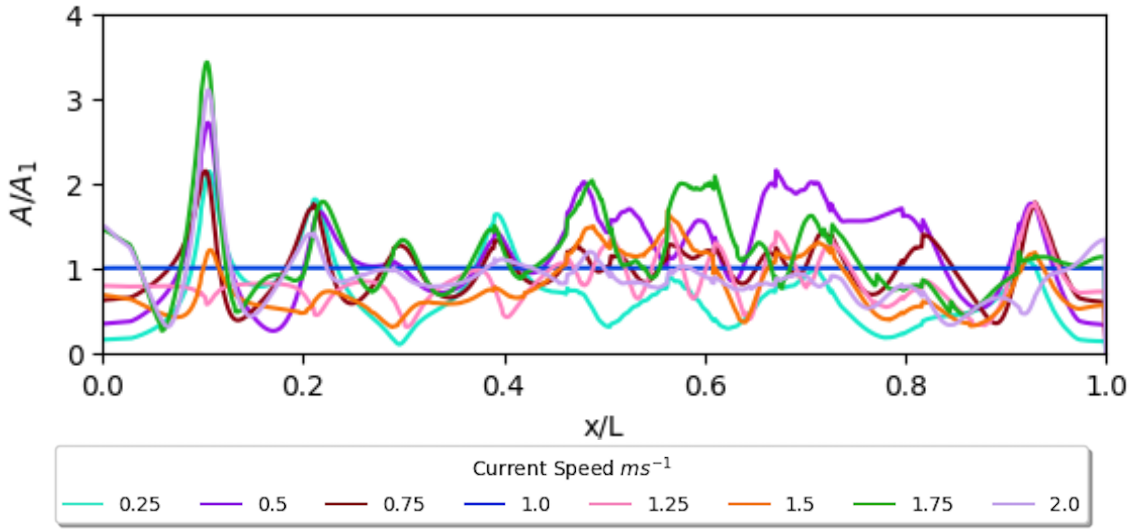

Figure 7-24: A normalised comparison of the influence of current speed on the RMS crossflow displacement for a current angle of 90 degrees for Guignier's cable

There was generally no obvious trends regarding displacement for a current angle of 90 degrees, as can be observed in Figure 7-24. All current speeds predicted a large amplitude for the RMS

displacement. The most obvious difference between current velocities was that as speed increased the mode of vibrations also increased. This is discussed in the following section.

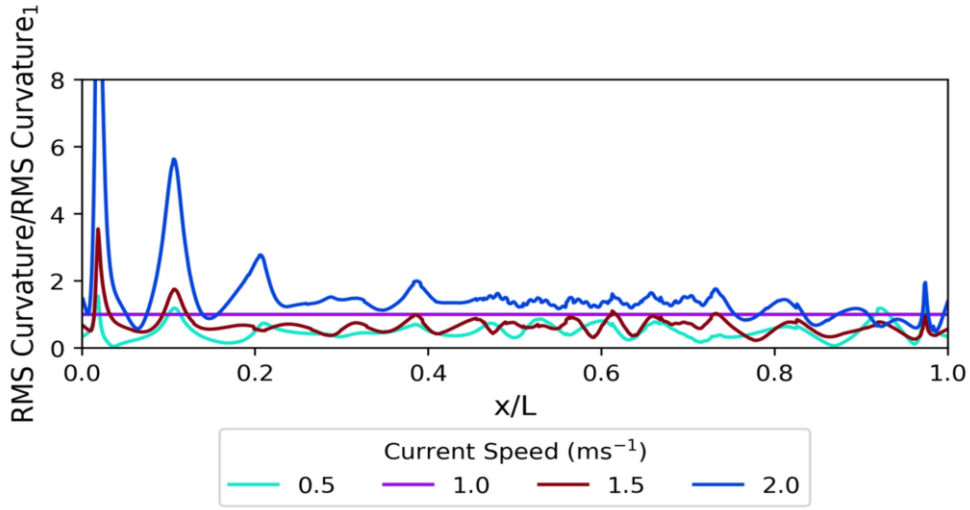

Figure 7-25: A normalised comparison of the influence of current speed on the RMS curvature for a current angle of 90 degrees for Substation cable

It can be observed in Figure 7-25 that there was no link between current speed and magnitude of RMS curvature. A speed of 2m/s does result in the largest RMS curvature, but this was followed by 1 m/s, then 1.5 m/s, and lastly 0.5 m/s. When comparing this to the RMS crossflow displacement, the behaviour was very similar over the cable length.

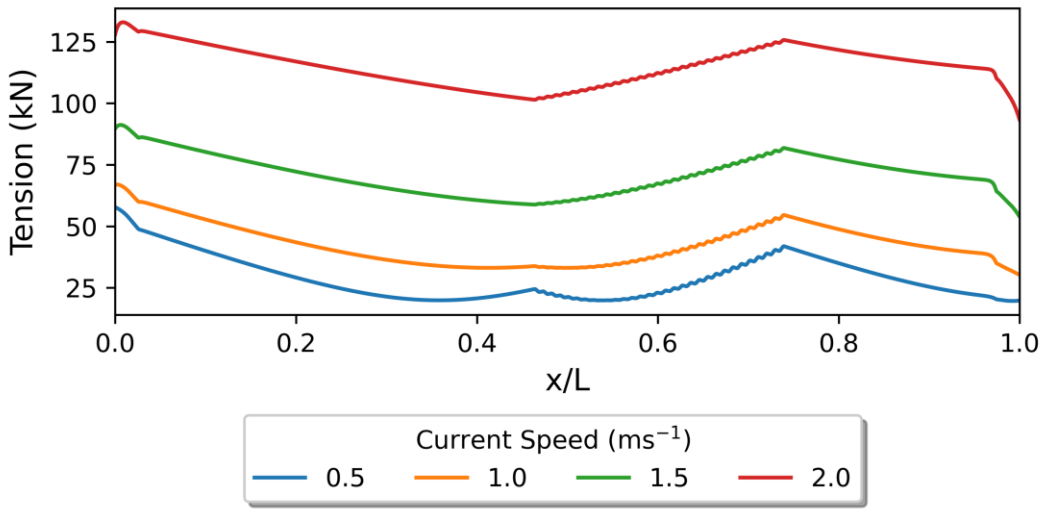

Figure 7-26: A comparison of the influence of current speed on the tension for a current angle of 90 degrees for Substation cable

There is a prevalent trend in Figure 7-26 where the greater the current speed the greater the tension. The tension profile with cable location was similar for all speeds. *P* equalled 2.96, 1.96, 2.54, 3.84 for current speeds 0.5, 1.0, 1.5, 2.0 m/s respectively. The VIV behaviour for all current speeds accounted for bending stiffness.

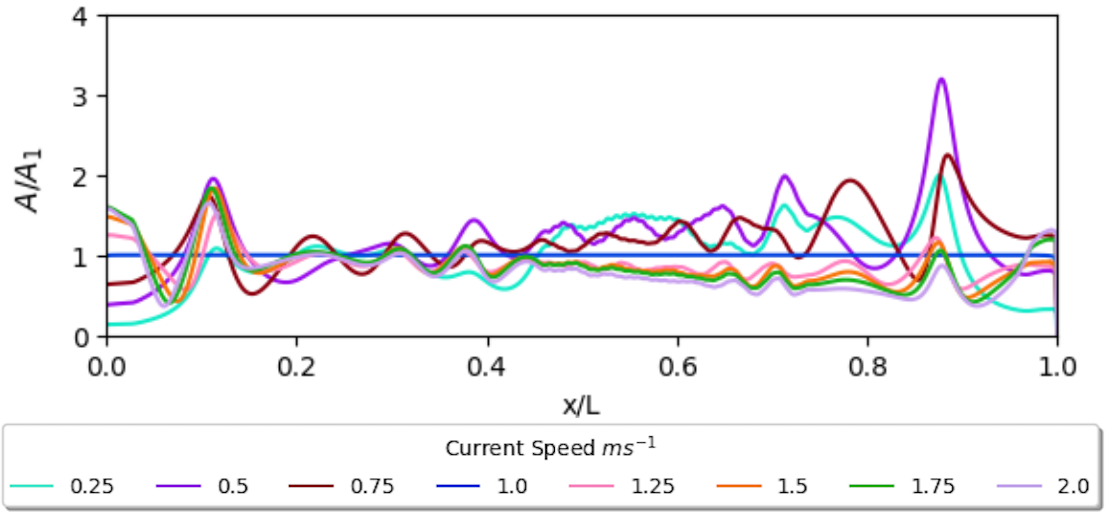

Figure 7-27: A normalised comparison of the influence of current speed on the RMS crossflow displacement for a current angle of 180 degrees for Guignier's cable

As current speed increases for a current angle of 180 degrees there are decreases in the RMS displacement towards the touchdown point, shown in Figure 7-27. The rate of the reduction in the amplitude of VIV at the touchdown section did decrease as the speed continued to increase but not to the same extent as for the other cables.

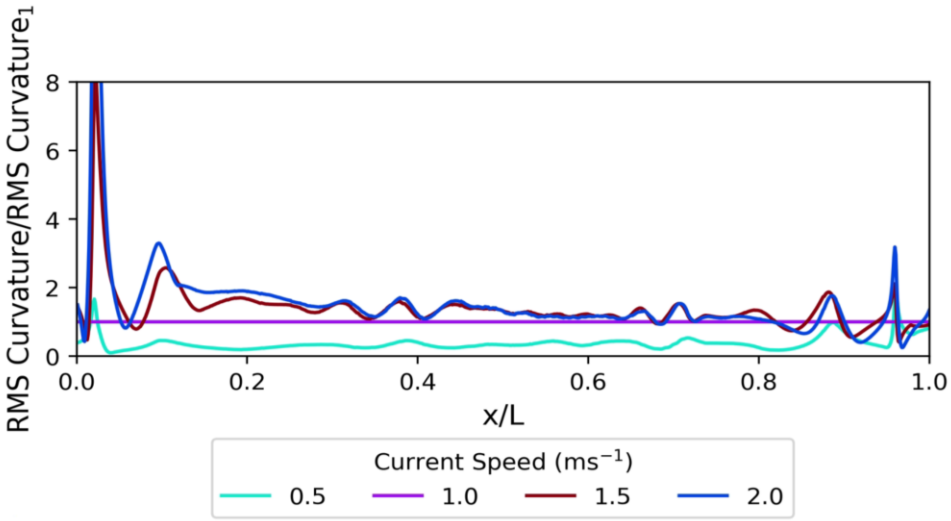

Figure 7-28: A normalised comparison of the influence of current speed on the RMS curvature for a current angle of 180 degrees for Substation cable

Figure 7-28 displays a trend where the larger the current speed the greater the RMS curvature. This behaviour was amplified at the hang-off point and the discrepancy between speeds greater than 0.5m/s decreased with cable length. This was due to cable deformation and the influence this had on the normal relative velocity. The greater the current speed the more pronounced the deformation. When comparing this to the RMSS crossflow displacement, both display similar trends where the largest current speeds peaked towards the hang-off point and decreased with cable length. However,

the peak for the crossflow displacement was smaller and the decrease larger relative to the normalised 1 m/s values compared to the RMS curvature behaviour.

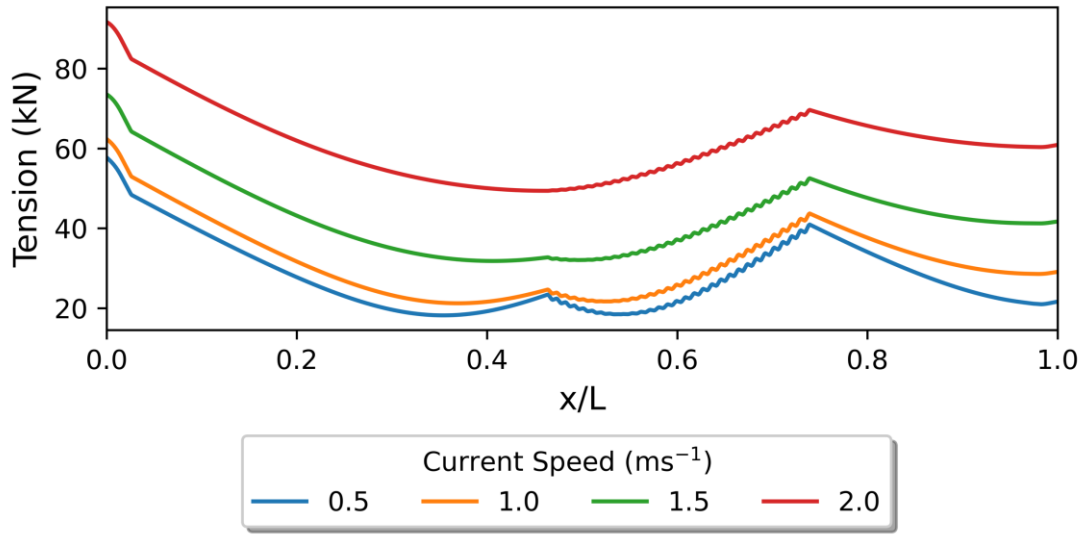

Figure 7-29: A comparison of the influence of current speed on the tension for a current angle of 180 degrees for Substation cable

The tension profiles in Figure 7-29 follow the expected trend of an increased magnitude with current speed. The profile changed with speed, the first peak was amplified at a current speed of 0.5 m/s. The amplification of this peak decreased as current speed increased. This was due to the increased drag forces and resultant cable deformation. *P* equalled 2.89, 1.27, 1.23, 1.49 for current speeds 0.5, 1.0, 1.5, 2.0 m/s respectively. For all current speeds the bending stiffness was important in determining the VIV behaviour.

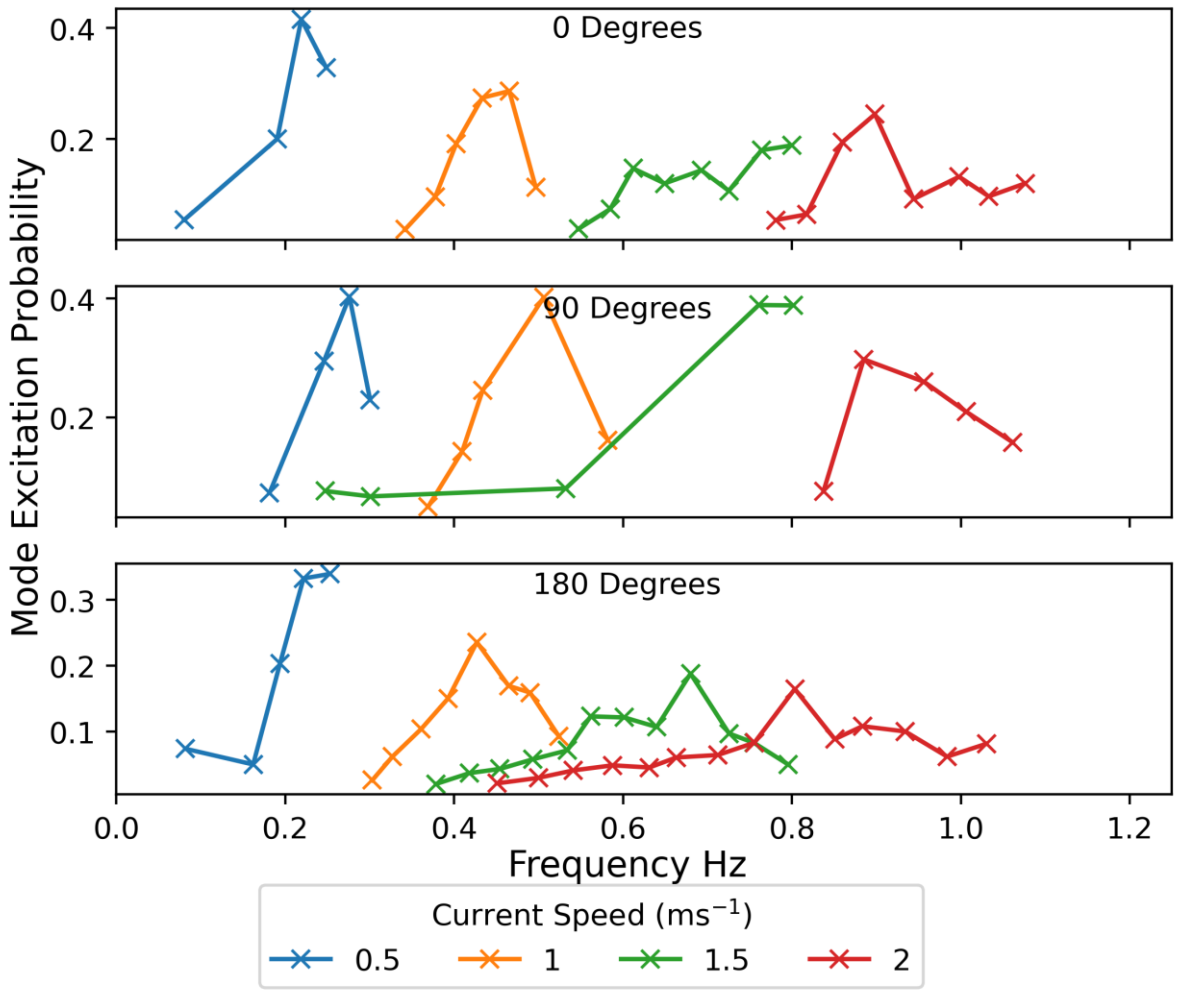

Figure 7-30: Comparison of the modal probabilities and corresponding frequency for different current speeds for Substation cable

Figure 7-30 shows the potentially excited modes over the cable length and the influence of current speed and angle. A current angle of 90 degrees predicts the fewest potential excitation modes for all current speeds. This was due to the incident current angle and the generally more uniform relative velocity over the cable's length. For current angles 0 and 180, due to the cable's shape and current flow direction, there are extreme variations from one cable section to the other. The current angle with the largest range of potentially excited modes was 180 degrees. For all current angles there was an obvious most probable excitation mode.

7.1.4 Frequency of Vibrations for a Uniform Current Profile

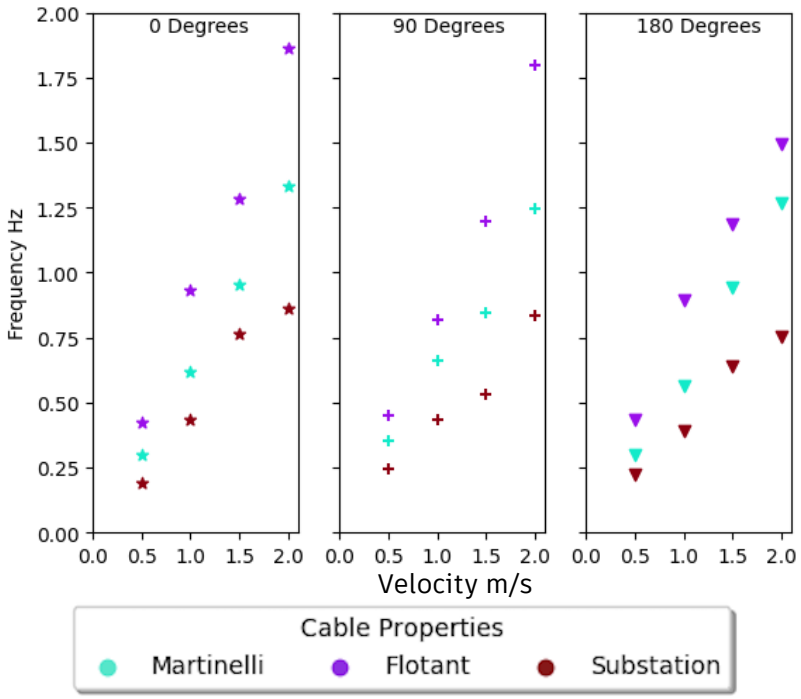

Figure 7-31: A comparison of the impact of the cable's properties on the vibration frequency

Generally, as is shown in Figure 7-31 there was a linear increase in frequency with current speed. There were some deviations from this trend, especially notable at larger current speeds. Flotant vibrated at the largest frequency, followed by Martinelli and then Substation. This was attributed to the difference in bending stiffness, mass ratio, and the diameter of the cable. Slight deviations from this pattern were due to cable deformation, discrepancies in mode number excitation, and multiple modes of vibration with similar probabilities of excitation. For Flotant's cable, a current angle of 180 degrees resulted in much lower frequencies compared to the other current angles. This wasn't seen for Martinelli or Substation.

7.2 0-360° CURRENT ANGLE

The impact of all current degrees from 0 - 360 was investigated for Martinelli, Flotant, and Substation cables. The conditions were a uniform current profile of 1m/s.

7.2.1.1 Martinelli

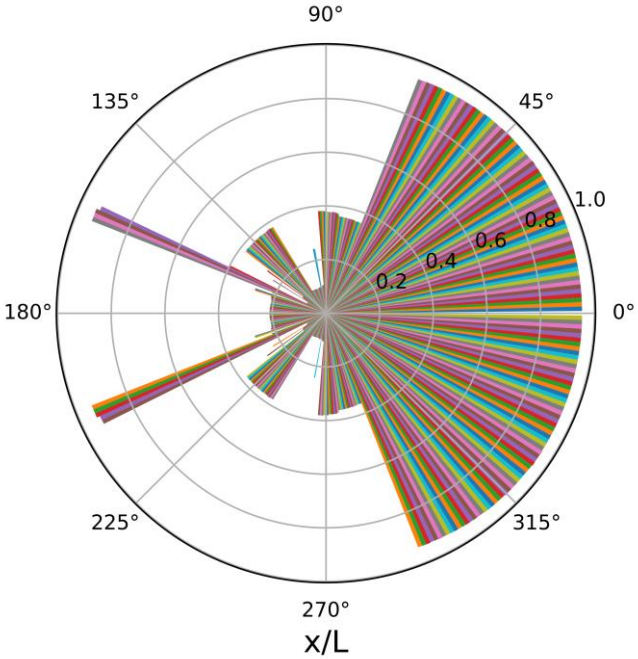

Figure 7-32: A plot comparing the location of the maximum RMS crossflow displacement along Martinelli's cable's length for every current degree from 0 - 360 for a uniform current of 1 m/s

The direction of current had a significant impact on the location of maximum displacement along the cable length, seen in Figure 7-32. For current angles less than 65 degrees the position of maximum displacement was predicted to be towards the touchdown point. For current angles greater than 65 degrees the location was towards the hang off point except, for a few outliers between angles 155 and 205 degrees.

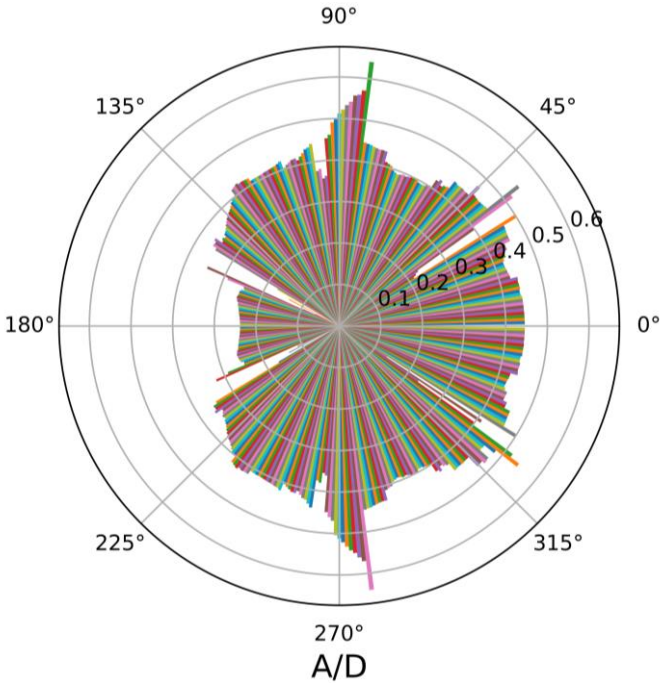

Figure 7-33: A plot comparing the amplitude of the maximum RMS crossflow displacement along Martinelli's cable's length for every current degree from 0 - 360 for a uniform current of 1 m/s

As is shown in Figure 7-33 the largest RMS displacement was observed at the current angles ranging from 80-90 degrees, where the relative current velocity was largest, and the impact of cable deformation was minimal. There were notable outliers at angles 30, 155, 205, and 330 degrees. These are attributed to difficulties in modelling the relative velocity at these sections and are a noted shortcoming of the modelling software. This shortcoming can be explained by Shear7 struggling to accurately capture the VIV behaviour for small angles of inclination. This behaviour was only prevalent at certain current angles due to a combination of both the cable deformation and the incident current angle impact on the relative velocity. This in turn altered the predicted excitation modes.

Discounting the outliers, outside of the 80-90 degrees range the RMS displacement was generally around 0.4 – 0.5 *A/D* for 0-150 degrees. From 155 to 180 degrees a decrease in displacement to around 0.25 *A/D* was seen. This was likely due to the cable deformation at this angle and the knock-on impact on the relative velocity resulting in smaller displacement predictions.

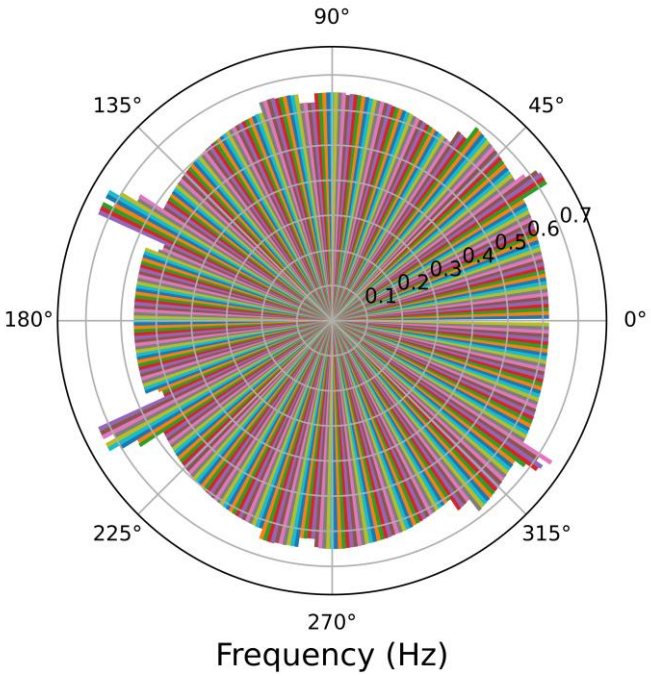

Figure 7-34: A plot comparing the most dominant frequency of vibration along Martinelli's cable's length for every current degree from 0 - 360 for a uniform current of 1 m/s

When analysing the frequency of vibrations, shown in Figure 7-34, there was not as strong a dependence on current direction as for the other parameters. The frequency for all angles fell within the range of 0.55 - 0.65 Hz. The current angle between 135-180 degrees did result in smaller frequency of vibrations, below 0.6 Hz, whereas the rest of the current angles were above this.

7.2.1.2 Flotant

When considering the influence of current direction on various outputs, Flotant's cable resulted in more definitively noticeable trends compared to Martinelli's cable.

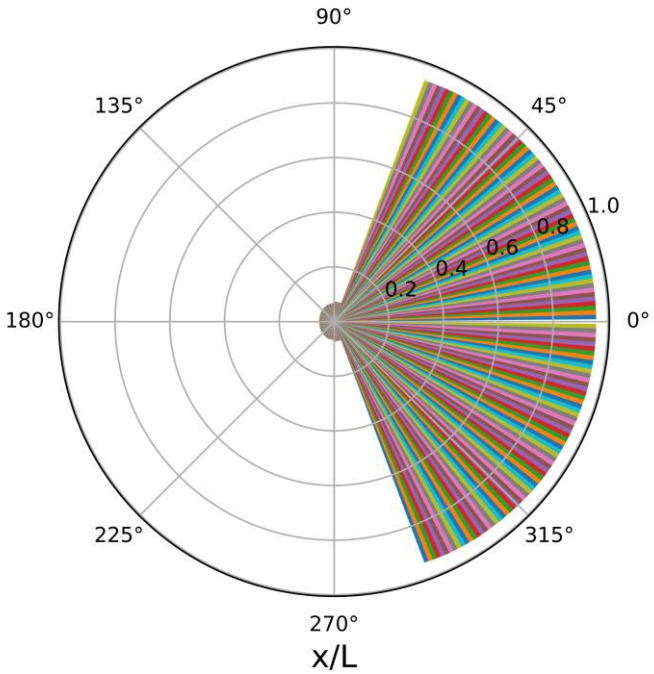

Figure 7-35: A plot comparing the location of the maximum RMS crossflow displacement along Flotant's cable's length for every current degree from 0 - 360 for a uniform current of 1 m/s

Regarding the location of maximum displacement along the cable length, for currents angles in range of 0 - 75 degrees the position of maximum displacement was located towards the touchdown point. This is shown in Figure 7-35. For current angles larger than 75 degrees the predicted location of maximum RMS displacement was located very close to the hang-off point. This was due to the cable orientation being significantly impacted by current direction and the induced deformation. The trend of location and dependency on current direction was consistent across all angles with no outliers observed.

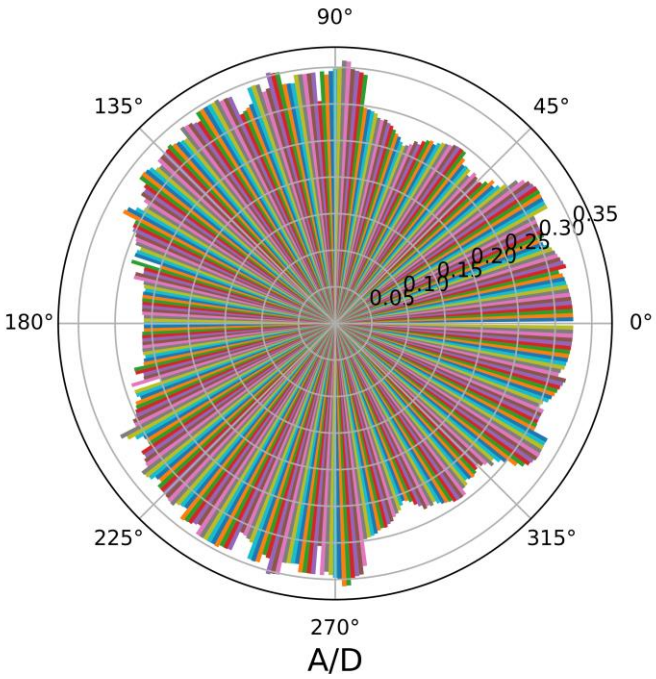

Figure 7-36: A plot comparing the amplitude of the maximum RMS crossflow displacement along Flotant's cable's length for every current degree from 0 - 360 for a uniform current of 1 m/s

The amplitude of maximum displacement was strongly impacted by the current angle, seen in Figure 7-36. The largest magnitudes of vibrations were observed between 90-150 degrees with a displacement just below 0.5 *A/D*. The lowest magnitudes of vibrations were observed at angles 165-180 and 40-80 degrees with displacements around 0.37 *A/D*. This was likely due to the normal relative velocity profile at these angles and was similar to the trend seen for Martinelli, except without the anomalous results.

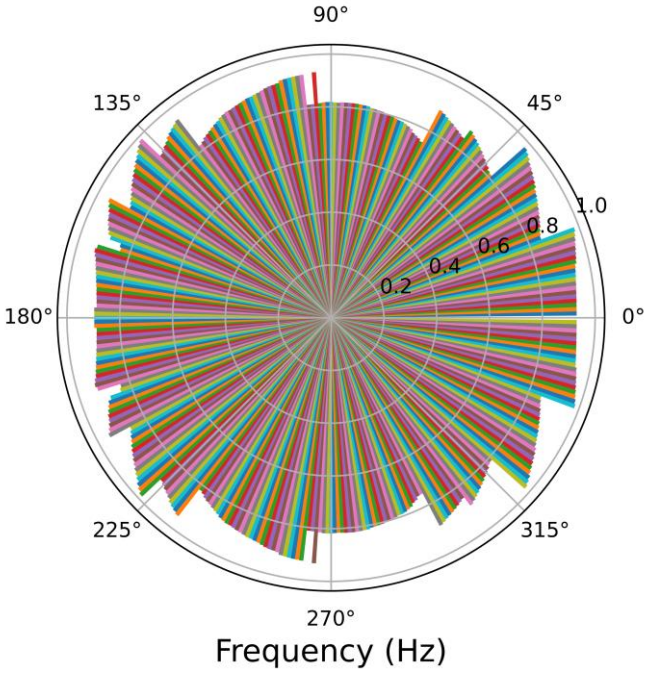

Figure 7-37: A plot comparing the most dominant frequency of vibration along Flotant's cable's length for every current degree from 0 - 360 for a uniform current of 1 m/s

The frequency of vibrations for Flotant cable varied with angle, shown in Figure 7-37. The magnitude of the frequency was within the range of 0.7 – 1.0 Hz for all the current angles. The lowest frequency was observed between 55 - 95 degrees with a value of around 0.8 Hz. There is no overarching obvious trend observed.

7.2.1.3 Substation

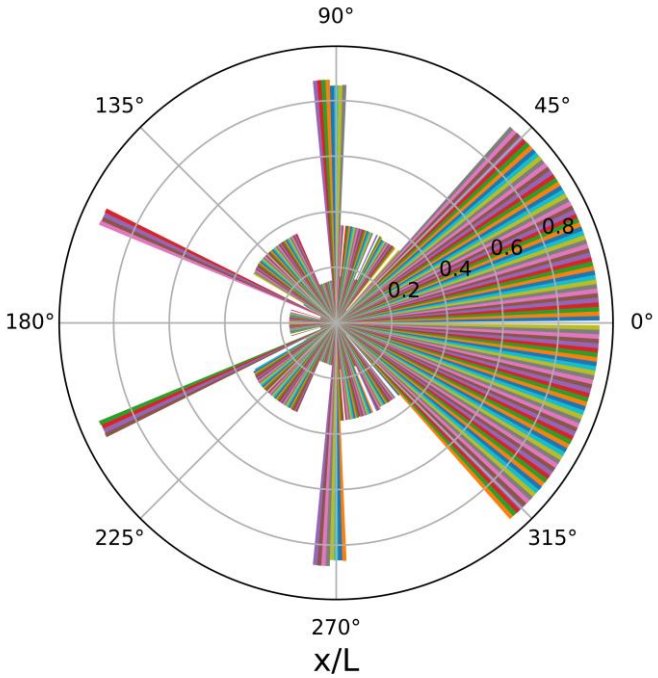

Figure 7-38: A plot comparing the location of the maximum RMS crossflow displacement along Guignier's cable's length for every current degree from 0 - 360 for a uniform current of 1 m/s

Substation cable similarly shows that the location of maximum displacement varied greatly depending on current direction, seen in Figure 7-38. From a current angle range of 0 - 50 degrees the location of the greatest displacement was towards the touchdown point. After this, excluding the 85 - 95 and 155 - 160 degree ranges, the largest displacements were seen towards the hang-off point. Substation was the largest and heaviest cable and as such was the least susceptible to deformation. This lack of deformation generally meant that less extreme variations in displacement were seen over the cable length. This was likely responsible for changes in location of maximum displacement at certain angles, unlike Flotant which follows a much more obvious trend.

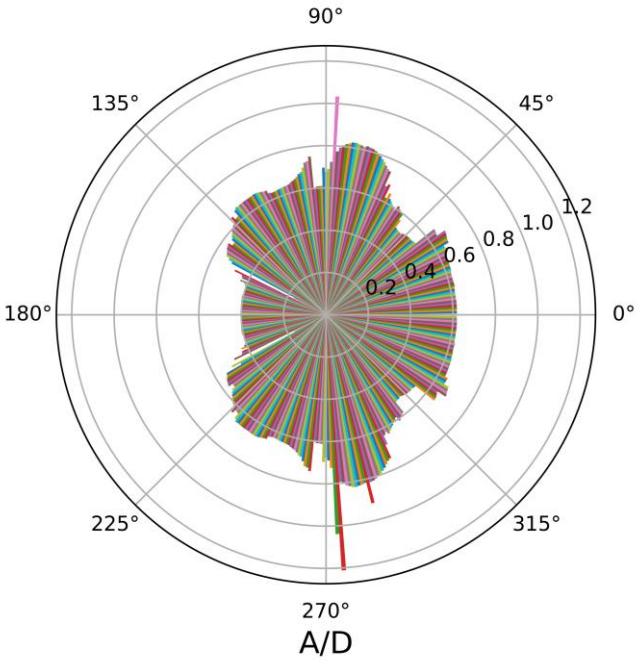

Figure 7-39: A plot comparing the amplitude of the maximum RMS crossflow displacement along Guignier's cable's length for every current degree from 0 - 360 for a uniform current of 1 m/s

Regarding the maximum RMS displacement, shown in Figure 7-39, the current angle was shown to greatly influence the magnitude. The *A/D* between angles 0-40 degrees was around 0.45 before dropping to 0.35*A/D* from 40-50 degrees. After this, it significantly increased to over 0.6 A/D up to 85 degrees. The maximum amplitude then was 0.45 until 135 degrees where it reduced as the angle increased to a low of 0.3 at 180 degrees. There are multiple anomalous results seen in Figure 7-39, for example, current angles 155 and 87 degrees. This has been noted before for Martinelli's cable.

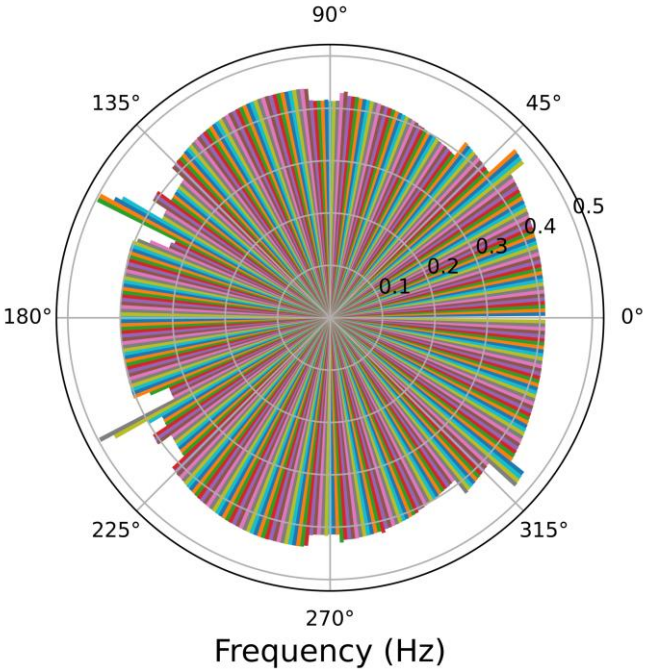

Figure 7-40: A plot comparing the most dominant frequency of vibration along Guignier's cable's length for every current degree from 0 - 360 for a uniform current of 1 m/s

For Substation cable, the variation in frequency over all current angles was the lowest out of all the cables, highlighted in Figure 7-40. The vast majority of frequencies were contained within the range from 0.4 – 0.45 Hz. This was likely due to the reduction in deformation compared to the other cables meaning large variations in relative velocity over the cable length were reduced.

7.3 Shear Current Profile

Five different current profiles (see Figure 3-20) were investigated to determine the influence they have on the RMS crossflow displacement and the frequency of vibrations. The cable used in this study was Martinelli and a sea surface current speed of 1 m/s was chosen. Shear7 reported multiple different modes of vibrations along the cable. To allow for comparison, initially, the most probable excitation mode was compared. To better understand the influence and range of vibration frequencies over the cable length, these were compared separately.

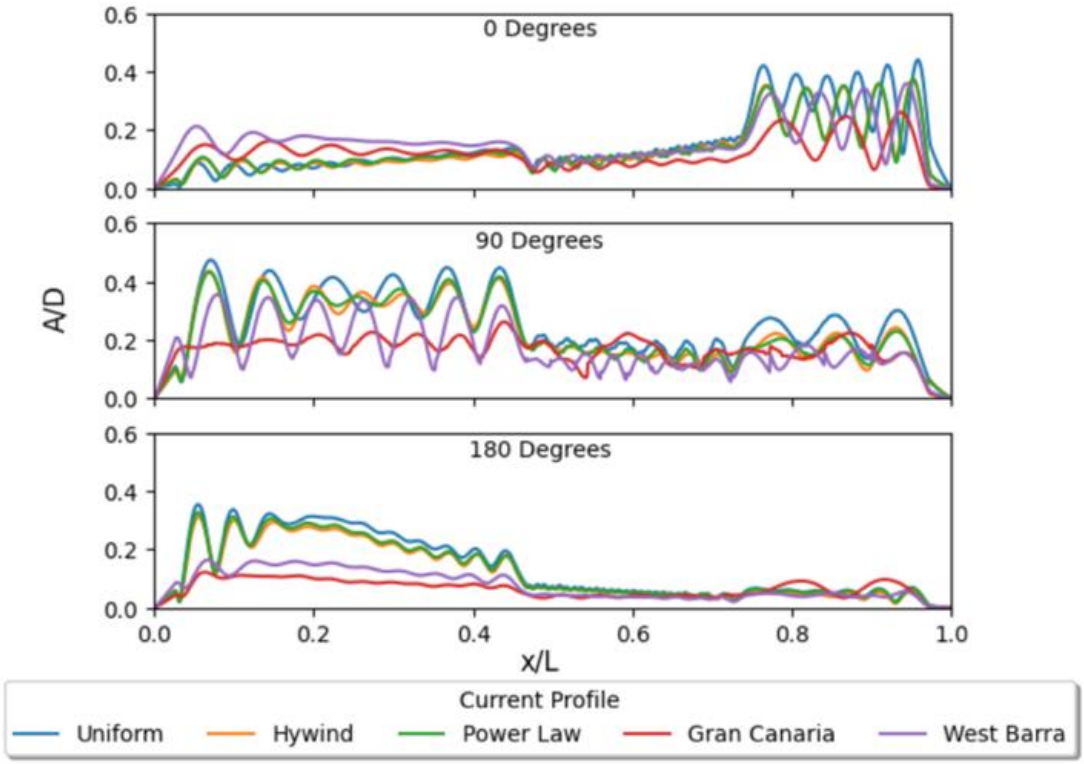

Figure 7-41: A comparison of the RMS crossflow displacement for different current profiles assuming a sea surface speed of 1 m/s

Figure 7-41 shows how significant an influence the current profile had on the amplitude of vibrations. This is important as different sites can have substantially different current profiles, meaning, certain locations may require additional suppression techniques to reduce VIV.

When considering VIV along the hang-off section, current profiles Hywind and Power Law resulted in a similar displacement profile to the uniform profile. This was due to the similar relative velocities at

this section. West Barra and Gran Canaria, however, were substantially different, with Gran Canaria deviating the most. This was due to both the reduced cable deflection and also the lower relative velocity impacting VIV behaviour at the hang-off point.

For a current angle of 0 degrees, all current profiles resulted in the largest RMS displacement observed over the full cable length being towards the touchdown section, highlighting even for highly sheared flows there was still a notable location susceptible to larger vibrations. A uniform profile resulted in a significantly larger displacement at the touchdown compared to any other current profile. Over the full cable length, reductions in amplitude observed compared to the uniform profile were: 13% Hywind, 12% Power Law, 20% Gran Canaria and an increase in 7% for West Barra. The West Barra result was out of keeping with this trend due to excitation of low modes.

Hywind, Power Law, and Uniform current profiles had similar VIV displacement profiles for a current angle of 90 degrees. The current profiles most significantly deviated from one another towards the touchdown section. West Barra and Gran Canaria showed much smaller amplitudes of displacement than the other current profiles. Over the full cable length, the reductions in amplitude observed were 12% Hywind, 11% Power Law, 34% Gran Canaria and 32% for West Barra. The reductions in amplitude were due to the shear current profiles producing lower relative velocity along the cable length. Cable deformation had a smaller influence for this current angle than for either a current angle of 0 or 180 degrees.

For a current angle of 180 degrees the largest vibrations for all current profiles were observed towards the hang-off point. The current profiles Uniform, Power Law, and Hywind all resulted in similar RMS displacement over the full cable length to each other. Gran Canaria and West Barra again deviated, the predicted displacement was substantially lower at the hang-off point, but the variation over the full cable length was much smaller. This was due to these current profiles resulting in substantially less cable deflection, and thus less extreme differences in relative velocity over the cable length, compared to the other current profiles. Over the full cable length reductions in amplitude observed were 12% Hywind, 8% Power Law, 51% Gran Canaria and 44% for West Barra compared to a uniform current profile.

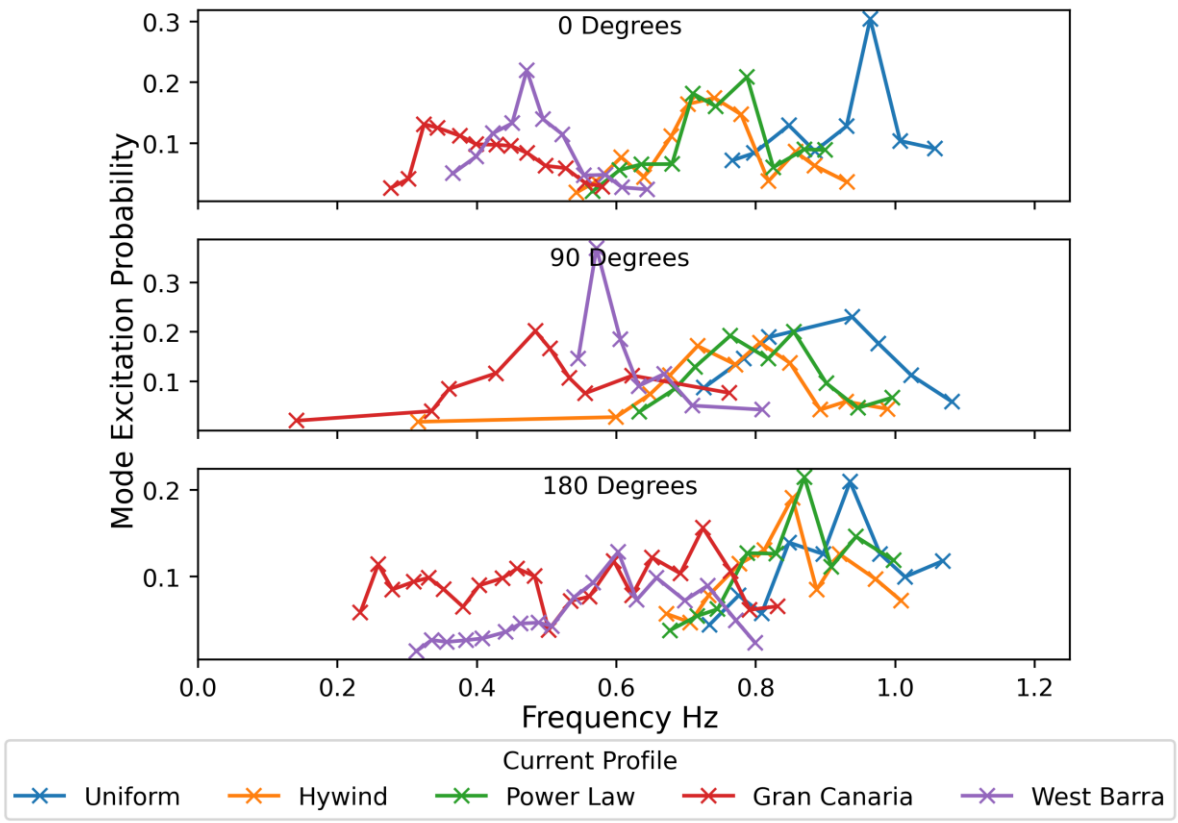

Figure 7-42: A comparison of the mode excitation probability and frequency of vibration for different current profiles assuming a sea surface speed of 1 m/s

When comparing the mode excitation probabilities shown in Figure 7-42, all current angles and profiles resulted in the excitation of numerous modes. There is a general trend over all angles where a uniform profile resulted in the largest excitation modes. For a current angle of 0 degrees, there was an obvious most probable frequency of vibration for all current profiles. The most probable excitation frequency wasn't as prominent for an angle of 90 degrees with a wider range of similarly probable excitation modes. The maximum probable excitation frequency was not as sharply defined with a more gradual increase. A current angle of 180 degrees exhibited similar behaviour to the angle of 90 degrees, however, for the current profiles of Gran Canaria and West Barra the range of possible excitation modes was substantially larger than for the other angles. In addition, the maximum excitation probability was not as prominent

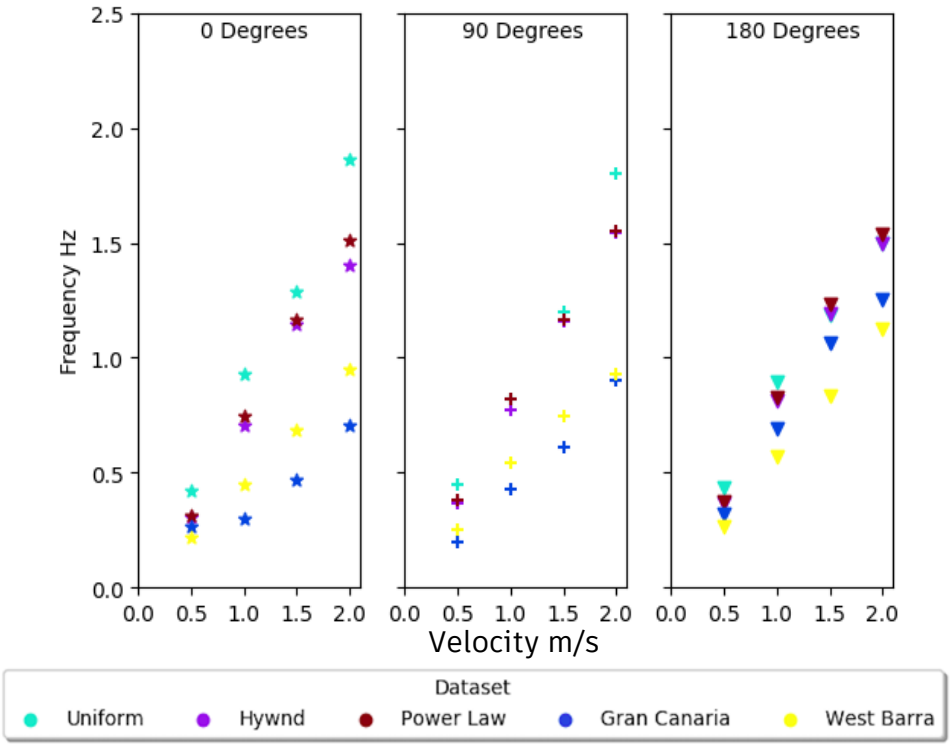

Figure 7-43: A comparison of the vibration frequency for different current profiles assuming a sea surface speed of 1 m/s

The frequency of vibrations for the different current profiles are shown in Figure 7-43. The general trend was that the current profiles with the larger relative velocity over the full cable length resulted in higher frequency of vibrations, this trend was clearly shown for current angles 0 and 90 degrees. The uniform profile resulted in the greatest frequency, followed by the power law profile, very closely followed by the Hywind profile, followed by the West Barra profile and lastly by the Gran Canaria profile.

However, the current angle of 180 degrees deviated from this trend, there was less discrepancy between the frequency of vibrations for all current profiles. The previously seen trend was not as obviously defined. It was predicted this was likely due to the frequency of vibrations being dominated by the upper most section of the cable for which Uniform, Hywind and Power Law have very similar profiles. When considering the other profiles West Barra had a lower relative velocity along this section compared to Gran Canaria. A current angle of 180 degrees resulted in the smallest frequency of vibrations compared to the other current angles for the uniform profile, but larger for Gran Canaria and West Barra, and similar for Hywind and Shear Power Law profiles. This tighter grouping exemplifies the smaller dependency on current profile at this current angle.

7.4 CONCLUSION

The variations in current parameters to which the power cable was exposed to are shown to greatly influence the VIV behaviour. The current speed, direction, and shear profile were the parameters investigated and their impact on the RMS crossflow displacement, frequency of vibrations, and the location of maximum displacement along the cable length studied.

When comparing the impact of a shear current profile against a uniform current profile reductions in RMS displacement were consistently observed. For a current angle of 0 degrees, changing from a uniform current profile resulted in reductions of: 13% Hywind profile, 12% Power Law profile, 20% Gran Canaria profile, and an increase in 7% for West Barra profile. The West Barra result was out of keeping with this trend due to the excitation of low high displacement modes. For a current angle of 90 degrees reductions of: 12% Hywind profile, 11% Power Law profile, 34% Gran Canaria profile, and 32% for West Barra profile were seen. For a current angle of 180 degrees the reductions observed were: 12% Hywind profile, 8% Power Law profile, 51% Gran Canaria profile, and 44% for West Barra profile. For current angles of 0 and 90 degrees the reductions in amplitude were most significant towards the touchdown point, where the greatest difference in current speed between shear and uniform profiles was observed. For 180 degrees the greatest differences in RMS displacement were at the hang-off point, where the largest amplitude of vibration was seen for this angle. The discrepancy here was likely due to the shear profile not resulting in as large cable deformation, most impactfully along the lower section. This means that the top section towards the hang-off point wasn't displaced too such a large degree as for the uniform current. In turn, resulting in a lower relative velocity compared to the less sheared current profiles.

When comparing the influence of current angle, substantially different RMS crossflow displacement profiles along the cable length were observed. This was due to the changes in the normal relative velocity along the cable length. It was difficult to quantify this impact in terms of discrepancies in the overall magnitude of RMS displacement, instead, it was chosen to focus on the location of maximum displacement along the cable length, highlighting the impact of the angle of the current. For a uniform current profile, a current angle of 0 degrees saw the largest displacement towards the touchdown point, 90% along the cable length. A current angle of 90 degrees had the largest displacement towards the hang-off point, 10% along the cable length. A current angle of 180 degrees had the largest displacement approximately 5% from the hang-off point. These large variations in location were due to the deformation of the cable which altered the angle of inclination and allowed extreme and localised vibrations of large amplitude at certain locations along the cable length.

When analysing the effect of current speed, the most notable observations are that there was an almost linear increase in the frequency of vibrations with current speed, and the greater the current speed the more localised the largest RMS displacement was to a certain section along the cable. The increase in frequency expectedly occurred due to higher mode excitation which occurred with greater relative velocity. The increased localisation of large displacements was noted to be due to more substantial deformation of the cable occurring as the current speed increased. This in turn altered the normal relative velocity profile along the cable length resulting in certain sections being exposed to much greater values than others.

8 RESULTS AND DISCUSSION – CABLE CONFIGURATION

8.1 DIFFERENT CABLE CONFIGURATIONS

Additional cable configurations were investigated to determine the influence this had on the VIV behaviour. The cable layouts were taken from Flotant's project sites at Gran Canaria and West Barra (Oud et al., 2021), and a double wave configuration from Guignier (Guignier et al., 2020b). These configurations were a tethered steep wave at Gran Canaria, Figure 2-4, a steep wave at West Barra, Figure 2-6, and a double wave for Guignier, Figure 2-5. Gran Canaria is a deep-water site (250 m) using a 460m cable length and a lower maximum current speed compared to West Barra which is a shallower water site (100 m) with faster currents with cable length 200m. The Gran Canaria cable was deemed unsuitable to use at the West Barra site because it is very light and subjected to too large deformation resulting in compression at touchdown point. Guignier is a 100m deep site with a 366m long cable. The properties for these cables are shown in the methodology section in Table 3-3.

The current profiles scaled for 107m water depth are shown in Figure 8-1.

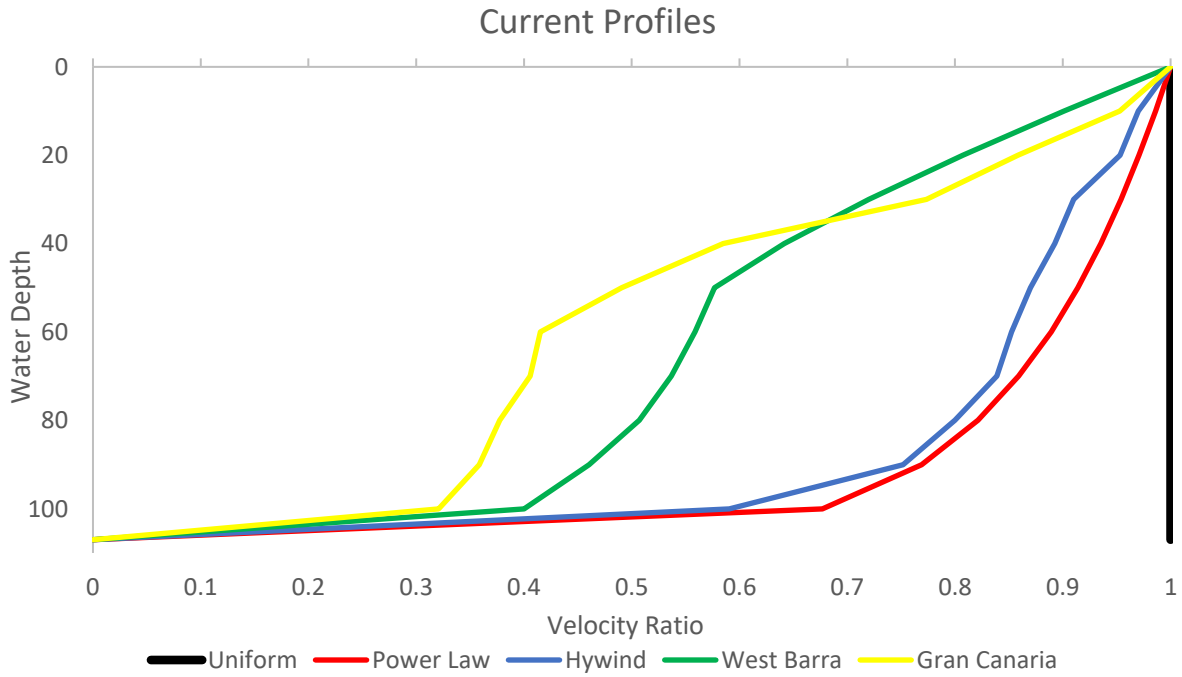

Figure 8-1: Comparison of the current profiles investigated against water depth

The current profiles are not smooth due to the site data availability. For Hywind there was only current measured at 5 depths over 107m, West Barra and Gran Canaria have measurements for every 10 metres of water depth. West Barra measurements extend to a depth of 90m and Gran Canaria 240m. This is shown in Table 3-4. Due to the large distances between the data points substantial extrapolation was required resulting in the uneven profiles observed.

8.1.1 Gran Canaria Tethered

8.1.1.1 Sheared Current Profile

The plots below are for the Gran Canaria site, with the relevant sheared current profile and water depth from measured site conditions. The cable used for Gran Canaria was the same as the Flotant cable. The current speed scaling factor operated as such, a factor of 1 represents the maximum 50-year current conditions from the site. This is shown in Table 3-4.

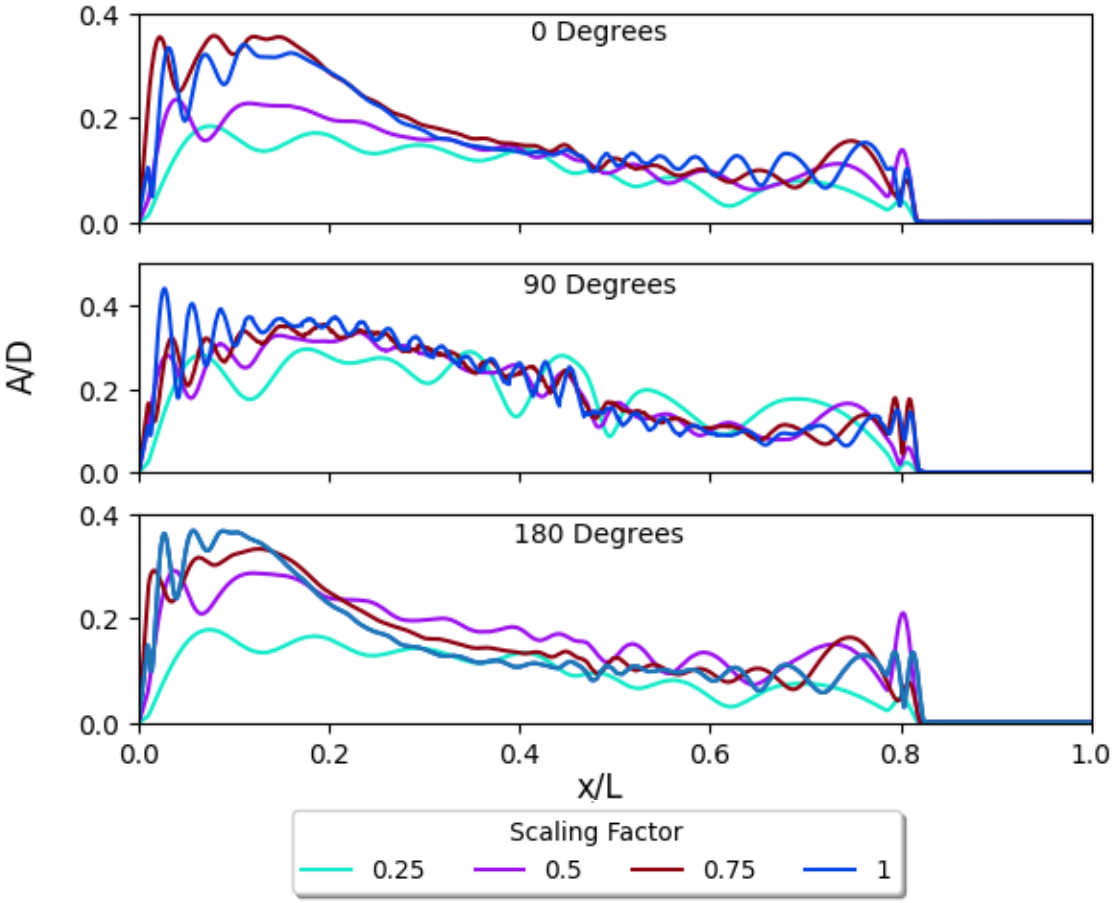

Figure 8-2: A comparison of the RMS crossflow displacement for changing current angles and speeds for a tethered lazy wave configuration for a shear current profile

Figure 8-2 shows that the VIV behaviour for a tethered lazy wave was dependent on current direction, but less so compared to the previous lazy wave configuration. There was no displacement from 0.8 – 1.0 *x/L* because the cable was resting along the seabed at this point. The displacement towards the hang-off point was larger than the touchdown point for all current directions and speeds. This was different from the other configurations where extreme variations were observed between hang-off and touchdown point depending on the current direction. A current angle of 90 degrees resulted in the largest RMS displacement over the cable length, which was due to the plane of the cable being normal relative to current direction. The difference between angle 0 and 180 degrees was minimal. This differed hugely from the lazy wave configuration where for these current angles almost opposite

displacement profiles are seen. The introduction of a tether severely limited the cable deformation at the hang-off point, meaning there was a reduction in the variation in the normal relative velocity over the cable's length. There was a common trend for all current angles, where, with increased depth and length along the cable the RMS displacement decreased. This was partly due to the shear current profile as well as the cable configuration.

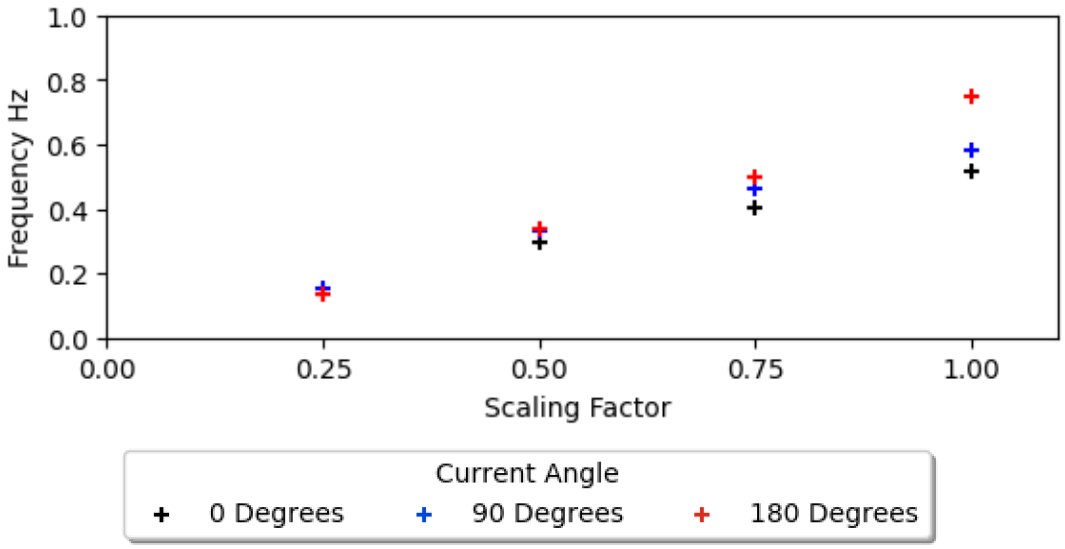

Figure 8-3: A comparison of the impact of the shear current speed and direction on the vibration frequency for a tethered lazy wave

There is a notable trend observed where a current angle of 180 degrees resulted in the greatest frequency followed by 90 degrees, and lastly by 0 degrees, shown in Figure 8-3. Despite the similar crossflow displacement profiles, the angle of inclination of the cable relative to the current flow had an influence on the excitation of higher modes of vibration. For a current angle of 180 degrees the, limited but still relevant, deformation of the cable resulted in greatest relative velocity towards the hang-off point and hence the larger frequency of vibration. A current angle of 90 degrees was less influenced by cable deformation as the full cable length experienced large relative normal velocity and wasn't influenced as significantly by the angles of inclination. A current angle of 0 degrees resulted in the lowest frequency vibration due to the shear current profile and the limitations to cable deformation because of the tether preventing excessive bending.

8.1.2 Uniform

The Flotant power cable was calibrated to be deployed at deep water sites with low current speed and was noted to struggle in higher current velocities. The tethered lazy wave cable configuration was also noted to not operate within required safety constraints for larger current speeds. The results below are unrealistic since both cable choice and configuration would not be chosen for any site with such environmental conditions.

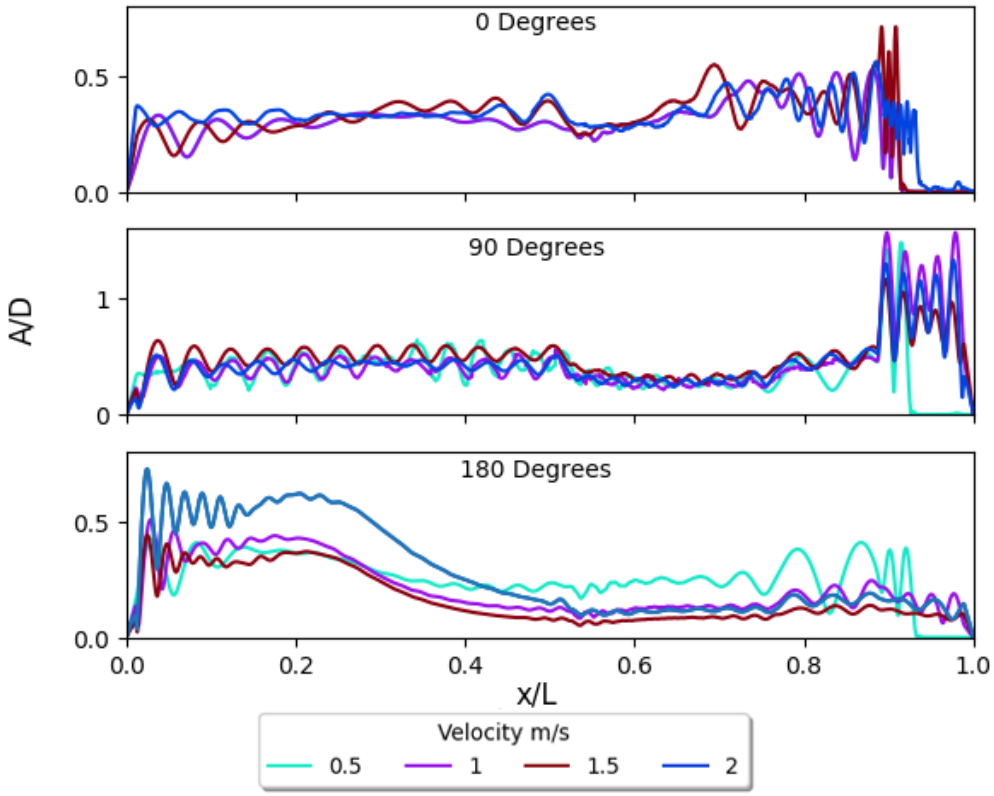

Figure 8-4: A comparison of the RMS crossflow displacement for a tethered lazy wave configuration and varying current speeds for a uniform current profile

The reason for such large RMS displacement towards the touchdown point was due to the uniform current profile resulting in much larger velocities towards the seabed than the site measured shear current profile. This allowed the section of the cable that was previously resting along the seabed to become excited and taught. This resulted in the vibrations seen from 0.8 – 1 *x/L* where they weren't observed previously, as can be seen in Figure 8-4. This in turn influenced the VIV behaviour of the full cable length. In reality this situation should not occur, the cable has already been noted as unsuitable for site conditions with such large current velocities.

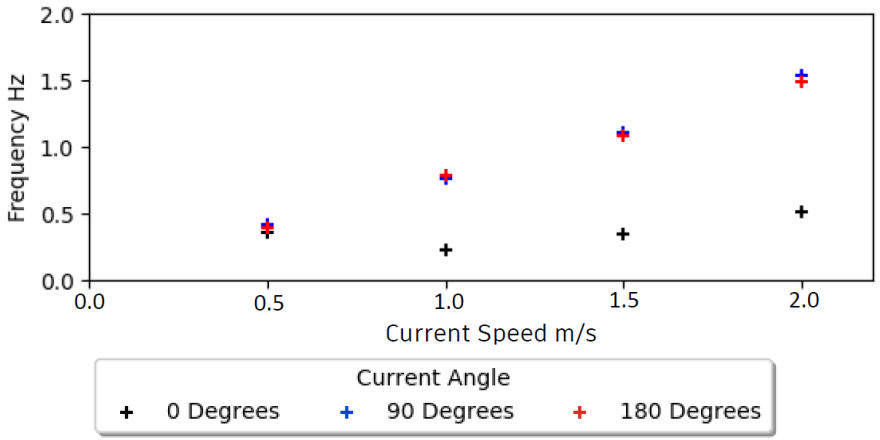

Figure 8-5: A comparison of the impact of the current speed and direction on the vibration frequency for a tethered lazy wave

The frequencies of vibrations predicted were within a similar range for all current angles, shown in

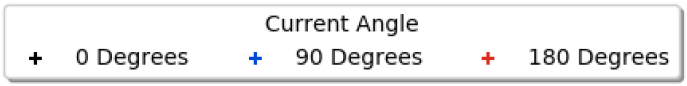

Figure 8-5. A general trend emerges where a current angle of 180 degrees resulted in the lowest predicted frequency, and an angle of 0 the largest. This was the opposite trend as seen for the shear current profile. This highlights the sensitivity of the VIV behaviour to the current profile; a uniform current profile allowed for substantial vibration and cable deflection at the touchdown point whereas the site measured shear current profile didn't.

8.2 West of Barra

The site conditions for the West of Barra were such that the current speed was much greater compared to Gran Canaria. The exact difference is shown in Table 3-4. The configuration chosen was a steep wave with no tether. The current profile is shown in Figure 8-1. The current speed scaling factor operated as such, a factor of 1 represents the maximum 50-year current conditions from the site and is shown in Table 3-4.

8.2.1 Shear Current Profile

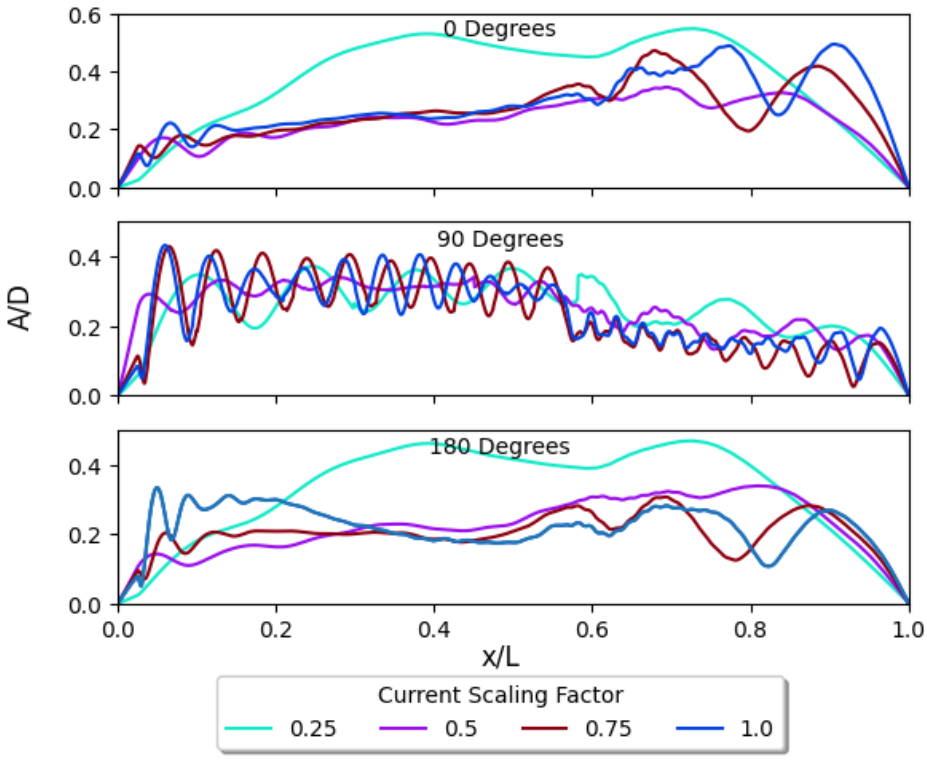

Figure 8-6: A comparison of the RMS crossflow displacement for a steep wave configuration and varying current speeds for a shear current profile

The current speed had a substantial impact on the VIV behaviour, this is highlighted in Figure 8-6. For both angles 0 and 180 degrees at a scaling factor speed of 0.25, the displacement profile was very similar, albeit at different magnitudes. Both these angles experienced low mode VIV excitation. This was likely due to such a low current speed not resulting in any relevant cable deformation, and thus, the relative velocity was similar for both current angles.

As the current speed increased, the RMS displacement profile for angles 0 and 180 began to diverge. For a current angle of 0 degrees a general trend was seen where the largest amplitude of vibrations were towards the touchdown point. This was noted to be due to cable deformation resulting in greater relative velocity at this point and thus greater VIV excitation. As the current speed increased the location of maximum displacement shifted closer to the touchdown point.

For a current angle of 180 degrees a different trend was seen. It didn't exemplify the previously observed trend for a lazy wave configuration where the largest displacement was constrained towards the hang-off point with, relatively, much smaller displacement seen at the touchdown section. This was likely due to the steep wave configuration being constrained so that it was unable to deform to such an extent as the lazy wave configuration, so extreme amplitude discrepancies at the hang-off point relative to the touchdown section didn't occur.

As expected, a current angle of 90 degrees didn't exhibit the same RMS displacement profile at the lower current speeds as the other current angles. This was because the current angle was perpendicular to the spatial plane where the cable was initially located before any deformation occurred. This meant the cable was exposed to a greater relative velocity and higher mode VIV excitation occurred. For a current angle of 90 degrees, the largest vibrations along the cable length were observed at the section extending from the hang-off point to the cable mid-point (0.5 *x/L*), after this a steady decrease in displacement occurred. This trend was likely due to the shear current profile reducing the relative velocity and the VIV interference from the buoyancy modules.

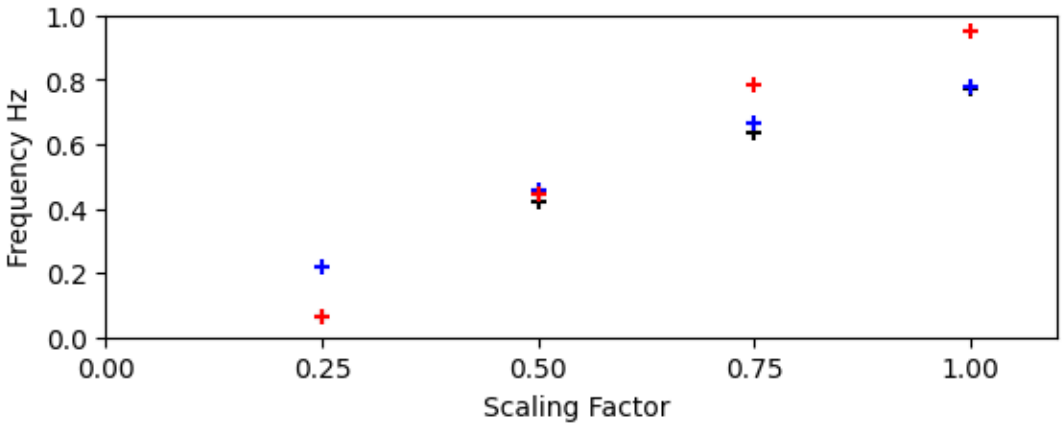

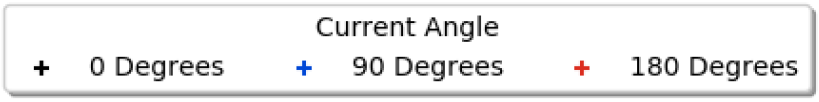

Figure 8-7: A comparison of the impact of the current speed and direction on the vibration frequency for a steep wave and shear current profile

When comparing the frequency of vibration shown in Figure 8-7, at a scaling factor of 0.25 a current angle of 90 degrees resulted in a frequency of vibration up to four times larger than the other current angles. This was previously noted to be due to the angle of inclination resulting in low mode VIV excitation for current angles 0 and 180 degrees. For a scaling factor of 0.5 similar, frequency was seen for all current angles. As current speed increased past this point a current angles of 180 degrees resulted in sizeably larger frequencies of vibration compared to angles 0 and 90, which resulted in similar frequencies of excitation.

8.2.2 Uniform Current Profile

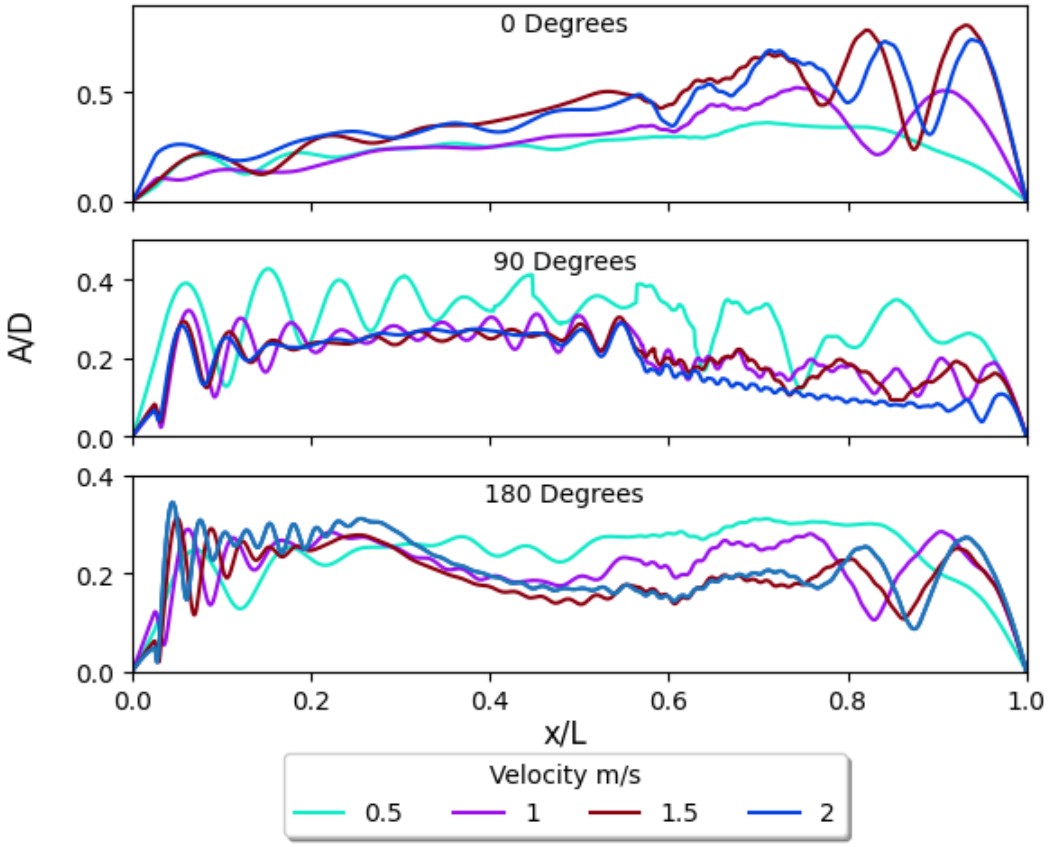

Figure 8-8: A comparison of the RMS crossflow displacement for a steep wave configuration and varying current speeds for a uniform current profile

When observing the RMS displacement in Figure 8-8 and comparing this to Figure 8-6 it can be seen that both the overall profiles were similar, even if different magnitudes of displacement were seen. The variation in displacement along the cable length was increased for current angles 0 and 180 degrees compared to the shear current profile. This was most notable for 180 degrees, where

previously the vibrations at the hang-off point were smaller until a large scaling factor was reached. The reasoning for the difference in the uniform current profile response was that greater deformation occurred over the full cable length and the current speed was larger than for the sheared profile site conditions.

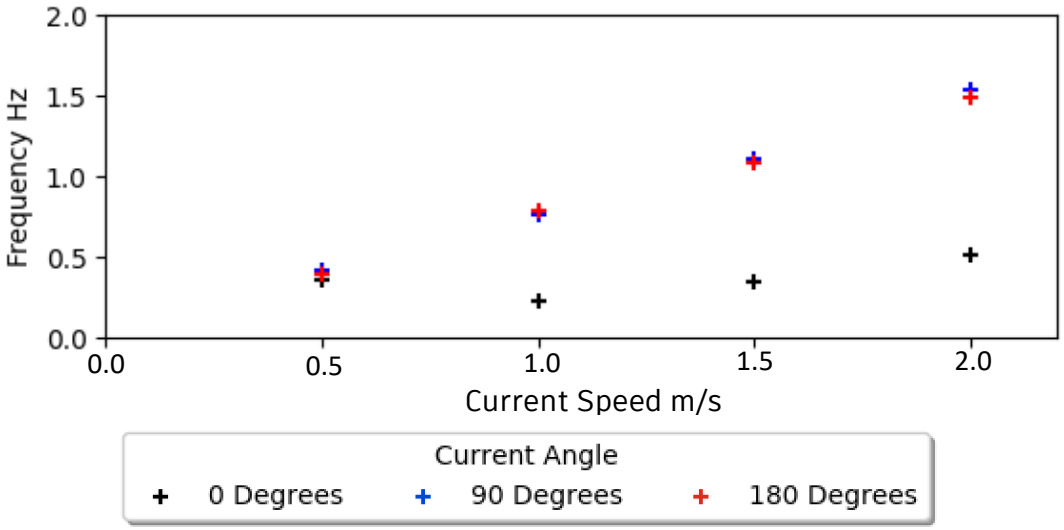

Figure 8-9: A comparison of the impact of the current speed and direction on the vibration frequency for a steep wave and uniform current profile

When comparing the frequency seen in Figure 8-9, the most notable observation was that a current angle of 0 degrees resulted in the lowest magnitude of vibrations for all speeds by a significant margin, when the current speed was greater than 0.5 m/s. This was due to the steep wave configuration and low modes of excitation being predicted, despite substantially large normal relative velocity. Current angles of 90 and 180 degrees weren't as influenced by this. This was also notably different from the shear profile, and showed how impactful the current profile was in terms of mode of vibration and location of maximum displacement. The VIV frequency for angles 90 and 180 degrees were very similar for all current speeds.

8.3 Substation Guignier Double Wave

A double wave cable was modelled, the shape of the cable was emulated from the work of Guignier, Figure 8-10. The cable used in this model was Substation and the shear power law current profile was chosen as specific site data was not available.

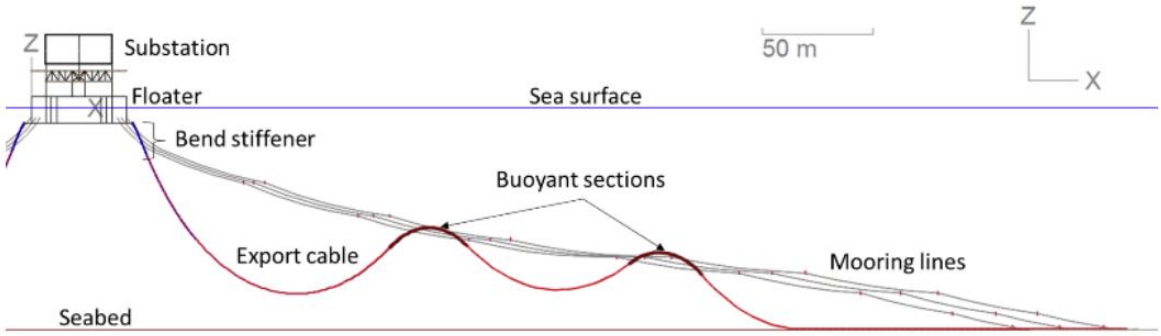

Figure 8-10: Guignier Double Wave Cable Configuration (Guignier et al., 2020)

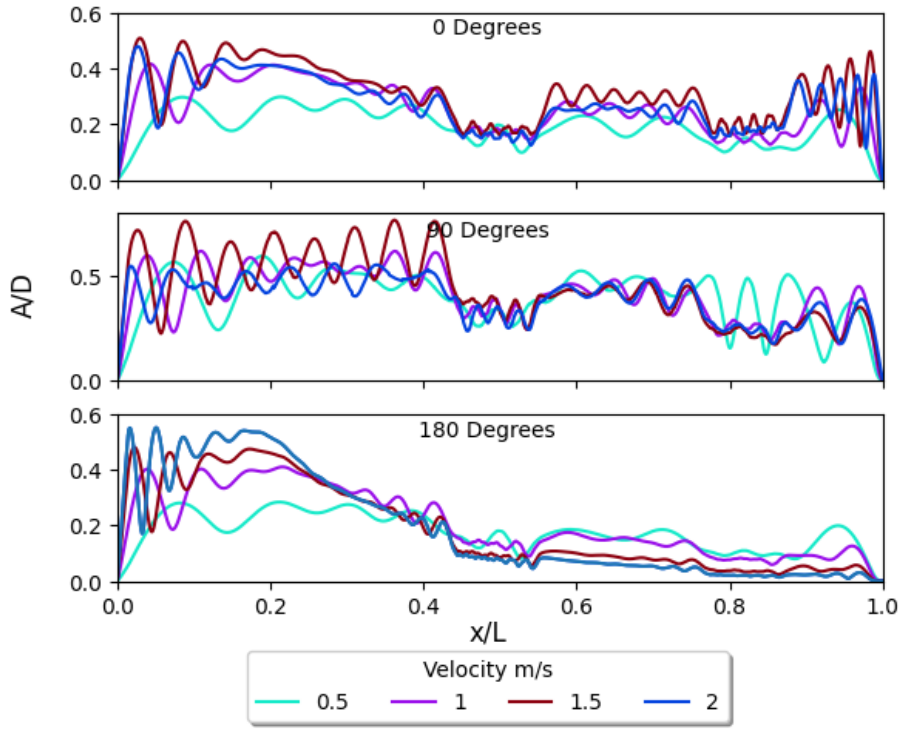

Figure 8-11: A comparison of the RMS crossflow displacement for a double laze wave configuration and varying current speeds for a shear power law current profile

Figure 8-11 shows the influence that the double wave cable configuration shape had on the RMS displacement. The impact of the buoyancy modules was evident with all current angles showing a decrease along the sections where these were located. For a current angle of 0 degrees, large displacements at the hang-off, mid-section, and touchdown section for all current speeds 1m/s and greater could be seen. This was notably different than for a lazy wave configuration where the largest amplitudes of vibrations were generally concentrated towards the touchdown point. The double wave configuration wasn't as susceptible to deformation for this current angle, likely due to being much longer and having two buoyancy module sections.

A current angle of 90 degrees resulted in a similar displacement profile to an angle of 0 degrees with notable vibrations along the hang-off, mid-section, and touchdown sections. A notable trend was that

the RMS displacement decreased along the cable length to a greater extent than for an angle of 0 degrees. This was likely most influenced by the shear current profile.

A current angle of 180 degrees shows a prominent trend for all current speeds, with this exaggerated as the speed increased. The largest RMS displacement was observed at the hang-off point, this then decreased rapidly along the cable length, with an especially notable drop at the upper buoyancy section. This rapid decrease in RMS displacement was most influenced by the cable deformation, allowing for substantial normal relative velocity variations along the cable length with the greatest values towards the hang-off point. The shear current profile also influenced the behaviour. Compared to the other angles, the most drastic discrepancies in the magnitude of displacement were seen for this angle of current propagation.

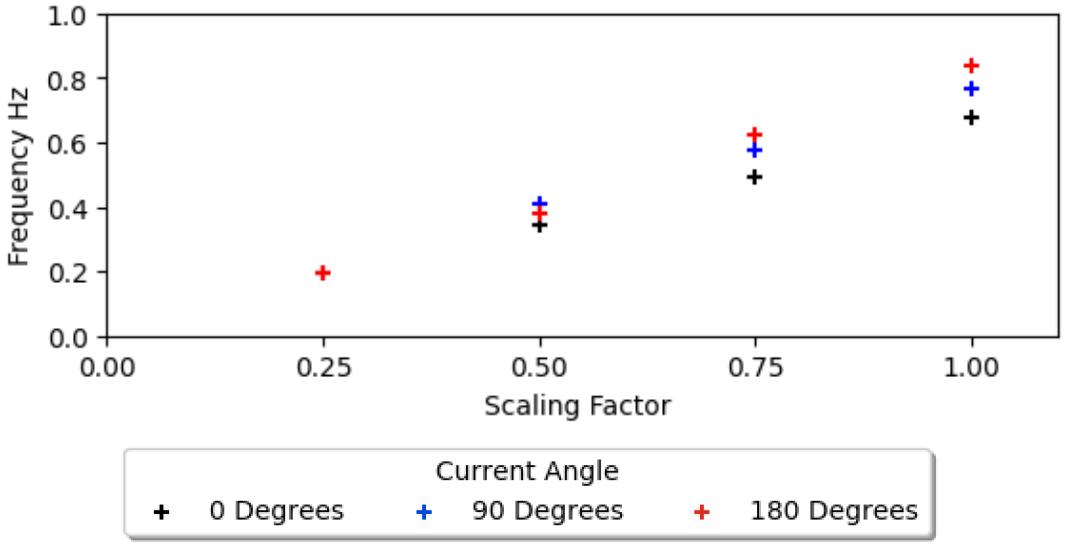

Figure 8-12: A comparison of the impact of the current speed and direction on the vibration frequency for a double lazy wave and shear power law current profile

When looking at the frequency of vibrations shown in Figure 8-12, it can be seen that a current angle of 180 degrees generally resulted in the greatest frequency of vibration. This was followed by a current angle of 90 degrees and lastly 0 degrees.

8.4 Comparing Different Configurations Flotant Cable

Figure 8-13 compares the different VIV profiles for four different cable configurations: lazy wave, steep wave, tethered lazy wave, and double wave. The cable properties were kept consistent across all configurations by using the Flotant cable properties. The current profile was kept constant by using the shear power law profile with the current speed at the surface being 1m/s. As the cables were different lengths and at different depths the x-axis was normalised with regards to the respective cable lengths.

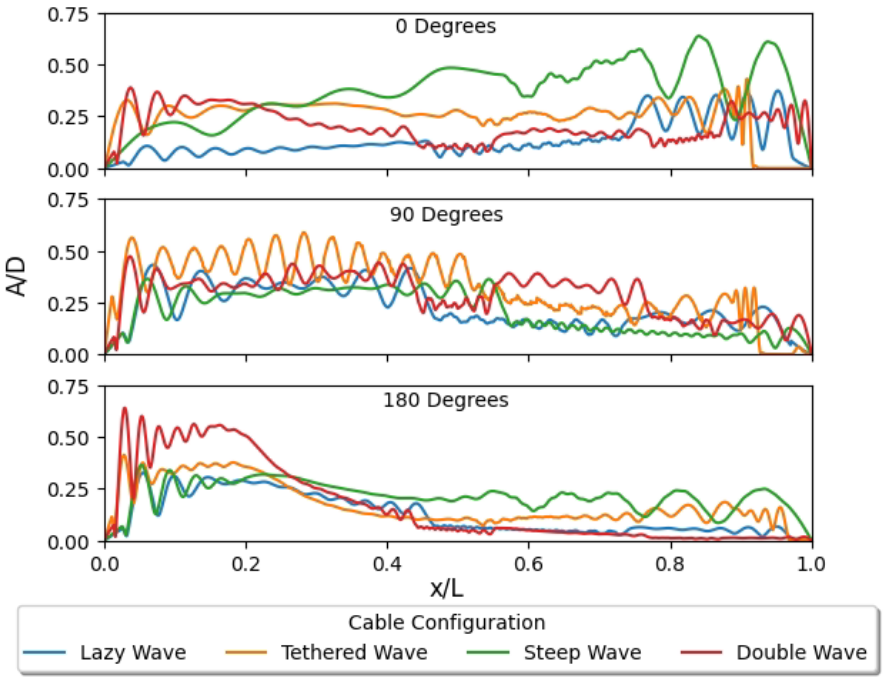

Figure 8-13: A comparison of the RMS crossflow displacement for varying cable configurations for a shear power law current profile

It can be observed from Figure 8-13 that the cable configuration had a notable impact on the VIV behaviour. All cable configurations showed that the buoyancy section had an impact on VIV profile, generally leading to suppression of vibrations.

When considering a current angle of 0 degrees, a general trend can be observed that the section closest to the touchdown point experienced more significant amplitudes of vibrations compared to the other current angles. The rest of the cable also vibrated at a lower magnitude of displacement compared to the other current angles. The severity of the discrepancies between displacement at the touchdown point and the rest of the cable was dependent on the cable configuration. The lazy wave shape showed much larger displacement at the touchdown section relative to its displacement at the hang-off point, compared to the other configurations. The RMS displacement profiles for the tethered and double wave configurations showed less dependency on location along the cable length, with prominent RMS displacement observed over the full cable. The steep wave's profile was notably different from the other cable configurations. It was at a much higher amplitude but lower mode number.

A current angle of 90 degrees results in very similar behaviours for all configurations. This behaviour being that the largest amplitude of displacement was observed at the hang-off point, and this tapers down along the cable length to a much lower magnitude towards the touchdown section. This was to be expected as the current direction was perpendicular to the cable plane and thus cable configuration

has a lesser influence on normal relative velocity. The trend of reducing with depth was due to the current profile following a power law and the normal relative velocity decreasing.

A current angle of 180 degrees produced similar profiles for all cable configurations, the largest vibrations were observed towards the hang-off point and reduced along the cable's length to a minimum at the touchdown section. The largest displacement at the hang-off point was to be expected, due to the cable deformation which resulted in decreasing the angle of inclination at this section, and the larger relative current velocity from the shear current profile. It was noted that the double wave configuration resulted in much more extreme variations in amplitude over the full length compared to the other cable configurations.

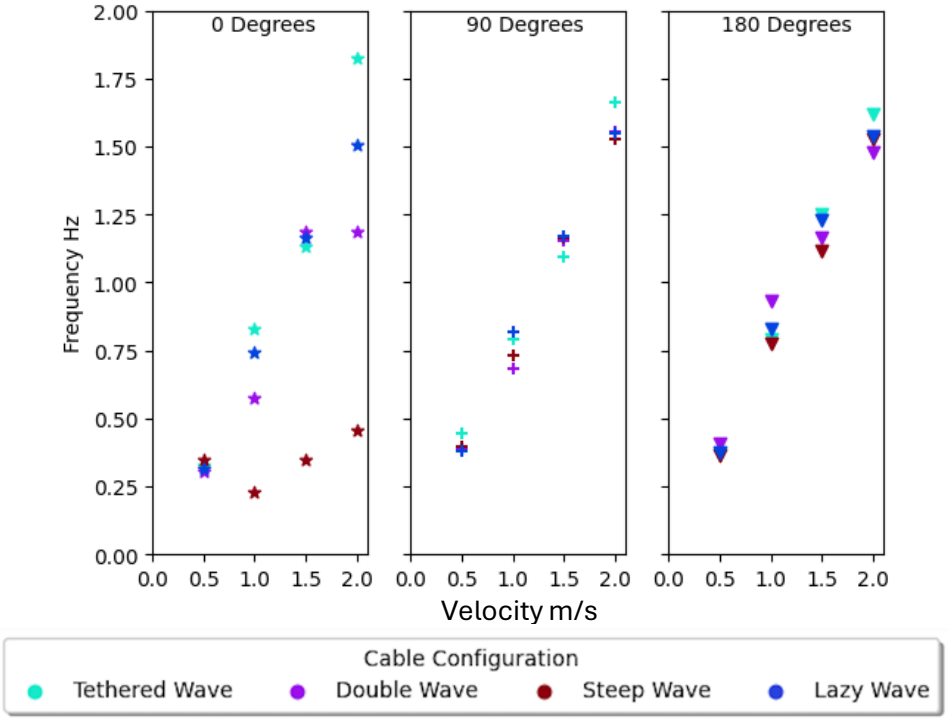

Figure 8-14: A comparison of the vibration frequency for varying cable configurations for a shear power law current profile

The frequency of the vibrations is compared in Figure 8-14. The general trend was that the tethered wave results in highest frequency of vibrations, followed by lazy wave, then double wave and finally the steep wave, with some deviations from this trend noted. Except for a current angle of 0 degrees, all configurations generally resulted in the frequency of vibrations being similar.

At a current angle of 0 degrees the cable was susceptible to large cable deformation for all configurations and, thus, the large dependency on this resulted in anomalous frequency predictions. The reason for the steep wave configuration to result in such low vibrations at current angle 0 was due to excessive bending along the bottom section. The Flotant cable was noted to be unacceptable

for use in the West Barra site due to large current resulting in compression at touchdown point. The excessive bending resulted in reducing the normal relative velocity along the whole cable length.

Current angles 90 and 180 degrees didn't show as much dependency on cable configuration. For 90 degrees this was due to the current propagation direction being perpendicular to the cable's initial plane, meaning relative velocity was kept more consistent along the full length and for different shapes. For a current angle of 180 degrees, this was due to the relatively limited deformation for all configurations and the cable section with the most dominant frequency was located towards the hang-off point. All different configurations had relatively similar normal relative velocity profiles at this position. Neither the length of cable nor the water depth appeared to have a substantial influence on frequency of vibration with no obvious dependency observed.

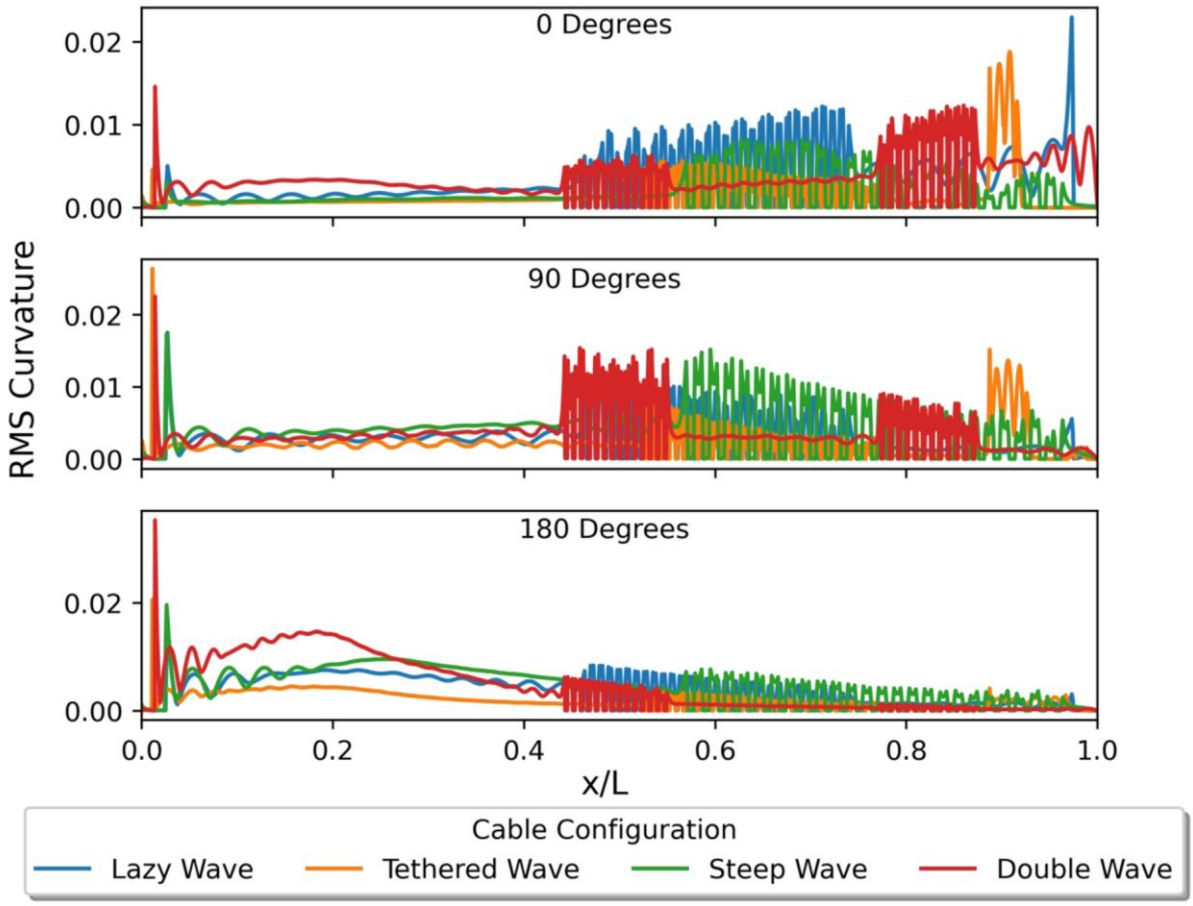

8-15: RMS curvature for different cable configurations

8.5 CONCLUSION

The lazy wave, double wave, steep wave, and tethered lazy wave cable configurations were investigated. The RMS crossflow displacement was seen to vary substantially between the different cable shapes and responded independently to changes in the current profile. When considering the current angle, similar behaviours were seen in regard to the locations of maximum VIV amplitude. For a current angle of 0 degrees, significant amplitudes of vibrations were seen towards the touchdown point. For a current angle of 90 degrees the largest vibrations were in the top half of the cable closest to the sea surface. For a current angle of 180 the greatest magnitudes of vibrations were within 10-20% along the cable length from the hang-off point.

The differences between maximum and minimum RMS displacement, however, were notably different for each cable configuration. The double wave configuration had similar RMS displacement over the full cable length for current angles 0 and 90 degrees, between 0.2-0.5 *A/D*. However, for a current angle of 180 degrees there were a range of amplitudes of vibrations between 0.05-0.65 *A/D* over the full cable length. Extreme vibrations were observed at the hang-off point before quickly tapering off to near-zero displacement. The RMS crossflow displacement for the lazy wave configuration showed a large dependency on the current direction, with all angles resulting in substantially different VIV behaviour. The lazy wave had a range in amplitude of 0.1-0.45 *A/D* for an angle of 0, 0.25-0.45 *A/D* for an angle of 90, and 0.05-0.35 *A/D* for an angle of 180. A steep wave showed an unexpected RMS displacement profile for a current angle of 0 degrees, large RMS displacements were observed over the full cable length in the range of 0.2-0.65 *A/D*. This was noted as likely due to lower modes of excitation predicted. A similar displacement profile was seen for current angles 90 and 180 degrees. For 90 degrees the largest displacement was 20-30% along the cable length with a range of 0.1-0.3 *A/D*. For 180 degrees the largest displacement was around 10-20% along the cable length with a range of 0.25-0.35 *A/D*. A tethered wave, despite having a similar initial shape to the steep wave, displayed markedly different behaviour to this configuration. This was likely due to the tether limiting cable deformation. Overall, the RMS displacement for the steep wave showed less dependency on the current direction when compared to the other configurations. For a current angle of 0 degrees, the largest displacement was towards the touchdown point with a range of amplitude from 0.25-0.25 *A/D*. For an angle of 90 degrees, the peak amplitude occurred 5-30% along the cable length with a range over the full cable length between 0.3-0.55 *A/D*. For 180 degrees, the largest displacement was towards the hang-off point and there was a range in displacement between 0.1-0.3 *A/D*.

When comparing the frequency of vibrations of the different configurations there was a strong dependency on both the current angle and the cable shape observed. A current angle of 0 degrees showed the greatest variation between the configurations. In terms of ranking the greatest to smallest VIV frequency, the order of the cable configurations were lazy wave, tethered wave, double wave, and steep wave. When comparing the difference between the configurations, relative to the tethered wave frequency, a double wave was ~83%, tethered wave was ~0.67%, and the steep wave was ~27%. For the other current angles there was much less discrepancy between the configurations and no real obvious trend was seen.

9 Results and Discussion - Additional Influencing Factors

9.1 Modules as Attachments Instead of Line Segments

The impact of modelling buoyancy modules as attachments instead of line segments was investigated. Modelling as attachments works within Shear7 by providing a buoyancy lift force on the cable at determined locations. However, the diameter and mass ratio of the modules are not considered by Shear7. This was done to determine whether this had an influence on the VIV behaviour, and if so, the extent of this influence. Modelling as line segments was preferred, this ensured that the diameter difference of the buoyancy module relative to the cable was factored into the VIV behaviour within Shear7. The cable chosen for comparison in this study was Martinelli with a uniform current profile in a lazy wave configuration.

Table 9-1: A comparison of the RMS displacement for when modelling the buoyancy modules as attachments or line segments

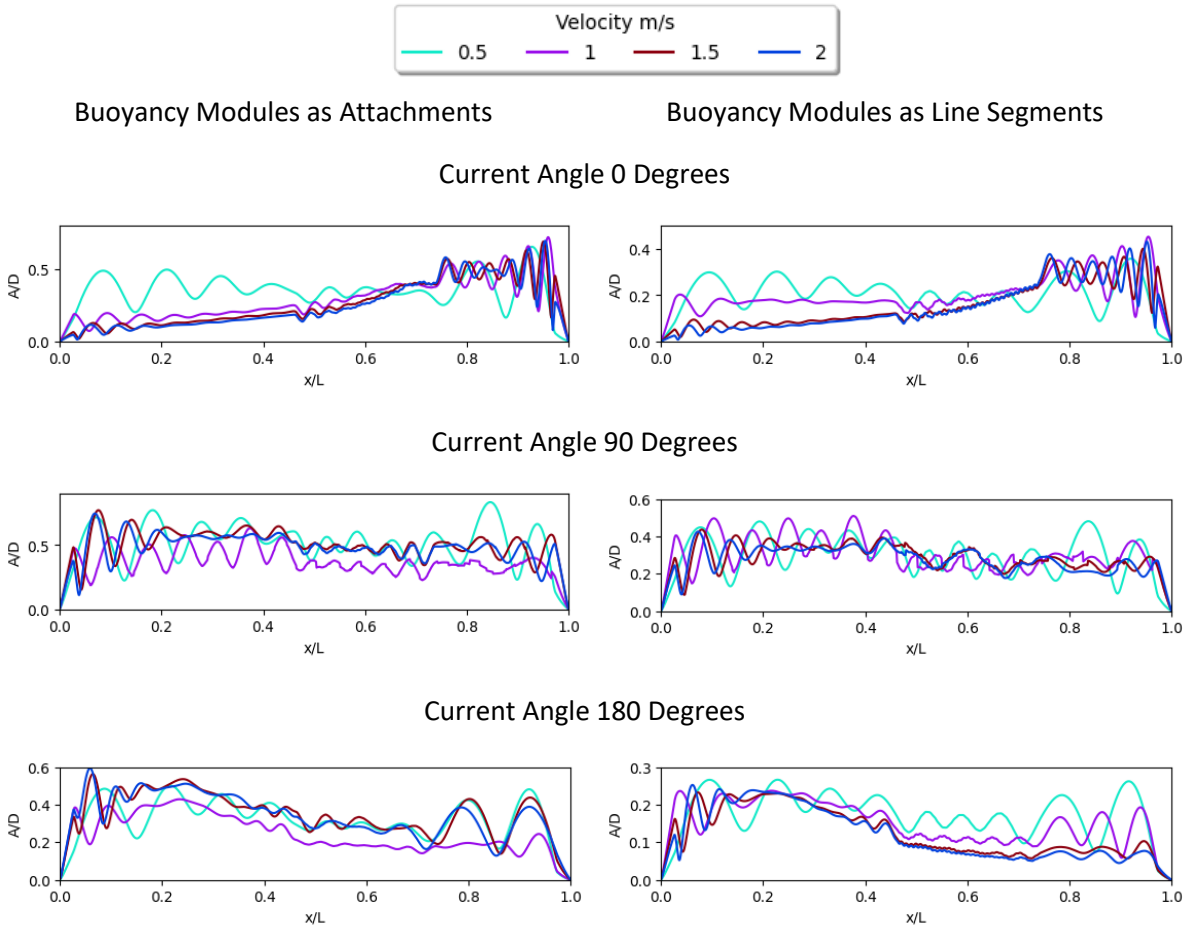

Modelling as attachments produced much larger vibrations for all current angles and velocities. Without the interference to VIV development, due to the change in diameter from the buoyancy modules, a different vibration profile occurred. This predominantly manifested as a greater RMS

displacement with similar relationships between length along cable and relevant significant displacement observed in both models. It has been documented in various studies, highlighted in Chapter 2.7.2, that the introduction of buoyancy modules resulted in the excitation of different frequencies due to changes in diameters. This can impact the RMS displacement and the fatigue damage rate. The results in Table 9-1 show this behaviour, with the buoyancy modules modelled as attachments resulting in substantially larger vibrations for all current angles, as well as predicting different modes of vibration. The overall profile of the RMS displacement was similar for both models with the locations of maximum vibrations consistent.

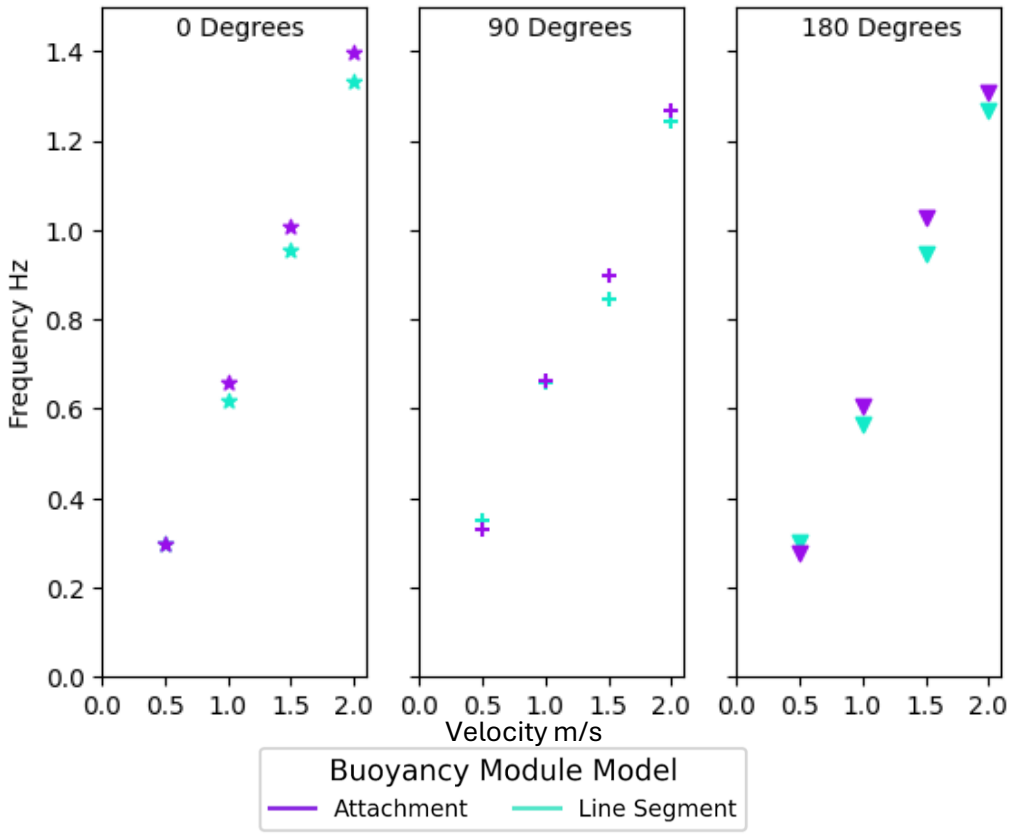

Figure 9-1: A comparison of the vibration frequency when modelling buoyancy modules as segments or attachments

When comparing the frequency of vibrations for the different buoyancy modelling methods, modelling as attachments resulted in greater frequencies observed, as shown in Figure 9-1. The inclusion of buoyancy modules as line segments resulted in the disruption of the vortex-induced vibrations due to the change in diameter.

Without adequate validation for a full-scale power cable with buoyancy modules over a lazy wave configuration available it was difficult to decide which method of modelling produced optimal results.

However, considering the attachment model ignored any VIV interaction of the buoyancy modules, which is known to be invalid, it was chosen to model the modules as line segments.

9.2 Different Buoyancy Module Distribution

The original buoyancy module distribution was 1m of cable to 0.8m of buoyancy module. This ratio was adjusted to observe the influence this had on the VIV behaviour. The still water static cable position of the cable was kept consistent through the simulations by adjusting the density of the buoyancy module segments. Increasing the distance between the modules will impact the excitation of the intra-buoyancy module cable segment as well as disturbing the VIV excitation along the rest of the cable length.

The length of the buoyancy module was adjusted as well to determine the influence this would have on the overall VIV behaviour. The current profile was kept uniform at 1m/s. Martinelli, Flotant, and Substation cables were investigated. The ratio of cable to buoyancy module was defined by the following:

$$R_{CBM} = L_C / L_{BM}$$

Where R_{CBM} represents the ratio of cable length between buoyancy modules, L_C, to length of buoyancy modules, L_{BM}.

9.2.1 Buoyancy Module Length of 0.5m

The buoyancy module length was set to 0.5m for these simulations, and the length of the cable was adjusted to satisfy the specified ratios.

9.2.1.1 Martinelli

For Martinelli, the density of the cable was too large for a ratio of 3 to 1 so there are no results for this distribution ratio.

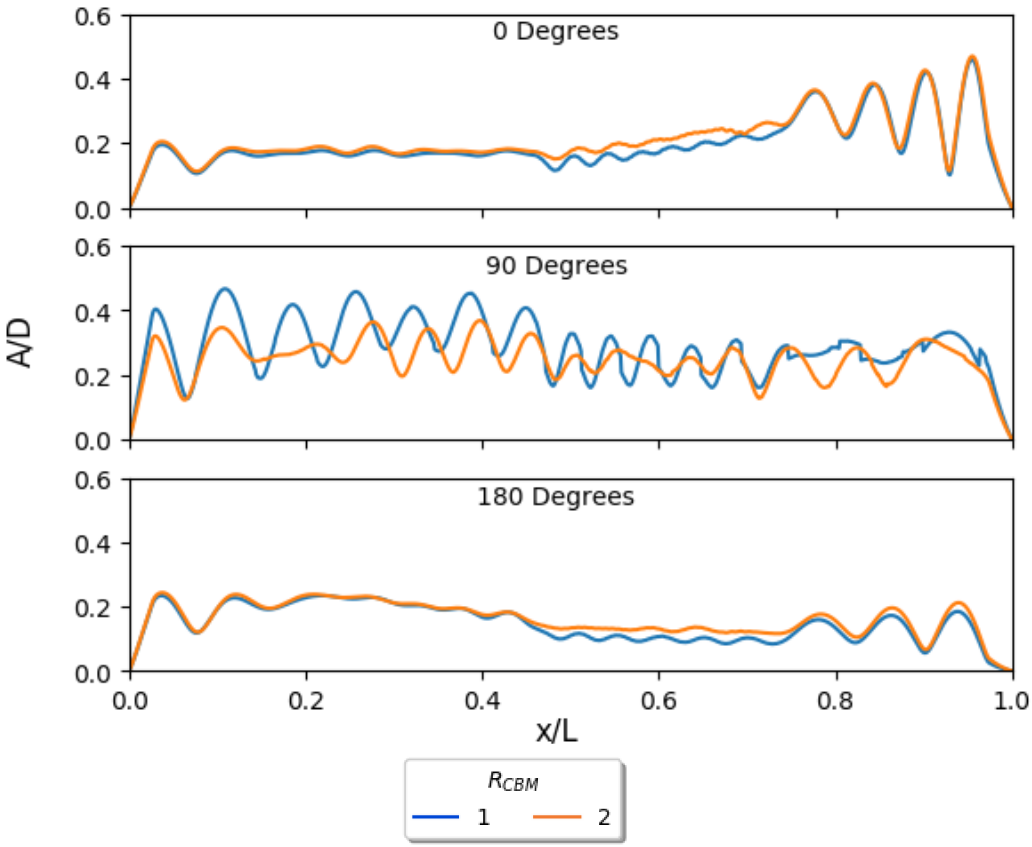

Figure 9-2: A comparison of the RMS displacement for different buoyancy module ratios for a buoyancy modules length of 0.5m (Martinelli)

The buoyancy module distribution is shown, in Figure 9-2, to influence the VIV behaviour for all current angles. Current angles 0 and 180 degrees vibrate at a greater amplitude for the larger cable to buoyancy module ratio, this difference was minimal however, with the greatest discrepancies at the mid-section of the cable where the buoyancy modules were located. Otherwise, the cables vibrated at very similar amplitudes and RMS displacement profiles. However, a current angle of 90 degrees substantially deviated from this trend, with the ratio of 1 to 1 producing larger amplitude of vibrations.

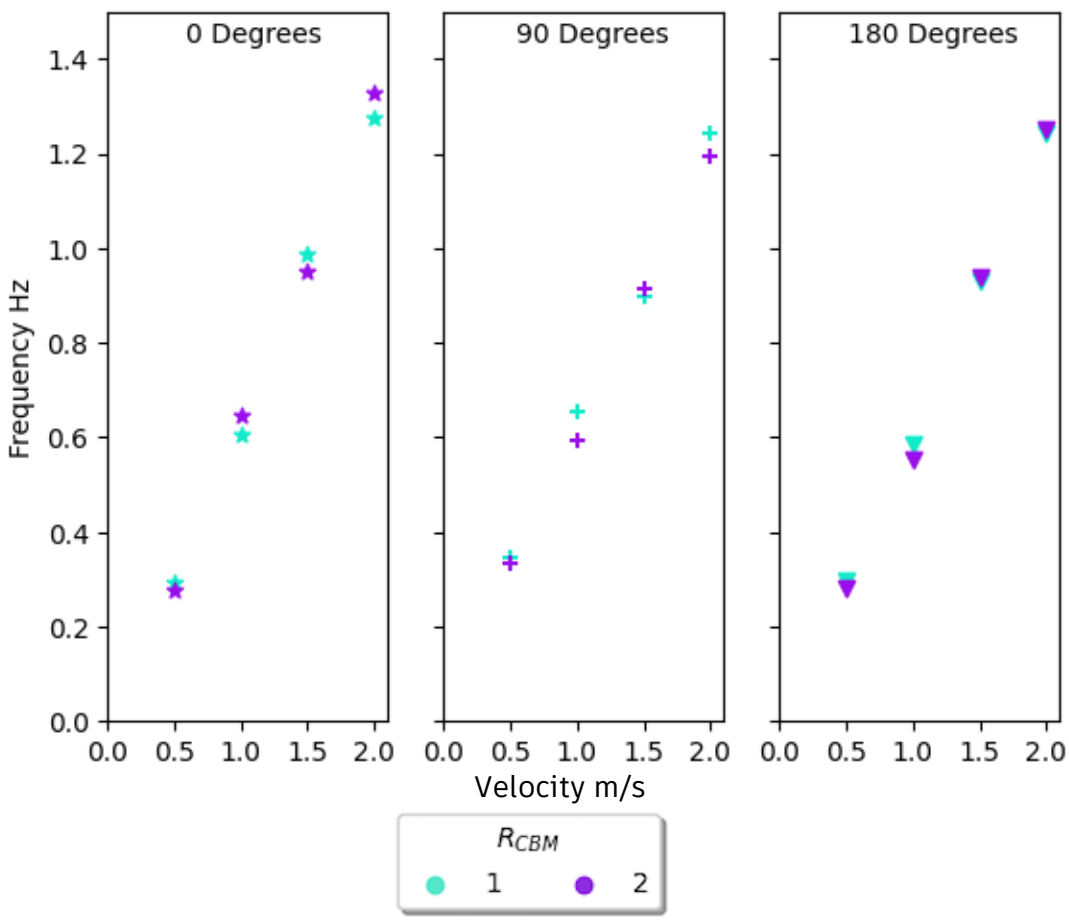

Figure 9-3: A comparison of the vibration frequency for different buoyancy module ratios with a buoyancy module length of 0.5m (Martinelli)

Observing Figure 9-3, the most obvious trend was that a current angle of 0 degrees results in greatest frequency of vibrations, with angles 90 and 180 degrees similar in magnitude. When comparing the impact of the buoyancy module ratio there was little discernible pattern across the current angles and current speed. The largest frequency of vibration for different ratio of buoyancy modules was independent for each angle and current speed.

9.2.1.2 Flotant

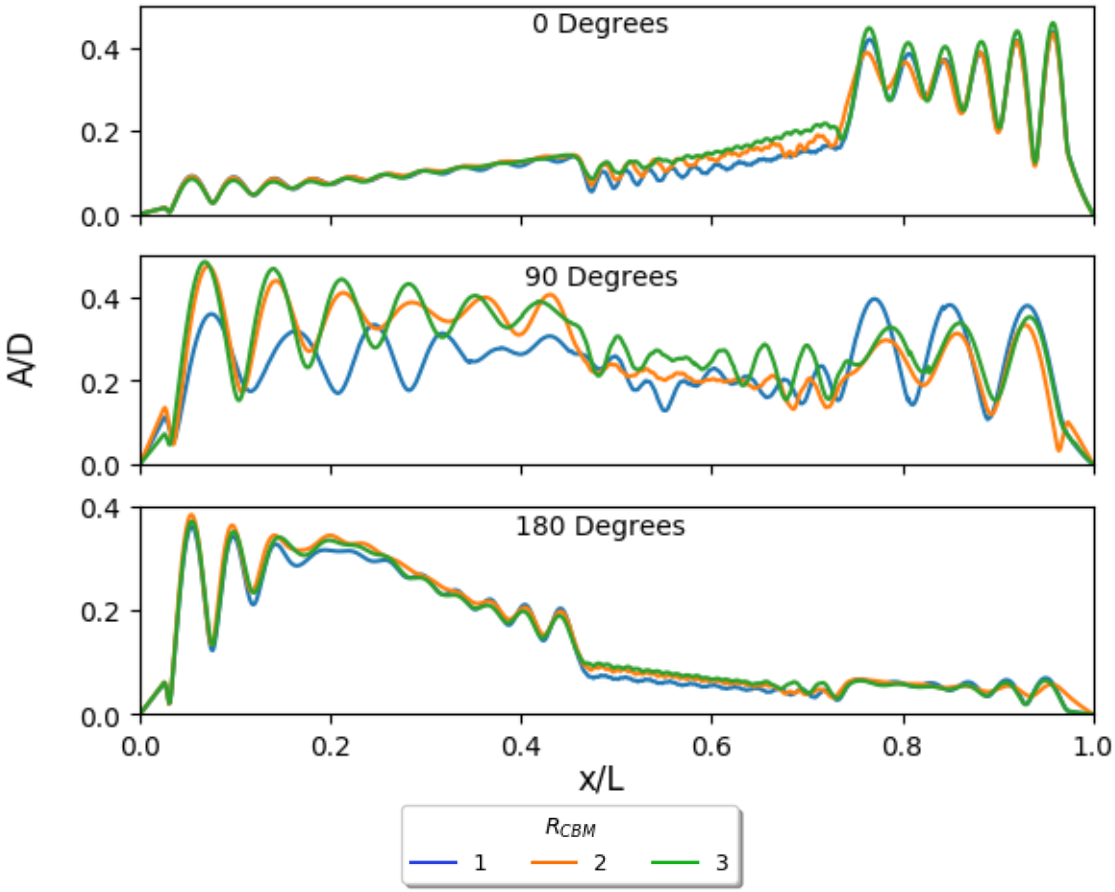

Figure 9-4: A comparison of the RMS displacement for different buoyancy module ratios for a buoyancy modules length of 0.5m (Flotant)

When considering the buoyancy module distribution for the Flotant cable, it was shown in Figure 9-4 to have a significant impact. There was an obvious trend for all current angles where the greater the distribution ratio the greater the RMS displacement. This is to be expected, a greater section of exposed cable resulted in greater induced vibrations due to less interference with changes in diameter due to the buoyancy modules. The difference between the buoyancy module ratios was dependent on current angles. A current angle of 0 degrees showed little difference at the upper section but notable differences along the mid and bottom sections of the cable. A current angle of 90 degrees showed large discrepancies over the full cable length. A current angle of 180 degrees showed larger differences towards the hang-off point and along the mid-section compared to the touchdown section.

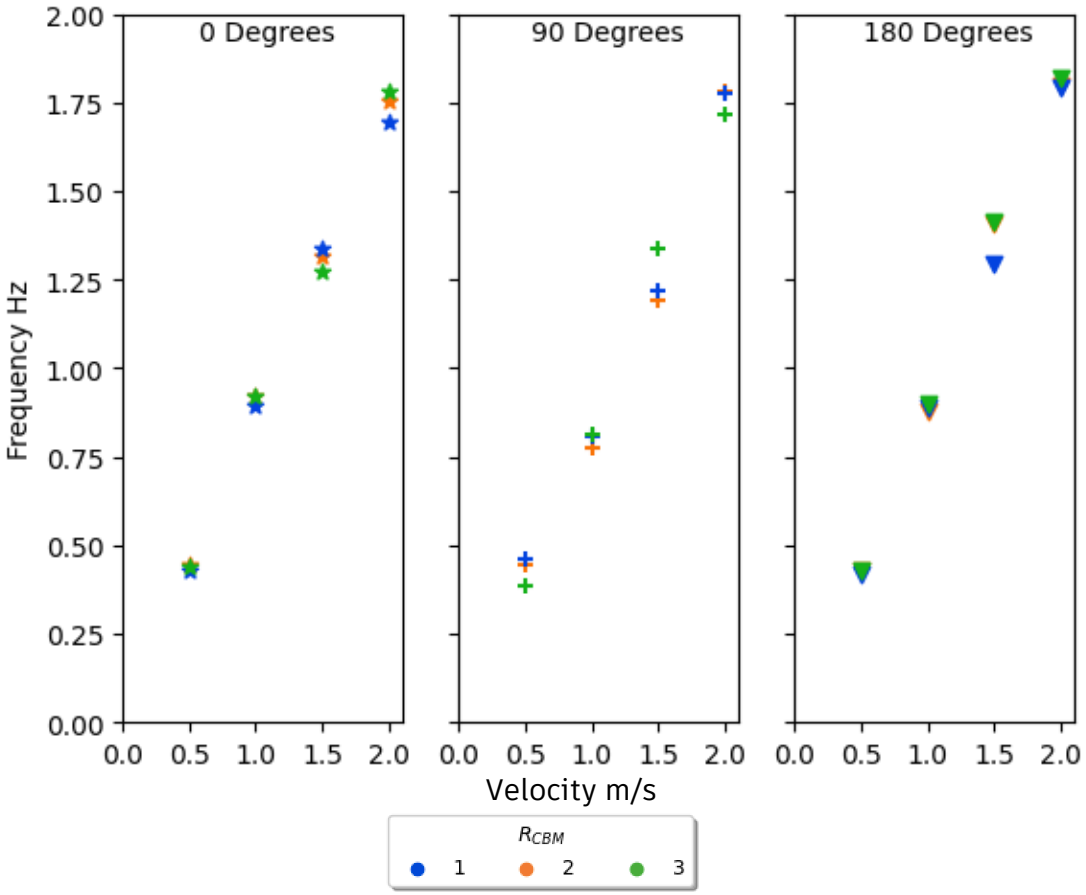

Figure 9-5: A comparison of the vibration frequency for different buoyancy module ratios with a buoyancy module length of 0.5m (Flotant)

A general trend seen in Figure 9-5, with multiple outliers, was that a cable to buoyancy module ratio of three resulted in the greatest frequency of vibration. This was likely due to the reduced buoyancy module influence as more cable section was exposed.

9.2.1.3 Substation

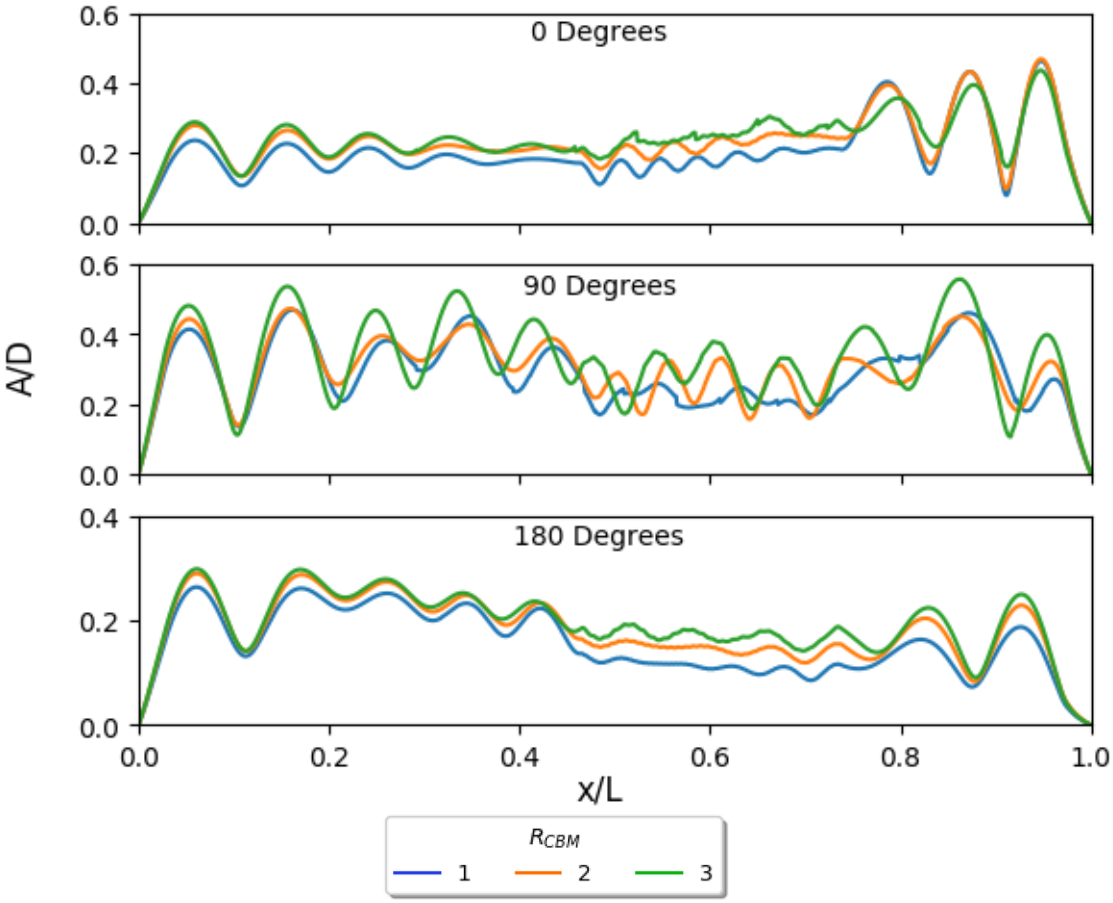

Figure 9-6: A comparison of the RMS displacement for different buoyancy module ratios for a buoyancy modules length of 0.5m (Guignier)

The RMS displacement profile for the Substation cable follows the same trend as for the Flotant cable, shown in Figure 9-6. The larger the cable to buoyancy module distribution ratio the greater the RMS displacement. This behaviour was replicated due to the same reasons described in the Flotant section above. The discrepancy between the magnitude of the RMS crossflow displacement of the buoyancy module ratios was larger than for Flotant.

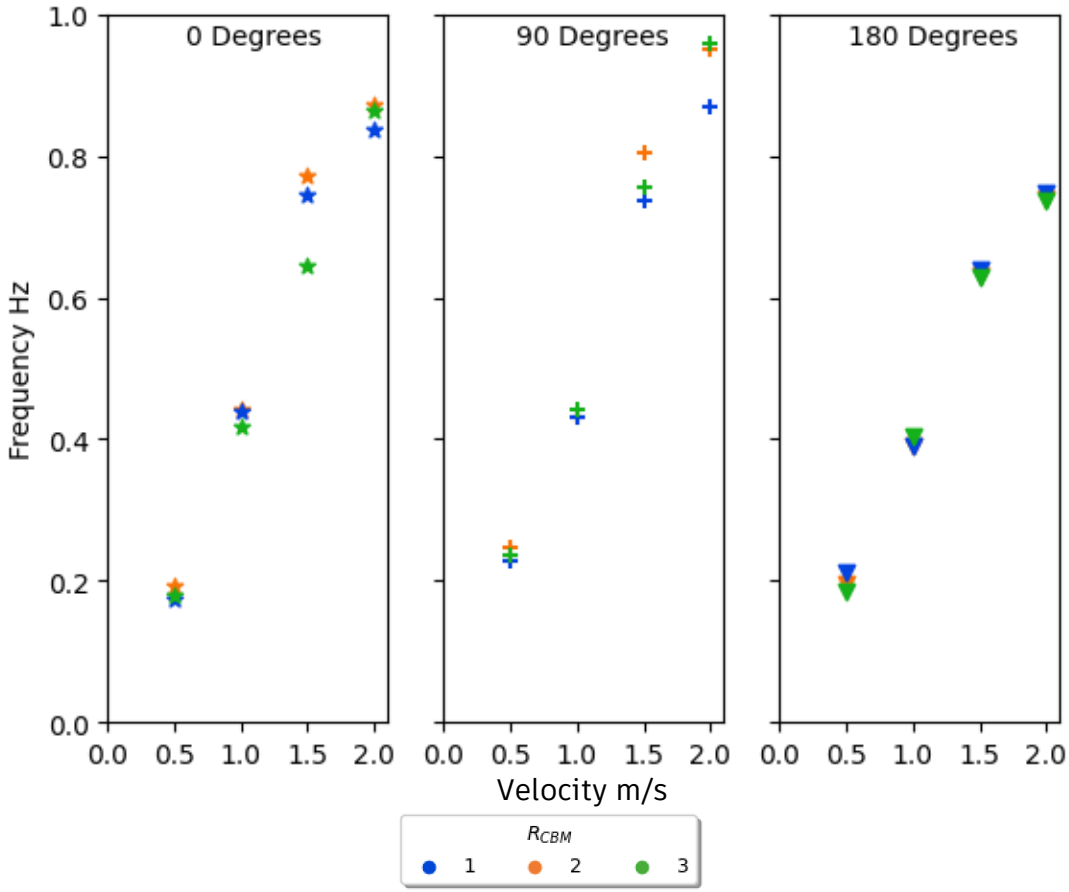

Figure 9-7: A comparison of the vibration frequency for different buoyancy module ratios with a buoyancy module length of 0.5m (Guignier)

The ratio of the buoyancy modules has no consistent trend for all current angles as is seen in Figure 9-7. There was also not a linear increase in the frequency of vibration with current speed. For a current angle of 90 degrees, it was noted that a R_{CBM} of 1 results in the lowest frequency of vibration for all current speeds. A current angle of 180 degrees predicted the lowest frequency of vibration compared to the other current angles.

9.2.2 Buoyancy Module Length of 1m

The figures below are for a buoyancy module length of one metre. This meant that the number of buoyancy modules over the cable length was halved compared to the plots shown in the above section.

9.2.2.1 Martinelli

Again, a ratio of 3 to 1 was incapable of being modelled due to density limitations of the buoyancy modules imposed by the large mass ratio of Martinelli's cable.

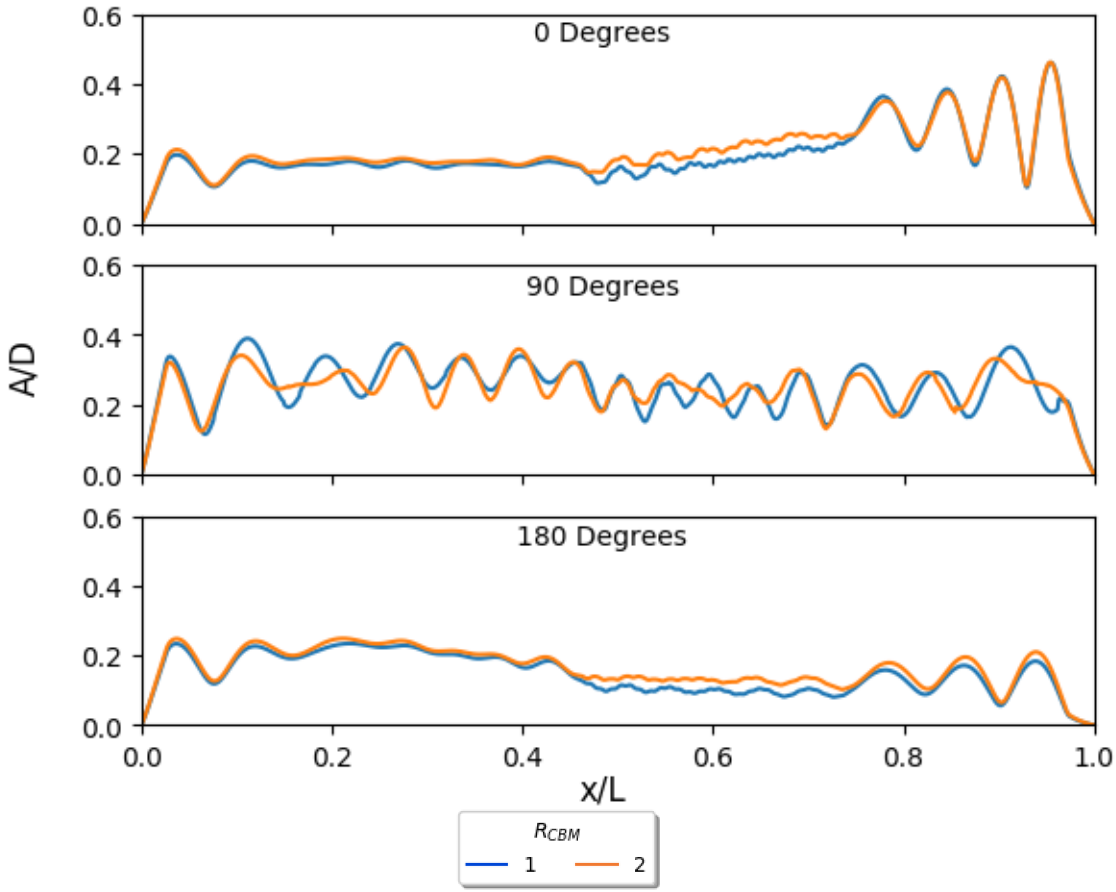

Figure 9-8: A comparison of the RMS displacement for different buoyancy module ratios for a buoyancy modules length of 1m (Martinelli)

Shown in Figure 9-8, the results followed a similar trend to that of a 0.5m length module, where the greater the distance between the modules the greater the amplitude of vibrations. The current angle of 90 degrees did not exemplify this trend but there was less discrepancy between the cable ratios than there was for a buoyancy module length of 0.5m.

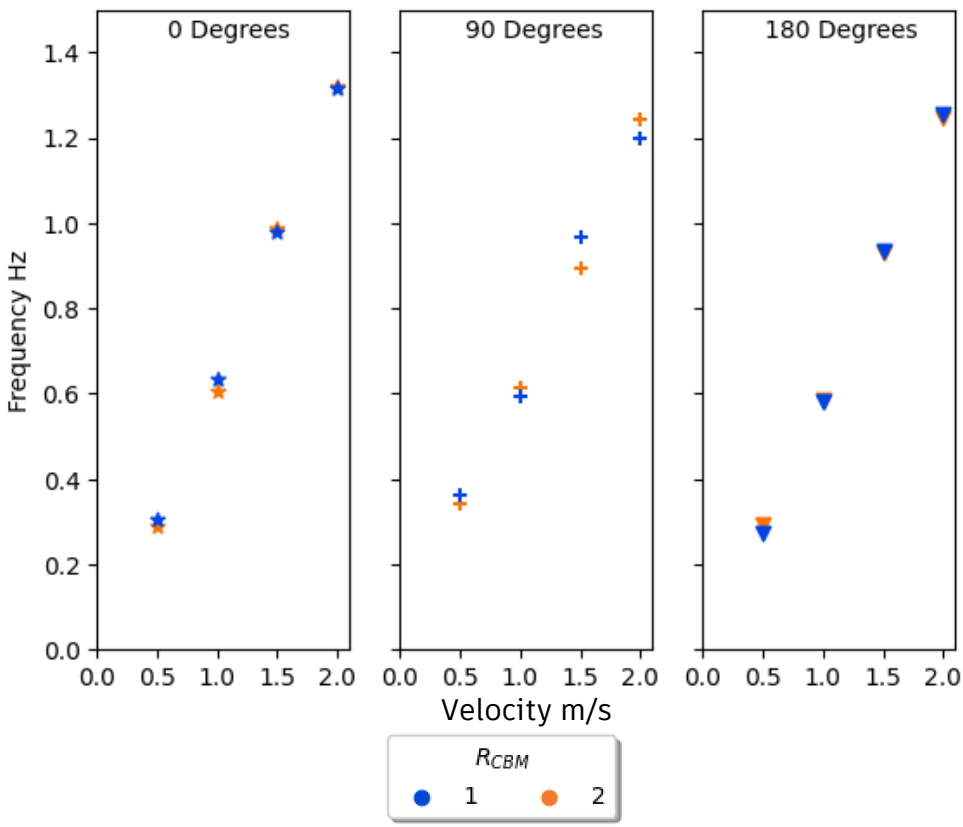

Figure 9-9: A comparison of the vibration frequency for different buoyancy module ratios with a buoyancy module length of 1m (Martinelli)

There is no overarching trend in terms of frequency for the buoyancy module ratio seen in Figure 9-9. A current angle of 0 degrees resulted in the largest frequency of vibrations compared to the other angles. The frequency discrepancy between the different ratios was minimal for all current angles.

9.2.2.2 Flotant

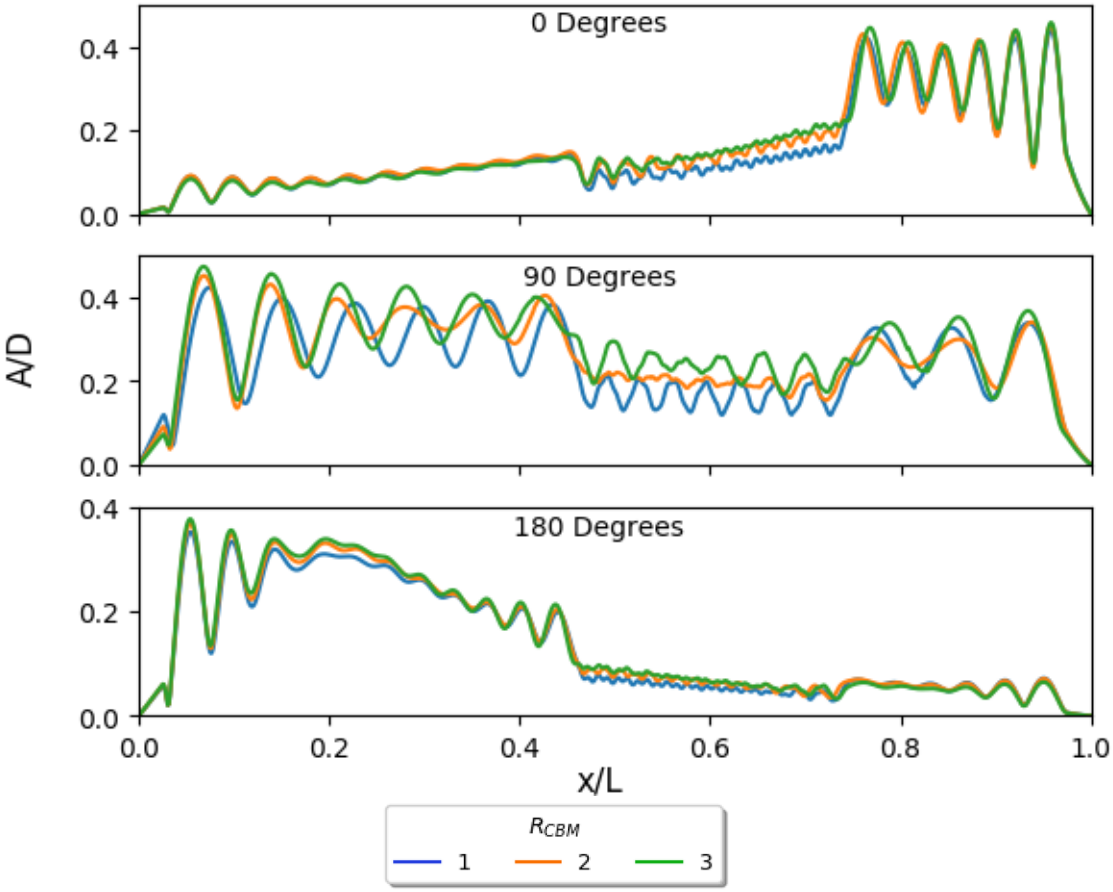

Figure 9-10: A comparison of the RMS displacement for different buoyancy module ratios for a buoyancy modules length of 1m (Flotant)

The trend observed in Figure 9-10 is very similar to that for a buoyancy module length 0.5m. This was noted to be due to the same reasons previously discussed in the section above. The greater the exposed cable length the greater the reduction of interference of the buoyancy modules.

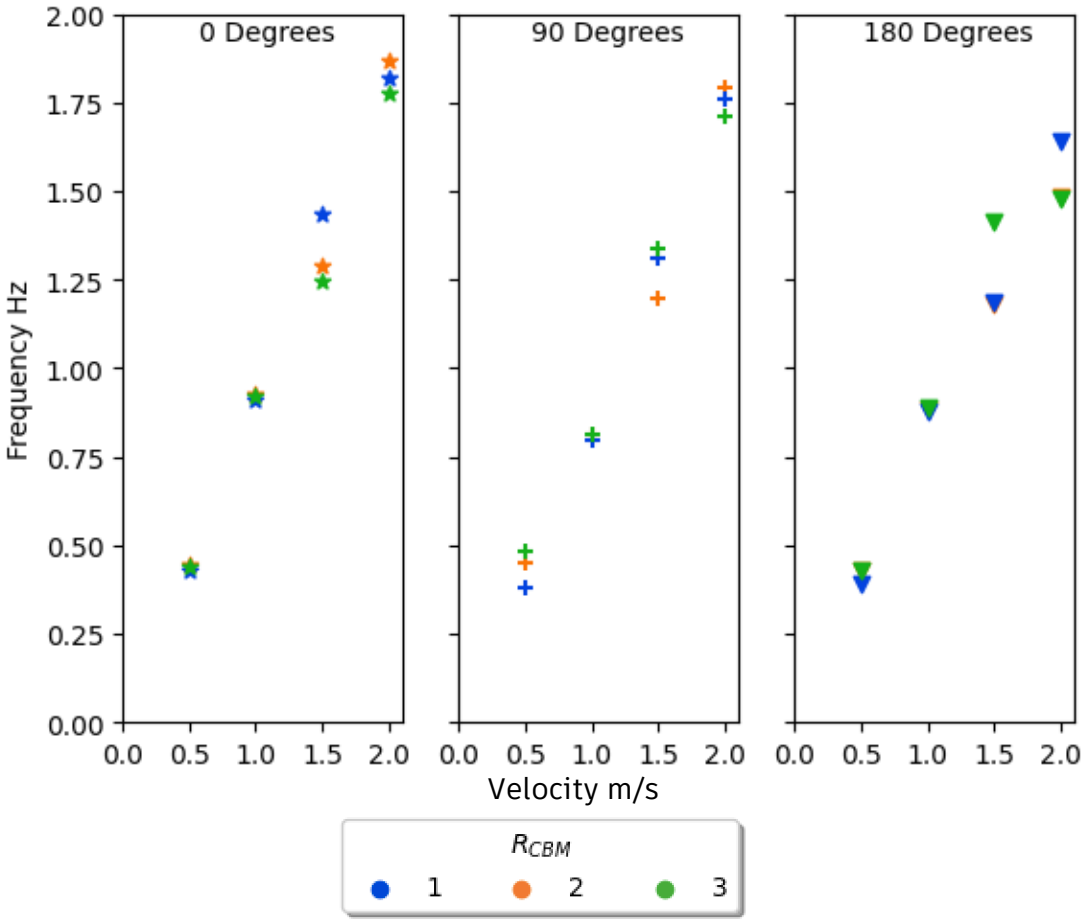

Figure 9-11: A comparison of the vibration frequency for different buoyancy module ratios with a buoyancy module length of 1m (Flotant)

When comparing the frequencies of vibrations seen in Figure 9-11 there were noted to be huge discrepancies and outliers for all current angles at certain current speeds. No discernible trend can be observed when relating the buoyancy module ratio to frequency and current speed. A current angle of 180 degrees predicted the lowest frequency of vibrations compared to angles 0 and 90 degrees.

9.2.2.3 Substation

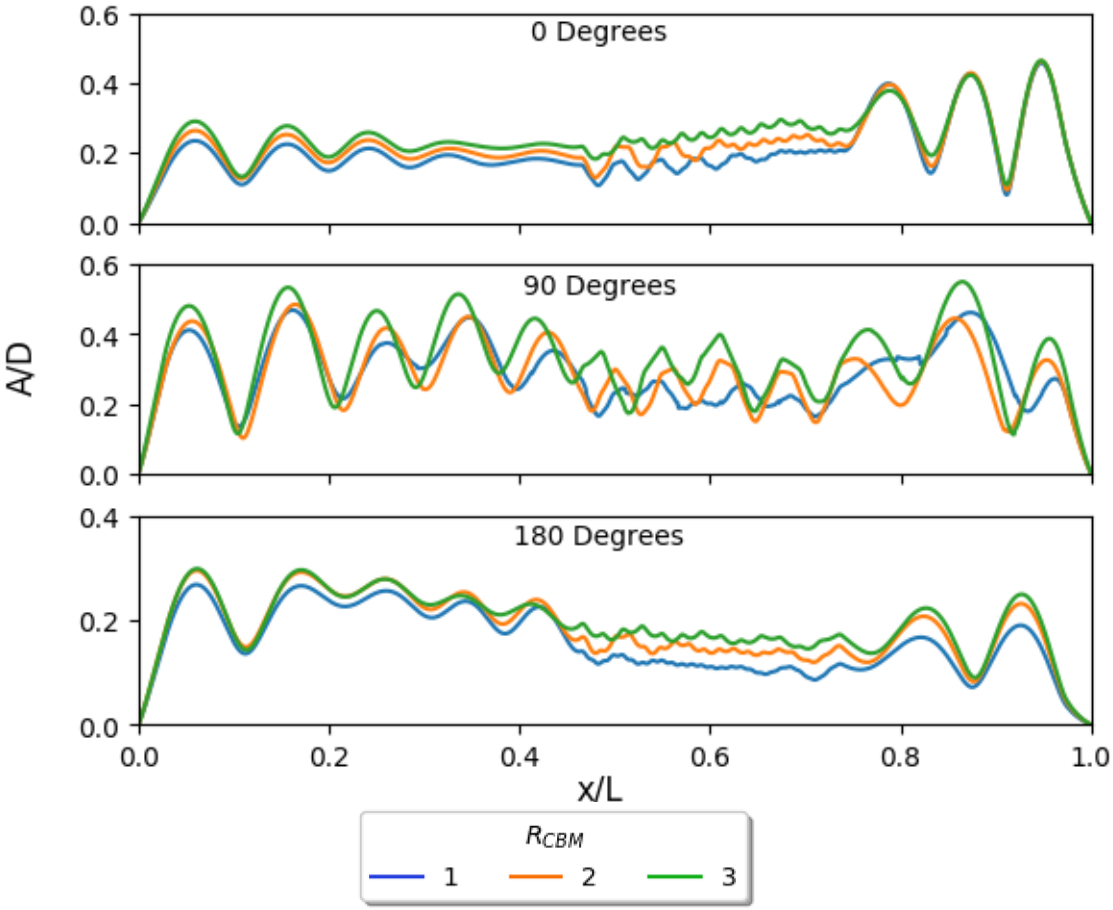

Figure 9-12: A comparison of the RMS displacement for different buoyancy module ratios for a buoyancy modules length of 1m (Guignier)

The trend shown in Figure 9-12 is again very similar to that of BM length 0.5m. This was noted to be due to the same reasons previously discussed. The results for all cables followed a very similar pattern, the greater the ratio of cable segment to buoyancy module the greater the RMS displacement. This was likely due to the increased length of exposed cable.

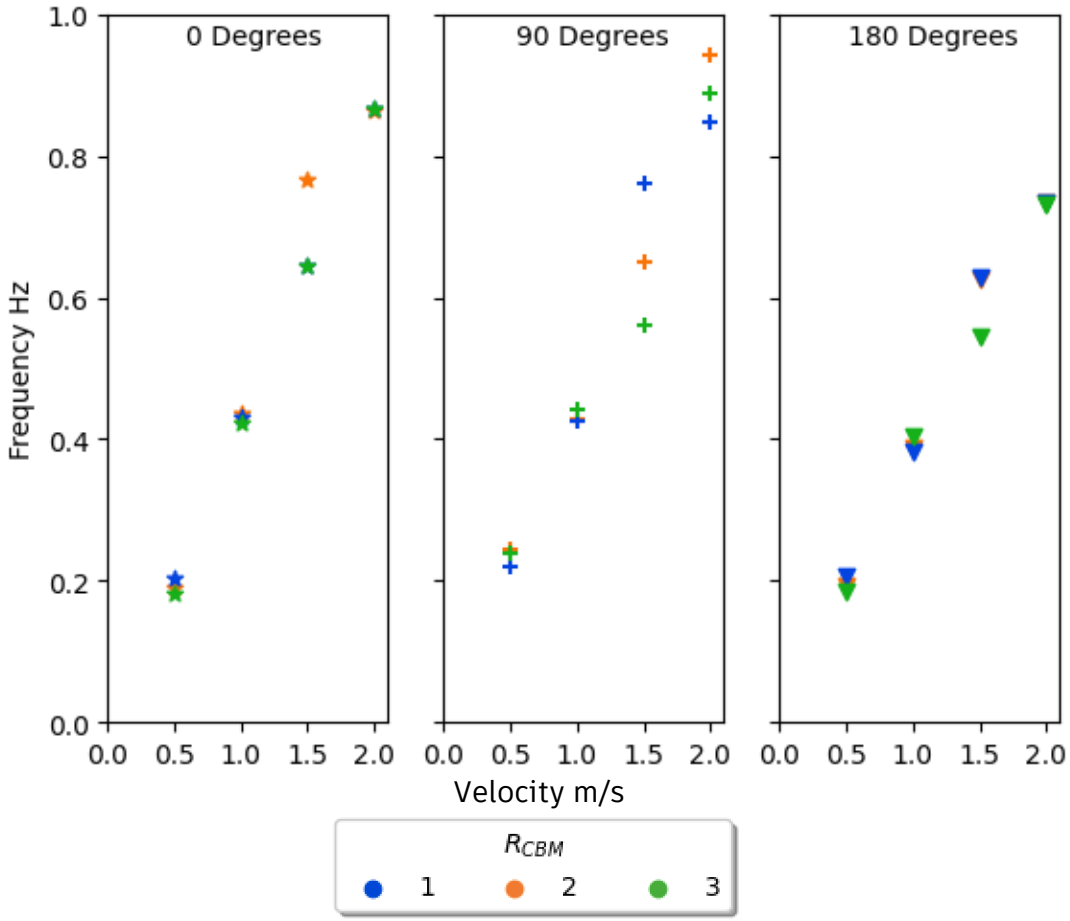

Figure 9-13: A comparison of the vibration frequency for different buoyancy module ratios with a buoyancy module length of 1m (Guignier)

When comparing the frequency of vibration, seen in Figure 9-13, the most obvious trend was that a current angle of 180 degrees resulted in the lowest frequency of vibrations. When comparing the impact of the buoyancy module ratio there was little discernible pattern across the current angles. A current angle of 90 degrees resulted in substantial variation in the predicted frequency, especially at current speeds greater than 1 m/s. The grouping for current angles 0 and 180 degrees, ignoring two outliers, were within ± 5%.

9.3 Buoyancy Module Length

The impact of varying the buoyancy module length was investigated. This reused the results from the previous section but repurposed them to allow easier comparison of this variable. The cable chosen for this study was Flotant and a uniform current profile of 1m/s was used. The length of the buoyancy module was increased while the length of the relevant cable section was also adjusted to accommodate this to keep the ratio consistent. The overall length of the buoyancy sections remained constant throughout. This meant for certain lengths and ratios that the buoyancy modules needed to

be adjusted at the end of the buoyancy section to accommodate this and ensure the overall buoyancy section length remained the same.

9.3.1 Buoyancy Module to Cable Ratio 1 to 1

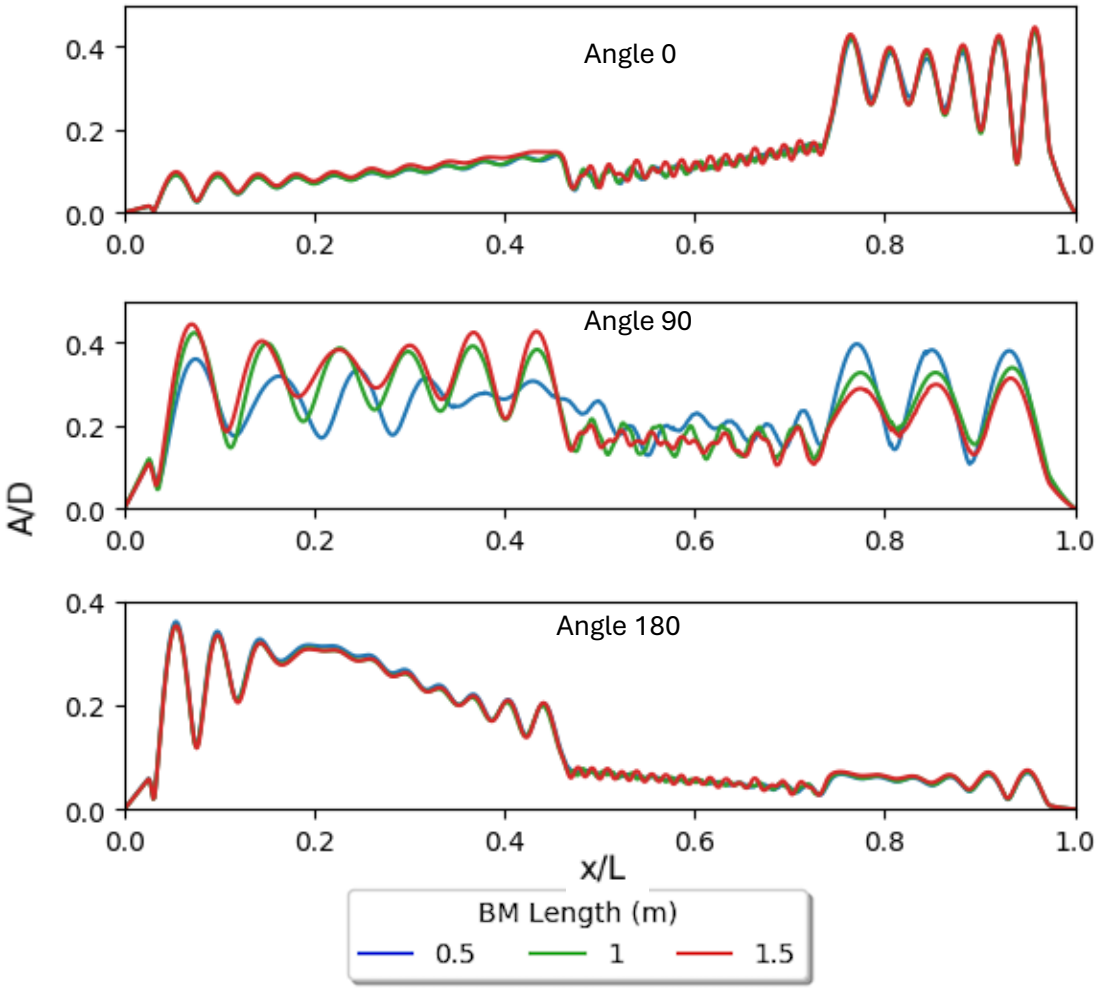

Figure 9-14: A comparison of the RMS displacement for different buoyancy module length for a buoyancy module to cable ratio of 1 to 1

The buoyancy module length for a 1 to 1 ratio seemed to have a minimal influence on the RMS displacement for current angles 0 and 180 degrees, as shown in Figure 9-14. There was a slight increase along the cable length for a longer buoyancy module for current angle 0 and a decrease at the hang-off point for longer buoyancy modules for current angle 180 but this was considered negligible. A current angle of 90 degrees showed a large variation in RMS crossflow displacement profile, depending on the buoyancy module length. The longer the buoyancy module the greater the displacement was at the hang-off point but the lower it was at the touchdown point. This was likely due to the influence of differing drag forces from changes in the buoyancy module arrangement and how this altered the cable deformation. The changes in cable deformation in turn influenced the normal relative velocity which determined the VIV behaviour.

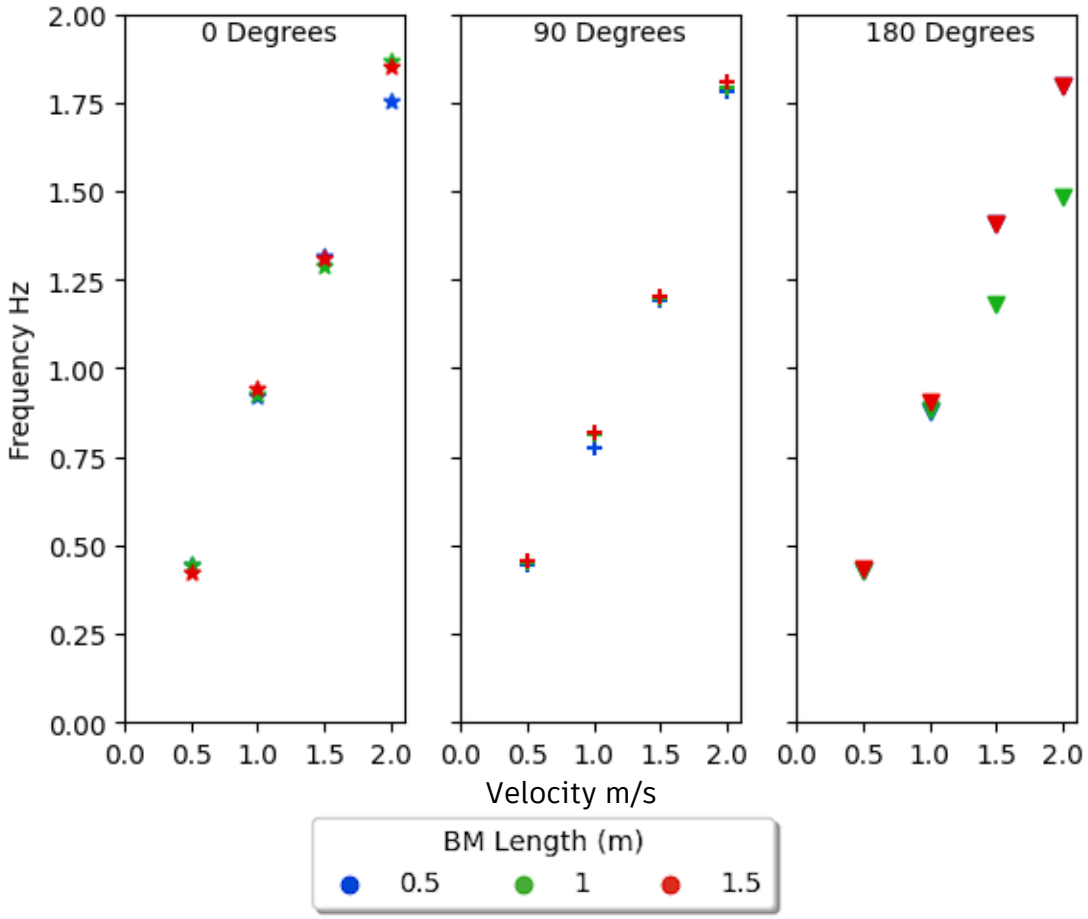

Figure 9-15: A comparison of the vibration frequency for different buoyancy module for a buoyancy module to cable ratio of 1 to 1

When comparing the frequency of vibrations shown in Figure 9-15 there is a trend present where the longer the buoyancy module the greater the frequency of vibration. There were some anomalies. This was potentially due to the longer buoyancy module length potentially exciting a greater frequency of vibrations along its section. However, the difference in frequency was minimal for all current angles.

9.3.2 Cable to Buoyancy Module Ratio of 2 to 1

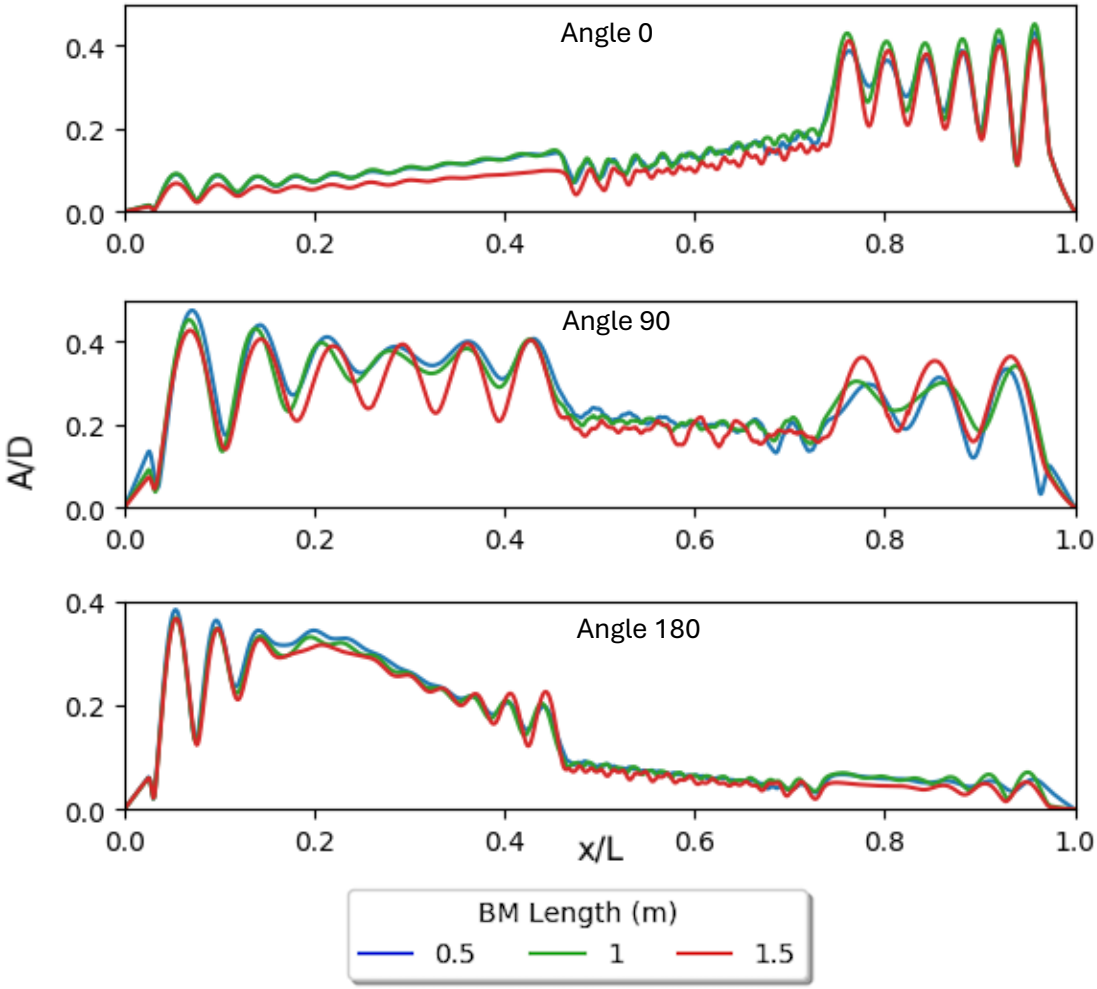

Figure 9-16: A comparison of the RMS displacement for different buoyancy module length for a buoyancy module to cable ratio of 2 to 1

There were much more notable changes in RMS displacement when varying the buoyancy module length for a ratio of 2 to 1 compared to the 1 to 1 ratio, seen in Figure 9-16. There was a notable drop in RMS displacement along the full cable length for all current angles as the BM length increased. The greatest discrepancy observed was for a buoyancy module of length 1.5m. The 0.5m and 1m lengths produced very similar displacement profiles for all current angles with a slight decrease in displacement for the 1m compared to the 0.5m. This was likely due to the longer buoyancy module disrupting the VIV interaction more substantially and suppressing the vibrations along the buoyancy section. Cable deformation will also have had an impact.

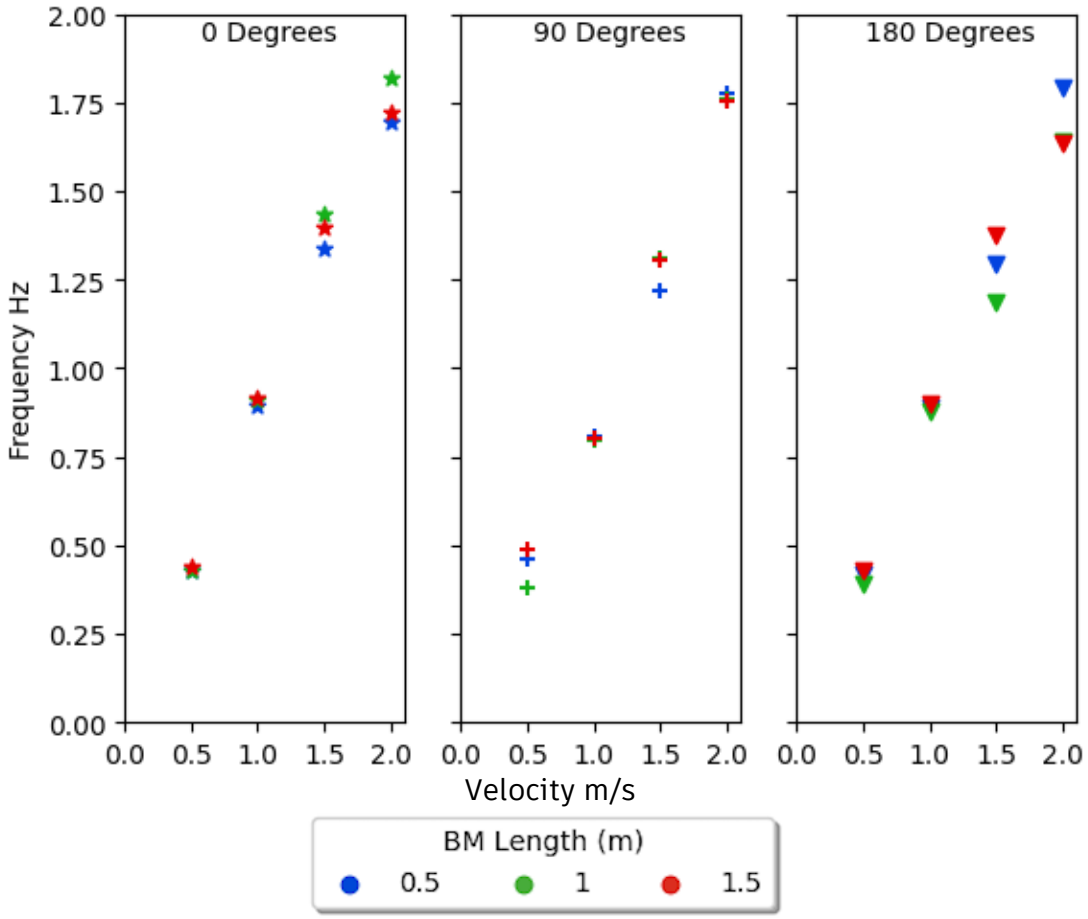

Figure 9-17: A comparison of the vibration frequency for different buoyancy module for a buoyancy module to cable ratio of 2 to 1

There was no obvious pattern or dependency of the frequency of vibrations on the length of the buoyancy module for a ratio of 2 to 1 seen in Figure 9-17. When comparing the frequency of vibrations for different current angles there were no overarching trends observable with all angles of propagation resulting in similar frequencies.

9.3.3 Cable to Buoyancy Module Ratio of 3 to 1

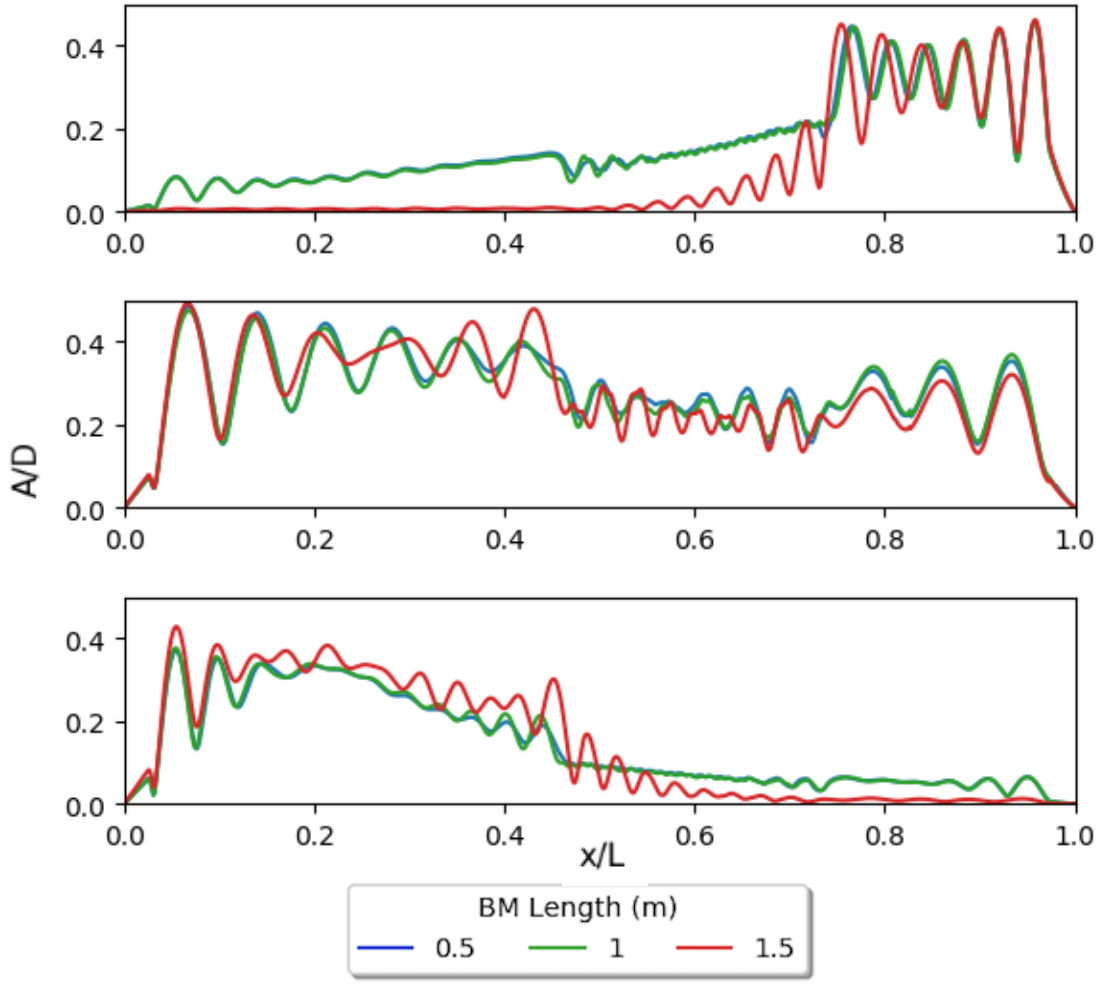

Figure 9-18: A comparison of the RMS displacement for different buoyancy module length for a buoyancy module to cable ratio of 3 to 1

As is shown in Figure 9-18 the buoyancy module lengths of 0.5 and 1m followed a very similar displacement profile with very little discrepancy for all current angles. Similar to the 2 to 1 ratio, a buoyancy module length of 1.5m resulted in a substantial change in the RMS displacement profile over the cable length. This was most notable for current angles 0 and 180 degrees. For a current angle of 0 degrees this resulted in close to zero amplitude of vibrations up to a length of 0.6 *x/L* followed by vibrations of large displacement at the same amplitude as for the maximum of the other buoyancy module lengths.

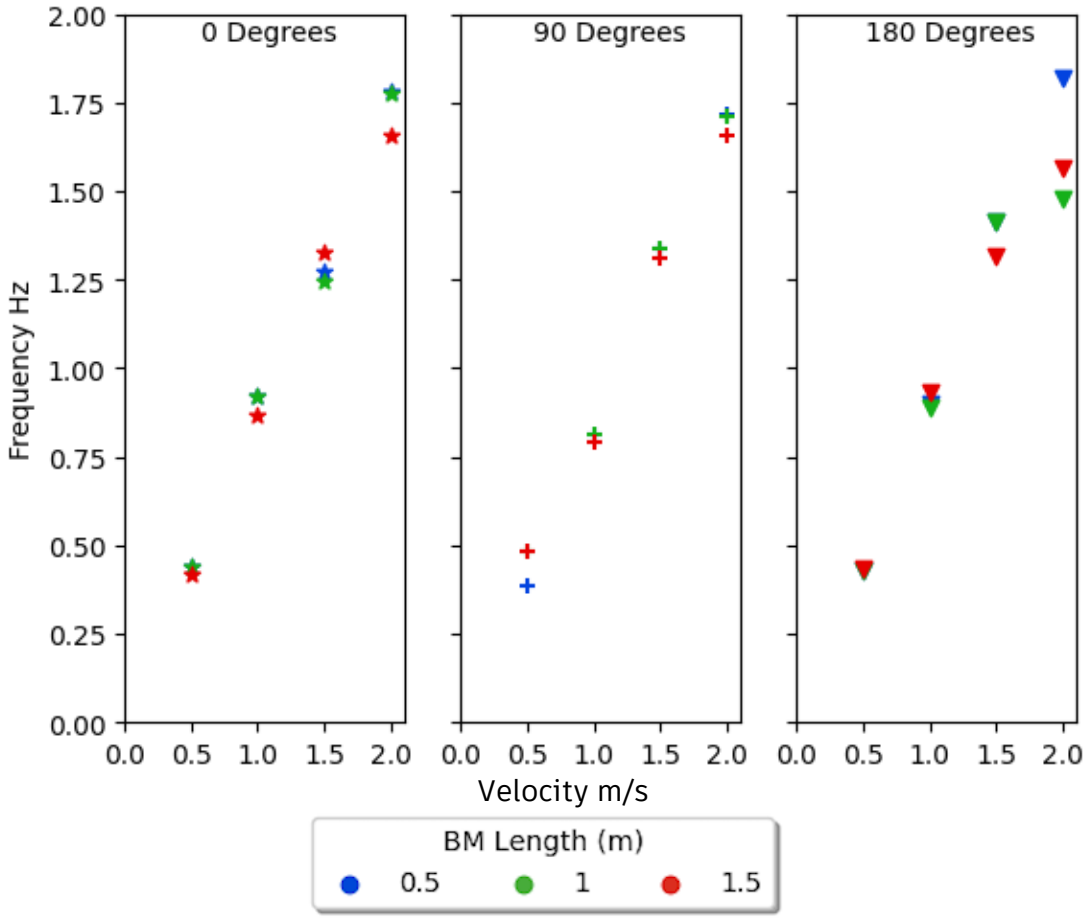

Figure 9-19: A comparison of the vibration frequency for different buoyancy module for a buoyancy module to cable ratio of 3 to 1

When comparing the frequency of vibrations seen in Figure 9-19 there was no definite trend over all current angles and speeds. However, on average the larger the buoyancy module length the lower the frequency of vibration. There were notable discrepancies to this trend.

9.4 Buoyancy Module Diameter

The buoyancy module diameter was varied to determine the influence this had on behaviour. To ensure this didn't impact the static cable position, the density of the module was adjusted to maintain the correct lazy wave shape at static location in still water. The cable tested was Flotant and a uniform current profile of 1m/s was used. The ratio of the diameters, R_D is outlined below.

$$R_D = D_{BM}/D_C$$

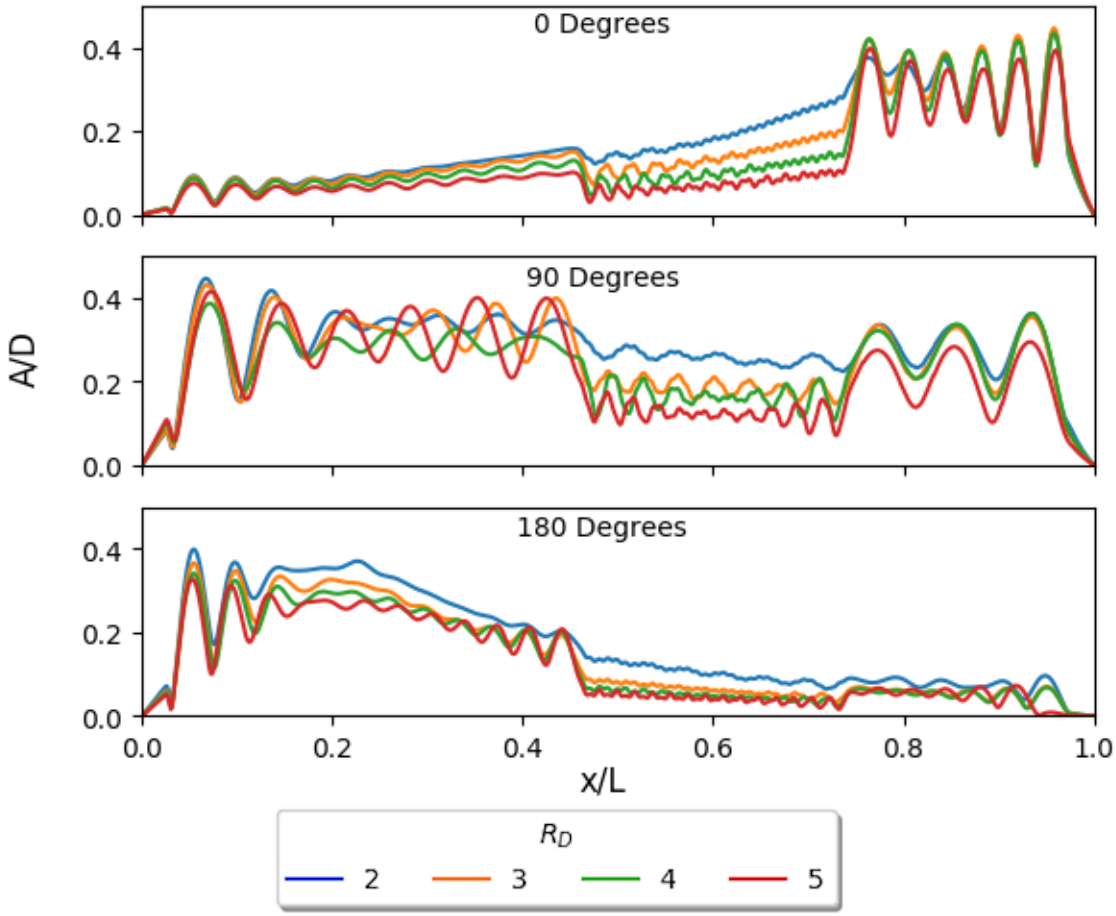

Figure 9-20: : A comparison of the RMS displacement for different buoyancy module diameters

The results in Figure 9-20 highlighted the substantial influence that the diameter of the buoyancy modules had on the RMS displacement. This was likely due to a variety of factors, including mass ratio, diameter change, cable deformation, induced drag forces, and mode of vibration. The greater the diameter of the buoyancy module the lower the amplitude of vibrations. A greater discrepancy in diameter between the cable and BM meant greater interference on the development of VIV along the buoyancy module section. This was particularly exemplified at a current angle of 90 degrees where, prior to buoyancy module mid-section, the displacement profile was similar for all diameter ratios but diverged greatly at this location for all ratios.

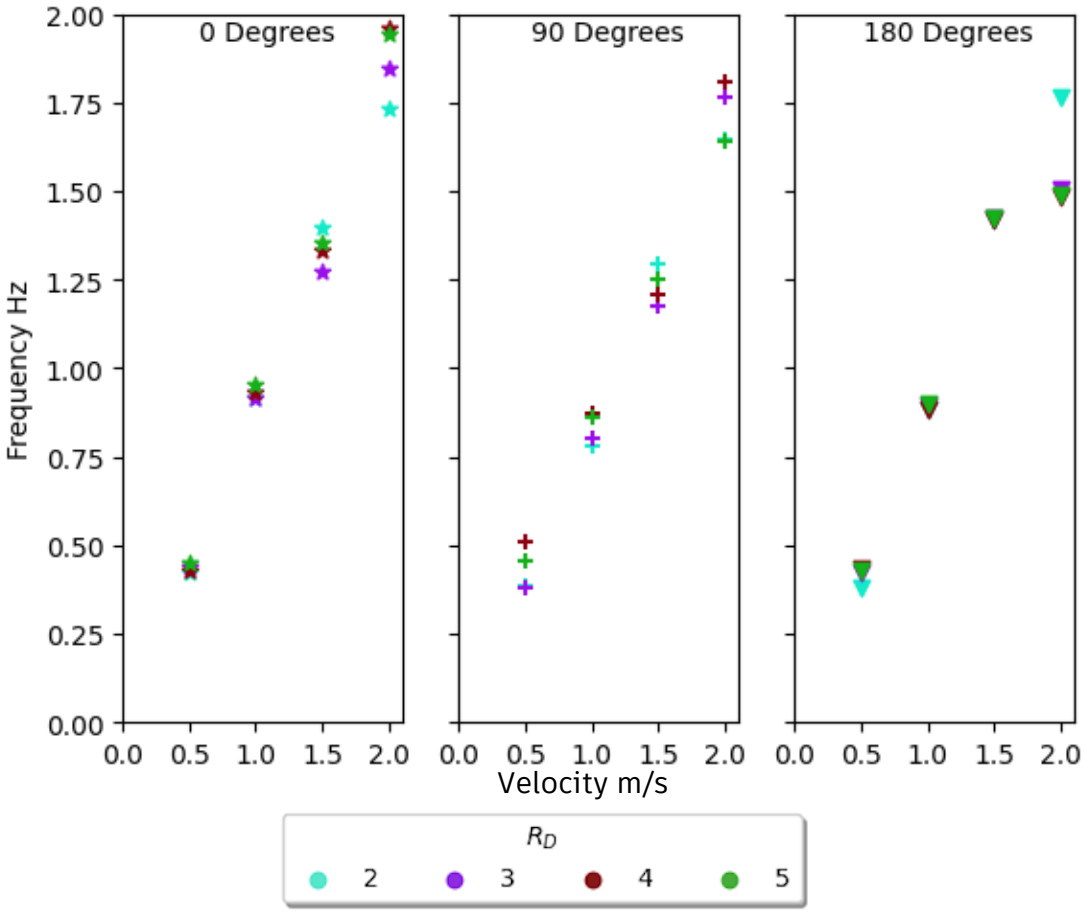

Figure 9-21: A comparison of the vibration frequency for different buoyancy module diameters

Shown in Figure 9-21, there were some notable variations in the frequency of vibrations as current speed varied, however, there was no overarching trend on the frequency dependency on different buoyancy module diameters. A current angle of 0 degrees resulted in the largest frequency of vibrations. For an angle of 180 degrees all ratios apart from the smallest didn't result in a significant increase in frequency as the speed increased from 1.5 to 2.0 m/s. This was predicted to be due to the limitations in cable deformation that could occur at this angle for the larger diameter buoyancy modules.

9.5 Marine Growth

9.5.1 Gran Canaria

The impact of marine growth was investigated, this was modelled as increasing the diameter and mass per unit length of the cable. The impact of bending stiffness and drag was not considered. The thickness of the cable was increased by 100mm from sea level to 40m depth and 50mm from 40m depth to the seabed. The marine growth was assumed to have a constant density of 1325 kgm^{-3}. This is generally a poor way to model marine growth as in reality it doesn't form uniformly, the majority of it is permeable, and discrepancies in its local geometry have significant influences on VIV and drag.

However, without access to relevant hydrodynamic data and no way to model this within OrcaFlex or Shear7, the described method was used, and the limitations are acknowledged.

The cable properties were that of Flotant, and the site was Gran Canaria with a tethered wave configuration and using the site specified shear current profile.

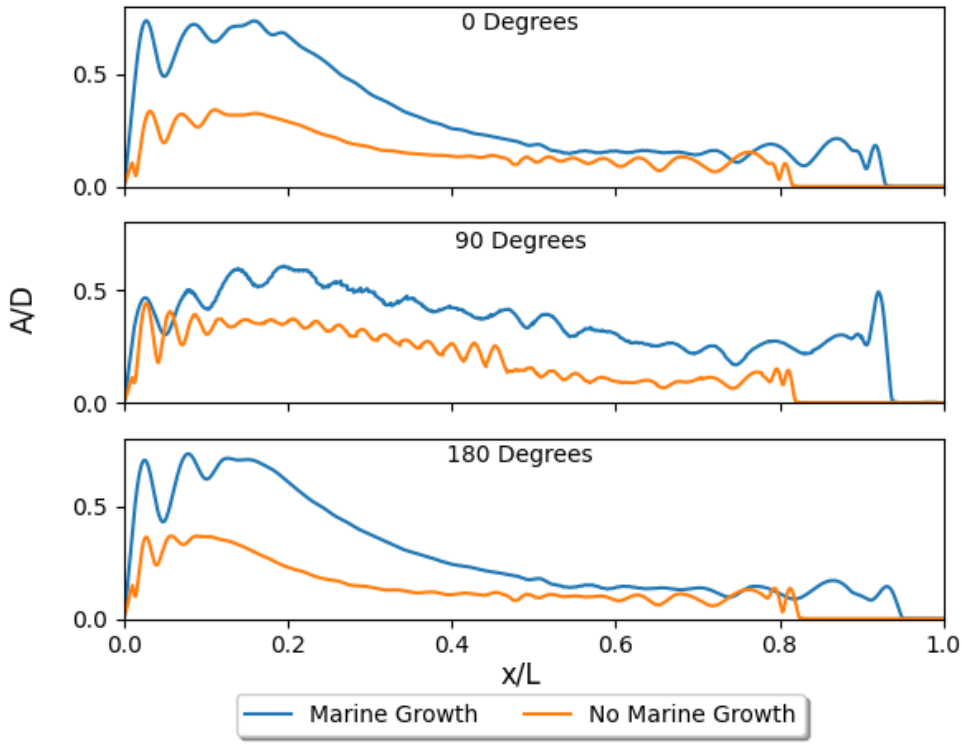

Figure 9-22: A comparison of the RMS displacement for the presence of marine growth for a tethered wave cable configuration and relevant site conditions

With the inclusion of marine growth, the RMS displacement was notably impacted, as shown in Figure 9-22. For all current angles there was an increase in RMS displacement over the entire cable length when marine growth was modelled. It is important to consider marine growth when modelling the full life of a cable as marine growth as it is known to impact risers.

Greater amplitudes of vibrations were likely due to the increase in diameter resulting in greater incident forces. For both simulations the diameter, *D*, was assumed to be the original cable diameter which will also have substantially impacted these results. With marine growth, additional sections of the cable along the seabed were also excited. This was likely due to the increased drag on the cable meaning additional cable was elevated off the seabed and thus susceptible to VIV.

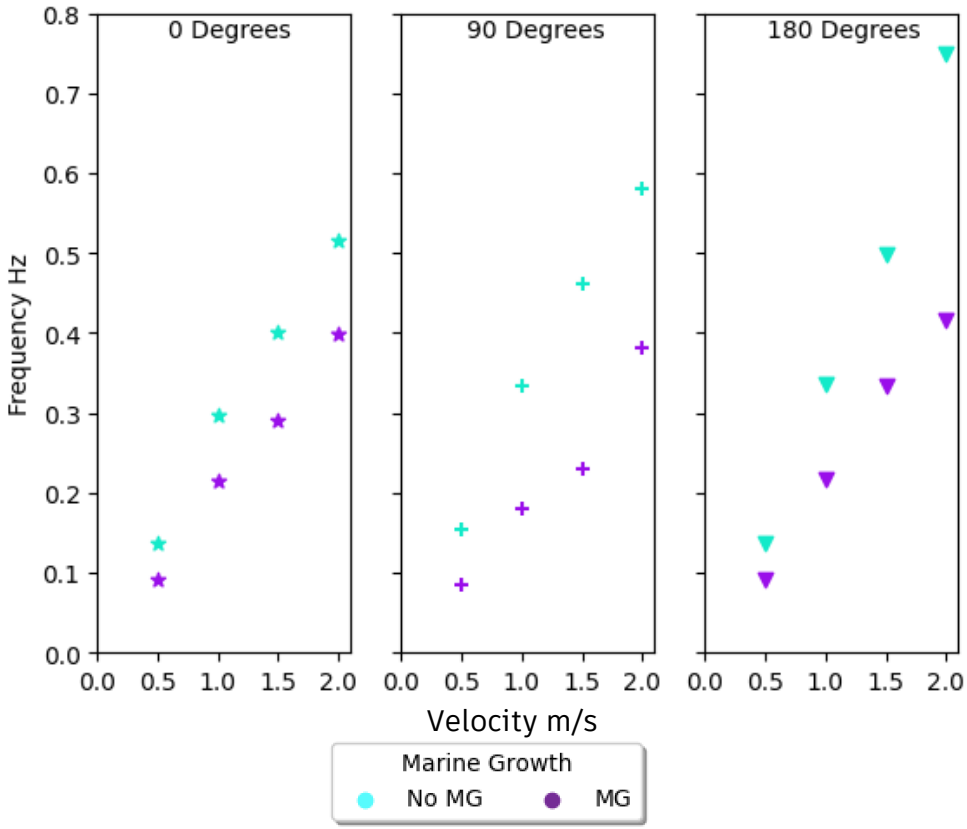

Figure 9-23: A comparison of the vibration frequency for the presence of marine growth for a tethered wave cable configuration and relevant site conditions

Comparing the frequencies seen in Figure 9-23, it can be observed that the inclusion of marine growth had a substantial impact on the vibration frequency for all current angles. The inclusion of marine growth resulted in reducing the frequency of vibrations by approximately 20% for 0 degrees, 25% 90 degrees, and 40% for 180 degrees. This was due to the increase in diameter and, as seen in Chapter 6.4, the lower the diameter the larger the modes of excitation. This trend was evident for all current angles.

9.5.2 West Bara

The impacts of marine growth were also considered for the West Barra site. The parameters used were the respective site current profile, steep wave configuration, and cable properties for the site.

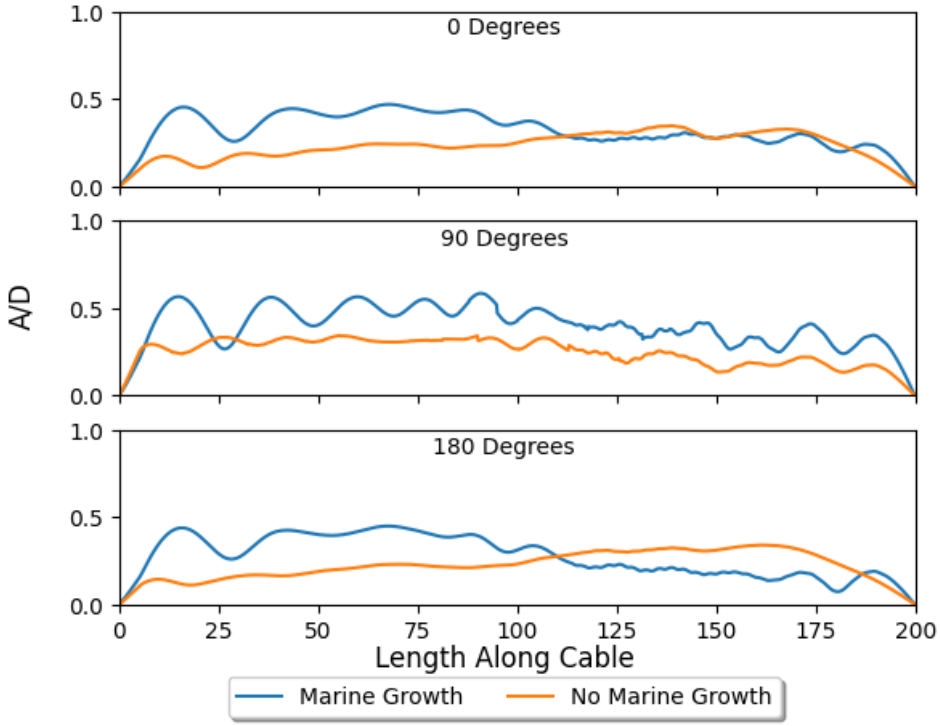

Figure 9-24: A comparison of the RMS displacement for the presence of marine growth for a steep wave cable configuration and relevant site conditions

As can be seen in Figure 9-24, marine growth was shown to impact the VIV profile for the West Barra site, however, the behaviour differed from what was seen for the Gran Canaria site. Unlike Gran Canaria there was no consistent increase in RMS displacement over the entire cable length for all current angles.

For a current angle of 0 degrees, the RMS displacement for the marine growth cable was larger at the hang-off point than the cable without marine growth, however, from the cable midsection to touchdown point the displacement profile was similar. This RMS displacement profile was likely due to the inclusion of marine growth resulting in a stiffer and heavier cable, meaning less deformation was able to occur relative to the cable without marine growth. The less extreme the cable deformation the less extreme the variations in normal relative velocity along the cable's length, meaning the less extreme the variations in amplitude. A current angle of 180 degrees also resulted in a similar displacement profile, in terms of both magnitude and location dependency, to the current angle 0 degrees. Again, this was due to the reduction in cable deformation.

A current angle of 90 degrees reproduced the trend shown for Gran Canaria and resulted in greater displacement over the full cable length. For a current angle of 90 degrees the normal relative velocity was already consistently larger over the full cable length, so deformation naturally had a reduced influence on RMS displacement.

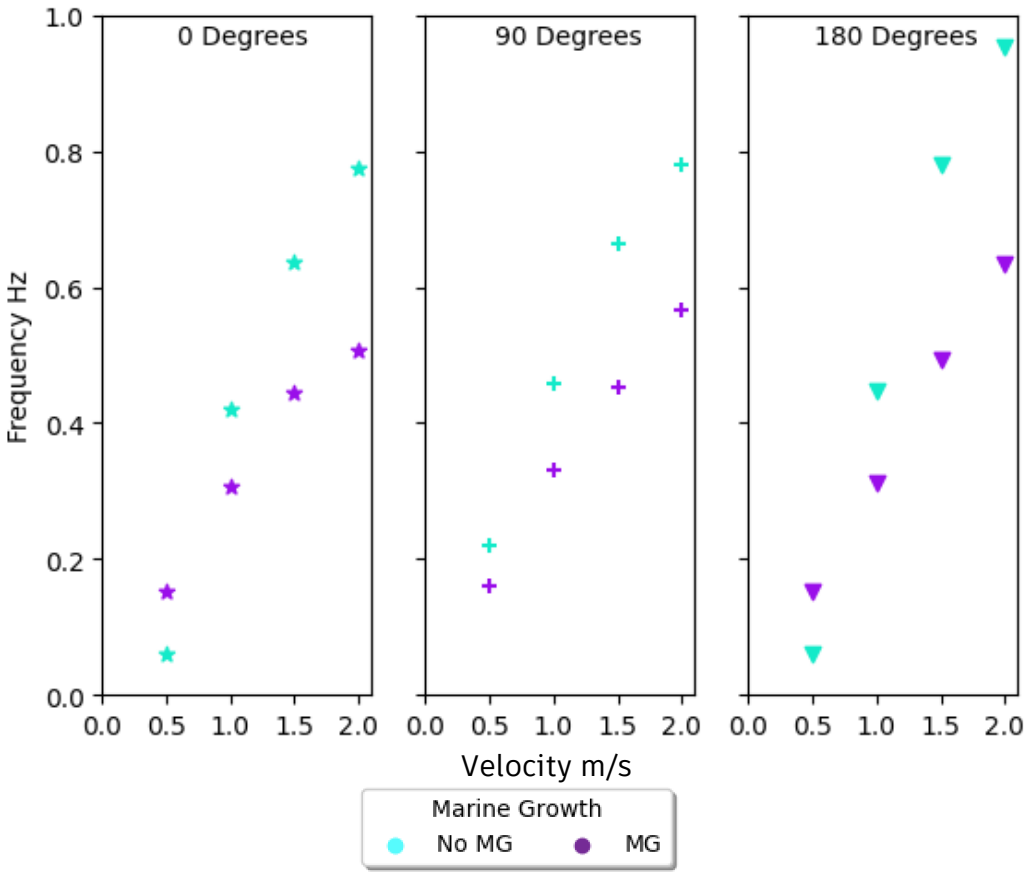

Figure 9-25: A comparison of the vibration frequency for the presence of marine growth for a steep wave cable configuration and relevant site conditions

When comparing Figure 9-25, it is noted to be similar to the previously observed trend in Figure 9-23, marine growth also has a notable influence on the vibration frequency for the West Barra site and cable. When comparing to the cable with no marine growth, if MG was modelled the frequency of vibrations was reduced. This was due to the increase in diameter and the similar relative velocities resulting in the thinner cable experiencing greater frequency of vibrations. This trend was evident for all current angles.

9.6 STRAKING

The impact of deploying helical straking was investigated. Helical straking was modelled along different sections of the cable. The method for modelling was using specifications from the Shear7 UserGuide and adjusting various parameters accordingly. The cable used for testing was Flotant and a uniform current profile of speed 1m/s was used. The numerical parameters used for modelling the helical straking and how they alter the properties of the cable are shown in Table 9-2.The straking was modelled by varying the mass, diameter, added mass coefficient and lift coefficient table based on the Shear7 UserGuide.

Table 9-2: Straking Properties

Mass kg/m	0.0337 (Original = 0.0229)
C_a	2
St	0.1
Bandwidth	0.25
Lift Coefficient Table	5
Damping A/D Still Water	0.4
Low V_r Regions	0.5
Diameter	1.25 * D_O

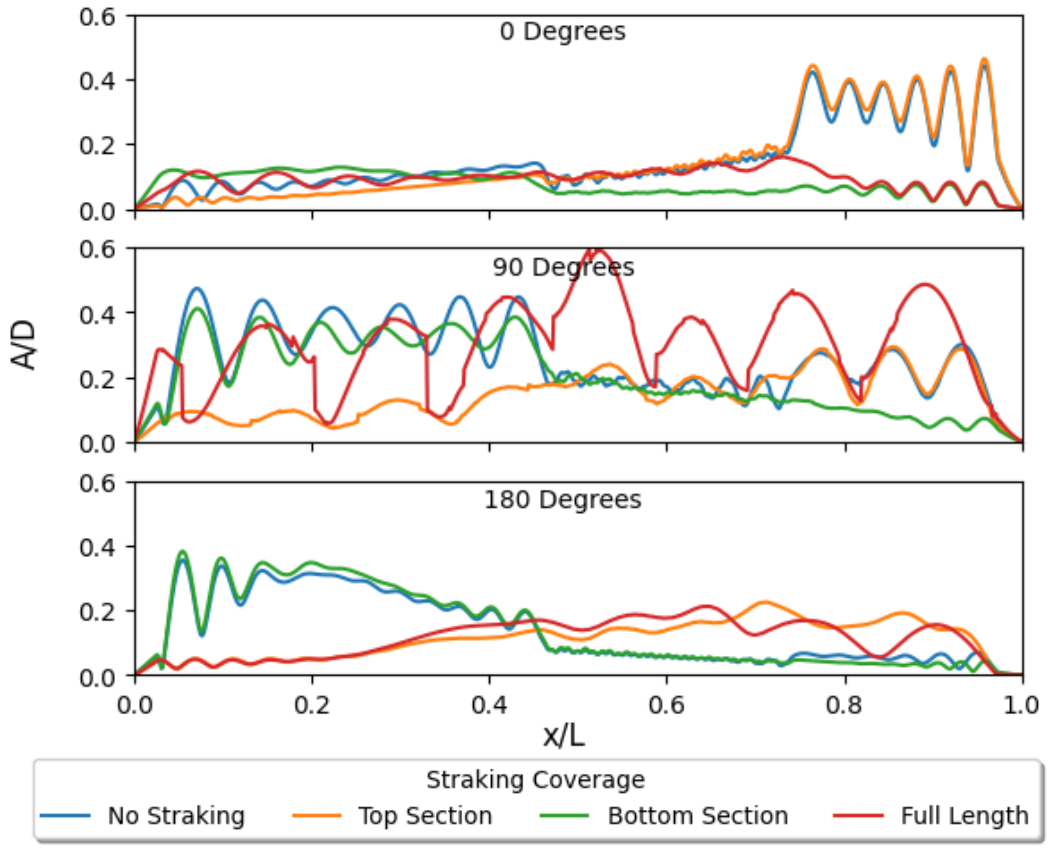

Figure 9-26: A comparison of the RMS displacement over the full cable length for different straking coverages

Figure 9-26 highlights the strong dependence of the RMS crossflow displacement on the section of the cable where straking was deployed. When compared to a power cable without straking, deploying straking over the full length of the power cable resulted in substantially differing behaviour, vibrating at lower mode numbers and different amplitudes. With full coverage over the cable's length, it was to be expected that different behaviour would be observed. For a current angle of 90 degrees a notably different displacement profile over the full cable length was seen compared to all other straking configurations. When comparing the vibrations profiles, for a current angle of 0, depending on the straking configuration, the VIV behaviour, in terms of both amplitude and frequency of vibrations, was similar to when straking was only deployed along the bottom section. For a current

angle of 180 degrees, this was also observed but instead for when straking was only deployed along the top section.

When considering the other straking coverages, it could be observed that for a current angle of 90 degrees the section of the cable where straking was not present resulted in similar RMS displacement profile compared to the fully non-straked cable. The sections that were straked, however, were substantially suppressed and vibrated at very low amplitudes. Either side of the buoyancy section, the section without straking closely followed the non-straked cable's VIV profile. This suggests that the buoyancy module and lazy wave bend section resulted in splitting the cable into two different potential excitation zones. This would mean that the VIV behaviour is strongly dependent on two different excitation frequencies, separated by the buoyancy section, at the touchdown and hang-off points. This could result in different fatigue profiles and different fatigue life factors being required for the pre and post buoyancy sections.

For current angles of 0 and 180 degrees, different behaviour was seen. If straking was only present along the top section of the cable, then similar VIV behaviour as for the non-straked cable at an angle of 0 degrees was observed. If straking was only present along the bottom section, then similar VIV behaviour as for the non-straked cable at angle of 180 degrees was observed. The result of this was that even if only straking the section particularly prone to vibrations, depending on the current angle, then the VIV behaviour along the full cable length was suppressed. This could lead to cost savings by reducing the amount of straking required.

When comparing whether the VIV behaviour was dominated by tension or bending stiffness, the parameter *P* from Eq. 3.19 was used, and the results are shown in Table 9-3. All straking configurations over all current angles were shown to have a large influence on the dynamic behaviour of the cable. There was a substantial decrease in the value of *P* when straking was deployed compared to when not. This indicates that when straking is deployed, the cable response is dictated by bending stiffness over tension.

Table 9-3: Impact of straking coverage on the structural dynamic behaviour

Current Angle	No Straking	Full Straking	Bottom Section Straking	Top Section Straking
0	2.70	0.15	0.16	0.20
90	45.8	1.48	1.48	1.26
180	7.19	0.54	0.40	0.58

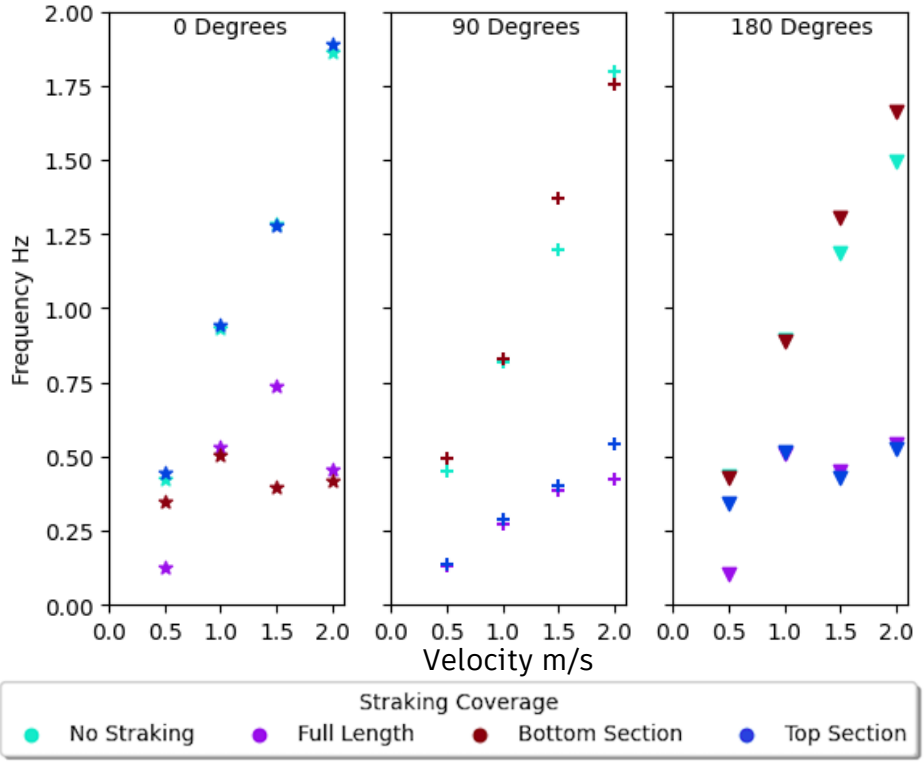

Figure 9-27: A comparison of the vibration frequency for different straking coverages

Shown in Figure 9-27, the cable without straking resulted, on average, in the largest frequency of vibrations across all current angles. This was to be expected as it was allowed to vibrate without any deployed suppression methods influencing the VIV response.

For a current angle 0, the top section straking coverage had similar frequency to the non-straked cable. This was because VIV was dominated by the interactions towards the touchdown point at this current angle due to the cable deformation that occurred. Straking along the top section of the cable didn't influence the VIV at the touchdown point.

The cable with bottom section straking coverage resulted in a similar VIV frequency as the non-straked cable for both 90 and 180 degrees. This was likely due to at both these current directions the cable section towards the hang-off point dominated the VIV response and thus the frequency of vibration. Deploying straking towards the touchdown point only suppressed the VIV along here which didn't impact the most dominant frequency at the hang-off point.

The fully straked cable resulted in the lowest frequency of vibrations for all current angles and speeds. These interactions show how important it is to factor in the current direction when deploying straking as under certain conditions it may be unnecessary along certain sections of the cable length.

9.7 Removal of Buoyancy Modules

The impact of removing buoyancy modules was investigated. This was modelled to highlight how sensitive the VIV response was to any changes in the buoyancy module number as there is no current preferred deployment number. At each iteration one buoyancy module was removed from the top and bottom ends of the buoyancy section. Subsequent removal of buoyancy modules resulted in increasing the depth of the sag and hog bend. The cable configuration was originally a lazy wave shape, Martinelli's cables properties, and a uniform current profile of 1m/s.

For all current angles, as the number of modules removed increased the touchdown point became closer to the hang-off point in the spatial plane. This was to be expected, the less the number of buoyancy modules the faster the cable approached the seabed as the cable configuration tended towards a catenary arrangement.

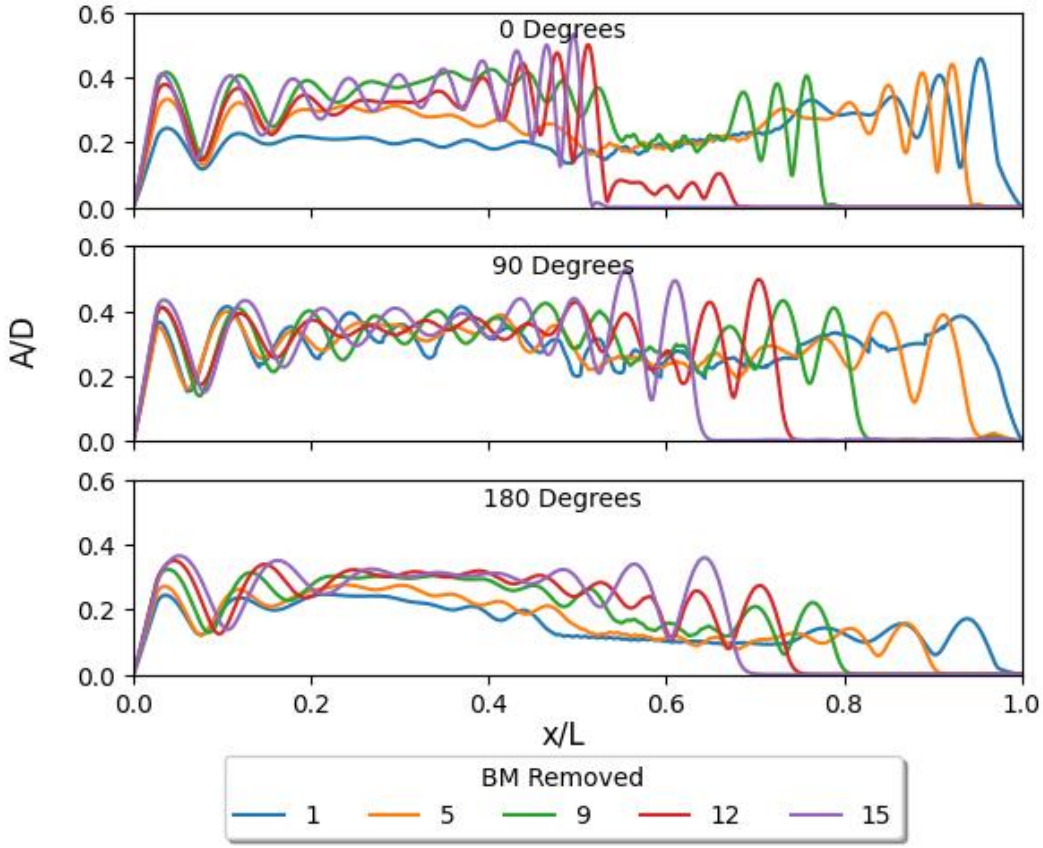

Figure 9-28: A comparison of the RMS displacement over the full cable length for different numbers of buoyancy modules

There were notable differences in the VIV behaviour as buoyancy modules were removed, as shown in Figure 9-28. The general trend is, that the greater the number of BM removed the less extreme the variations in the magnitude of the RMS displacement profile compared over the full cable length. This was due to decreases in the cable deformation for the same current speed as an increased length of

the power cable rested on the seabed. Earlier touchdown of the cable to the seabed was also seen as the buoyancy modules were removed.

When considering a current angle of 0 degrees, as the number of buoyancy modules was removed the mean RMS displacement up to the touchdown point increased, the touchdown point was earlier and the differences in amplitude over the full cable length were less. When comparing the difference in the RMS displacement amplitude at the hang-off point to the point of maximum displacement over the full cable length; for 12 buoyancy modules removed it was only ~25% greater compared to an increase of ~100% for when only 1 buoyancy module was removed.

For a current angle of 90 degrees, as the number of buoyancy modules removed increased the maximum displacement towards the touchdown point increased. The displacement profile towards the hang-off points remained similar for all buoyancy module numbers.

The RMS displacement profile for a current angle of 180 degrees showed a strong correlation to the number of buoyancy modules. As the number of buoyancy modules decreased there was an obvious increase in mean RMS crossflow displacement over the full cable length up to the touchdown point, with the most notable increases also observed at this point.

The removal of buoyancy modules changed the cable shape and meant it was less susceptible to large deformations. This in turn suppressed the more substantial variations of the normal relative velocity along the cable's length. This highlighted the dependence of the VIV behaviour on the cable configuration. Even when removing only a small number of modules the difference in the RMS crossflow displacement profile was significant. This was not only due to more of the cable being exposed, but also because the shape of the lazy wave cable was being altered (fewer modules lowered the sag and hog bends). Further to this, an increased portion of the cable ran along the seabed reducing the VIV towards the touchdown point and changing the effective length of the cable.

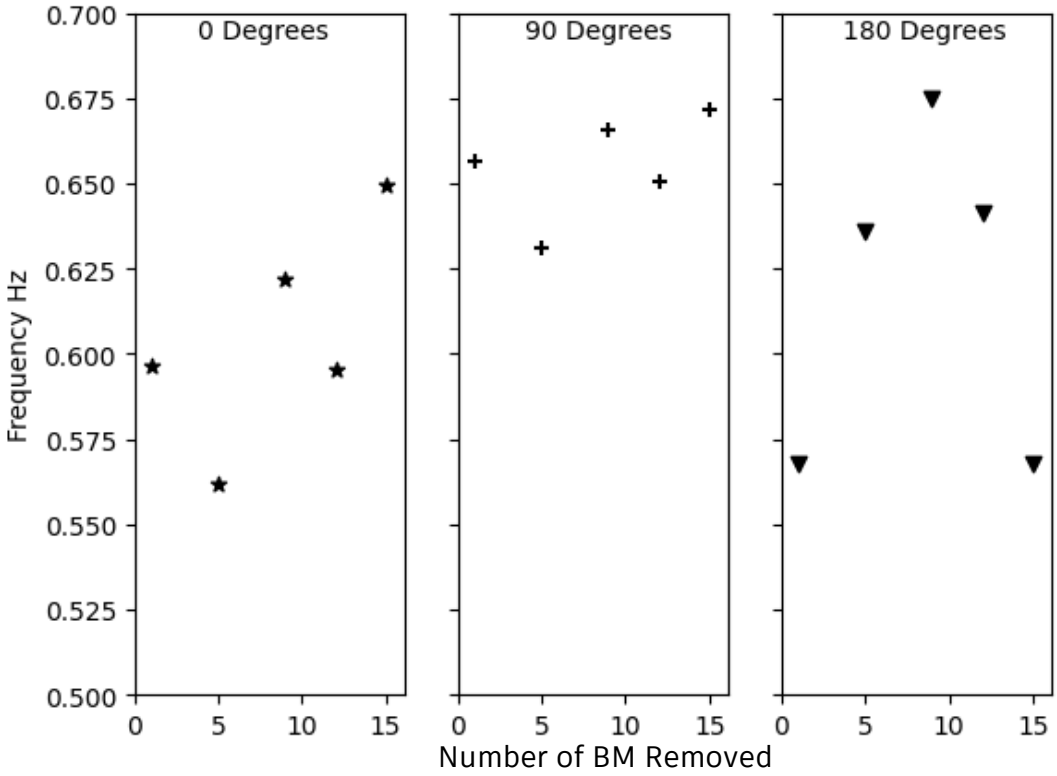

Figure 9-29: A comparison of the vibration frequency for different numbers of buoyancy modules

When considering the influence of the removal of buoyancy modules on the frequency of vibrations, current angles of 0 and 90 degrees resulted in a similar pattern where the greater the number of buoyancy modules removed the greater the frequency of vibrations. This is shown in Figure 9-29. This trend wasn't definite over every value but was discernible when comparing over the full data range. This behaviour was due to the removal of buoyancy modules altering the cable's position in the water and thus the normal relative velocity.

A current angle of 180 degrees, however, substantially deviated from the trend seen for angles 0 and 90 degrees. A current angle of 180 degrees resulted in a peak frequency observed when 9 modules were removed and decreased when either more or less modules were removed. As buoyancy modules were removed the depth of the sag and hog bend increased, meaning a greater portion of the cable towards the hang-off point was directly perpendicular to the direction of the current.

9.8 CONCLUSION

In addition to the cable properties, other external parameters that can influence the VIV behaviour were investigated. These were the straking, marine growth, and buoyancy module configuration. Different sections of the cable length were straked to determine the effect this had on the RMS crossflow displacement and the frequency of vibration. The straking deployment arrangements were for the full length of the cable, the section from hang-off point to start of buoyancy section, and the

section from the end of the buoyancy section to the touchdown point. Full straking coverage was found to, expectedly, drastically change the RMS displacement and mode of vibration for all current angles. An interesting observation was that if straking was only deployed along the top or bottom sections then the impact this had on the RMS displacement was dependent on current direction.

For a current angle of 0 degrees, if only the top end of the cable was straked then the VIV behaviour was very similar compared to a cable without any straking. This is because the most significant vibrations for a current angle of 0 degrees were observed at the touchdown section, so straking at the top section had little to no impact on the VIV behaviour. For a current angle of 180 degrees the opposite behaviour was observed. If straking was only deployed along the bottom section, then there was minimal impact on RMS displacement over the full cable length when compared to a cable without straking. For a current angle of 90 degrees, all straking configurations had an influence on the VIV profile compared to a cable without straking. If straking was present only on the bottom section of the cable, then this was the closest representation of the no straking profile. These results highlight how, depending on current direction, straking may be best deployed at certain locations along the cable length. When comparing the frequency, a general trend was observed where the closer the displacement profile was to the cable without straking, the closer the frequency in VIV that was observed.

The influence of marine growth on VIV behaviour was explored and found to noticeably alter the RMS displacement. For certain site conditions it can result in VIV over double the amplitude compared to a cable without marine growth. For the Gran Canaria site, overall, a similar displacement profile was seen for all current angles with the location of maximum displacement the same whether marine growth was present or not. The main difference was the magnitude of the vibrations, marine growth saw a substantial increase, up to double, for all current angles. For West Barra site the marine growth had a different influence on the VIV behaviour. It resulted in a mean increase in RMS displacement for all current angles. An angle of 0 degrees saw larger displacement at the hang-off point and similar at the touchdown section. An angle of 90 degrees saw an increase of the RMS displacement of 25-100% depending on location along the cable. For 180 degrees the amplitude was much larger at the hang-off point but lower towards the touchdown point. When comparing the influence of marine growth on the frequency, the inclusion of marine growth saw a reduction in the RMS displacement of 15-30%, depending on current angle and cable configuration.

The length, diameter, and ratio of cable to buoyancy module were all investigated. Increasing the diameter of the buoyancy module was found to reduce the magnitude of RMS displacement while having minimal influence on the frequency of vibration. This response was likely because a buoyancy

module with a larger diameter had greater interference on the VIV that develops along the cable sections. This resulted in a suppression of the VIV; thus, smaller displacement was seen.

The influence of altering the length of the buoyancy modules was found to be dependent on the ratio of cable to buoyancy module. For a ratio of 1 to 1, only a current angle of 90 degrees showed any changes. These changes being a slight increase in the RMS displacement along the upper section and a decrease along the lower section. When comparing the frequency, a trend was seen where the longest buoyancy module predicted the greatest frequency of VIV by 5-20%. For a cable to buoyancy module ratio of 2 to 1, buoyancy module lengths of 0.5 and 1m produced very similar displacement profiles. A buoyancy module length of 1.5m resulted in a near uniform decrease of 5-10% over the full cable length. No obvious trend can be discerned regarding the frequency. For a cable to buoyancy module ratio of 3 to 1, the 1.5m buoyancy module length resulted in significant discrepancies compared to the other lengths. Much larger localised extreme amplitudes were observed, especially for current angles 0 and 180 degrees. Outside of the touchdown section, for angle 0, and hang-off section, for angle 180, near to no displacement was predicted. When comparing the frequency of vibration, the 1.5m length produced the lowest estimations for all current angles.

When comparing the ratio of cable to buoyancy module, a general trend was seen where the greater the length of cable relative to buoyancy module the greater the RMS displacement. This was generally uniform across the cable lengths and buoyancy module lengths with a small increase of 5-10% seen.

10 RESULTS AND DISCUSSION – WAVES

Shear7 is a frequency domain model and as such cannot directly model the dynamic time-varying interaction of waves on a structure. Due to this, there is a gap between what is physically occurring and the numerical output from the model. The influence of the period of the waves and the potential excitation of natural frequencies of the cable was not captured. Further, the waves will disturb the VIV behaviour and impact the results. Without access to a reliable time-domain VIV model, these shortcomings are duly noted. To allow for the influence of waves to still be analysed a methodology has been proposed using time intervals equally spaced out through the wave period to capture the variable relative velocity induced by the waves. This full procedure is explained in more depth in the methodology section.

Due to the variability of normal relative velocity with time because of the introduction of waves, solely modelling the RMS crossflow displacement profile doesn't appropriately capture the potential VIV response. As such, the RMS stress was chosen as the parameter to be compared instead.

The default method within Shear7 to determine fatigue is to use a stress cycle relationship. The fatigue damage is calculated using the RMS stress, which is determined using the elastic modulus, outer diameter, and Shear7 predicted curvature. The Rayleigh formula is employed alongside a user specified SN curve to determine the fatigue damage rate. This method has been employed before by Fuglsang et al. (2023) and Dillon-Gibbons et al. (2017). One significant limitation with coupling OrcaFlex and Shear7 is the inability to model more than one S/N curve with the academic licence. This means that the stick-slip curve is unable to be factored in and, in addition, a linear SN curve is required which is not what is present in reality.

An alternative method is to use a bending stress curvature load factor (BSCLF) to predict the fatigue damage rate. This doesn't rely on the user specified elastic modulus or diameter. The methodology for determining the bending stress is shown in the equation below:

$$Stress = BSCLF \times Curvature$$

This stress is then used alongside the SN curve to determine the fatigue damage rate. The limitations with the SN curve have been discussed before and still apply to this method.

The limitations imposed by the linear SN curve mean that this will also skew all predicted fatigue damage. Due to this it was decided to compare the RMS stress for each different wave profile with the outer diameter used and the elastic modulus supplied from the cable properties. It is still stressed

that due to the inability to accurately model the expected stress of the internal components, due to the multi-layer properties and complex dependency on curvature, that the stress values presented are not intended to be accurate but provide a useful method for comparison. Determining the intra-cable behaviour and induced fatigue was not within the scope of this research.

The cable chosen for comparison in this section was Martinelli's and was in the lazy wave configuration.

Examples of how the normal relative velocity varied over a single wave period are shown in Figure 10-1. The wave period was 8 seconds, height 4m, direction 90 degrees with a colinear current of a uniform profile and 1m/s. The predicted VIV responses relative to each individual relative velocity is shown in Figure 10-2.

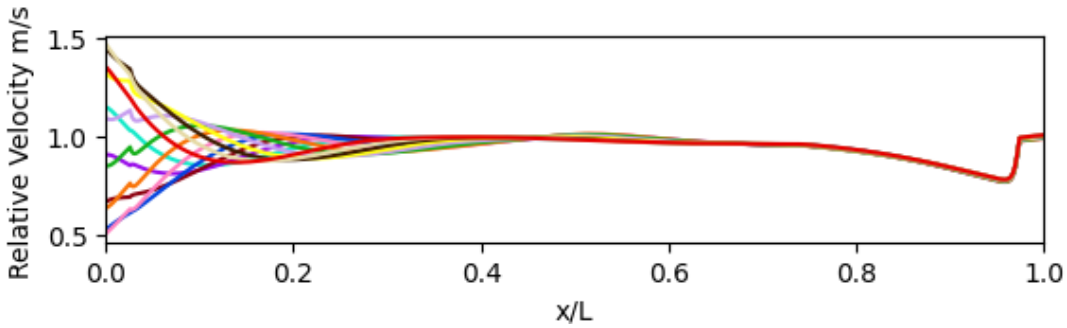

Figure 10-1: The different normal relative velocity profiles observed over each separate time instance over a full wave period

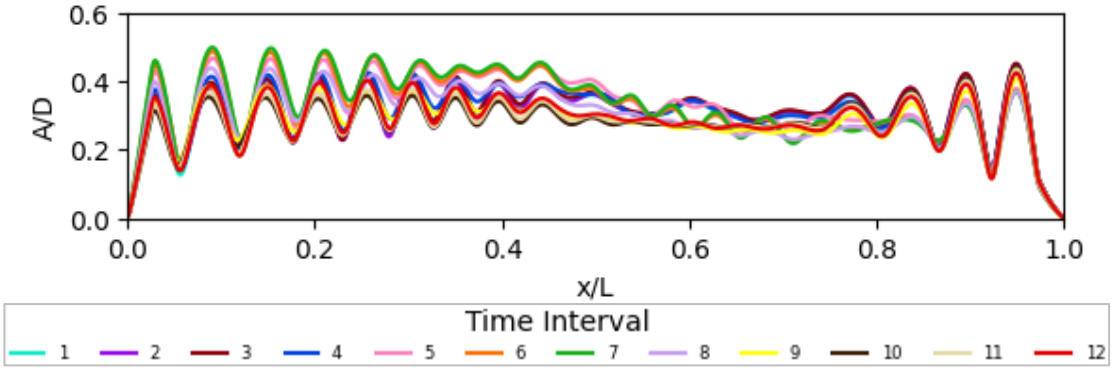

Figure 10-2: The different RMS displacements observed over each separate time instance over a full wave period

As is shown, the different normal relative velocity profiles over the wave period can have a substantial influence on the predicted RMS displacement profile. Additional calibration and validation of this method is required but is has been utilised previously by Dillon-Gibbons et al. 2017, and Fuglsang et al. 2023), and was the only method available for a frequency domain model.

10.1 Only Waves (No Subsea Currents)

An initial investigation on the influence of solely waves, with no sea current, on the VIV response was undertaken. Both the RMS displacement and the RMS stress were output for comparison. Twelve-time intervals were taken over the wave period. In this instance it was over a period of 8 seconds meaning a time interval spacing of 0.75s was used. The wave height used was 4m and was a regular Stokes 5th wave.

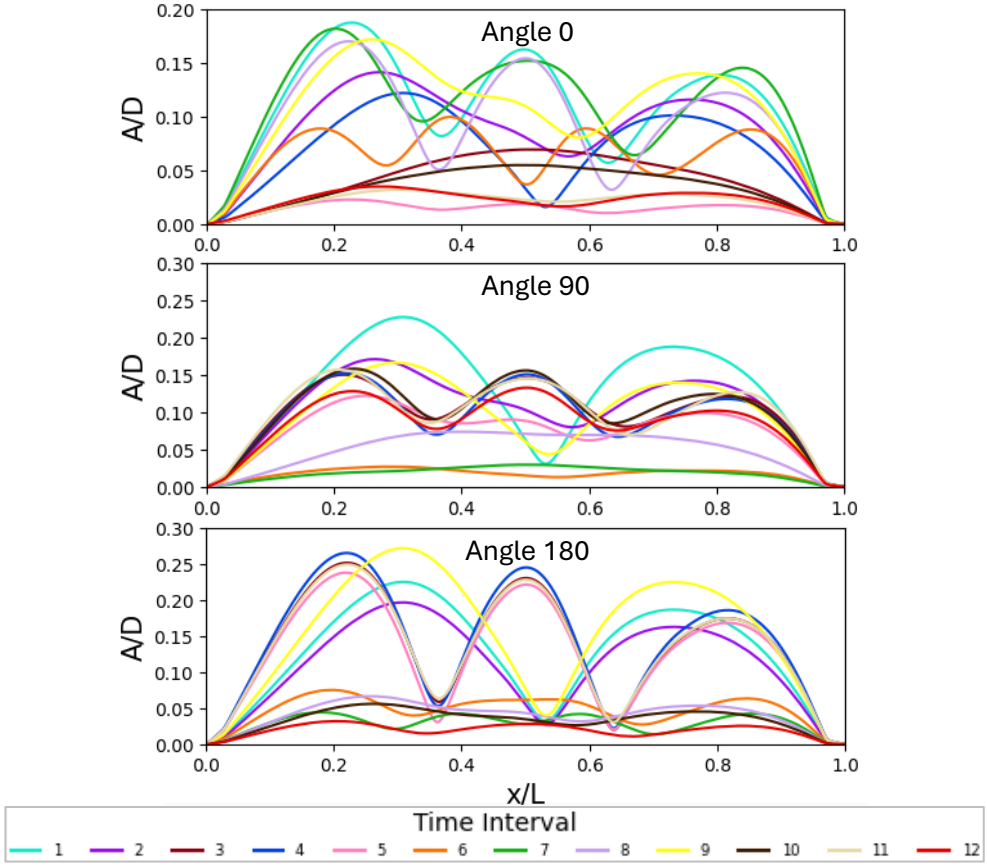

Figure 10-3: A comparison of the RMS displacement over sperate time intervals over a full wave period for wave angles 0, 90, and 180 degrees

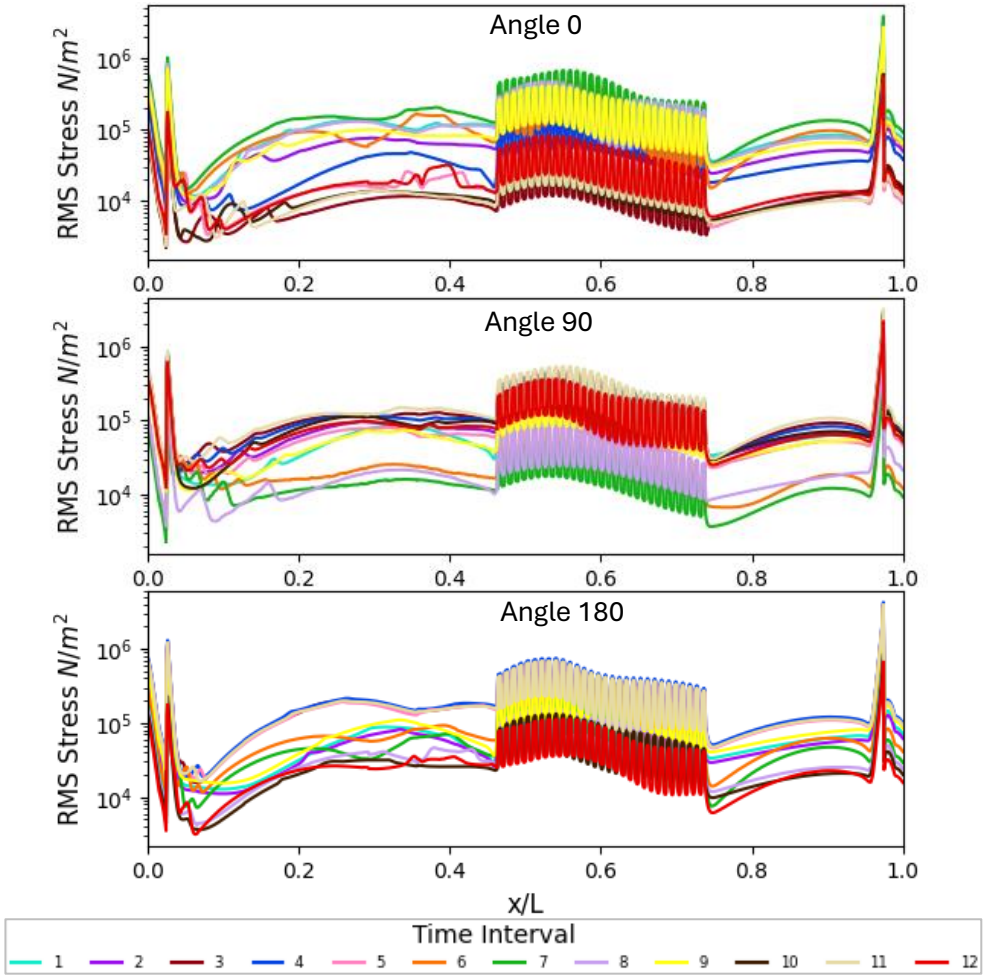

Figure 10-4: A comparison of the RMS stress over sperate time intervals over a full wave period for wave angles 0, 90, and 180 degrees

From Figure 10-3 and Figure 10-4 the wave direction was shown to have an influence on the induced RMS crossflow displacement. This was due to variations in the relative velocity that the cable was exposed to. Different wave directions resulted in different relative velocity profiles from both the cable configuration and the induced cable deformation.

When averaging over all time intervals the mean RMS stress for a current angle of 90 degrees was the largest, followed by 180 degrees, and lastly by 0 degrees. A current angle of 90 degrees resulted in the largest induced stress, due to the cable configuration and how the buoyancy mid-section was not as well positioned to absorb the wave-induced motions compared to the other angles. A current angle 0 allowed for the best absorption of the wave-induced relative velocity and cable deformation because of the orientation of the cable. The sag and hog bends were well positioned to absorb the induced displacement and diffuse the incident forces along the rest of the cable length. A current angle of 180 degrees fared better than 90 degrees due to motion absorption as well. However, this absorption was not as efficient as for a current angle of 0 degrees, this was because the initial acceleration due to the waves was away from rather than towards the buoyancy module mid-section.

When comparing the RMS stress over the different wave angles there was a similar behaviour seen, discounting the large stress peaks due to the bend stiffener. There was a gradual increase in the RMS stress from the hang-off point up to the start of the buoyancy section. At the buoyancy section large peaks in the stress are observed. This was due to the buoyancy modules and the manner of modelling the RMS stress. Shear7 considered the larger diameters of the buoyancy modules relative to the cable and assumed increases in stress due to these. After the cable midsection, the RMS stress decreased again until just after the buoyancy section. The stress then increased as the cable approached the touchdown point. The large stress at the hang-off and touchdown point was due to the large curvature here and the modelling of bend stiffeners. They were not considered in the analysis.

As can be seen in Figure 10-3 and Figure 10-4, the VIV behaviour can vary greatly depending on the time interval along the wave period that is chosen. This is predominantly due to the magnitude of the induced relative velocity from the incident wave and how this varies over the wave period. Going forward the time interval chosen for comparison was the one that induced the maximum mean RMS stress over the cable length. The maximum value of the RMS stress was chosen for comparison to be conservative.

10.2 Impact of Wave Height

The impact of the wave height on the RMS stress was investigated. The waves modelled had a period of 8 seconds and were colinear to the current direction. The predicted stress ($Stress_C$) was normalised by dividing by the RMS stress that was induced when solely current was modelled. The current profile was uniform, and the speed was varied to determine the influence this has on the current-wave interaction and deduce the relationship with wave height as well. All waves were modelled as colinear to the current direction.

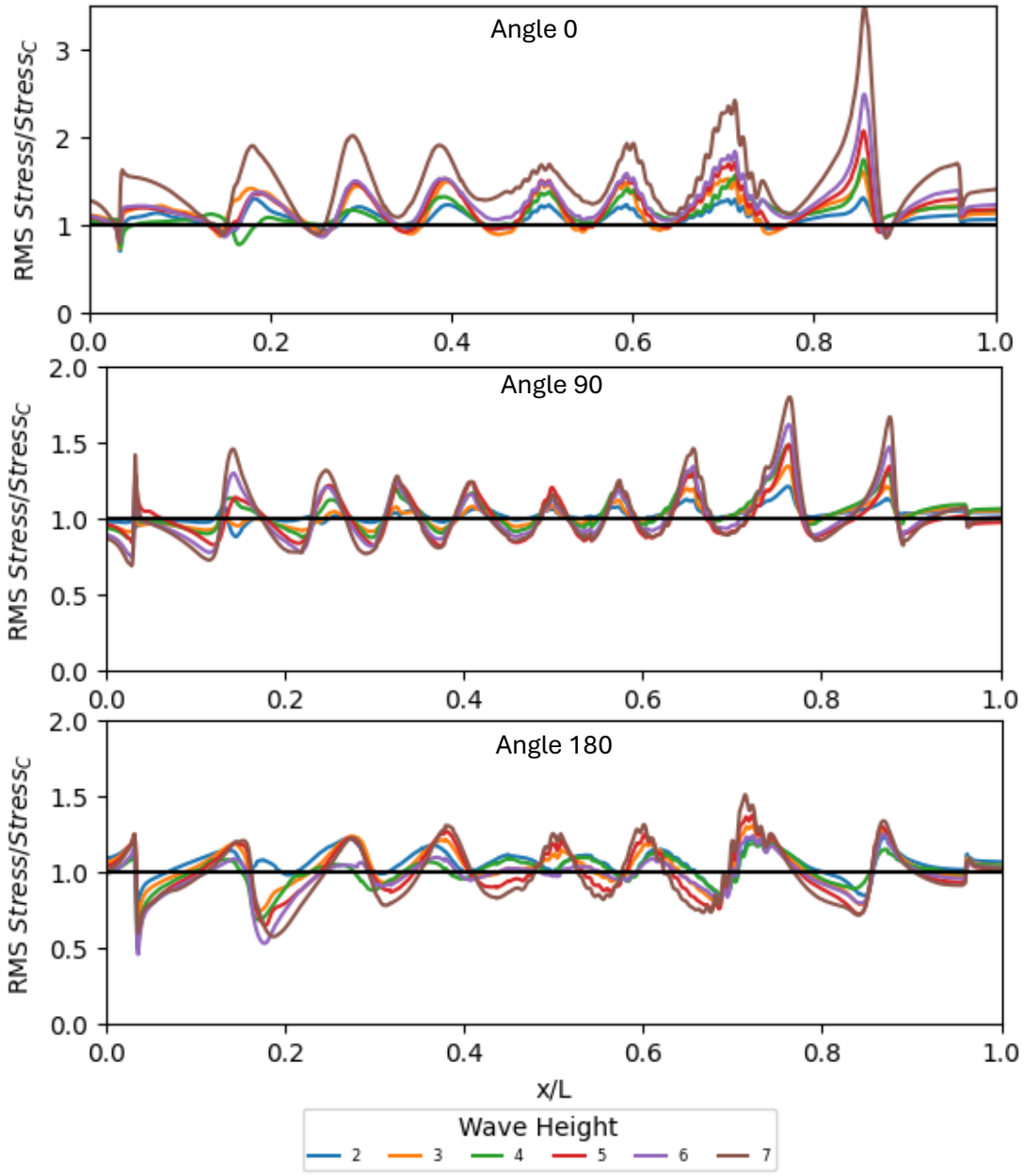

Figure 10-5: A comparison of the impact of the wave height on the RMS stress with a colinear current of uniform profile and speed 0.5 m/s

The inclusion of waves resulted in a change in the VIV behaviour when compared to just currents. Different modes of vibration were predicted causing the peak and troughs observed in the crossflow RMS displacement, as can be seen in Figure 10-5.

For a current angle of 0 degrees the inclusion of waves resulted in an increase in stress over the full cable length, this was especially noticeable towards the touchdown point. The larger the wave height the greater the induced stress. For a current angle of 90 degrees a similar observation was seen where the inclusion of waves resulted in an increase in the mean RMS stress, but not to such a large degree as for angle 0. Again, the larger the wave height the greater the increase in RMS stress compared to

when no waves were modelled. For a current angle of 180 degrees the mean stress over the full cable length was similar for all wave heights, including when no waves were modelled. The largest wave height resulted in the greatest difference compared to when no waves were modelled with larger increases in stress seen towards the touchdown point and decreases towards the hang-off point.

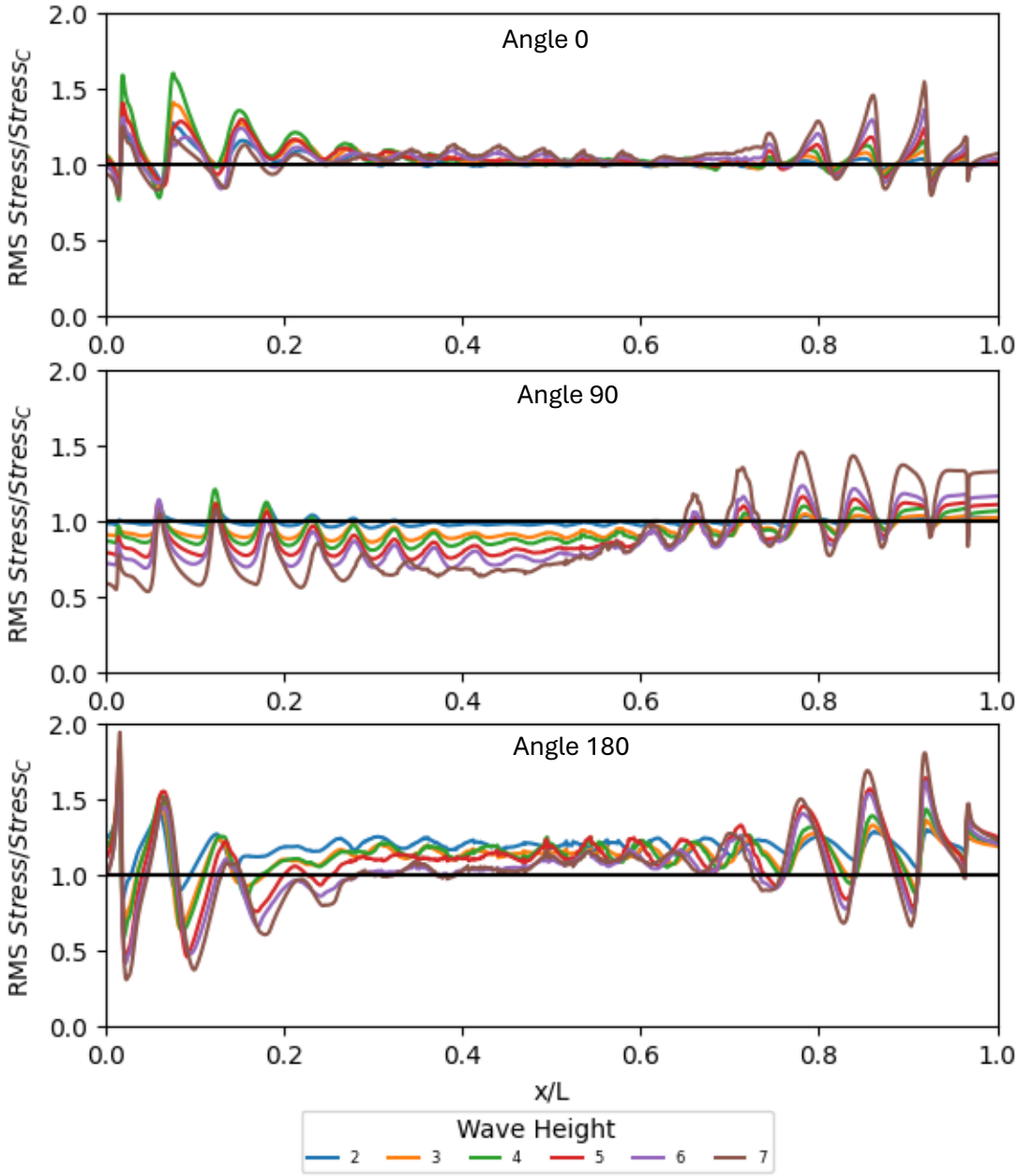

Figure 10-6: A comparison of the impact of the wave height on the RMS stress with a colinear current of uniform profile and speed 1 m/s

In Figure 10-6, the impact of waves for a current speed of 1 m/s are shown. For an angle of 0 degrees, the inclusion of waves resulted in an increase in the mean stress over the full cable length but to a lesser degree than for a current speed of 0.5 m/s. Over the full cable length, the larger the wave height the greater the mean induced stress, however, a wave height of 4m resulted in a larger stress towards

the hang-off point compared to a height of 7m. Towards the touchdown point the trend of increased stress with wave height is seen.

A trend is seen for an incident angle of 90 degrees where, as the wave height increased the stress at the hang-off point decreased while the stress towards the touchdown point increased. The location along the cable length where the mean RMS stress transition from being less than the current only RMS stress to greater than it changed with wave height. As the height increased this transition shifted earlier along the cable, towards the hang-off point. This change occurred in the range from 0.6 – 0.8 *x/L*.

For a current angle of 180 degrees the mean stress over the cable length was larger when waves were included compared to just current. A similar trend to an angle 90 degrees was seen where the larger the wave height the greater the stress at the touchdown point but the lower the induced stress at the hang-off point.

The largest discrepancies in the RMS stress are seen at the hang-off points for both angles 0 and 180 degrees and can be observed in Figure 10-7. These were due to the bend stiffener and difficulties in modelling this.

For a current angle of 0 degrees, if the bend stiffener interaction was discounted, a larger wave height led to greater induced RMS stress from the cable section extending from the hang-off point to the cable midsection, before returning to the similar magnitudes in RMS stress as for just current.

For a current angle of 90 degrees the RMS stress profile was different compared to the other current speeds. As wave height increased a larger stress was seen at the hang-off point before gradually decreasing along the cable length to just below the current only RMS stress at the touchdown section. The larger waves height showed a greater induced stress over the full cable length.

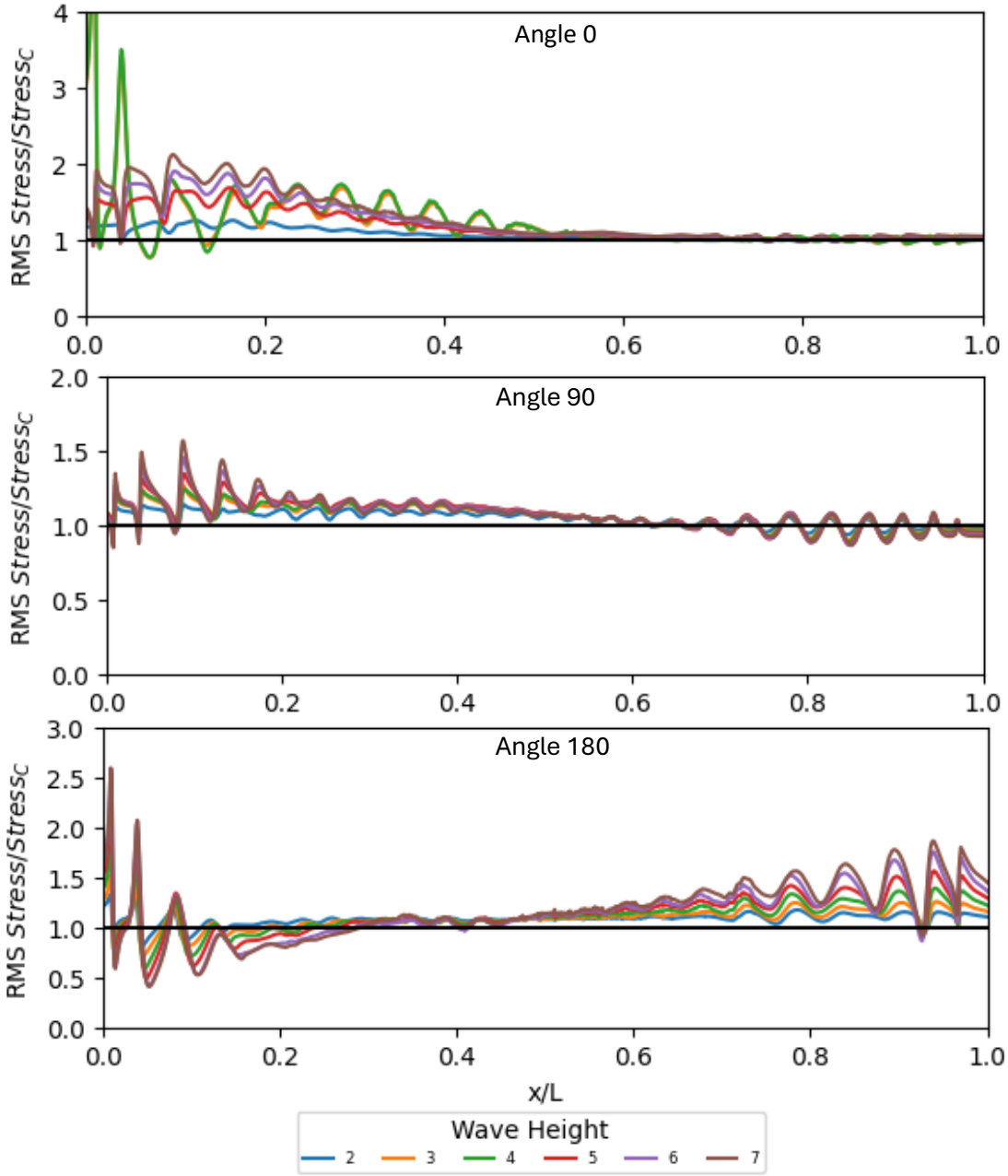

Figure 10-7: A comparison of the impact of the wave height on the RMS stress with a colinear current of uniform profile and speed 1.5 m/s

For an angle of propagation of 180 degrees there was substantial disagreement seen at the hang-off point. This was due to the bend stiffener and large curvatures observed. Past the immediate beginning of the cable, the RMS stress was lower than for just the current. As the location along the cable tended to zero the RMS stress continued to increase, passing from below the predicted RMS stress from only current at 20% along the cable length and continuing to increase until the touchdown point was reached where increases up to 90% were seen. The larger the wave height the greater the differences at both the hang-off and touchdown locations.

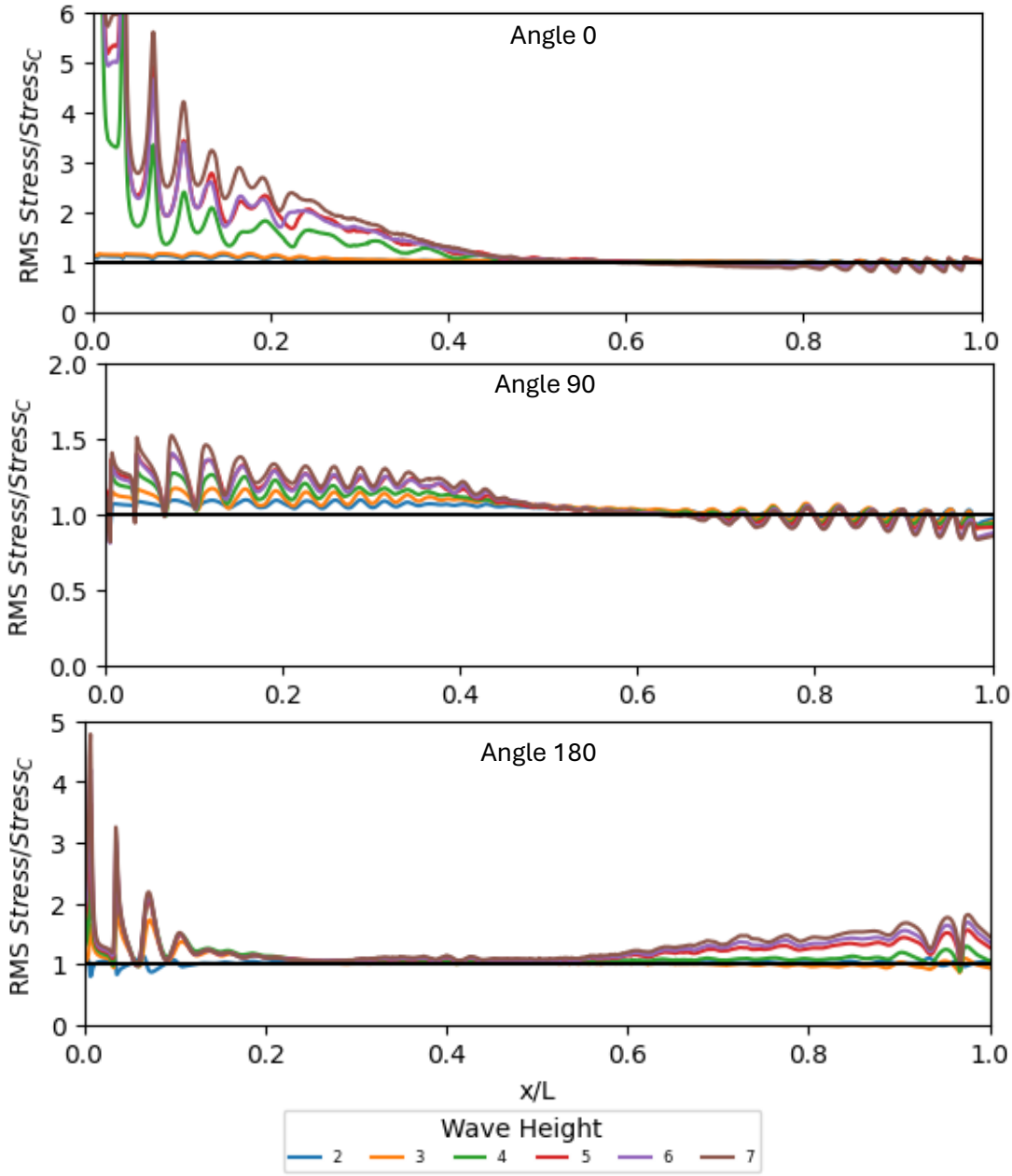

Figure 10-8: A comparison of the impact of the wave height on the RMS stress with a colinear current of uniform profile and speed 2 m/s

As can be observed from Figure 10-8, at an angle of 0 degrees large differences were observed towards the hang-off point for all wave heights of 4m and larger. This was due to cable deformation at larger current speeds resulting in reducing the relative velocity, relative to the rest of the cable, at this section due to the angle of inclination. The inclusion of waves induced platform motion as well as direct wave-induced relative velocities at the hang-off section of the cable. These in turn altered the angle of inclination which in turn allowed for VIV to occur where it was previously limited. The larger the wave height the larger the wave-induced normal relative velocity.

For an angle of 90 degrees a similar trend to 1.5 m/s is seen, just at a more exaggerated scale. The larger the wave height the greater the RMS stress. This was most notable towards the hang-off point before gradually decreasing towards the buoyancy section and actually resulting in a reduction in the RMS stress at the touchdown section compared to when just the current was modelled.

An angle of 180 degrees resulted in noticeable discrepancies in the RMS stress at the hang-off point. Large curvatures were seen here due to the bend stiffener and this location was where the wave-induced relative velocity was greatest. The stress decreased from the hang-off point towards the buoyancy section, where it was very similar to the stress predicted for just current. After the buoyancy section the stress increased again as the cable tended towards the touchdown point. The larger the wave height the greater the predicted stress over the full cable length.

At higher wave heights and current speeds, the curvature and bending stress at the hang-off point increased. This can lead to the cable section being more susceptible to large, induced stresses where it exits the bend stiffener. This interaction requires further investigation to fully understand how in certain extreme environments the cable will be exposed to large curvature as it exits the bend stiffener and the resultant influence this has on the induced stresses due to VIV.

10.3 Impact of Wave Period

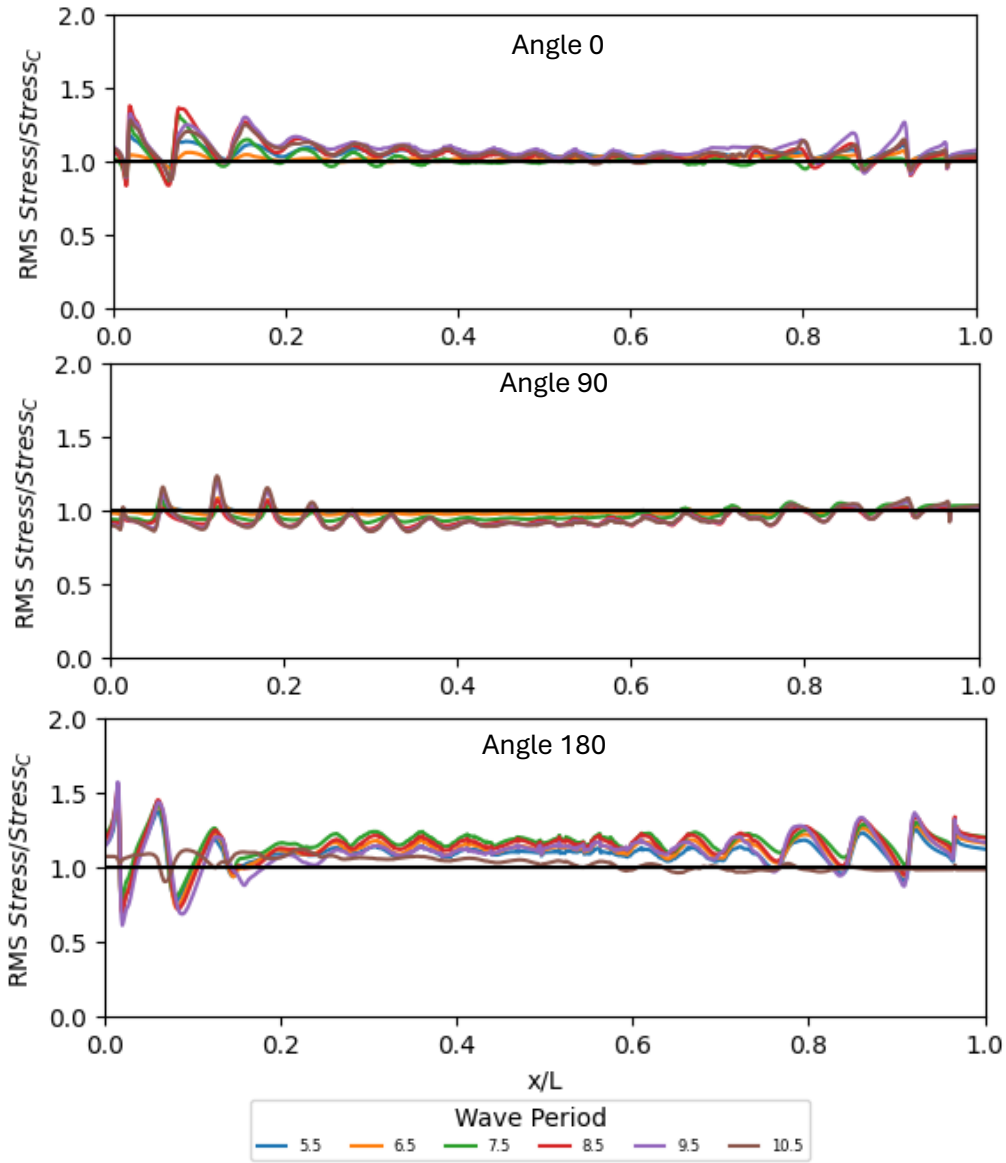

Figure 10-9: A comparison of the impact of the wave period on the RMS stress with a colinear current of uniform profile and speed 1 m/s

The impact of varying the wave period was investigated to determine the potential influence this had on the RMS stress. A current speed of 1 m/s with a uniform profile was included and was modelled as co-linear to the wave direction. A wave height of 6m and a regular Stokes 5th profile was used.

Figure 10-9 shows the RMS stress for the different wave regimes normalised against the RMS stress for a uniform current at the same propagation angle. The impact of the wave period was much less substantial compared to the wave height. There is no overarching obvious trend observed in the relationship between the wave period and the predicted RMS stress.

For an angle of propagation of 0 degrees the inclusion of waves resulted in an increase in the mean RMS stress over the full cable length for all wave periods. For an angle of 90 degrees, it resulted in a mean decrease in the RMS for all wave periods. For an angle of 180 degrees, it resulted in an increase in the RMS stress over the full cable length, this increase in stress was greater than for 0 degrees.

10.4 Impact of Wave Direction

The interaction between the angle of propagation of the waves and current relative to each other was investigated. It was shown that, in overall terms, the current had the more significant influence on the VIV behaviour, however, waves still had a noticeable impact. This was especially poignant under certain conditions where the induced RMS stress differed greatly than when modelling only currents. A uniform current profile was used with a speed of 1 m/s, the waves were of height 6m and period of 8 seconds.

In Figure 10-10, Figure 10-11, and Figure 10-12 the impact of varying the wave direction relative to current direction was investigated. The current angle of propagation was kept constant, and the direction of the incident wave angle was changed. The RMS stress was normalised by dividing the RMS stress of waves and current by the RMS stress of just the current.

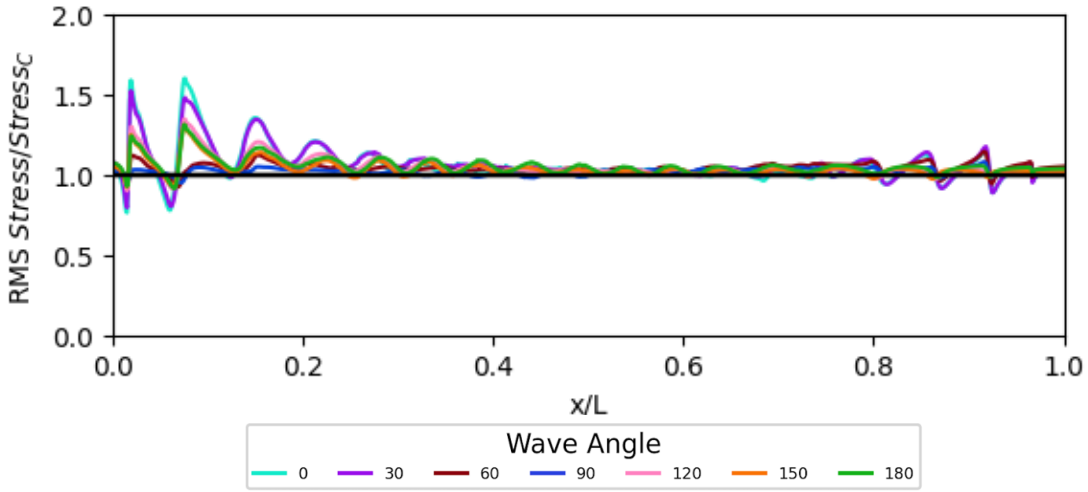

Figure 10-10: A comparison of the impact of the wave angle on the RMS stress with a current angle of 0 degrees, uniform profile and speed 1 m/s

Figure 10-10 shows that the inclusion of waves led to a greater induced stress over the full cable length for all wave angles when the angle of current propagation was 0 degrees. The most notable increases in the RMS stress were towards the hang-off point. At this point, the wave-induced relative velocity was largest. A wave angle of 0 degrees, colinear to the current direction, resulted in the greatest increase in the RMS stress. A trend can be seen where the predicted RMS stress decreased as the wave angle tended from 0 degrees to 90 degrees. The RMS stress then increased from a minimum mean RMS stress at angle 90 as the wave angle tended to 180 degrees. A colinear current angle

resulted in positively reinforcing the current-induced relative velocity. As the wave angle tended towards 90 degrees the wave-induced relative velocity on the cable in the current plane also decreased. This in turn resulted in an overall lower relative velocity and thus a smaller RMS stress was predicted.

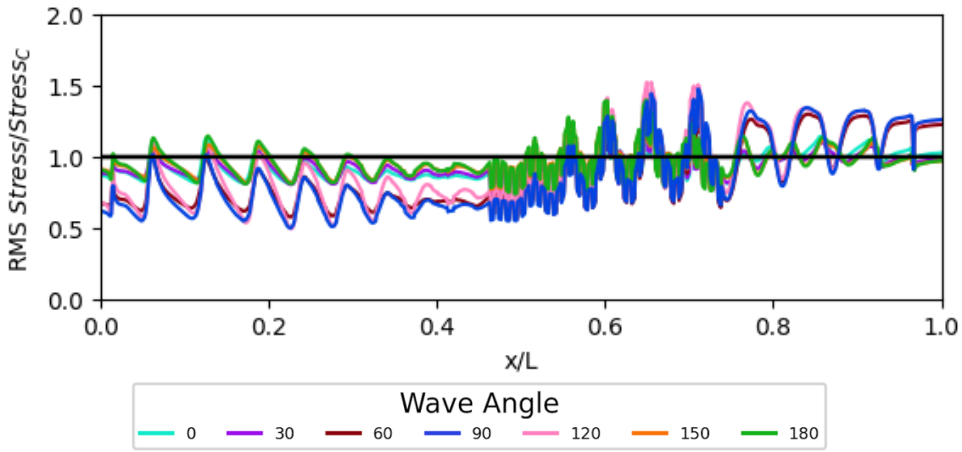

Figure 10-11: A comparison of the impact of the wave angle on the RMS stress with a current angle of 90 degrees, uniform profile and speed 1 m/s

All of the waves modelled for a current angle of 90 degrees resulted in a decrease in the RMS stress at the hang-off point and an increase towards the touchdown point, as shown in Figure 10-11. The greatest discrepancies in the induced RMS stress when compared to RMS stress for just current were seen for a current angle of 90 degrees, followed by 60 and then 120 degrees. The other wave angles showed a much smaller discrepancy. The large difference in the induced RMS stress around an angle of propagation of 90 degrees was likely due to the cable deformation and the influence this had on the wave induced relative velocity. An angle of 90 degrees was different from the other angles, because it was not limited to a specific plane and thus experienced changes in terms of both angle of inclination and the yaw angles relative to the current direction.

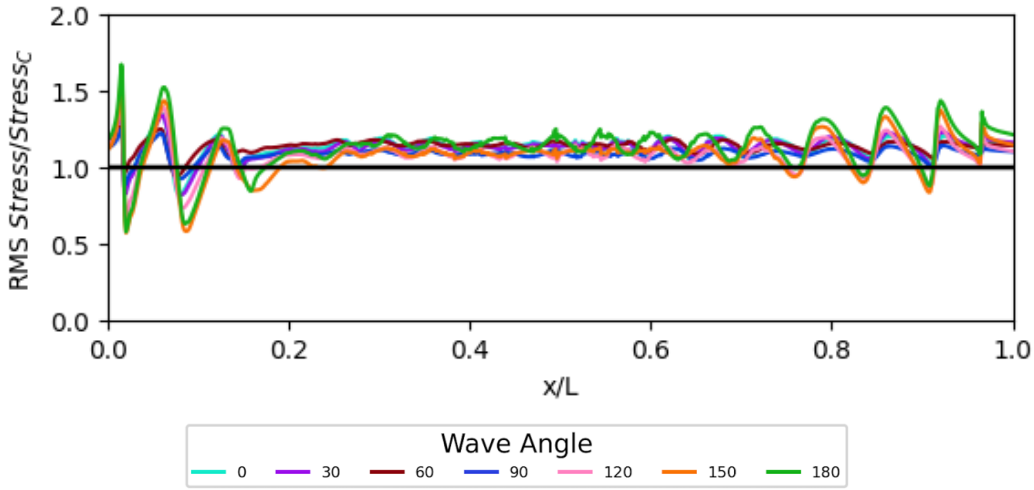

Figure 10-12: A comparison of the impact of the wave angle on the RMS stress with a current angle of 180 degrees, uniform profile and speed 1 m/s

Figure 10-12 shows that all of the wave angles modelled resulted in an increase in the RMS stress over the full cable length. The greatest disparity was seen for a co-linear angle of 180 degrees. A similar trend was seen as for a current angle of 0 degrees, where the RMS stress decreased as the wave angle of propagation tended towards an angle of 90 degrees and increased past this point. This is noted to be due to the same reasons discussed previously.

10.5 Conclusion - Waves

The influence of waves, in terms of height, period, and direction, was investigated by analysing the induced RMS stress along the full cable length. It was found that the greater the wave height the greater the induced stress for all current angles and current speeds with the magnitude of this increase dependent on these current properties. The current speed was varied to determine the influence this would have on the RMS stress induced by the waves. For an angle of 0 degrees, it was noted that an increase from 0.5 m/s to 1 m/s resulted in a decrease in the overall RMS stress compared to the RMS stress induced when no waves were present, only current. However, increasing the current speed further saw a notable increase in the RMS stress, up to 4 magnitudes greater than the RMS stress from just current, when waves were also modelled. An incident angle of 180 degrees showed a consistent trend where the greater the current speed the greater the increase in the predicted RMS stress when waves and current are modelled compared to just current. These discrepancies weren't as drastic as for angle 0. An incident angle of 90 degrees showed markedly different behaviour from the other angles. The mean RMS stress of both waves and current over the full cable length was within ±10% of the RMS stress from only current, this was independent of current speed. The different behaviours seen for the angles are noted to be due to the deformation of the cable. The introduction of waves on a taught cable can induce vibrations in sections that were otherwise experiencing too little relative velocity to see VIV.

When comparing the influence of wave period there is no evident trend seen. Under time-domain analysis the inclusion of waves may excite low frequency natural modes along the cable length but as Shear7 is a frequency domain model no such analysis was possible.

The impact of the wave direction when not colinear to current direction was also investigated. It is observed that a co-linear wave resulted in the greatest discrepancy in RMS stress when compared to only current. Additional remarks are that as the wave tended from colinear to perpendicular to current direction the discrepancy between RMS stresses decreased. The change in wave angle altered the normal relative velocity the cable experienced. With current still dominating in this regard, colinear resulted in the greatest constructive interference, complementing the current. As it tended to

perpendicular to the current, the interference of the waves in terms of normal relative velocity decreased. As the angle of the wave tended from perpendicular to opposite the current direction the RMS stress along the cable length began to increase before reaching a new maximum, smaller than when compared to the wave from a co-linear angle. This behaviour was observed for a current angle of 0, 90, and 180 degrees.

11 CONCLUDING REMARKS

Through this research the VIV of dynamic power cables, and the many different parameters that can influence this behaviour, have been investigated. The sensitivity of the VIV to different environmental and structural parameters was investigated. This was predominantly conducted through the coupled use of OrcaFlex and Shear7. These models were initially calibrated against scaled down experiments.

Other tools were also investigated: the Milan Wake Oscillator and the Iwans and Blevins Wake Oscillator models. The MWO particularly struggled with the large angles of inclination and predicted substantially different VIV behaviour compared to the other models. As such, it was discounted at the early preliminary stage. IBWO predicted more similar VIV responses when compared to Shear7 but at much greater amplitudes of crossflow displacement for all environmental conditions. The locations of maximum displacement along the cable length and the impact of current on this were similar for Shear7 and IBWO. This highlights the sensitivity of the VIV behaviour on the environmental parameters. For the majority of the research, Shear7 was the model of choice due to its calibration against experimental results and it is an up-to-date industry-standard software.

The current properties in which the power cable was exposed to were shown to greatly influence the VIV behaviour. The current speed, direction, and shear profile were all altered to observe the influence that this had on the RMS crossflow displacement, frequency of vibrations, and the location of maximum displacement along the cable length. When comparing the impact of a shear current profile against a uniform current profile reductions in RMS displacement and frequency of vibration were, generally, observed. For a current angle of 0 degrees changing from a uniform current profile to a shear current profile resulted in reductions of 13% for the Hywind profile, 12% for the Power Law profile, 20% for the Gran Canaria profile, and an increase in 7% for the West Barra profile. The West Barra result was out of keeping with the trend due to excitation of low modes. For a current angle of 90 degrees reductions of 12% for the Hywind profile, 11% for the Power Law profile, 34% for the Gran Canaria profile, and 32% for the West Barra profile were observed. For a current angle of 180 degrees the reductions observed were 12% for the Hywind profile, 8% for the Power Law profile, 51% for the Gran Canaria profile, and 44% for the West Barra profile. For current angles of 0 and 90 degrees the reductions in amplitude were most significant towards the touchdown point, where the greatest difference in current speed between shear and uniform profiles was observed.

When analysing the influence of current angle on the VIV behaviour substantially different RMS crossflow displacement along the cable length was observed for each current angle. This was due to

the changes in the normal relative velocity along the cable length. It was difficult to quantify this impact in terms of magnitude of RMS displacement due to the substantially different overall displacement profile. It was chosen to discuss the influence in terms of location of maximum displacement along the cable length instead to highlight the extreme variability. For a uniform current profile, an angle of 0 degrees saw the largest displacement towards the touchdown point, 90% along the cable length. A current angle of 90 degrees had the largest displacement towards the hang-off point, 10% along the cable length. A current angle of 180 degrees had the largest displacement approximately 5% from the hang-off point. These large variations in location were due to the deformation on the cable, altering the angle of inclination and allowing extreme, and localised, large RMS displacement at certain locations along the cable length. When analysing the effect of current speed, the most notable observations were that there was an almost linear increase in the frequency of vibrations with current speed. It was also noted that the greater the current speed the more localised and contained the largest RMS crossflow vibrations are to a certain section along the cable. This was due to more substantial deformation being observed as current speed increases which in turn resulted in more localised and extreme normal relative velocities at certain cable sections.

The configuration of the dynamic power cable was investigated to determine the influence this has on VIV behaviour. A lazy wave, double wave, steep wave, and tethered lazy wave cable configuration were analysed. When comparing the RMS displacement there were substantial discrepancies in the RMS crossflow displacement profile over the full cable length.

A trend observed across all cables was that a current angle of 0 degrees resulted in increasing the crossflow displacement seen towards the touchdown point more so than compared to the other angles. A current angle of 90 degrees had the most substantial displacement in the top half of the cable. A current angle of 180 degrees resulted in increasing the displacement most substantially at 10-20% along the cable length.

The differences between maximum and minimum RMS displacement over the full cable length, however, was notably different for each cable configuration. The double wave configuration had similar RMS displacement profiles for current angles 0 and 90 degrees, compared to an angle of 180 degrees which showed extreme vibrations at the hang-off point before quickly tapering off to near zero displacement for the rest of the cable length. The lazy wave configuration showed large dependence on current direction, with all angles resulting in substantially different VIV behaviour. A steep wave showed an unexpected profile for a current angle of 0 degrees, large RMS displacement was observed over the full cable length with this not localised to one section differing from other configurations. This was noted as likely due to lower mode of excitation predicted. For current angles

of 90 degrees and 180 degrees a similar displacement profile was seen where the largest displacement was located around 20-30% along the cable length. A tethered wave, despite having a similar initial shape to the steep wave displays markedly different behaviour to this configuration. This was likely due to the tether limiting cable deformation and thus extreme discrepancies in the relative velocity over the cable length. Overall, the RMS displacement showed less dependency on the current direction for the steep tethered wave compared to the other configurations.

The structural properties of the cable were examined to determine the influence this had on the VIV response. The effects of the bending stiffness, diameter, and mass ratio on the VIV behavior of the cable were all investigated. A significant proportion of the impacts of these parameters on the VIV behaviour could be attributed to the influence they have on the cable deformation. Deformation of the cable notably altered the relative velocity along the cable, which in turn, changed the VIV response. This was particularly noticeable for when the bending stiffness and density of the cable were altered. The lower the bending stiffness and the lower the density the greater the localisation of extreme displacements along the cable's length. For the diameter, generally, similar behaviour was seen where the smaller the cable's diameter the greater the variation in RMS displacement over the cable length. In addition, there were large changes in the VIV frequency where a linear increase with diameter was seen. There were no discernible trends on the impact of the mass ratio or flexural rigidity on the frequency of vibrations.

Additional cable influencing parameters were investigated. These were straking, marine growth, and the buoyancy module configuration. Different portions of the cable length were covered with straking to determine the influence this had on the RMS displacement and frequency of vibration. Full straking coverage was found to, expectedly, drastically change the RMS displacement and mode of vibration for all current angles. The most interesting observation was that if only the top end or bottom end of the cable was straked then the impact this had on the RMS displacement was dependent on current direction. For a current angle of 0 degrees, if only the top end of the cable was straked then it exhibited very similar VIV behaviour compared to a non-straked cable over the full cable length. This was because the most significant vibrations for a current angle of 0 degrees were observed at the touchdown section, so straking at the top section had little to no impact. For a current angle of 180 degrees the opposite was observed, where if straking was deployed only along the bottom section of the cable then there was minimal impact on RMS displacement over the full cable length compared to a cable with no straking. For a current angle of 90 degrees all straking configurations had an influence on the VIV response, but straking only on the bottom section most closely represented the no straking profile. This highlights how, depending on the current direction, straking may be best

deployed at certain locations along the cable length. When comparing the frequency of vibrations, a general trend was observed where the closer the displacement profile is to the no straking profile the closer the magnitude of the frequency was as well.

Marine growth was found to noticeably alter the RMS crossflow displacement, for certain site conditions it could result in vibrations over double the amplitude compared to when no marine growth was modelled. When comparing the influence of marine growth on frequency of vibration, the inclusion of marine growth saw a reduction of 15-30% depending on the current angle and cable configuration.

The length, diameter, and ratio of cable length intra buoyancy modules were all investigated. Increasing the diameter of the buoyancy module was found to reduce the magnitude of RMS displacement and had minimal influence on the frequency of vibration. This was likely due to a greater buoyancy module diameter relative to cable diameter having greater interference on the VIV over the cable sections. The influence of altering the length of the buoyancy modules was found to be dependent on the ratio of cable to buoyancy module. For a ratio of 1 to 1 only a current angle of 90 degrees showed any changes, with these being a slight increase in displacement on the upper section and decrease on the lower section. Comparing frequency, a lesser trend was seen where the longest buoyancy module predicted the greatest frequency. For a ratio of 2 to 1, buoyancy module lengths of 0.5 and 1m produced very similar displacement profiles with a length of 1.5m resulting in a near uniform decrease of 5-10% over the full cable length. No obvious trend can be discerned regarding the frequency of vibration for this ratio. For a ratio of 3 to 1, the 1.5m buoyancy module length resulted in large discrepancies compared to the other buoyancy module lengths. There were much greater, localised extreme amplitudes, especially for current angles 0 and 180 degrees, where outside of the touchdown and hang-off sections, respectively, there was near to no displacement predicted. Comparing the frequency, the 1.5m buoyancy module length produced the lowest estimations for all of the current angles. When comparing the ratio of the cable length to buoyancy module length, a general trend was seen where the greater the ratio the greater the RMS displacement. This was generally uniform across all the cable lengths and buoyancy module lengths with a small increase of 5-10% observed.

The influence of waves and the parameters in terms of height, period, and direction, were investigated by analysing the induced RMS stress along the full cable length. It is worth reiterating again the significant limitations that are imposed on all wave studies due to the use of a frequency domain model.

It was found that the greater the wave height the greater the RMS induced stress for all angles and current speeds. The current speed was varied to determine the influence this would have on the RMS stress induced by the waves.

For an angle of 0 degrees, it was noted that increasing the current speed from 0.5 m/s to 1 m/s resulted in a decrease in the RMS stress when this was normalised against the RMS stress from just modelling current at each respective speed. However, increasing the current speed further saw a notable increase, up to 4 magnitudes greater, when waves were modelled. An angle of propagation of 180 degrees showed a general trend where the greater the current speed the greater the stress when waves were modelled compared to when just current was modelled. The discrepancies weren't as drastic as for an angle of 0 degrees. Angle 90 showed markedly different behaviour, the mean RMS stress over the full cable for all current speeds was within ±10% of the RMS stress when just current was modelled. The different behaviours seen for the angles are noted to be due to the deformation of the cable. The introduction of waves on a taught cable can induce vibrations in sections that were otherwise experiencing too little relative velocity to see VIV. When comparing the influence of wave period, there was no evident trend seen. The impact of wave direction that is non-colinear to current direction is also investigated. It was observed that a co-linear wave resulted in the greatest discrepancy in the RMS stress over the full cable length when compared to only current. Additional remarks are that as the wave tended to perpendicular to the current direction the discrepancy compared to just current reached a minimum. As the wave tended from perpendicular to opposite the direction of the current the RMS stress began to increase again before reaching a new, lower, maximum compared to the co-linear angle.

The influence of all these parameters showcases how crucial further investigation and analysis is. More in-depth understanding is required to fully appreciate how site conditions can dictate the VIV behaviour and what potential mitigation strategies may be required in certain circumstances. Greater research on the fatigue life is necessary to comprehend how the cable life may be impacted by VIV and note when it is excessively dangerous.

11.1 LIMITATIONS

It is noted throughout this thesis that there are shortcomings due to the nature of using semi-empirical modelling. These shortcomings are identified and explained.

The dataset used for calibration and assigned numerical parameters dictate the predicted response. Without access to full-scale experimental results, the dataset used was calibrated using scaled-down experiments and subsequently validated at a similar scale. It is noted that this may have resulted in

disparities between what would be measured in the field, but without access to scaled relevant data, this was deemed the best approach.

There were noted to be difficulties in modelling small angles of inclination and certain incident current angles. This behaviour was only prevalent at certain current angles due to a combination of the cable deformation and the incident current angle impacting the relative velocity. This resulted in the prediction of excitation of low modes only. In future studies, the numerical model should be able to handle all potential incident relative velocities. This may require fine-tuning of the model for different conditions and lengths along the cable where the relative velocity substantially differentiates to allow for a more accurate prediction of the response. This will likely require full-scale validation to accurately determine what dataset is correct to use.

The response along the buoyancy module section was noted to be sensitive to the length, diameter, number, and ratio of the buoyancy module to inter-cable lengths. The understanding of the real-world VIV response along this section requires large-scale experimentation to be done to sufficiently appreciate the impact of travelling waves and the impact of the excitation of the cable on either side of the buoyancy module section.

The impact of the bend stiffener was noted to potentially result in a predicted large amplitude of displacement under certain wave and current conditions. This was due to the large, induced curvature of the cable immediately after exiting the stiffener. Further analysis of the sensitivity of the cable to different bend stiffener parameters would allow for a better understanding of the potential response and validate what is noted in this study.

Using a frequency domain model has notable limitations over a time-domain model for situations where there is a time varying flow, such as waves. This was noted in this study and accounted for in the methodology, but it does not make up for the large value that the use of a time-domain model would add. Without being able to account for the potential excitement of the cable due to the wave period there was notable value lost in this investigation. It would be advised to use a time-domain model to better understand and appreciate the VIV response of a dynamic power cable under wave environments.

11.2 Recommendations for Future Work

When considering the VIV response of dynamic power cables, it is important to factor in the cable deformation and response to incident loads. The site condition, cable configuration and cable properties are shown to be the predominant factors in determining the deformation response.

Without considering the cable deformation, the predicted VIV response will substantially deviate from the actual result. In the design of the cables, the impact that deformation has on the VIV response should be accounted for.

Further investigation on the use of straking along the power cable will provide better information on the potential influence on the VIV response. It has been seen that deploying only along certain sections of the cable may have a similar effect on suppressing the vibrations as compared to deploying along the full cable length. This would result in substantial cost savings. The suppression impact of the straking was found to be dependent on the incident current angle. Additional analysis of this could help to inform on the most effective locations for straking along the cable length, depending on site conditions and determine the potential cost savings.

The mooring system of the FOWT can greatly influence the induced motion of the turbine platform. This in turn can substantially impact the configuration of the cable and its response to environmental conditions. Further analysis of the platform's response and the influence this has on the power cable should be undertaken to determine whether this has notable impacts on the VIV response. The coupling between the platform's and the cable's response should be well investigated and understood.

Huge value would be added to this field if large-scale experimental analysis was conducted to better understand the impact that the cable configuration has and the impact of higher mode vibrations. This would require large investment but would allow for the validation of modelling results and a better understanding of the hydrodynamic response of the cable.

Due to the complex internal composition of the cable, the stick / slip phenomenon plays a role in the cable's response. Without correctly accounting for this behaviour the magnitude of the VIV response can be wrongly predicted. The exact influence of this needs to be further accounted for and well understood. This will also have a large impact on the fatigue of the cable. While the fatigue induced on the cable has not been accounted for in this study, due to previously discussed limitations regarding both accurate modelling and time restrictions, it is an area that requires further research. This would require further experimentation and complex specialised numerical models to adequately capture the full response of the cable's internal components.

12 BIBLIOGRAPHY

Ali, U., Islam, Md., Janajreh, I., Fatt, Y., & Alam, Md. M. (2021). Flow-Induced Vibrations of Single and Multiple Heated Circular Cylinders: A Review. In *Energies* (Vol. 14, Issue 24). https://doi.org/10.3390/en14248496

Allen, D. W., & Henning, D. L. (1997). Vortex-Induced Vibration Tests of a Flexible Smooth Cylinder as Supercritical Reynolds Number. *Proc. of the 7th ISOPE*, 680–685.

Bearman, P. W. (1969). On vortex shedding from a circular cylinder in the critical Reynolds number régime. *Journal of Fluid Mechanics*, *37*(3), 577–585. https://doi.org/10.1017/S0022112069000735

Beier, D., Schnepf, A., Steel, S. Van, Ye, N., & Ong, M. C. (2023). *Fatigue Analysis of Inter-Array Power Cables between Two Floating Offshore Wind Turbines Including a Simplified Method to Estimate Stress Factors*.

Bessel, F. (1828). *Untersuchungen über die Länge des einfachen Secundenpendels*.

Bingham, H. H., Weimer, D. K., and Griffith, W. (1952). *The cylinder and semicylinder in subsonic flow. Princeton University, Department of Physics. Tech. Rep.*

Bishop, R. E. D., & Hassan, A. Y. (1963). *The lift and drag forces on a circular cylinder in a flowing fluid.*

BLEVINS, R. D. (1974). *FLOW INDUCED VIBRATION OF BLUFF STRUCTURES.*

Blevins, R. D. (1977). Flow-induced vibration. *New York*.

Blevins, R. D., & Coughran, C. S. (2009). Experimental Investigation of Vortex-Induced Vibration in One and Two Dimensions With Variable Mass, Damping, and Reynolds Number. *Journal of Fluids Engineering*, *131*(10). https://doi.org/10.1115/1.3222904

Boo, S. Y., & Yang, H. (2019). Power cable design and dynamic analysis for a hybrid platform. *Proceedings of the International Offshore and Polar Engineering Conference*.

Boone, W., & Christiaan. (2015). *COPPER IN COMPARISON WITH ALUMINIUM AS COMMON MATERIAL IN CONDUCTORS OF LV AND MV CABLES*.

Bublitz, P. (1971). Messung der drucke und krafte am ebenen, querange- stromten kreiszylinder, Teil I: Untersuchungen am ruhenden kreiszylinder. *AVA-Bericht*, *11*.

Carneiro, D., Ellwanger, G., & Galgoul, N. (2008). *Contribution to the Evaluation of VIV Analyses Using Wake Oscillator and Vortex Tracking Models*. https://doi.org/10.1115/IPC2008-64297

Chaplin, J., Bearman, P. W., Cheng, Y., Fontaine, E., Graham, J. M. R., Herfjord, K., Huera-Huarte, F., Isherwood, M., Lambrakos, K., Larsen, C., Meneghini, J., Moe, G., Pattenden, R. J., Triantafyllou, M., & Willden, R. (2005). Blind predictions of laboratory measurements of vortex-induced vibrations of a tension riser. *Journal of Fluids and Structures*, *21*.

Chaplin, J. R., Bearman, P. W., Cheng, Y., Fontaine, E., Graham, J. M. R., Herfjord, K., Huera Huarte, F. J., Isherwood, M., Lambrakos, K., Larsen, C. M., Meneghini, J. R., Moe, G., Pattenden, R. J., Triantafyllou, M. S., & Willden, R. H. J. (2005). Blind predictions of laboratory measurements of

vortex-induced vibrations of a tension riser. *Journal of Fluids and Structures*, *21*(1 SPEC. ISS.), 25–40. https://doi.org/10.1016/j.jfluidstructs.2005.05.016

Chaplin, J. R., & King, R. (2018). Laboratory measurements of the vortex-induced vibrations of an untensioned catenary riser with high curvature. *Journal of Fluids and Structures*, *79*, 26–38. https://doi.org/https://doi.org/10.1016/j.jfluidstructs.2018.01.008

Chen, S. S. (1977). FLOW-INDUCED VIBRATIONS OF CIRCULAR CYLINDRICAL STRUCTURES - 1. STATIONARY FLUIDS AND PARALLEL FLOW. *Shock and Vibration Digest*. https://doi.org/10.1177/058310247700901006

Chen, W. L., Zhang, Q. Q., Li, H., & Hu, H. (2015). An experimental investigation on vortex induced vibration of a flexible inclined cable under a shear flow. *Journal of Fluids and Structures*, *54*, 297–311. https://doi.org/10.1016/j.jfluidstructs.2014.11.007

Chen, W., Li, M., Guo, S., & Gan, K. (2014). Dynamic analysis of coupling between floating top-end heave and riser's vortex-induced vibration by using finite element simulations. *Applied Ocean Research*, *48*, 1–9. https://doi.org/https://doi.org/10.1016/j.apor.2014.07.005

Chen, Z. S., & Kim, W. J. (2010). Numerical investigation of vortex shedding and vortex-induced vibration for flexible riser models. *International Journal of Naval Architecture and Ocean Engineering*. https://doi.org/10.3744/JNAOE.2010.2.2.112

Cheng, Y., Tang, L., & Ji, C. (2021). Nonlinear Analysis of Bidirectional Vortex-Induced Vibration of A Deepwater Steep Wave Riser Subjected to Oblique Currents. *China Ocean Engineering*, *35*(6), 852–865. https://doi.org/10.1007/s13344-021-0075-3

Clausen, T., & D'Souza, R. (2001). Dynamic risers key component for deepwater drilling, floating production. *Offshore Magazine*.

CODAN. (2017). Insuring Offshore Cables, an insurers' perspective. *6TH Annual Advanced Submarine Power Cable and Interconnection Forum*.

Constantinides, Y., Stover, M., Steele, A., & Santala, M. (2016). CFD Modeling and Validation of Steel Lazy-Wave Riser VIV. In *ASME 2016 35th International Conference on Ocean, Offshore and Arctic Engineering*. https://doi.org/10.1115/OMAE2016-54945

CoreWind. (2020). *D3.1 Review of the state of the art of dynamic cable system design*.

Coser, T. B., Strohaecker, T. R., López, F. S., Bertoni, F., Wang, H., Hebert, C. B., Silveira, L., Dos Santos Paiva, M. V., & Maioli, P. (2016). Submarine power cable bending stiffness testing methodology. *Proceedings of the International Offshore and Polar Engineering Conference*, *2016-Janua*, 24–30.

Dai, T., Sævik, S., & Ye, N. (2020). Experimental and numerical studies on dynamic stress and curvature in steel tube umbilicals. *Marine Structures*. https://doi.org/10.1016/j.marstruc.2020.102724

Dawson, C., & Marcus, M. (1970). DMC – A computer code to simulate viscous flow about arbitrarily shaped bodies. *1970 Heat Transfer and Fluid Mechanics Institute (Ed. T. Sarpkaya)*, 323–338.

de Wilde, J., Heijnsdijk, R., & de Ridder, E.-J. (2021). *D 5.5 – Report on VIV (Hydrodynamic) behaviour*. https://flotantproject.eu/wp-content/uploads/2021/11/210430_FLT-D5.5_VIV_test_v0.pdf

Delizisis, P., Grivas, K., Wilde, J. De, Resvanis, T. L., Georgallis, G., & Ridder, E.-J. de. (2022). *NUMERICAL INVESTIGATION OF THE EFFECT OF VORTEX INDUCED VIBRATIONS (VIV) PARAMETERS ON THE BEHAVIOR OF SUBMARINE POWER CABLES: A COMPARISON WITH SCALED DOWN EXPERIMENTAL RESULTS*. 1–10.

Dillon-Gibbons, C., Kilner, A., & Marcollo Dr, H. (2017). Consideration of HVIV Response of SLWRs. In *The 27th International Ocean and Polar Engineering Conference* (p. ISOPE-I-17-528).

DNV GL. (2012). *Electrical Power Cables in Subsea Applications*.

DNV GL AS. (2016). *Subsea power cables for wind power plants DNVGL-ST-0359*.

DNVGL. (2016). Subsea power cables for wind power plants. *Dnvgl-St-0359*, *June*, 1–40.

dos Santos, M. V. F., Morooka, C. K., Caire, M., Franciss, R., & Matt, C. G. C. (2014). *A Comparative Study of a Free Span Pipeline Through Numerical Simulations*. https://doi.org/10.1115/OMAE2014-24069

Du Buat, P. (1822). *Chevalier Du Buat's principles of hydraulics*.

Durakovic, A. (2020). *UK Prime Minister: Offshore Wind to Power Every Home by 2030*. OffshoreWIND. https://www.offshorewind.biz/2020/10/06/uk-prime-minister-offshore-wind-to-power-every-home-by-2030/#:~:text=UK Prime Minister Boris Johnson,GW target to 40 GW.

El Mountassir, O., & Strang-Moran, C. (2018). *Offshore Wind Subsea Power Cables: Installation, Operation and Market Trends*.

El-Zein, A., Mohamed, Kh., & Talaat, M. (2020). Water trees in polyethylene insulated power cables: Approach to water trees initiation mechanism. *Electric Power Systems Research*, *180*, 106158. https://doi.org/https://doi.org/10.1016/j.epsr.2019.106158

EPSRC Cabledyn Project (2022). Engineering and Physical Sciences Research Council through CableDyn: Subsea Power Cable Dynamics Under Complex Ocean Environment (EP/W015102/1). https://gow.epsrc.ukri.org/NGBOViewGrant.aspx?GrantRef=EP/W015102/1

Fu, S., Wang, J., Baarholm, R., Wu, J., & Larsen, C. M. (2013). *VIV of Flexible Cylinder in Oscillatory Flow*. https://doi.org/10.1115/OMAE2013-10348

Fuglsang, A., Bauer, P., Marcollo, H., Dillon-Gibbons, C., & Kusangaya, A. (2023). COMPARISON OF VESSEL MOTION INDUCED-VIV RESPONSE OF LAZY-WAVE AND W-SHAPED FOWT POWER CABLE CONFIGURATIONS. *OMAE 2023*.

Fung, Y. C. (1960). Fluctuating lift and drag acting on a cylinder in a flow at supercritical Reynolds numbers. *J. Aerospace Sci.*, *27*, 801–814.

Gabbai, R. D., & Benaroya, H. (2005). An overview of modeling and experiments of vortex-induced vibration of circular cylinders. In *Journal of Sound and Vibration*. https://doi.org/10.1016/j.jsv.2004.04.017

Gao, Y., Liu, L., Pan, G., Fu, S., Chai, S., & Shi, C. (2022). Numerical prediction of vortex-induced vibrations of a long flexible riser with an axially varying tension based on a wake oscillator model. *Marine Structures*, *85*, 103265. https://doi.org/https://doi.org/10.1016/j.marstruc.2022.103265

Gerrard, J. H. (1961). An experimental investigation of the oscillating lift and drag of a circular cylinder shedding turbulent vortices. *J. Fluid Mech. 11,* 215–227.

Goldman, R. L. (1958). Karman vortex forces on the vanguard rocket. *Shock Vibration Bull.*, *26*, 171–179.

Govardhan, R. N., & Williamson, C. H. K. (2006). Defining the "modified Griffin plot" in vortex-induced vibration: Revealing the effect of Reynolds number using controlled damping. *Journal of Fluid Mechanics*. https://doi.org/10.1017/S0022112006000310

Griffiths, T. (2022). *Hydrodynamics and On-Bottom Stability of Subsea Cables and Small Diameter Pipelines*.

Guignier, L., Mariani, R., Cottet-Emard, A., Toumit, S., & Choisnet, T. (2020a). DESIGN OF DYNAMIC HIGH VOLTAGE CABLES FOR FLOATING SUBSTATION Lucie. *OMAE2020*, *1*(1997), 1997–1998.

Guignier, L., Mariani, R., Cottet-Emard, A., Toumit, S., & Choisnet, T. (2020b). DESIGN OF DYNAMIC HIGH VOLTAGE CABLES FOR FLOATING SUBSTATION Lucie. *OMAE2020*, *1*(1997), 1997–1998.

Han, Q., Ma, Y., Xu, W., Lu, Y., & Cheng, A. (2017). Dynamic characteristics of an inclined flexible cylinder undergoing vortex-induced vibrations. *Journal of Sound and Vibration*, *394*, 306–320. https://doi.org/https://doi.org/10.1016/j.jsv.2017.01.034

Harnois, V., Johanning, L., & Thies, P. R. (2013). Wave Conditions Inducing Extreme Mooring Loads on a Dynamically Responding Moored Structure. *EWTEC 2013 Proceedings*.

Hu, H., Yan, J., Sævik, S., Ye, N., Lu, Q., & Bu, Y. (2022). Nonlinear bending behavior of a multilayer copper conductor in a dynamic power cable. *Ocean Engineering*, *250*, 110831. https://doi.org/https://doi.org/10.1016/j.oceaneng.2022.110831

Humphreys, J. S. (1960). On a circular cylinder in a steady wind at transition Reynolds numbers. *J. Fluid Mech.*, *9*, 603–612.

IEC 60840. (2004). : *Power cables with extruded insulation and their accessories for rated voltages above 30 kV up to 150 kV - Test methods and requirements*.

Iwan, W. D., & Blevins, R. D. (1974). A Model for Vortex Induced Oscillation of Structures. *Journal of Applied Mechanics*, *41*(3), 581–586. https://doi.org/10.1115/1.3423352

Jaiswal, V., & Vandiver, J. K. (2007). VIV Response Prediction for Long Risers with Variable Damping. *OMAE*.

Jia, L., Liu, Y., Zhang, M., Fu, S., & Ren, H. (2022). Experimental Research on Vortex-Induced Force Characteristics of Flexible Riser with Buoyancy Module and Strakes. In *Applied Sciences* (Vol. 12, Issue 12). https://doi.org/10.3390/app12126180

Jin, Y., & Dong, P. (2016). A novel Wake Oscillator Model for simulation of cross-flow vortex induced vibrations of a circular cylinder close to a plane boundary. *Ocean Engineering*, *117*, 57–62. https://doi.org/https://doi.org/10.1016/j.oceaneng.2016.03.057

Johannesson, P., Lang, X., Johnson, E., & Ringsberg, J. W. (2022). Mechanical Reliability Analysis of Flexible Power Cables for Marine Energy. In *Journal of Marine Science and Engineering* (Vol. 10, Issue 6). https://doi.org/10.3390/jmse10060716

Jonkman, J., Fylling, I., Nichols, J., Larsen, T., Hansen, A., Kohlmeier, M., Nygaard, T., Maus, K., Pascual Vergara, J., Merino, D., Karimirad, M., Gao, Z., Moan, T., Shi, W., & Park, H. (2010). Offshore code comparison collaboration within IEA wind task 23: Phase IV results regarding floating wind Turbine modeling. *European Wind Energy Conference and Exhibition 2010, EWEC 2010*.

Jordan, S. K., & Fromm, J. E. (1972). Oscillatory drag, lift and torque on a circular cylinder in a uniform flow. *Phys. Fluids*, *15*, 371–376.

Kang, Z., Zhang, C., Chang, R., & Ma, G. (2019). A numerical investigation of the effects of Reynolds number on vortex-induced vibration of the cylinders with different mass ratios and frequency ratios. *International Journal of Naval Architecture and Ocean Engineering*. https://doi.org/10.1016/j.ijnaoe.2019.02.012

Karlsen, S. (2010). Fatigue of copper conductors for dynamic subsea power cables. *Proceedings of the International Conference on Offshore Mechanics and Arctic Engineering - OMAE*. https://doi.org/10.1115/OMAE2010-21017

Karlsen, S., Roger, S., Heide, K., Lund, S., Eggertsen, F., & Osborg, P. A. (2009). Dynamic Deep Water Power Cables. *RAO / CIS Offshore*.

Keefe, R. T. (1962). An investigation of the fluctuating forces acting on a stationary cylinder in a subsonic stream, and of the associated sound field. *J. Acous. Soc. Am. 34*, 1711–1719.

Kim, S. W., Sævik, S., Wu, J., & Leira, B. J. (2021). Simulating High-Mode Vortex-Induced Vibration of a Riser in Linearly Sheared Current Using an Empirical Time-Domain Model. *Journal of Offshore Mechanics and Arctic Engineering*, *143*(4). https://doi.org/10.1115/1.4049246

Kim, S. W., Sævik, S., Wu, J., & Leira, B. J. (2022). Time domain simulation of marine riser vortex-induced vibrations in three-dimensional currents. *Applied Ocean Research*, *120*, 103057. https://doi.org/https://doi.org/10.1016/j.apor.2022.103057

Klamo, J. T., Leonard, A., & Roshko, A. (2005). On the maximum amplitude for a freely vibrating cylinder in cross-flow. *Journal of Fluids and Structures*. https://doi.org/10.1016/j.jfluidstructs.2005.07.010

Kumar, P. R., & Nallayarasu, S. (2020). *Experimental Investigation of Vortex Induced Vibration of Cross Flow Response for a Flexible Cable Under Uniform Current*. https://doi.org/10.1115/OMAE2020-18596

Le Cunff, C., Averbuch, D., & Biolley, F. (2004). Influence of current direction on VIV of a steel catenary riser. *Proceedings of the International Conference on Offshore Mechanics and Arctic Engineering - OMAE*, *1 A*, 23–30. https://doi.org/10.1115/OMAE2004-51014

Lee, S., Paik, K.-J., & Srinil, N. (2020). Wake dynamics of a 3D curved cylinder in oblique flows. *International Journal of Naval Architecture and Ocean Engineering*, *12*, 501–517. https://doi.org/https://doi.org/10.1016/j.ijnaoe.2020.07.005

Lee, S.-J., Lee, J.-D., Jun, S.-H., Yoo, K.-K., Joo, Y.-S., Han, S.-K., & Park, S.-G. (2017). Parametric Study of VIV Fatigue Analysis for SCR. In *The 27th International Ocean and Polar Engineering Conference* (p. ISOPE-I-17-228).

Lekkala, M. R., Mohamed, L., Hafiz, M. F. U., & Kim, D. K. (2020). A practical technique for hydrodynamic coefficients modification in SHEAR7 for fatigue assessment of riser buoyancy

modules under vortex-induced vibration. *Ocean Engineering*, *217*, 107760. https://doi.org/https://doi.org/10.1016/j.oceaneng.2020.107760

Li, X., Chen, D., Gu, H., & Bai, F. (2021). Three-dimensional vortex-induced vibration analysis of catenary-type risers under flow with different incident angles. *Ocean Engineering*, *240*, 109978. https://doi.org/https://doi.org/10.1016/j.oceaneng.2021.109978

Lienhard, J. H. (1966). Synopsis of lift, drag, and vortex frequency data for rigid circular cylinders. *Washington State University College of Engineering*.

Ma, B., & Srinil, N. (2021). *Numerical Prediction of 3-D Vortex-Induced Vibration of Catenary Riser In Planar and Non-Planar Flows*. https://doi.org/10.1115/OMAE2021-61830

Ma, B., & Srinil, N. (2023). Prediction model for multidirectional vortex-induced vibrations of catenary riser in convex/concave and perpendicular flows. *Journal of Fluids and Structures*, *117*, 103826. https://doi.org/10.1016/j.jfluidstructs.2022.103826

Macovsky, M. S. (1958). *Vortex-induced vibration studies David Taylor Model Basin.*

Marinet. (2015). *Development of new highly dynamic power cables design solutions for floating offshore renewable energy applications*.

Marta, M., Mueller-Schuetze, S., Ottersberg, H., Isus, D., Johanning, L., & Thies, P. R. (2015). Development of dynamic submarine MV power cable design solutions for floating offshore renewable energy applications. *9th International Conference on Insulated Power Cables*.

Martinelli, L., Lamberti, A., Ruol, P., Ricci, P., Kirrane, P., Fenton, C., & Johanning, L. (2010). *Power Umbilical for Ocean Renewable Energy Systems-Feasibility and Dynamic Response Analysis*.

Marty, A., Berhault, C., Damblans, G., Facq, J.-V., Gaurier, B., Germain, G., Soulard, T., & Schoefs, F. (2020). Marine growth effect on the hydrodynamical behavior of a submarine cable under current and wave conditions. *Journees de l'Hydrodynamique*.

Marty, A., Schoefs, F., Soulard, T., Berhault, C., Facq, J. V., Gaurier, B., & Germain, G. (2021). Effect of roughness of mussels on cylinder forces from a realistic shape modelling. *Journal of Marine Science and Engineering*, *9*(6). https://doi.org/10.3390/jmse9060598

Mathiesen, M., Meyer, A. K., & Kvingendal, B. (2014). *Hywind Buchan Deep Metocean Design Basis RE2014-002*. 129.

McGregor, D. M. (1957). An experimental investigation of the oscillating pressures on a circular cylinder in a fluid stream. In *University of Toronto Institute for Aerospace Studies (UTIAS), Tech. Note 14.*

Nasution, F. P., Sævik, S., & Gjøsteen, J. K. Ø. (2012). Fatigue analysis of copper conductor for offshore wind turbines by experimental and FE method. *Energy Procedia*, *24*, 271–280. https://doi.org/10.1016/j.egypro.2012.06.109

National Physical Laboratory. (1969). Strouhal number of model stacks free to oscillate. In *NPL Aero Rep.*

Nexans. (2013). *Submarine Power Cables*.

Nicholls-Lee, R., Thies, P. R., Dulieu-Barton, J. M., Ólafsson, G., Hughes, R., Hernandez Arroyo, A., Xu, G., & Cartlidge, N. (2022). Non-destructive examination (NDE) methods for dynamic subsea cables for offshore renewable energy. *Progress in Energy*, *4*(4), 42011. https://doi.org/10.1088/2516-1083/ac8ccb

NREL. (1996). *Definition of the Semisubmersible Floating System for Phase II of OC4*. *September*.

Okpokparoro, S., & Sriramula, S. (2023). Reliability analysis of floating wind turbine dynamic cables under realistic environmental loads. *Ocean Engineering*, *278*, 114594. https://doi.org/https://doi.org/10.1016/j.oceaneng.2023.114594

Oud, G., Koop, A., Valenchon, C., & Trebaol, Q. (2021). *D.4.6 - Hydrodynamic Assessment / Dynamic modelling of Power Cable (Dynamic cabling and floater)*. https://flotantproject.eu/wp-content/uploads/2021/11/210430-FLT_WP4_D4.6_Hydrodynamic_Assessment_Dynamic_modelling_of_Power_Cable_v1.pdf

Pan, P., Shuhong, X., Pengjing, S., & Haitao, W. (2019). Full Scale Fatigue Test on Dynamic Submarine Power Cable. *Jicable'19*, *1*, 6–11.

Phillips, O. M. (1956). The intensity of aeolian tones. *J. Fluid Mech.*, 1, 607– 624.

Poon, C., O'Halloran, S. M., Connolly, A., Barrett, R. A., & Leen, S. B. (2023). Fretting wear and fatigue in submarine power cable conductors for floating offshore wind energy. *Tribology International*, *186*, 108598. https://doi.org/https://doi.org/10.1016/j.triboint.2023.108598

Qiao, D., Yan, J., & Ou, J. (2014). Fatigue analysis of deepwater hybrid mooring line under corrosion effect. *Polish Maritime Research*. https://doi.org/10.2478/pomr-2014-0032

Qu, Y., Wang, P., Fu, S., & Zhao, M. (2023). Vortex-induced vibrations of a top tensioned riser subjected to flows with spanwise varying directions. *International Journal of Mechanical Sciences*, *242*, 107954. https://doi.org/https://doi.org/10.1016/j.ijmecsci.2022.107954

Raghavan, K., & Bernitsas, M. M. (2011). Experimental investigation of Reynolds number effect on vortex induced vibration of rigid circular cylinder on elastic supports. *Ocean Engineering*, *38*(5), 719–731. https://doi.org/https://doi.org/10.1016/j.oceaneng.2010.09.003

Ren, H., Zhang, M., Cheng, J., Cao, P., Xu, Y., Fu, S., & Liu, C. (2020). Experimental Investigation on Vortex-Induced Vibration of a Flexible Pipe under Higher Mode in an Oscillatory Flow. In *Journal of Marine Science and Engineering* (Vol. 8, Issue 6). https://doi.org/10.3390/jmse8060408

Rentschler, M. U. T., Adam, F., & Chainho, P. (2019). Design optimization of dynamic inter-array cable systems for floating offshore wind turbines. *Renewable and Sustainable Energy Reviews*. https://doi.org/10.1016/j.rser.2019.05.024

Resvanis, T. L., Jhingran, V., Vandiver, J. K., & Liapis, S. (2012). Reynolds number effects on the Vortex-Induced Vibration of flexible marine risers. *Proceedings of the International Conference on Offshore Mechanics and Arctic Engineering - OMAE*. https://doi.org/10.1115/OMAE2012-83565

Ross, A., & Mckinnon, G. (2018). Orcina Project 1405 Wind Turbine Validation Report. *Orcina Ltd.*

Sarpkaya, T. (1995). Hydrodynamic damping, flow-induced oscillations, and biharmonic response. *J. Offshore Mech. Arctic Eng.*, *117*, 232–238.

Sarpkaya, T. (2004). A critical review of the intrinsic nature of vortex-induced vibrations. *Journal of Fluids and Structures*. https://doi.org/10.1016/j.jfluidstructs.2004.02.005

Sarpkaya, T. "Sarp." (2010). *Wave Forces on Offshore Structures*. Cambridge University Press. https://doi.org/DOI: 10.1017/CBO9781139195898

Schmidt, L. V. (1965). Measurements of fluctuating air loads on a circular cylinder. *J. Aircraft 2*, 49–55.

Schwabe, M. (1935). Uber druckermittlung in der instationaren ebenen Stromung. *NACA Tech. Memo TM-1039*.

Silva, V., Sagrilo, L., & Vignoles, M. (2018). Lazy-Wave Buoyancy Length Reduction Based on Fatigue Reliability Analysis. *Journal of Offshore Mechanics and Arctic Engineering*, *140*. https://doi.org/10.1115/1.4038937

Sobhaniasl, M., Petrini, F., Karimirad, M., & Bontempi, F. (2020). Fatigue Life Assessment for Power Cables in Floating Offshore Wind Turbines. *Energies 2020*, *13*.

Sonerud, B., Eggertsen, F., Nilsson, S., Furuheim, K., & Evenset, G. (2012). Material considerations for submarine high voltage XLPE cables for dynamic applications. In *Annual Report - Conference on Electrical Insulation and Dielectric Phenomena, CEIDP*. https://doi.org/10.1109/CEIDP.2012.6378924

Srinil, N., Ma, B., & Zhang, L. (2018). Experimental investigation on in-plane/out-of-plane vortex-induced vibrations of curved cylinder in parallel and perpendicular flows. *Journal of Sound and Vibration*, *421*, 275–299. https://doi.org/https://doi.org/10.1016/j.jsv.2018.02.021

Stabile, G., Matthies, H. G., & Borri, C. (2018). A novel reduced order model for vortex induced vibrations of long flexible cylinders. *Ocean Engineering*. https://doi.org/10.1016/j.oceaneng.2018.02.064

Strouhal, V. (1878). Uber eine besondere art der tonerregung. *Ann. Phys. Chem.*

Taormina, B., Bald, J., Want, A., Thouzeau, G., Lejart, M., Desroy, N., & Carlier, A. (2018). A review of potential impacts of submarine power cables on the marine environment: Knowledge gaps, recommendations and future directions. *Renewable and Sustainable Energy Reviews*, *96*, 380–391. https://doi.org/10.1016/j.rser.2018.07.026

Thies, P. R., Harrold, M. J., & Johanning, L. (2019). Load and fatigue evaluation for 66kV floating offshore wind submarine dynamic power cable. *10th International Conference on Insulated Power Cables*.

Thies, P. R., Harrold, M., Johanning, L., Grivas, K., & Georgallis, G. (2019). Performance evaluation of dynamic HV cables with Al conductors for floating offshore wind turbines. *ASME 2019 2nd International Offshore Wind Technical Conference, IOWTC 2019*. https://doi.org/10.1115/IOWTC2019-7536

Thies, P. R., Johanning, L., & Dobral, C. (2017). Parametric sensitivity study of submarine power cable design for marine renewable energy applications. *Proceedings of the International Conference on Offshore Mechanics and Arctic Engineering - OMAE*. https://doi.org/10.1115/OMAE201762208

Thies, P. R., Johanning, L., & Smith, G. H. (2012a). Assessing mechanical loading regimes and fatigue life of marine power cables in marine energy applications. *Proceedings of the Institution of Mechanical Engineers, Part O: Journal of Risk and Reliability*. https://doi.org/10.1177/1748006X11413533

Thies, P. R., Johanning, L., & Smith, G. H. (2012b). Assessing mechanical loading regimes and fatigue life of marine power cables in marine energy applications. *Proceedings of the Institution of Mechanical Engineers, Part O: Journal of Risk and Reliability*, *226*(1), 18–32. https://doi.org/10.1177/1748006X11413533

Tjahjanto, D., & Ab, A. B. B. (2019). *B8-4 B8-4 Large HVAC export cables under tensile loading Close and Return B8-4 B8-4*. 6–11.

Trarieux, F. L. (2004). *An investigation of vortex induced vibrations of subsea risers and umbilicals from offshore field measurements*. *May*.

Triantafyllou, M. S., Hover, F. S., Techet, A. H., & Yue, D. K. P. (2003). *Vortex-Induced Vibrations of Slender Structures in Shear Flow BT - IUTAM Symposium on Integrated Modeling of Fully Coupled Fluid Structure Interactions Using Analysis, Computations and Experiments* (H. Benaroya & T. J. Wei, Eds.; pp. 313–327). Springer Netherlands.

Vandiver, J. K., Swithenbank, S. B., Jaiswal, V., & Jhingran, V. (2006). *Fatigue Damage From High Mode Number Vortex-Induced Vibration* (pp. 803–811). https://doi.org/10.1115/OMAE2006-92409

Vickery, B. J. and Watkins, R. D. (1962). Flow-induced vibrations of cylindrical structures. *In Proceedings of the First Australiasian Conference,* 213– 241.

Vieira, D. P., Franzini, G. R., Cenci, F., & Fujarra, A. L. C. (2021). Experimental Investigation of Vortex-Induced Vibrations on Yawed and Inclined Flexible Cylinders. *Journal of Offshore Mechanics and Arctic Engineering*, *144*(1). https://doi.org/10.1115/1.4051650

Viespoli, L. M., Johanson, A., Alvaro, A., Nyhus, B., & Berto, F. (2020). Subsea power cable sheathing: An investigation of lead fatigue performance. *Procedia Structural Integrity*, *28*, 344–351. https://doi.org/10.1016/j.prostr.2020.10.040

Warren, W. F. (1962). *An experimental investigation of fluid forces on an oscillating cylinder.*

Weaver, W. Jr. (1961). Wind-induced vibrations in antenna-members. *ASCE 87*, 141–149.

Weerheim, R. (2018). *Development of dynamic power cables for commercial floating wind farms Literature Assignment*.

Williamson, C. H. K., & Govardhan, R. (2004). Vortex-induced vibrations. *Annual Review of Fluid Mechanics*. https://doi.org/10.1146/annurev.fluid.36.050802.122128

Wu, J., Lekkala, M. K. R., & Ong, M. C. (2020). Numerical Investigation of Vortex-Induced Vibrations of a Flexible Riser with Staggered Buoyancy Elements. In *Applied Sciences* (Vol. 10, Issue 3). https://doi.org/10.3390/app10030905

Wu, J., Lie, H., Fu, S., Baarholm, R., & Constantinides, Y. (2017). *VIV Responses of Riser With Buoyancy Elements: Forced Motion Test and Numerical Prediction*. https://doi.org/10.1115/OMAE2017-61768

Wu, J., Lie, H., Larsen, C. M., & Baarholm, R. J. (2015). *An Empirical Heave Induced VIV Prediction Model*. https://doi.org/10.1115/OMAE2015-42065

Xu, W., Ma, Y., Ji, C., & Sun, C. (2018). Laboratory measurements of vortex-induced vibrations of a yawed flexible cylinder at different yaw angles. *Ocean Engineering*, *154*, 27–42. https://doi.org/https://doi.org/10.1016/j.oceaneng.2018.01.113

Xu, W., Qin, W., & Gao, X. (2018). Experimental Study on Streamwise Vortex-Induced Vibration of a Flexible, Slender Cylinder. In *Applied Sciences* (Vol. 8, Issue 2). https://doi.org/10.3390/app8020311

Yang, S. H., Ringsberg, J. W., & Johnson, E. (2018). Parametric study of the dynamic motions and mechanical characteristics of power cables for wave energy converters. *Journal of Marine Science and Technology (Japan)*. https://doi.org/10.1007/s00773-017-0451-0

Yin, D. (2022). Heave Motion Induced Vortex-Induced Vibrations of a Full-Scale Steel Lazy Wave Riser. *Journal of Offshore Mechanics and Arctic Engineering*, *144*(4). https://doi.org/10.1115/1.4054265

Yuan, Z., Bao, S., Lin, J., Zhang, Z., Yu, Q., & Liu, Z. (2021). An overview of the vessels for electrical submarine cable laying. *Journal of Physics: Conference Series*, *1865*(3), 32083. https://doi.org/10.1088/1742-6596/1865/3/032083

Zhang, B., Chai, Y., Li, F., & Chen, Y. (2022). Three-dimensional nonlinear vortex-induced vibrations of top-tension risers considering platform motion. *Ocean Engineering*, *263*, 112393. https://doi.org/https://doi.org/10.1016/j.oceaneng.2022.112393

Zhang, J., Zeng, Y., Tang, Y., Guo, W., & Wang, Z. (2021). Numerical and Experimental Research on the Effect of Platform Heave Motion on Vortex-Induced Vibration of Deep-Sea Top-Tensioned Riser. *Shock and Vibration*, *2021*, 8866051. https://doi.org/10.1155/2021/8866051

Zhang, Y., & Tan, Z. (2011). *An Investigation of Fatigue Damage due to VIV in Flexible Riser With Different Methodologies* (pp. 25–33). https://doi.org/10.1115/OMAE2011-49036

Zhao, S., Cheng, Y., Chen, P., Nie, Y., & Fan, K. (2021). A comparison of two dynamic power cable configurations for a floating offshore wind turbine in shallow water. *AIP Advances*, *11*(3), 35302. https://doi.org/10.1063/5.0039221

Zhou, C., Xu, G., Huang, Z., Zhang, D., Ye, N., & Sævik, S. (2017). *The Study on the Influence of Pipe-Soil Interaction on VIV for Different Free Span Types*. https://doi.org/10.1115/OMAE2017-61117

Zhu, J., Ren, B., Dong, P., & Chen, W. (2023). Vortex-induced vibrations of a free spanning submarine power cable. *Ocean Engineering*, *272*, 113792. https://doi.org/https://doi.org/10.1016/j.oceaneng.2023.113792